Equilibrium adsorption and diffusional characteristics of H2 and CO2 in clathrate hydrates for development of gas separation processes

博 士 学 位 論 文

論文題目

Equilibrium adsorption and diffusional characteristics of H_2 and CO_2 in clathrate hydrates for development of gas separation processes

（ガス分離プロセス開発に向けたクラスレートハイドレートにおける H_2 と CO_2 の平衡吸着および拡散特性に関する研究）

提　出　者　　東北大学大学院環境科学研究科
環境化学・生態学コース
学籍番号　B1GD1304
氏名　小松　博幸

指導教員	**Richard Lee Smith, Jr.** 教 授
研究指導教員	渡邉 賢　准教授
審査委員 （○印は主査）	○ Richard Lee Smith, Jr. 教 授 1 駒井　武　　教 授　　2 猪股 宏　　教 授 （工学研究科）

提　出　者　略　歴		
ふりがな 氏 名	こまつ　ひろゆき 小松　博幸	昭和 61 年 6 月 3 日生
本 籍	秋田県	国籍

履　歴　事　項		
【学　歴】		
平成 17 年 4 月 1 日	東北大学工学部 化学・バイオ工学科	入学
平成 21 年 3 月 25 日	同	卒業
平成 21 年 4 月 1 日	東北大学大学院 環境科学研究科 博士課程前期 2 年の課程	入学
平成 23 年 3 月 25 日	同	修了
平成 23 年 4 月 1 日	東北大学大学院 環境科学研究科 博士課程後期 3 年の課程	進学
平成 26 年 3 月 26 日	同	修了
平成　年　月　日		
【職　歴】		
平成　年　月　日		
平成　年　月　日		
平成　年　月　日		

備考(1)　履歴事項は、大学入学から年次にしたがって記入すること。

(2)　修士課程の修了年月日は、学位記授与式年月日を記入すること。

Equilibrium adsorption and diffusional characteristics of H_2 and CO_2 in clathrate hydrates for development of gas separation processes

Hiroyuki Komatsu

A thesis submitted in partial fulfillment of
the requirements for the degree of
Doctor of Philosophy (Ph. D.)
in the Graduate School of Environmental Studies

Tohoku University
Sendai, Japan

March 26, 2014

Equilibrium adsorption and diffusional characteristics of H_2 and CO_2 in clathrate hydrates for development of gas separation processes

by
Hiroyuki Komatsu

Tohoku University
March 26, 2014

Thesis Committee

Richard Lee Smith Jr.
Committee Chair
Graduate School of Environmental Studies

Takeshi Komai
Graduate School of Environmental Studies

Hiroshi Inomata
Graduate School of Engineering

To my parents

Acknowledgements

I would like to take this opportunity to thank the people and organizations that have helped me accomplish this work.

First of all, I would like to offer my special gratitude to my research adviser Professor Richard Lee Smith Jr. for his guidance and invaluable advice throughout this work. I appreciate for giving me the great opportunity to study in his laboratory.

I would like to offer my gratitude to Professor Hiroshi Inomata for his support not only for this work but throughout my life. His encouragement and invaluable advice are appreciated.

I would like to offer my gratitude to Professor Takeshi Komai for serving on the committee and for making excellent and constructive suggestions on this work.

I would like to offer my gratitude to Dr. Masaru Watanabe for his support not only for this work but throughout my life. His encouragement and contribution to this work are appreciated. I appreciate the opportunity for working with him.

I would like to offer my gratitude Dr. Yoshiyuki Sato for providing guidance and contribution to this work, especially technique of chemical engineering measurement. I appreciate for giving me the opportunity to work with him.

I would like to offer my gratitude Dr. Masaki Ota for his support not only for this work but throughout my life. His encouragement and constructive discussion throughout this work have been appreciated. I appreciate for giving me the opportunity to work with him.

I would like to offer my gratitude Professor Cor J. Peters, Dr. Taku M. Aida, Dr. Masafumi Takesue, Dr. Takaaki Hoshina, Dr. Hiroshi Machida, Mr. Hiroki Yoshioka, Dr. Masayuki Iguchi and Dr. Takumi Ono for their support and constructive discussion throughout this work. I appreciate them for giving me this opportunity.

I would like to thank colleagues and members of the Smith Laboratory and Inomata Laboratory who cannot all be listed but would like to mention some members: Mr. Yasuaki Matsuo, Mr. Satoshi Ishizeki, Mr. Tatsuya Sagara, Mr. Hidemasa Machikawa, Mr. Toru Kawasumi, Mr. Ikuo Ushiki, Mr. Keisuke Takeda, Mr. Daisuke Saito, Mr. Koichiro Nomura, Mr. Naoki Hosaka, Mr. Yuya Hiraga, Ms. Chihiro Abe, Ms. Kaori Ishida, Mr. Kyouhei Osato, Mr. Shigeki Kubota, Ms. Chio Nomiyama, Mr. Taichi Shimizu, Mr. Kenji Oshima, Mr. Haruyuki Kitajima, Mr. Atsushi Hayasaka, Mr. Suguru Toyama, Ms. Asako Otomo, Ms. Emi Yoshida, Ms. Junko Hirama, Ms. Rina Yanbe, Ms. Aya Kato, Ms. Shiori Baba, Ms. Shiho Matsuda, Mr. Ryoma Maruta, Mr. Takuya Morioka, Mr. Keisuke Okada, Ms. Momoko Kato, Mr. Yasuaki Kumagai, Mr. Rui Takeuchi, Mr. Yoshimasa Higashino, Mr. Yukihiro Kanaguri, Mr. Musashi Goto, Mr. Hiroki Kujiraoka, Mr. Kazuki Miyagawa, Mr. Kento Koyama, Ms. Nanami Numaga and Mr. Takaaki Yoshii.

I would like to acknowledge the experimental support of Dr. Satoshi Takeya (National Institute of Advanced Industrial Science and Technology) and Dr. Shunsuke Mochizuki, Ms. Mana Nemoto, Mr. Mikio Kikuchi, Mr. Hiroaki Saito and Mr. Syunsuke Kayamori.

I would like to gratefully acknowledge Japan Society for the Promotion of Science for partial financial support of this research through a Grant-in-Aid for Scientific Research and a doctoral course fellowship.

I am grateful to Ms. Natsuki Chubachi for her strong love and support during my graduate study.

Finally, I would like to thank my mother and father and all family members for providing unfailing support and love throughout my life.

Hiroyuki Komatsu

Tohoku University, Sendai Japan

March 2014

Table of Contents

Chapter 1

Introduction

1.1 Clathrate hydrates as energy resources

The increasing demand for energy to supply the needs of society and the escalating human population has led to accelerated mining and combustion of fossil fuels. Massive fossil fuel consumption has brought about increased levels of atmospheric carbon dioxide. Against this background of worldwide trends, natural gas is expected to be a future energy resource as the world moves from liquid-based fossil fuels to gas-based renewable fuel sources that include hydrogen. Natural gas is characterized by a lower discharge of CO_2 at the time of combustion than coal or petroleum. Thus, techniques for gas recovery, storage, transportation, separation along with methods for sequestration are needed both in the present and for the future. Clathrate hydrates in the form of natural gas hydrates are energy resources, but clathrate hydrates can also act as storage media or provide selective separations and they have the possibility of being able to sequester carbon. In the next section, methane clathrate hydrates that exist in the ocean and permafrost

zones of the world, will be introduced. Then, clathrate hydrates that can be used in hydrogen storage are overviewed. Finally, semi-clathrate hydrates that have potential for gas separations are discussed. The subject of this thesis is regarding the properties and characteristics of clathrate hydrates for gas separation processes.

1.1.1 Methane clathrate hydrate

Clathrate hydrates are crystalline compounds that have water as its hydrogen-bonding framework. Cages within the structure of these compounds provide the means for inclusion of gas molecules as in the schematic diagram (Figure 1-1).

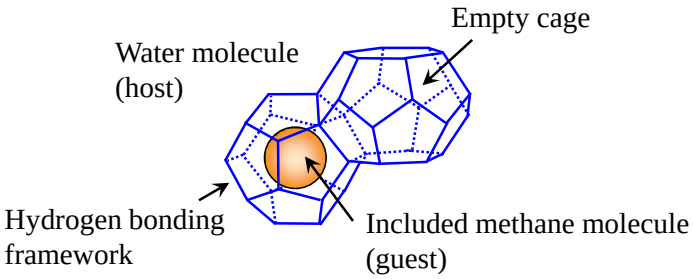

Figure 1-1. Schematic diagram of methane clathrate hydrate.

Methane clathrate hydrates are usually called natural gas hydrates or gas hydrates. Gas clathrate hydrates have been confirmed in many regions of the world by bottom-simulating reflector (BSR) measurements[1-4] and by actual recovery with sampling.[5-7] Worldwide amounts of organic carbon bound in these natural gas hydrates can be conservatively estimated to total twice the amount of carbon found in all known fossil fuels on the Earth.[8,9] Natural gas resources in the form of clathrate hydrates have been estimated to be up to 50 times that of conventional petroleum reserves, with as much as 2500-20000 trillion cubic meters of methane being available.[10] These huge

amounts of natural gas hydrates exist below ocean floors and in permafrost zones around a number of regions in the world.[4-7,11] In the Canadian Arctic off the Mackenzie Delta, thermal stimulation tests were conducted in 2002 by the Japex, JNOC and GSC [12], and depressurization tests to produce methane from hydrate were conducted in 2008 by JOGMEC and NRCan.[13] In the Prudhoe Bay Unit on the Alaska North Slope, tests of natural gas extraction from methane hydrate using CO_2-CH_4 exchange methodology were conducted by Japan Oil, JOGMEC, ConocoPhillips and the U.S. Department of Energy[14,15] in which CO_2 was injected to produce methane from hydrate in 2008. This technology was developed, and tests were performed with a mixtures of CO_2 and N_2 to demonstrate the production of natural gas successfully in 2012. The recovery of methane from hydrates under the seafloor methods has been investigated in Japan (Figure 1-2).[16,17] A detailed treatise on natural gas hydrates is available in the monograph by Sloan and Koh.[18]

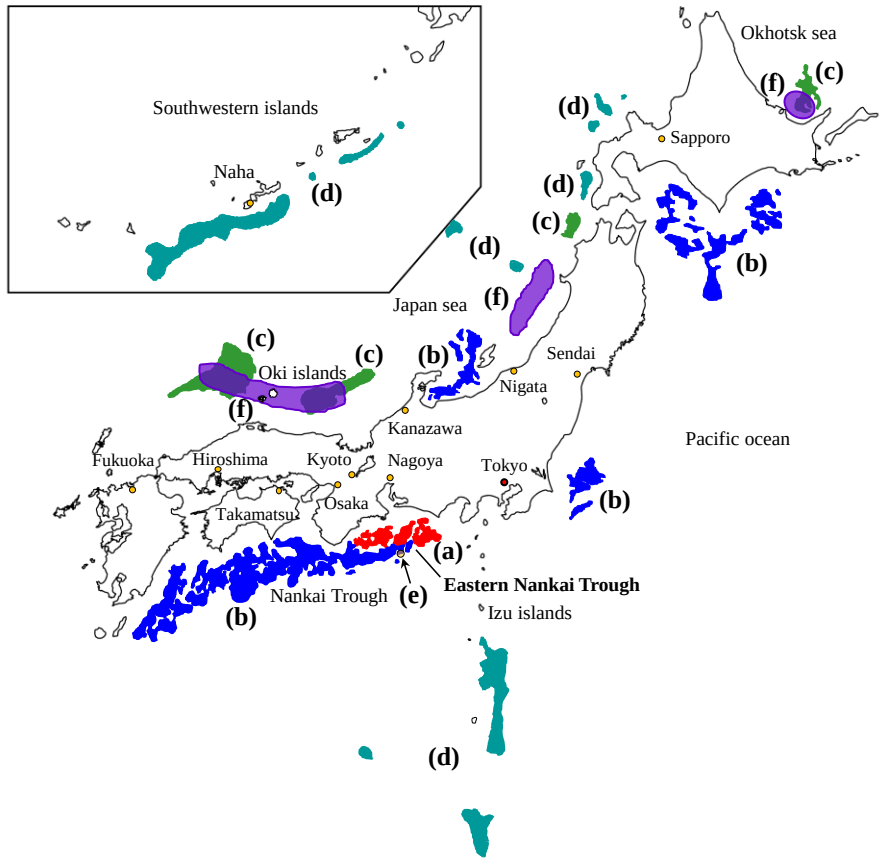

Figure 1-2. Distribution chart of bottom-simulating reflector (BSR) around Japan[19] showing points of the production test in Eastern Nankai trough[20] and regions of newly discovered methane hydrates[21-23]: (a): red zone[19] methane hydrate concentrated zones are confirmed partially by detailed surveys: 5,000 km^2; (b): blue zone[19] probable methane hydrate concentrations: 61,000 km^2; (c): green zone[19] unconfirmed methane hydrate concentrations: 20,000 km^2; (d): blue-green zone[19] surveys insufficient for evaluation: 36,000 km^2; (e): decompression procedure is underway for recovery of methane gas from methane hydrates probably in 2012[20]; (f): purple zone presence of methane hydrates confirmed and some recovery has been made of methane hydrate or gas by research groups at Meiji university, Kitami Institute of technology, and Tokyo university.[21-23]

1.1.2 Carbon dioxide sequestration in the marine sediment

Geological sequestration is regarded as a leading candidate for carbon dioxide capture and storage (CCS).[24] Among all CSS options, ocean sequestration may be the most feasible choice for long-term storage of captured anthropogenic CO_2. Since the pressures and temperatures at ocean depths are suitable for CO_2 clathrate hydrate formation,[25,26] techniques for CO_2 sequestration as clathrate hydrates have been investigated. When CO_2 is injected into the sea floor, a hydrate stratum is generated which forms a self-sealed structure. These hydrates sink toward the deep sea bottom where they stabilize in the long term.[27,28] The CO_2 leakage rate during sequestration into marine sedimentary strata was simulated, and the results show that the effectiveness of CO_2 ocean sequestration depends mainly on the injection conditions, the site geology and the chemical-physical behavior of CO_2 in the marine environment.[29] Additionally, the technique of CCS with combination of the methane in recovery[30] and the integrated gasification combined cycle (IGCC) [31,32] has been proposed.

1.1.3 Clathrate hydrate in hydrogen storage applications

Applications of clathrate hydrate have been considered in the development of many types of renewable resources such as in distributed energy systems[33,34] with hydrogen or biogas systems. Hydrogen clathrate hydrates form structure II at high pressures (≈ 200 MPa)[35] because molecular size of hydrogen is very small. Organic liquids such as tetrahydrofuran (THF) stabilize the structure of the clathrate hydrate above 273 K at atmospheric pressure as shown schematically in Figure 1-3.[36]

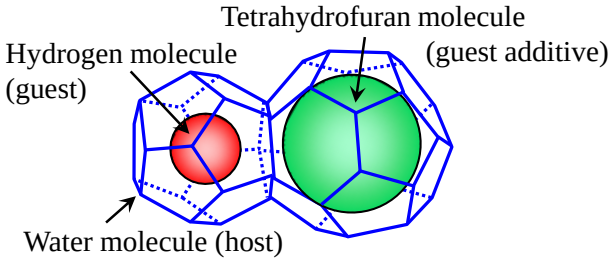

Figure 1-3. Schematic diagram of hydrogen-tetrahydrofuran binay clathrate hydrate.

The amount of hydrogen that can be stored in 5.6 mol% THF clathrate hydrate is lower than 1.05 wt% at 270 - 278 K (temperature cycled method) and 60 MPa,[37] at 277 K and 200 MPa[38] for occupancy of hydrogen in all larger hexakaidecahedral ($5^{12}6^4$) cavities (L-cage) with THF molecules. In H_2-0.6 mol% THF or acetone binary clathrate hydrates formed from ice particles, hydrogen storage can be increased to *ca*. 3.5 wt% at 255 K and 74 MPa due to occupancy of L-cages with 4 hydrogen molecules.[39] Clathrate hydrates have characteristics such as complete recovery of H_2 without using high temperature[36] and repeated use without degradation [40] so that the H_2 + guest additive molecule binary clathrate hydrate can be anticipated as a hydrogen storage material. Other potential applications for H_2 clathrate hydrates are as buffer or membrane materials. With the exception of H_2, the applications of clathrate hydrate for fuel storage and transportation have been investigated.[41,42]

1.1.4 Semi-clathrate hydrates for gas separations

Clathrate hydrate systems for gas separations have been investigated along with their physical properties.[43-47] A semi-clathrate hydrate is formed when an ionic compound such as a quaternary ammonium salt (QAS) replaces part of the water in the hydrogen bonding framework. A

semi-clathrate hydrate is shown schematically in Figure 1-4.

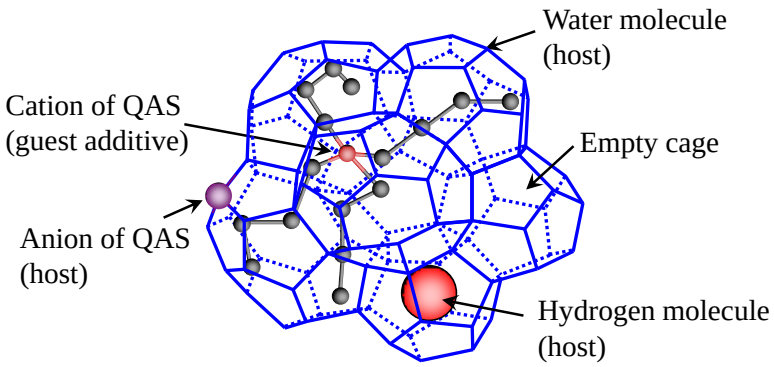

Figure 1-4. Schematic diagram of quaternary ammonium salt (QAS) semi-clathrate hydrate.

Semi-clathrate hydrates investigated in terms of gas separation media,[48-55] because they are more stable than THF clathrate hydrates.[56] In semi-clathrate hydrates, QAS replaces a small percentage of H_2O molecules to form a hydrate framework with the tetra-*n*-butyl ammonium cation (TBA^+) being included as guest molecule or guest additive and anions (Br^-) substituting some number of host molecules.[57] Semi-clathrate hydrates can be used repeatedly in many applications because the included salts are involatile unlike organic additives such as THF. The characteristics of semi-clathrate hydrates vary greatly according to the type of QAS that is added, so that the gas adsorption behavior depends on many factors that have not been elucidated yet. A better understanding of the role of QAS in semi-clathrate hydrate applications can be obtained by varying some of the anions systematically, so that characteristics of the particles formed can be related to gas adsorption behavior. In this thesis, the effect of the anion (Br^-, Cl^- and F^-) of the TBA salt on the adsorption characteristics of semi-clathrate hydrate is investigated.

Typical structures of semi-clathrate hydrates are tetragonal structure-I (TS-I), hexagonal structure-I (HS-I) and super cubic structure-I (SCS-I) for TBA salts as discussed in Chapter 2. The

structures of semi-clathrate hydrates depend on the anion species and the concentration of the TBA salt. For TBAB semi-clathrate hydrate, the dissociation temperatures for these structures which are important for practical application are different.[56] For TBA chloride (TBAC) semi-clathrate hydrate, structure TS-I forms regardless of the concentration of TBAC,[58] thus there are not clear metastable phases[59] such as those observed for TBAB semi-clathrate hydrates.[56] For TBA fluoride (TBAF) semi-clathrate hydrates, two structure types have been observed as TS-I[60] and SCS-I,[60,61] in which there are not clear metastable phases, regardless of the structure.[61,62] Thus, structure characteristics for TBAF and TBAC semi-clathrate hydrates are distinctly different from TBAB semi-clathrate hydrates.

Investigations regarding the structure and phase equilibria of semi-clathrate hydrates have been reported, however, studies regarding the gas adsorption rate of semi-clathrate hydrate particles are scarce. Maximum theoretical H_2 storage capacity depends on the clathrate or semi-clathrate hydrate structure,[63] thus control of hydrate structure is an important issue in the use of semi-clathrate hydrate as separation media.

1.2 Goal and objectives

The goal of this thesis is to assess clathrate hydrates as separation media for H_2/CO_2 gas mixtures. To make progress towards the goal, the following objectives were formulated according to chapter arrangement:

Objective 1 is to summarize the literature on available structural information and properties of clathrate hydrates, especially with respect to potential applications with the target gases H_2 and CO_2 (Chapter 2).

Objective 2 is to understand the effect that the anion of the TBA salt and hydrate crystal structure has on the phase equilibria of H_2 and CO_2 + TBA salt + water systems and to estimate probable operating conditions for a gas separation process (Chapter 3).

Objective 3 is to develop a kinetic model for gas adsorption in clathrate hydrate particles that describes gas adsorption behavior and to understand mechanisms of gas adsorption and gas diffusion (Chapter 4).

Objective 4 is to analyze the gas adsorption behavior of semi-clathrate hydrate particles for the purpose of estimating the gas separation potential of semi-clathrate hydrates for the target gases and gas mixtures (H_2, CO_2, and H_2 and CO_2) (Chapter 5).

1.3 References

1. Miller JJ, Lee MW, Vonhuene R. An analysis of a seismic-reflection from the base of a gas hydrate zone, offshore peru. Aapg Bull. 1991;75:910-924.
2. Hyndman RD, Spence GD. A seismic study of methane hydrate marine bottom simulating reflectors. J Geophys Res-Sol Ea. 1992;97:6683-6698.
3. Singh SC, Minshull TA, Spence GD. Velocity structure of a gas hydrate reflector. Science. 1993;260:204-207.
4. Kastner M, Claypool G, Robertson G. Geochemical constraints on the origin of the pore fluids and gas hydrate distribution at Atwater Valley and Keathley Canyon, northern Gulf of Mexico. Mar Petrol Geol. 2008;25:860-872.
5. Kida M, Suzuki K, Kawamura T, Oyama H, Nagao J, Ebinuma T, Narita H, Suzuki H, Sakagami H, Takahashi N. Characteristics of natural gas hydrates occurring in pore-spaces of marine sediments collected from the Eastern Nankai Trough, off Japan. Energ Fuel. 2009;23:5580-5586.
6. Ryu BJ, Riedel M, Kim JH, Hyndman RD, Lee YJ, Chung BH, Kim IS. Gas hydrates in the western deep-water Ulleung Basin, East Sea of Korea. Mar Petrol Geol. 2009;26:1483-1498.
7. Pohlman JW, Kaneko M, Heuer VB, Coffin RB, Whiticar M. Methane sources and production in the northern Cascadia margin gas hydrate system. Earth. Planet. Sci. Lett. 2009;287:504-512.
8. Collett TS. Energy resource potential of natural gas hydrates. Aapg Bulletin. 2002;86:1971-1992.
9. Demirbas A. Methane hydrates as potential energy resource: Part 2-Methane production processes from gas hydrates. Energ Convers Manage. 2010;51:1562-1571.
10. *World Energy Outlook 2008*.International Energy Agency; 2008.
11. Demirbas A. Methane from gas hydrates in the Black Sea. Energ Source Part A. 2010;32:165-171.
12. GFZ. Mallik 2002: Spatial and Temporal Variation of Temperature During a Gas Hydrate Production. 2009; http://www.gfz-potsdam.de/portal/gfz/Struktur/Departments/Department+4/sec41/M2_Projekte/030+abgeschlossene+Projekte/A110+Mallik. Accessed February 20, 2013.
13. GEO. Gas Hydrates-Not So Unconventional. 2009; http://www.geoexpro.com/article/Gas_HydratesNot_So_Unconventional/b9d997f9.aspx. Accessed February 20, 2013.
14. DOE. Fossil Energy: DOE's Methane Hydrate Field Studies. 2012;

http://www.fossil.energy.gov/programs/oilgas/hydrates/fieldstudies.html. Accessed February 20, 2013.

15. NETL. The National Methane Hydrates R&D Program DOE/NETL Methane Hydrate Projects. 2013; http://www.netl.doe.gov/technologies/oil-gas/FutureSupply/MethaneHydrates/projects/DOEProjects/MH_06553HydrateProdTrial.html. Accessed February 20, 2013.
16. MH21. Japan's Methane Hydrate R&D Program. 2011; http://www.mh21japan.gr.jp/english/infomation/558/. Accessed February 20, 2013.
17. Uchida T, Tsuji T. Petrophysical properties of natural gas hydrates-bearing sands and their sedimentology in the Nankai Trough. Resour Geol. 2004;54:79-87.
18. Sloan ED, Koh CA. *Clathrate hydrates of natural gases, 3rd Ed.*CRC Press; Boca Raton. 2007.
19. MH21. Latest BSR distribution chart (2009). 2009; http://www.mh21japan.gr.jp/english/mh21-1/2-2/. Accessed February 20, 2013.
20. MH21. First marine production test for methane hydrate. 2012-2013; http://www.mh21japan.gr.jp/mh21/kss/. Accessed February 20, 2013.
21. Methane hydrate in Japanese Sea and Okhotsk Sea. *Nippon Keizai Shimbun* 2012/10/29, 2012.
22. Future generation energy. Discovered widely methane hydrate around Japan. *Tokyo Shimbun.* 2012/10/30, 2012.
23. Presence of methane hydrate in Japanese Sea and Okhotsk Sea. *Nikkei Shimbun.* 2012/10/30, 2012.
24. Metz B, Davidson O, de Coninck H, Loos M, Meyer L. *IPCC Special Report on Carbon Dioxide Capture and Storage*2005.
25. Aya I, Yamane K, Yamada N. Simulation experiment of CO_2 storage in the basin of deep-ocean. Energ Convers Manage. 1995;36:485-488.
26. Brewer PG, Friederich C, Peltzer ET, Orr FM. Direct experiments on the ocean disposal of fossil fuel CO_2. Science. 1999;284:943-945.
27. Harrison WJ, Wendlandt RF, Sloan ED. Geochemical interactions resulting from carbon-dioxide disposal on the sea-floor. Appl Geochem. 1995;10:461-475.
28. Lee S, Liang LY, Riestenberg D, West OR, Tsouris C, Adams E. CO_2 hydrate composite for ocean carbon sequestration. Environ Sci Technol. 2003;37:3701-3708.
29. Li Q, Wu ZS, Li XC. Prediction of CO_2 leakage during sequestration into marine sedimentary strata. Energ Convers Manage. 2009;50:503-509.

30. White CM, Smith DH, Jones KL, Goodman AL, Jikich SA, LaCount RB, DuBose SB, Ozdemir E, Morsi BI, Schroeder KT. Sequestration of carbon dioxide in coal with enhanced coalbed methane recovery - A review. Energ Fuel. 2005;19:659-724.
31. Cormos CC. Evaluation of power generation schemes based on hydrogen-fuelled combined cycle with carbon capture and storage (CCS). Int J Hydrogen Energ. 2011;36:3726-3738.
32. Li M, Rao AD, Samuelsen GS. Performance and costs of advanced sustainable central power plants with CCS and H_2 co-production. Appl Energ. 2012;91:43-50.
33. Alarcon-Rodriguez A, Ault G, Galloway S. Multi-objective planning of distributed energy resources: A review of the state-of-the-art. Renew Sust Energ Rev. 2010;14:1353-1366.
34. Mohammed YS, Mustafa MW, Bashir N, Mokhtar AS. Renewable energy resources for distributed power generation in Nigeria: A review of the potential. Renew Sust Energ Rev. 2013;22:257-268.
35. Mao WL, Mao HK, Goncharov AF, Struzhkin VV, Guo QZ, Hu JZ, Shu JF, Hemley RJ, Somayazulu M, Zhao YS. Hydrogen clusters in clathrate hydrate. Science. 2002;297:2247-2249.
36. Florusse LJ, Peters CJ, Schoonman J, Hester KC, Koh CA, Dec SF, Marsh KN, Sloan ED. Stable low-pressure hydrogen clusters stored in a binary clathrate hydrate. Science. 2004;306:469-471.
37. Strobel TA, Taylor CJ, Hester KC, Dec SF, Koh CA, Miller KT, Sloan ED. Molecular hydrogen storage in binary THF-H_2 clathrate hydrates. J Phys Chem B. 2006;110:17121-17125.
38. Ogata K, Hashimoto S, Sugahara T, Moritoki M, Sato H, Ohgaki K. Storage capacity of hydrogen in tetrahydrofuran hydrate. Chem Eng Sci. 2008;63:5714-5718.
39. Sugahara T, Haag JC, Warntjes AA, Prasad PSR, Sloan ED, Koh CA, Sum AK. Large-cage occupancies of hydrogen in binary clathrate hydrates dependent on pressures and guest concentrations. J Phys Chem C. 2010;114:15218-15222.
40. Yoshioka H, Ota M, Sato Y, Watanabe M, Inomata H, Smith RL, Peters CJ. Decomposition kinetics and recycle of binary hydrogen-tetrahydrofuran clathrate hydrate. AIChE J. 2011;57:265-272.
41. Chatti I, Delahaye A, Fournaison L, Petitet JP. Benefits and drawbacks of clathrate hydrates: a review of their areas of interest. Energ Convers Manage. 2005;46:1333-1343.
42. Koh CA, Sloan ED, Sum AK, Wu DT. Fundamentals and applications of gas hydrates. Annu Rev Chem Biomol. 2011;2:237-257.
43. Kang SP, Lee H. Recovery of CO_2 from flue gas using gas hydrate: Thermodynamic verification

through phase equilibrium measurements. Environ Sci Technol. 2000;34:4397-4400.

44. Linga P, Adeyemo A, Englezos P. Medium-pressure clathrate hydrate/membrane hybrid process for postcombustion capture of carbon dioxide. Environ Sci Technol. 2008;42:315-320.

45. Adeyemo A, Kumar R, Linga P, Ripmeester J, Englezos P. Capture of carbon dioxide from flue or fuel gas mixtures by clathrate crystallization in a silica gel column. Int J Greenh Gas Control. 2010;4:478-485.

46. Song YC, Wan XJ, Yang MJ, Jiang LL, Liu Y, Dou BL, Zhao JF, Wang SR. Study of selected factors affecting hydrate-based carbon dioxide separation from simulated fuel gas in porous media. Energ Fuel. 2013;27:3341-3348.

47. Tang J, Zeng D, Wang C, Chen Y, He L, Cai N. Study on the influence of SDS and THF on hydrate-based gas separation performance. Chem Eng Res Des. 2013;91:1777-1782.

48. Shimada W, Ebinuma T, Oyama H, Kamata Y, Takeya S, Uchida T, Nagao J, Narita H. Separation of gas molecule using tetra-*n*-butyl ammonium bromide semi-clathrate hydrate crystals. Jpn J Appl Phys Part 2. 2003;42:L129-L131.

49. Kamata Y, Yamakoshi Y, Ebinuma T, Oyama H, Shimada W, Narita H. Hydrogen sulfide separation using tetra-*n*-butyl ammonium bromide semi-clathrate (TBAB) hydrate. Energ Fuel. 2005;19:1717-1722.

50. Duc NH, Chauvy F, Herri JM. CO_2 capture by hydrate crystallization - A potential solution for gas emission of steelmaking industry. Energ Convers Manage. 2007;48:1313-1322.

51. Li SF, Fan SS, Wang JQ, Lang XM, Liang DQ. CO_2 capture from binary mixture via forming hydrate with the help of tetra-*n*-butyl ammonium bromide. J Nat Gas Chem. 2009;18:15-20.

52. Zhong DL, Ye Y, Yang C, Bian Y, Ding K. Experimental investigation of methane separation from low-concentration coal mine gas ($CH_4/N_2/O_2$) by tetra-*n*-butyl ammonium bromide semiclathrate hydrate crystallization. Ind Eng Chem Res. 2012;51:14806-14813.

53. Xu CG, Zhang SH, Cai J, Chen ZY, Li XS. CO_2 (carbon dioxide) separation from CO_2-H_2 (hydrogen) gas mixtures by gas hydrates in TBAB (tetra-*n*-butyl ammonium bromide) solution and Raman spectroscopic analysis. Energy. 2013;59:719-725.

54. Park S, Lee S, Lee Y, Seo Y. CO_2 capture from simulated fuel gas mixtures using semiclathrate hydrates formed by quaternary ammonium salts. Environ Sci Technol. 2013;47:7571-7577.

55. Fan SS, Li SF, Wang JQ, Lang XM, Wang YH. Efficient capture of CO_2 from simulated flue gas by formation of TBAB or TBAF semiclathrate hydrates. Energ Fuel. 2009;23:4202-4208.

56. Oyama H, Shimada W, Ebinuma T, Kamata Y, Takeya S, Uchida T, Nagao J, Narita H. Phase

diagram, latent heat, and specific heat of TBAB semiclathrate hydrate crystals. Fluid Phase Equilib. 2005;234:131-135.

57. Davidson DW. *Water - A Comprehensive Treatise*. Vol 2.Plenum Press; New York. 1973.

58. Rodionova T, Komarov V, Villevald G, Aladko L, Karpova T, Manakov A. Calorimetric and structural studies of tetrabutylammonium chloride ionic clathrate hydrates. J Phys Chem B. 2010;114:11838-11846.

59. Aladko LS, Dyadin YA. Clathrate formation in the Bu_4NCl-NH_4Cl-H_2O system. Mendeleev Commun. 1996:198-200.

60. Dyadin YA, Terekhova IS, Polyanskaya TM, Aladko LS. Clathrate hydrates of tetrabutylammonium fluoride and oxalate. J Struct Chem. 1976;17:566-571.

61. Komarov VY, Rodionova TV, Terekhova IS, Kuratieva NV. The cubic superstructure-I of tetrabutylammonium fluoride $(C_4H_9)_4NF \cdot 29.7H_2O$ clathrate hydrate. J Inclusion Phenom Macro. 2007;59:11-15.

62. Sakamoto J, Hashimoto S, Tsuda T, Sugahara T, Inoue Y, Ohgaki K. Thermodynamic and Raman spectroscopic studies on hydrogen + tetra-*n*-butyl ammonium fluoride semi-clathrate hydrates. Chem Eng Sci. 2008;63:5789-5794.

63. Strobel TA, Koh CA, Sloan ED. Hydrogen storage properties of clathrate hydrate materials. Fluid Phase Equilib. 2007;261:382-389.

Chapter 2

Literature review

2.1 Introduction

Fundamental properties for applications with clathrate hydrates are important in the development of new technologies. In this chapter, the characteristics of clathrate hydrates are reviewed with a focus on crystal structure, phase equilibria, clathrate hydrate formation and dissociation kinetics for the purpose of proposing new gas separation methods and gas storage options. On the basis of the theory of clathrate hydrates, semi-clathrate hydrates formed with quaternary ammonium salts (QAS) are introduced as inclusion compounds that have many favorable properties.

2.2 Clathrate hydrate structure

2.2.1 Theory of classical structure

The structure of a clathrate hydrate depends on the guest molecules in the cavity of its cages

that are composed of hydrogen-bonded water molecules. Clathrate hydrates, which are crystalline solids, typically form when small (< 0.9 nm) guest molecules such as CH_4 or CO_2 become surrounded by water molecules under appropriate conditions of temperature and pressure so that a cage structure forms around the guest molecule. Figure 2-1 shows the types of structures of clathrate hydrates, and Table 2-1 summarizes their geometric characteristics.

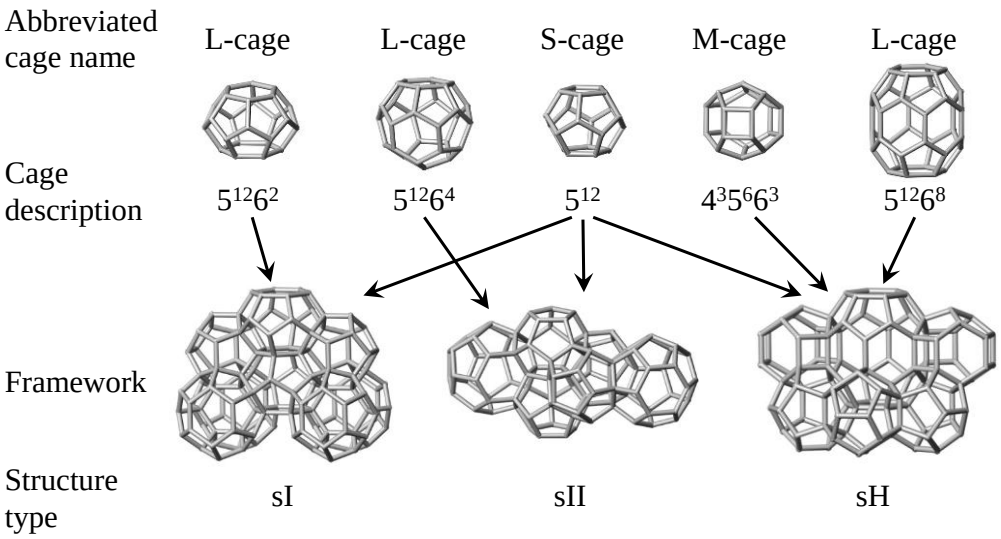

Figure 2-1. Hydrate crystal structure type and their framework cages

Table 2-1. Geometric characteristics of clathrate hydrate crystal structures

	Structure type						
Characteristic	sI		sII		sH		
Cage	Small	Large	Small	Large	Small	Medium	Large
Description	5^{12}	$5^{12}6^2$	5^{12}	$5^{12}6^4$	5^{12}	$4^35^66^3$	$5^{12}6^8$
Number of cages per unit cell	2	6	16	8	3	2	1
Average cage radius [Å]	3.95	4.33	3.91	4.73	3.91	4.06	5.71
Coordination number*	20	24	20	28	20	20	36
Number of waters per unit cell	46		136		34		

*Number of oxygens at the periphery of each cage.

The formed hydrate crystal structure depends on the ratio between the van der Waals diameter and the free space diameter. The free space diameter is defined as the length that remains after subtracting the van der Waals diameter of water molecule (2.8 Å) from the average cavity diameter (Table 2-1). Table 2-2 summarizes the relationship between the ratio of the van der Waals diameter and the free space diameter according to the structure type.

Table 2-2. Relationship between guest molecule van der Waals diameter (d_{vdw}), free space diameter (d_{fs}) and structure for clathrate hydrates

Guest molecule		d_{fs} for sI		d_{fs} for sII		Structure type formed
		5^{12}(5.10 Å)	$5^{12}6^2$(5.86 Å)	5^{12}(5.02 Å)	$5^{12}6^4$(6.64 Å)	
Molecule	d_{vdw} [Å]	(d_{vdw} / d_{fs}) for each cage type				
He	2.28	0.447	0.389	0.454	0.342	sII
H_2	2.72	0.533	0.464	0.542	0.408	
Ne	2.97	0.582	0.507	0.592	0.446	
Ar	3.8	0.745	0.648	0.757	0.571	
Kr	4.0	0.784	0.683	0.797	0.601	
N_2	4.1	0.804	0.700	0.817	0.616	
O_2	4.2	0.824	0.717	0.837	0.631	
CH_4	4.36	0.855	0.744	0.868	0.655	sI
Xe	4.58	0.898	0.782	0.912	0.687	
H_2S	4.58	0.898	0.782	0.912	0.687	
CO_2	5.12	1.00	0.834	1.02	0.769	
C_2H_6	5.5	1.08	0.939	1.10	0.826	
c-C_3H_6	5.8	1.14	0.990	1.16	0.871	
$(CH_2)_3O$	6.1	1.20	1.04	1.22	0.916	sII
C_3H_8	6.28	1.23	1.07	1.25	0.943	
i-C_4H_{10}	6.5	1.27	1.11	1.29	0.976	
n-C_4H_{10}	7.1	1.39	1.21	1.41	1.07	

Guest molecules that are smaller than O_2 (4.2 Å) typically form structure II for which a higher proportion of S-cages exist than for structure I (Table 2-1) because small guest molecules are more stable in an S-cage than in an L-cage. Guest molecules that are larger than CH_4 (4.36 Å) typically form structure I as this structure has a higher proportion of L-cages than structure II (Table 2-1) as the larger guest molecules are stable in the L-cage of structure I. Guest molecules such as $(CH_2)_3O$ for which the van der Waals diameter is larger than 6 Å form structure II because the guest molecule cannot be included in the L-cage of structure I. Guest molecules such as methylcyclohexane (MCH) for which the van der Waals diameter is larger than 7.5 Å form structure H due to the size of the L-cage of structure H (Figure 2-1). In this case, additional gas molecules such as CH_4 are needed for inclusion in S-cage and M-cage for structure H because the number of the L-cages of sH per unit cell is limited to one (Table 2-1).

2.2.2 Semi-clathrate hydrate systems

Figure 2-2 shows typically semi-clathrate hydrate crystal structures, and Table 2-3 summarizes ideal semi-clathrate hydrate crystal structures. A semi-clathrate hydrate differs from a clathrate hydrate in that an additive QAS replaces some of the water molecules in the clathrate hydrate structure. Table 2-4 summarizes reported semi-clathrate hydrate structures.

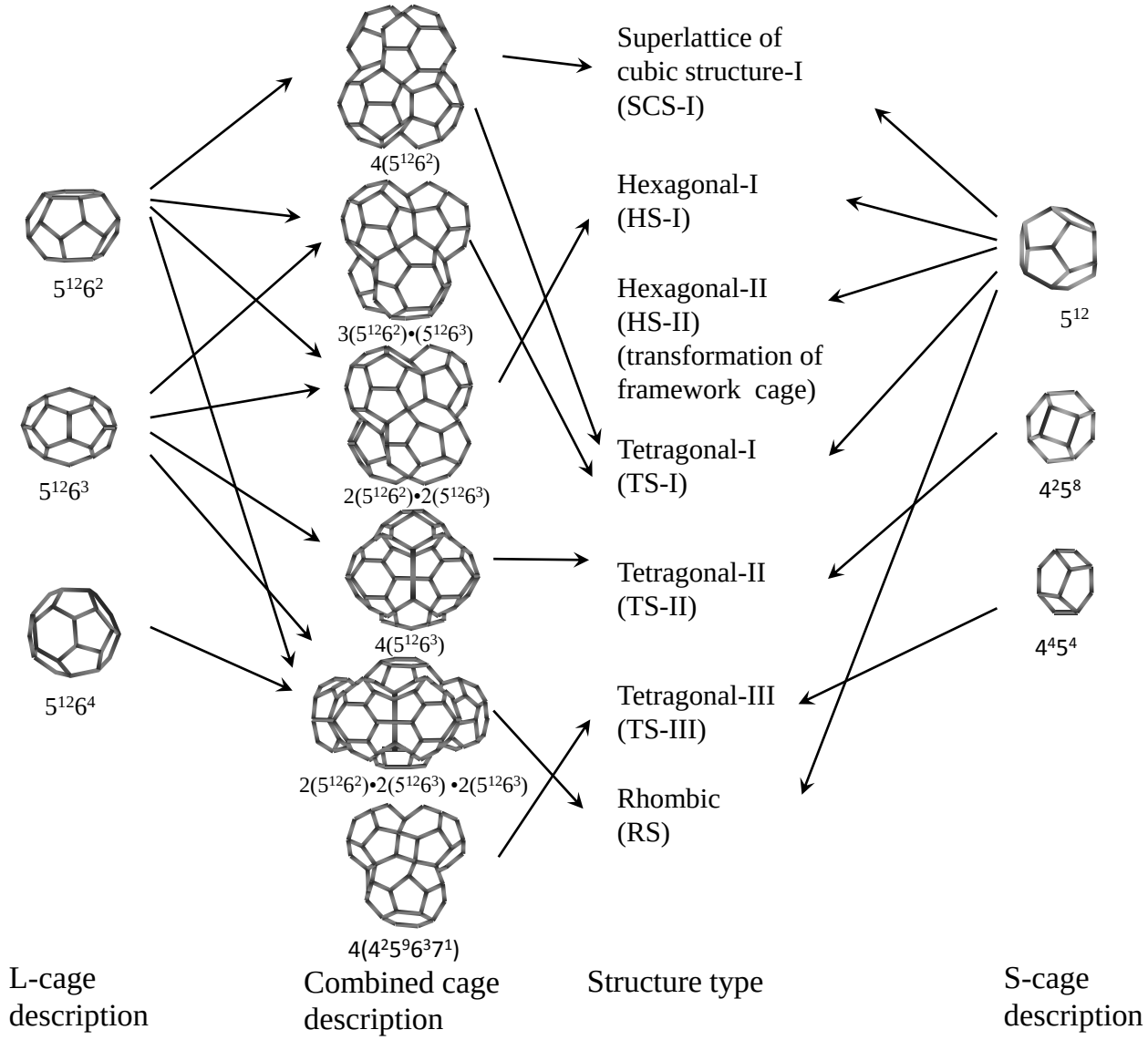

Figure 2-2. Semi-clathrate hydrate crystal structure. S-cage is gas included cage, and combined L-cage is quaternary ammonium salt (QAS) included cage.

Table 2-3. Ideal crystal structures of semi-clathrate hydrate.

Structure type	$N_{\mathrm{ideal,\ H_2O}}$	Lattice constants [Å]			Cage description							Reference
		a	b	c	$4^4 5^4$	$4^2 5^8$	5^{12}	$5^{12}6^2$	$5^{12}6^3$	$5^{12}6^4$	$7^1 6^3 5^9 4^2$	
		Number of cages in unit cell										
Hexagonal (HS-I)	40	12.4		12.5			3	2	2			McMullan(1959)[1]
Hexagonal (HS-II)	68	12.1		19.7			8			4		McMullan(1970)[2]
Tetragonal I(TS-I)	172	23.5		12.3			10	16	4			McMullan(1963)[3]
Tetragonal II (TS-II)	68	15.4				4			8			Solobovnikov(1979)[4]
Tetragonal III (TS-III)	108	16.894		17.111	4						16	Lipkowski(1994)[5]
Rhombic (RS)	148	23.5	19.9	12.1			14	4	4	4		Alekseev(1982)[6]
Superlattice of cubic structure-I (SCS-I)	368						16	48				Dyadin(1976)[7]

$N_{\mathrm{ideal,\ H_2O}}$: ideal number of water molecules per unit cell

Table 2-4. Reported semi-clathrate hydrate crystal structures.

Guest molecule	Crystal system	$N^*_{H_2O}$	$N_{additive\ QAS}$	Lattice constants [Å]			Cage description							Reference
							5^44^4	4^25^8	5^{12}	$5^{12}6^2$	$5^{12}6^3$	$5^{12}6^4$	$7^16^35^94^2$	
				a/α	b/β	c/γ	Number of cages in unit cell							
$(C_4H_9)_3PO$	orthorhombic	34.5	4	23.479	19.949	12.136			14	4	4	4		Alekseev[6]
$(C_4H_9)_4NF$	cubic	28.6	12	24.4										Dyadin[7]
$(C_4H_9)_4NF$	tetragonal	32.3	5	23.5		12.3								Dyadin[7]
$(C_4H_9)_4NF$	tetragonal	32.8	5	23.52		12.3								McMullan[3]
$(C_4H_9)_4NF$	tetragonal	34	5	23.78		12.53								McMullan[1]
$(C_4H_9)_4NF$	cubic	29.7	12	24.375					2	6				Komarov[8]
$(C_4H_9)_4NCl$	tetragonal	24.5		23.608		12.561			10	16	4			Rodionova[9]
$(C_4H_9)_4NCl$	rhombic	24		29	21	11.8								Rodionova[9]
$(C_4H_9)_4NCl$	tetragonal	29.7		23.733		12.153			10	16	4			Rodionova[9]
$(C_4H_9)_4NCl$	tetragonal	32.2		23.737		12.492			10	16	4			Rodionova[9]
$(C_4H_9)_4NCl$	tetragonal	32.1	5	23.77		12.61								McMullan[1]
$(C_4H_9)_4NBr$	Trigonal	2.33	6	16.609/90°		38.853/120°								Lipkowski[10]
$(C_4H_9)_4NBr$	monoclinic	24	6	28.5	16.9/125°	16.5								Gaponenko[11]
$(C_4H_9)_4NBr$	tetragonal	25.7	24	23.9		50.8								Gaponenko[11]
$(C_4H_9)_4NBr$	tetragonal	31.5	10	33.4		12.7								Gaponenko[11]
$(C_4H_9)_4NBr$	tetragonal	30.5	5	23.65		12.5								McMullan[1]
$(C_4H_9)_4NBr$	orthorhombic	36.3	2	21.3	12.9	12.1								Gaponenko[11]
$(C_4H_9)_4NBr$	orthorhombic	38	2	21.06	12.643	12.018			6	4	4			Shimada[12]
$(C_4H_9)_4NBr$	tetragonal	32.8	5	23.57		12.3			10	16	4			Davidson[13]
$(C_4H_9)_4NBr$	-	26												Oyama[14]
$(C_4H_9)_4NBr$	-	32												Oyama[14]

Guest molecule	Crystal system	$N^*_{H_2O}$	$N_{additive\ QAS}$	Lattice constants [Å]			Cage description							Reference
							$5^4 4^4$	$4^2 5^8$	5^{12}	$5^{12}6^2$	$5^{12}6^3$	$5^{12}6^4$	$7^1 6^3 5^9 4^2$	
				a/α	b/β	c/γ	Number of cages in unit cell							
$(C_4H_9)_4NOH$	cubic	28.3	12	24.6										Dyadin[15]
$(C_4H_9)_4NOH$	tetragonal	32.3	5	23.6		12.6								Dyadin[15]
$(C_4H_9)_4NNO_3$	tetragonal	26	6	23.3		13.2								Dyadin[15]
$(C_4H_9)_4NNO_3$	tetragonal	31.8	5	23.5		12.5								Dyadin[15]
$(C_4H_9)_4NHCO_2$	cubic	27.5	12	24.6										Dyadin[16]
$(C_4H_9)_4NHCO_2$	tetragonal	31.6	5	23.5		12.4								Dyadin[16]
$(C_4H_9)_4NHCO_2$	tetragonal	33	5	23.77		12.34								McMullan[1]
$(C_4H_9)_4NCH_3CO_2$	cubic	25.9	12	24.5										Dyadin[16]
$(C_4H_9)_4NCH_3CO_2$	tetragonal	30.7	5	23.62		12.38								McMullan[1]
$(C_4H_9)_4NCH_3CO_2$	tetragonal	31.4	5	23.6		12.2								Dyadin[16]
$(C_4H_9)_4NC_2H_5CO_2$	cubic	26	12	24.7										Dyadin[16]
$(C_4H_9)_4NC_2H_5CO_2$	tetragonal	31.6	5	23.7		12.5								Dyadin[16]
$(C_4H_9)_4NC_2H_5CO_2$	hexagonal	36.8	3	12.1		36.7								Dyadin[16]
$(C_4H_9)_4NC_3H_7CO_2$	cubic	31.7	1.33	12.3										Dyadin[16]
$(C_4H_9)_4NC_3H_7CO_2$	tetragonal	32.6	5	23.5		12.4								Dyadin[16]
$(C_4H_9)_4NC_3H_7CO_2$	tetragonal	35	4.44	23.6		12.5								Dyadin[16]
$(C_4H_9)_4NC_3H_7CO_2$	tetragonal	40.4	4	23.7		12.4								Dyadin[16]
$(C_4H_9)_4NC_4H_9CO_2$	cubic	31.6	1.33	12.4										Dyadin[16]
$(C_4H_9)_4NC_4H_9CO_2$	-	39.5		23.59		12.43								Beurskens[17]
$(C_4H_9)_4NC_4H_9CO_2$	-			12.31										Beurskens[17]
$(C_4H_9)_4NC_4H_9CO_2$	tetragonal	39.7	4	23.5		12.3								Dyadin[16]
$(C_4H_9)_4NC_4H_9CO_2$	tetragonal	39.8	4	23.322		12.278								Rodionova[9]

Guest molecule	Crystal system	$N^*_{H_2O}$	$N_{additive\ QAS}$	Lattice constants [Å]			Cage description							Reference
							5^44^4	4^25^8	5^{12}	$5^{12}6^2$	$5^{12}6^3$	$5^{12}6^4$	$7^16^35^94^2$	
				a/α	b/β	c/γ	Number of cages in unit cell							
$(C_4H_9)_4NC_5H_{11}CO_2$	tetragonal	40.4	4	23.7		12.5								Dyadin[16]
$(C_4H_9)_4NC_6H_5CO_2$	-	39.5	4											McMullan[3]
$(C_4H_9)_4N$-i-$C_3H_7CO_2$	tetragonal	31.8	5	23.8		12.4								Dyadin[16]
$(C_4H_9)_4N$-i-$C_3H_7CO_2$	cubic	24.8	15	26.8										Dyadin[16]
$(C_4H_9)_4N$-i-$C_3H_7CO_2$	tetragonal	39.4	4	23.8		12.7								Dyadin[16]
$(i\text{-}C_5H_{11})_4NF$	tetragonal	27	4	16.894		17.111	4						16	Lipkowski[5]
$(i\text{-}C_5H_{11})_4NF$	tetragonal	32.7	5	23.729		12.466			10	16	4			Lipkowski[5]
$(i\text{-}C_5H_{11})_4NF$	orthorhombic	38	2	12.08	21.61	12.822								Lipkowski[5]
$(i\text{-}C_5H_{11})_4NF$	orthorhombic	38.9	2	11.88	21.53	12.7			6	4	4			Lipkowski[5]
$(i\text{-}C_5H_{11})_4NF$	orthorhombic	40	2	12.08	21.61	12.82								McMullan[1]
$(i\text{-}C_5H_{11})_4NCl$	orthorhombic	38.3	2	11.98	21.48	12.83								McMullan[1]
$(i\text{-}C_5H_{11})_4NI$	orthorhombic	38	8	12.1	21.6	49.9								Dyadin[15]
$(i\text{-}C_5H_{11})_4PBr$	tetragonal	32	4	15.4		12		4			8			Solodovnikov[4]
$[(C_4H_9)_4N]_2HPO_4$	tetragonal	64.2	2.5	23.55		12.34								McMullan[1]
$[(C_4H_9)_4N]_2C_2O_4$	cubic	57.3	6	24.6										Dyadin[16]
$[(C_4H_9)_4N]_2C_2O_4$	tetragonal	64	2.5	23.8		12.4								Dyadin[16]
$[(C_4H_9)_4N]_2C_2O_4$	tetragonal	67	2.5	23.63		12.31								McMullan[1]
$[(C_4H_9)_4N]_2CH_2C_2O_4$	tetragonal	60.3	2.5	23.5		12.2								Dyadin[16]
$[(C_4H_9)_4N]_2CH_2C_2O_4$	tetragonal	63.3	2.5	23.6		12.5								Dyadin[16]
$[(C_4H_9)_4N]_2(CH_2)_2C_2O_4$	tetragonal	60.2	2.5	23.4		12.4								Dyadin[16]
$[(C_4H_9)_4N]_2(CH_2)_2C_2O_4$	tetragonal	62.6	2.5	23.6		12.6								Dyadin[16]
$[(C_4H_9)_4N]_2(CH_2)_3C_2O_4$	cubic	55.2	6	24.5										Dyadin[16]

Guest molecule	Crystal system	$N^*_{H_2O}$	$N_{\text{additive QAS}}$	Lattice constants [Å]			Cage description							Reference
				a/α	b/β	c/γ	5^44^4	4^25^8	5^{12}	$5^{12}6^2$	$5^{12}6^3$	$5^{12}6^4$	$7^16^35^94^2$	
							Number of cages in unit cell							
$[(C_4H_9)_4N]_2(CH_2)_3C_2O_4$	tetragonal	64.5	5	23.5		25.3								Dyadin[16]
$[(C_4H_9)_4N]_2CrO_4$	tetragonal	68	2.5	23.68		12.4								McMullan[1]
$[(C_4H_9)_4N]_2WO_4$	tetragonal	60	2.5	23.52		12.37								McMullan[1]
$[(C_5H_{11})_4N]_2CrO_4$	orthorhombic	74.2	1	12.18	21.53	12.67								McMullan[1]
$[(C_5H_{11})_4N]_2WO_4$	orthorhombic	80.7	1	12.06	21.39	12.7								McMullan[1]

$N^*_{H_2O}$: reported number of water molecules per unit cell, $N_{\text{additive salt}}$: number of included additive salt in semi-clathrate hydrate per unit cell.

Many types of semi-clathrate hydrate crystal structures have been reported other than the typical ones shown in Figure 2-2. The number of water molecules per unit cell $N^*_{H_2O}$ is different from the ideal number N_{ideal,H_2O} because the additive QAS replaces some number of water molecules in the hydrate structure. The $N^*_{H_2O}$ is different for each literature report because it is possible for water molecules to be included in the various cages.[8] In the application of semi-clathrate hydrates to gas separations, it is necessary to understand the effect of additive salts on the formed structures, which is one of the key topics in this thesis

2.3 Phase equilibria of clathrate hydrate systems

2.3.1 Effect of guest molecule on the phase equilibria of clathrate hydrates

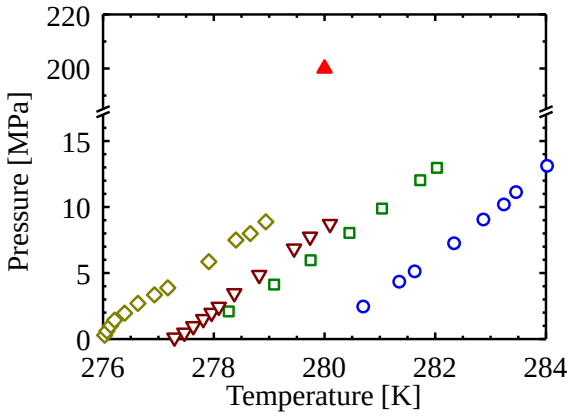

Figure 2-3. Phase equilibria of H_2 + water system (▲),[18] H_2 + tetrahydrothiophene + water system (◇),[19] H_2 + furan + water system (▽),[19] H_2 + tetrahydrofuran (THF) + water system (□) [20] and H_2 + cyclopentane + water system (○). [20]

Figure 2-3 shows the effect of a guest additive molecule on the phase equilibria of H_2 clathrate hydrates. Pure hydrogen hydrate forms structure II at high pressures (≈200 MPa),[18] because the

molecular size of hydrogen is very small. To reduce the equilibrium pressure of H_2 clathrate hydrate for the purpose of storing hydrogen in technological applications, a guest molecule can be added to promote the formation of stable structures and allow hydrogen to be included in some of the cages at low pressures (≈6 MPa).[21] The stability of the clathrate hydrate varies greatly according to the guest additive molecule. Some proposed guest additive molecules for structure II clathrate hydrates are tetrahydrofuran (THF),[21,22] cyclopentane (CP),[20,23] tetrahydrothiophene [19] and furan,[19] and those for structure H clathrate hydrates are 1,1-dimethylcyclohexane,[24] methyl *tert*-butyl ether[24] and methylcyclohexane.[24]

2.3.2 Phase equilibria of semi-clathrate hydrates

Table 2-5 summarizes the phase equilibria data of semi-clathrate hydrates with gases.

Table 2-5. Summary of phase equilibria of semi-clathrate hydrates with gases.
TBAB: tetra-*n*-butyl ammonium bromide, TBAC: tetra-*n*-butyl ammonium chloride, TBAF: tetra-*n*-butyl ammonium fluoride, TBPB: tetra-*n*-butyl phosphonium bromide, TBAN: tetra-*n*-butyl ammonium nitrate, TPAF: tetra-*i*-pentyl ammonium fluoride, TMA: trimethylamine

Salt	Concentration [mol%]	Gas	T [K]	P [MPa]	Data type	Ref.
TBAB	4.0	CH_2F_2	286-290	0.18-1.2	P-T	Imai[25]
TBAB	3.6	H_2	285-287	0.13-14	P-T	Hashimoto[26]
TBAB	0.6-7	H_2	279-287	0.49-15	P-T	Hashimoto[27]
TBAB	0.6	none	280-280	3.6-21	P-T	Arjmandi[28]
	0.6	H_2	280-283	4.2-23		
	4.0	H_2	286-289	3.6-23		
	0.3-2.3	CH_4	287-297	1.4-41.4		
	0.6	N_2	285-293	4.7-34		
	0.6-4.0	CO_2	286-291	1.2-4.1		
	0.3-4.0	Natural gas	280-292	0.098-9.5		

Salt	Concentration [mol%]	Gas	T [K]	P [MPa]	Data type	Ref.
TBAB	0.29-0.61	N_2	279-284	0.66-2.9	P-T	Duc [29]
	0.29-9.4	CO_2	279-291	0.29-9.4		
	0.29	CO_2(16-22%) + N_2	282-295	0.55-5.3		
TBAB	0.3-0.6	CO_2	279-288	0.3-2.5	P-T	Lin[30]
TBAB	0.3-4.7	none	276-286	0.1	x-T	Sun [31]
TBAB	2.3-4.4	CH_4	282-291	0.5-7.0	P-T	Sun[32]
TBAB	0.3-3.4	CH_4	281-295	0.5-11.0	P-T	Li[33]
TBAB	0.3-1.4	CH_4 (30 %)+N_2 (60%)+O_2	282-290	1.0-6.6	P-T	Zhong[34]
TBAB	0.14-2.67	CO_2 (19-40 %)+H_2	274-289	0.25-7.3	P-T	Li[35]
TBAB	0.3	H_2S	291-296	0.17-0.68	P-T	Mohammadi[36]
		CH_4	284-290	1.3-11		
TBAB	0.3-5.3	CO_2, N_2, CH_4, H_2	278-295	0.46-15	P-T	Mohammadi[37]
TBAB	0.3-2.3	CO_2 (15-85%)+N_2	277-293	1.1-16	P-T	Mohammadi[38]
TBAB	0.05-0.3	CO_2(15-75%)+H_2	281-293	1.6-16	P-T	Mohammadi[39]
TBAB	0.3-1.4	CO_2, CO, H_2	283.1-291	4.7-6.6	P-T	Wang[40]
TBAB	0.3-0.6	CO_2	280-289	0.40-3.4	P-T	Li[41]
TBAC	0.3-0.6	〃	280-289	0.47-3.8		
TBAF	0.3-0.6	〃	286-294	0.53-3.0		
TBAB	1.1-3.6	N_2	285-295	0.1-25	P-T	Deschamps[42]
	1.1-3.6	CO_2	285-290	0.1-2.25		
	3.6	N_2(75%)+CO_2	285-293	0.1-9.2		
	3.6	CH_4(50%)+CO_2	285-292	0.1-3.2		
TBAB	3.6	H_2	287-287	13-24	P-T	Deschamps[43]
TBAC	3.3	〃	289-290	15-30		
TBPB	3.0	〃	285-287	12-23		
TBAB	3.7	H_2	286-287	3.6-16	P-T	Chapoy[44]
TBAB	0.3-7.7	N_2	280-290	4.0-9.2	P-T	Lee [45]
TBAF	0.8-5.3	〃	293-302	2.0-9.7		
TBAB	0.6-7.7	CO_2	286-292	1.1-4.6	P-T	Lee[46]
		CH_4	286-294	2.1-9.2	T-x	
TBAB	0.29	CH_4(54%)+N_2	276-282	0.51-1.8	P-T	Sun[47]
TBAB	0.5-3.0	CO_2(40%)+H_2	283-290	2.5-5.0	P-T	Kim[48]
TBAB	0.3-1.4	CO_2(20-75%)+N_2	281-290	1.9-5.9	P-T	Meysel[49]
TBAB	0.3-1.4	CO_2 (40-60%)+CH_4	286-293	3-6.5	P-T	Acosta[50]
TBAB	0.6-7.7	CO_2(40%)+H_2	282-290	1.1-8.1	P-T	Park [51]
TBAF	0.8-5.3	〃	293-301	1.1-7.8	P-T	

Salt	Concentration [mol%]	Gas	T [K]	P [MPa]	Data type	Ref.
TBAB	0.293	CO_2(15%)+CH_4	282-291	0.78-8.9	P-T	Fan [52]
TBAC	0.293	〃	280-288	0.90-8.4		
TBAF	0.293	〃	284-291	0.61-9.5		
TBAB	0.3-1.4	CO_2	280-285	0.44-2.8	P-T	Godishala[53]
+	+	〃	281-284	0.60-3.0		
NaCl	1.1-3.3	〃	284-288	0.82-3.6		
		〃	284-287	0.85-3.6		
		〃	284-289	0.83-3.9		
		〃	285-288	0.84-3.8		
TBAC	3.23	C_2H_6	288-288	0.55-3.4	P-T	Makino [54]
		H_2	288-289	0.55-4.6		
		N_2	289-290	0.61-4.6		
		CH_4	289-292	0.61-4.9		
		CO_2	289-293	0.36-4.4		
TBAC	3.5	CO_2	288-292	0.1-2.0	P-T	Mayoufi[55]
TBAN	3.7	〃	278-282	0.1-2.0		
TBPB	3.0	〃	281-289	0.1-2.0		
TBAF	0.6-5.5	none	291-301	0.1	x-T	Sakamoto[56]
	1.8-3.4	H_2	298-303	0.22-37.6	P-T	
TBAF	0.1-1.2	CH_4	285-300	1.1-10	P-T	Mohammadi [57]
	0.1-1.2	CO_2	285-299	0.89-5.0	P-T	
	0.4-1.2	N_2	291-296	3.9-10	P-T	
TBPB	0.276-7.3	CO_2	285-289	0.1-1.7	P-T	Mayoufi[58]
TBPB	2.6	H_2	282-296	0.11-165	P-T	Fujisawa[59]
TBPB	0.2-2.8	CO_2	283-292	0.17-4.9	P-T	Suginaka[60]
		CH_4	283-292	0.15-5.1		
		N_2	283-287	0.48-5.0		
TBPB	0.3-7.4	CO_2	284-291	1.3-3.6	P-T	Shi[61]
	0.3-7.4	N_2	282-292	7.2-17		
TBAN	3.7	CO_2, N_2, CH_4	282-291	1.2-33	P-T	Du[62]
TBAN	0.050-0.394	CO_2	280.0-288.3	1.9-14	P-T	Shi[63]
TPAF	-	CH_4	307-320	0.58-27	P-T	Hughes[64]
TMA	4.7-8.3	H_2	276-301	0.31-173	P-T	Ogata[65]

There have been many phase equilibrium data reported for TBAB semi-clathrate hydrates. However, the phase equilibrium data for other semi-clathrate hydrates are not plentiful and so the

effect of the additive salt on the phase equilibrium data of pure gases or gas mixtures is difficult to compare. One of the important topics of this thesis is to make a systematic study on the variation of the salts and the phase equilibria of semi-clathrate hydrates.

2.4 Clathrate hydrate formation and dissociation kinetics

Much literature is available on CH_4 clathrate hydrate or CO_2 clathrate hydrate dissociation and formation kinetics. Many analytical techniques have been proposed for qualifying and quantifying individual (CH_4 or CO_2) clathrate hydrate dissociation and formation kinetics. Among the methods, material balance methods have been the most widely used.[66-74] Other techniques that are used are XRD,[75] neutron diffraction[76] and Raman[71] methods. Particle size analysis is essential in experimental techniques because the particle size of hydrates greatly affects formation and dissociation kinetics. Particle sizes can be selected in the experimental method by using classifiers (e.g. sieves) or they can be measured in situ by sonic or chemical techniques such as focused beam reflectance method (FBRM) [68] or by Zetasizer nano ZS particle-size analyzers.[66]

2.4.1 Methane clathrate hydrate dissociation kinetics

In the study of methane hydrate dissociation kinetics, pressure perturbation, thermal perturbation, or mechanical perturbations (e.g. shock) are candidates. Literature related to the investigation of the methane clathrate hydrate dissociation is shown in Table 2-6. In the literature,[77,78] temperature differences between bulk fluid and hydrate phases have been assumed to be a single driving force.

Table 2-6. Literature for investigations of methane hydrate dissociation. Temperature (*T*), pressure (*P*), additive condition and analytical method were surveyed. The ΔE_{Kd} and ΔE_D are the activation energy of the hydrate dissociation and that of the diffusion in hydrate, respectively. Dissociation of methane hydrate is generally by depressurization.[67,70,71,73] Kamath et al. studied methane hydrate dissociation with a thermal fluid.[77,78]

Method	*T* range [K]	*P* range [MPa]	Particle size [μm]	Additive	ΔE_{Kd} [kJ/mol]	ΔE_D [kJ/mol]	Reference
MB	286 – 307	2.86 – 7.61	-	-	-	-	Kamath (1987) [77]
MB	283 – 296	4.03 – 5.72	-	NaCl	-	-	Kamath (1991) [78]
MB	274 – 283	0.17 – 6.97	*ca.* 16	-	78.3	-	Kim (1987) [70]
MB	264 – 269	0.1 – 2.15	-	-	96.12	1167.0 (0.96)[*1]	Liang (2005) [73]
MB	264 – 271	0.1 – 3.74	-	Activated carbon	26.03	1496.2 (1)[*1]	
MB	273 – 276	0.1 – 5.07	-	Activated carbon	88.98	379.0 (0.67)[*1]	
MB	264 – 269	0.1 – 2.15	-	SDS	96.43	1446.6 (0.97)[*1]	
MB & PSA	275 – 281	3.19 – 6.21	~ 26 (ethane) [79]	-	81	-	Clarke (2001) [67]
MB & Raman	268 – 273	0.1 – 0.5	100 – 250	-	-	229 (0.95)[*1]	Komai (2004) [71]

MB: material balance, PSA: on-line particle size analyzer.

[*1] Estimate by using Arrhenius plot (determination coefficient).

2.4.1.1 Thermal fluid studies

Kamath *et al*. investigated methane hydrate dissociation kinetics with warm water[77] or brine[78] injection and the hydrate dissociation rate was described as a function of a temperature driving force at the hydrate/water interface and interfacial area.[77,78,80] The dissociation rates of methane clathrate hydrate are strongly influenced by brine salinity with the dissociation rate for 15 wt% brine being 40 times larger than that by pure warm water when temperature-driving force without the effect of salinity, ΔT^0, was 4.5 K.[78] Application of brine, such as that available in surface waters, may be an effective method to enhance the production of methane gas from hydrate reservoirs. Kamath *et al*.[77] hypothesized that hydrate dissociation was a heat transfer limited process and the water generated from hydrate dissociation continually forms a thin liquid film on the surface of the remaining hydrate resulting in a resistance to heat transfer. The heat transfer of dissociating hydrates was considered to be analogous to nucleation boiling phenomenon, in which the degree of convection depends on the size of the gas bubbles and the bubble generation frequency at the hydrate surface. Thus, the rate of heat transfer for hydrate dissociation can be expected to be strong functions of the temperature gradient across the interfacial film. Kamath *et al*.[77] assumed that the dissociation rate was directly proportional to the surface area of the hydrate, so that their formulation was as follows:

$$\frac{q_g}{\phi_H A} = a(\Delta T)^b \qquad (2\text{-}1)$$

where q_g is the gas production rate from hydrate dissociation, ϕ_H is volume fraction of hydrate in the core holder, A is the core cross-sectional area, and a and b are correlation parameters that depend on

injection fluid and hydrate type. The ΔT in Eq. (2-1) is the actual temperature driving force. Their results could be correlated with Eq. (2-1).[77,78,80] Kamath *et al*. summarized *a* and *b* for previous results by standardizing the units of q_g and *A*.[81] Constants *a* and *b* for the methane hydrate dissociation by water,[77] the methane hydrate dissociation by brine (concentration of NaCl range was from 5 to 15 wt %) [78] were 1.451×10^{-7} scc/(cm^2·s) and 2.16, 1.353×10^{-7} scc/(cm^2·s) and 2.195, respectively. In their results, the constant *a* for methane hydrate dissociation by water[77] was larger than that for brine, [78] which is unusual. [78] These experimental data are influenced by experimental conditions such as the thermal content of the injection. Although heat transfer for hydrate dissociation has many complicated features, it can be expressed by relatively simple equations.

2.4.1.2 Depressurization studies

Whereas Kamath *et al*. investigated methane hydrate dissociation kinetics with thermal fluids [77,78] Kim *et al*. investigated methane hydrate dissociation kinetics with depressurization under, different pressures at isothermal conditions and modeled the phenomena by assuming the driving force was independent of the fugacity of that at the equilibrium pressure of the methane hydrate.[70] Kim *et al*.[70] hypothesized that the dissociation process includes desorption of the guest molecule at certain points and that the mass-transfer of the molecule to the bulk phase could be represented as;

$$\frac{dn_{\text{guest}}}{dt} = -K_d A\left(f_{eq} - f_s\right) \qquad (2\text{-}2)$$

where n_{guest} is the moles of guest molecules in the hydrate phase, *t* is the reaction time, f_{eq} and f_s are the fugacities at the hydrate equilibrium pressure and that for the solid surface, respectively. The

K_d in Eq. (2-2) is the decomposition rate constant for the hydrate dissociation and A is the surface area between bulk fluid and hydrate phases. Arrhenius-type plots were made with the use of Eq. (2-2) and experiments made at various temperatures, to determine the activation energy for the methane hydrate dissociation to gas and liquid water that was found to be 78 kJ/mol [70]. Subsequent work by that group used on-line particle size analysis that allowed an improved estimation of the activation energy (81 kJ/mol).[67]

Hydrate dissociation can be written as an overall expression that separates the kinetics of desorption of the guest molecule from the hydrate cage from the mass transfer of the molecule in the bulk phase as:[79]

$$\frac{1}{K_d} = \frac{1}{k_r} + \frac{1}{k_m} \qquad (2\text{-}3)$$

where k_r and k_m are the desorption rate constant and mass transfer coefficient from the reaction point to bulk phase. Correlation with this model for ethane hydrate dissociation to gas and liquid water, showed that the obtained intrinsic rate constants had an activation energy of 104 kJ/mol,[79] which implies that the activation energy varies according to the species of the guest molecule when one considers the difference in activation energy values for methane and ethane.

Although the literature tends to focus on dissociation kinetics above the ice point, there are some studies on kinetics below the ice point.[71,73] Liang *et al*. investigated the temperature effect on hydrate dissociation kinetics using a material balance method.[73] In their experiments, methane hydrates were prepared with or without porous wet activated carbon or sodium dodecyl sulfate (SDS). Comparison of the preparation methods showed that methane hydrate dissociated the

fastest in the presence of activated carbon, and in the presence of the surfactant sodium dodecyl sulfate (SDS). Liang *et al*. developed a mathematical model to describe the decomposition kinetics of methane hydrates below the ice point for which the decomposition process was assumed to occur in two steps. The first step was the destruction of the clathrate host lattice and desorption of the methane molecule at the surface of the hydrate particle that was proposed in the study of Kim *et al*.[70] and that was described by Eq.(2-2). The second step was diffusion of the methane molecule through a porous ice layer, in which they assumed that the fugacity of gas varied linearly in the direction of the thickness of the porous ice layer mentioned above so that the gas diffusion rate was formulated as:

$$\frac{dn_{\mathrm{d}}}{dt} = \frac{D}{L} A_{\mathrm{s}} \left(f_{\mathrm{s}} - f_{\mathrm{g}} \right) \tag{2-4}$$

where n_{d} is the cumulative moles of gas, D is the diffusion coefficient of the gas molecule in the porous ice layer, L is the thickness of the porous ice layer, and f_{g} is the fugacity of gas molecule in vapor phase. At quasi-equilibrium conditions, the left-hand side of Eq. (2-2) equals to that of Eq.(2-4), thus, Eq. (2-5) can be developed by eliminating the fugacity for the solid surface:

$$\frac{dn_{\mathrm{d}}}{dt} = \left(\frac{1}{\frac{1}{K_{\mathrm{d}} A_{\mathrm{s}}} + \frac{L}{D A_{\mathrm{s}}}} \right) \left(f_{\mathrm{eq}} - f_{\mathrm{g}} \right) \tag{2-5}$$

Temperature dependence of the decomposition rate constant shows that the activation energy (ΔE_{a}) is strongly dependent on the preparation method. The ΔE_{a} for methane hydrate dissociation in the presence of activated carbon above the ice point (26 kJ/mol), below the ice point (89 kJ/mol), that in the presence of SDS below ice point (96 kJ/mol) and that without SDS below ice point (96

kJ/mol) show a wide range of values. The decomposition rate constant depends weakly on the temperature above the ice point, and the activation energy (26 kJ/mol) is remarkably lower than values in previous literature, 78[70] and 81 kJ/mol.[67] Liang *et al*.[73] thought that these differences could be interpreted by results reported by Circone *et al*.,[82] who observed that when hydrates decompose above the ice point by rapid depressurization, there are large differences between sample temperature and the external bath temperature unlike for the case of the decomposition of hydrate below the ice point. Sample temperatures are buffered in a narrow temperature range below the ice point by the latent heat of water and thus tend to be insensitive to the external bath temperature. Following this line of reasoning, the dissociation rate of hydrate above the ice point is probably affected according to the rate of heat flow from the external bath. Therefore, Liang *et al*. thought that the activation energy (26 kJ/mol) determined with Eq. (2-5) above the ice point should not be taken as the true activation energy.

Komai *et al*. used *in-situ* Raman spectroscopy to follow hydrate dissociation in real time.[71] *In-situ* Raman spectroscopy is a feasible tool to follow conformational changes in solid structures, at isothermal or isobaric conditions. The optical cell had a sapphire window and had an internal volume of about 10 cm^3, in which powdered methane hydrates with an average diameter range of about 100-250 μm were loaded. Pressure was held constant by a regulator and a micrometering valve. The relationship that they used for data reduction was:

$$3\left(1-I(t)^{2/3}\right)-2\left(1-I(t)\right)=\phi\frac{6Dt}{r_0^2} \qquad (2\text{-}6)$$

where $I(t)$ is the integrated Raman intensity for an elapsed time t, ϕ is a dimensionless parameter

derived from the driving force for hydrate dissociation, r_0 is the initial hydrate radius, and D is the diffusion coefficient of methane in the ice layer.

Using Eq.(2-6), Komai *et al*.[71] found that the dissociation rates of methane hydrate at 0.1 MPa (272.7 and 271.2 K) were considerably faster than those at 0.25 and 0.5 MPa, and that the dissociation rates at 271.2 and 268.2 K became smaller after about 100 min. This indicates a type of self-preservation that occurs for the clathrate hydrate structure through the renewal of a surface layer coated with ice[83,84] or formation of quasi-liquid layers (QLL).[75,76,85,86]

2.4.2 CO_2 clathrate hydrate formation kinetics

In the study of CO_2 hydrate formation kinetics, ice particles or aqueous solutions are generally used. For the hydrate formation from the aqueous solutions, solubility and mass transfer or diffusion to the bulk phase by guest molecules has to be considered. Literature related to the investigation of the CO_2 clathrate hydrate formation is shown in Table 2-7.

Table 2-7. Literature for investigations of CO_2 hydrate formation kinetics. Temperature (T), pressure (P), additives and analytical methods were surveyed. The ΔE_{K_F} and ΔE_D are the activation energy of the hydrate formation and that of the diffusion in hydrate, respectively. Literature studies form CO_2 hydrates by pressurization. [66,68,69,72,74-76,87]

Method	T range [K]	P range [MPa]	Particle size [μm]	Additive	ΔE_{K_F} [kJ/mol]	ΔE_D [kJ/mol]	
MB	274 – 278	1.59 – 2.79	-	-	53.7 (0.13)[*1]	-	Malegaonkar (1997) [74]
MB	273 – 277	2.5 – 3.4	-	NaCl & Porous media	35.2 (0.92)[*1, 2]	-	Lee (2002) [72]
MB	273 – 277	2.0 – 3.0	-	Surfactant & Porous media	-	-	Kang (2010) [69]
MB &PSA	274 – 279	1.6 – 3.0	1 – 25 (t = 2320 s)	-	45.2 (0.25)[*1]	-	Clarke (2005) [68]
MB & PSA	275 – 279	2.01 – 3.05	-	-	402 (0.98)[*1]	-	Bergeron (2008) [66]
PD	276	2.9 – 3.9	-	-	-	-	He (2011)[87]
ND	230 – 263	6.2	*ca.* 200	-	-	27.3	Henning (2000) [76]
XRD	233 – 273	0.98 – 1.47	*ca.* 150	-	20	39	Takeya (2000) [75]

MB: material balance, PSA: on-line particle size analyzer, PD: pressure decay, ND: neutron diffraction, XRD: X-ray diffraction.

[*1] Estimate by using Arrhenius plot (determination coefficient), [*2] CO_2 hydrate in pure water at a temperature range from 273.2 to 276.2 K.

2.4.2.1 Formation of clathrate hydrates from aqueous solutions

He *et al*. investigated the influence of supersaturation on induction time and half-life decay time for both CO_2 and methane hydrate systems.[87] The degree of supersaturation, S^*, is defined by relationship between the initial pressure and equilibrium pressure ($S^* = P_{initial}/P_{eq} - 1$). The induction time for the CO_2 + water system was shorter (*ca*. 53 min) than for the methane + water system (*ca*. 108 min) at very low degrees of supersaturation (*ca*. 0.45), however, as the degree of supersaturation increased, the induction times become larger such that at high degrees of supersaturation, induction times of CO_2 + water (*ca*. 50 min when S^* was 0.54) became longer than those of methane + H_2O (*ca*. 4 min when S^* was 0.54). The critical size of nuclei is defined by a relationship between the interfacial tension and the Gibbs energy,[88] and the Gibbs energy is proportional to the ratio of initial and equilibrium pressure. Therefore, the results of He *et al*. indicate that the interfacial tension between water and gas hydrate in the CO_2 + water system changes with the degree of supersaturation. He *et al*. scaled decay time half-life, $t_{scale\text{-}half}$, by using the pressure change to eliminate the influence of the absolute value of the decay pressure half-life as given by eq. (2-7) below.

$$t_{scale-half} = \frac{t_{half}}{P_{initial} - P_{half}} \qquad (2\text{-}7)$$

The scaled decay time half-life for the CO_2 system (*ca*. 1) was shorter than that for the methane system (*ca*. 1.5) for the same range of degree of supersaturation (0.6 – 0.8). The results revealed that the crystal growth of CO_2 hydrates is faster than that for methane hydrates.

Malegaonkar *et al*. measured CO_2 hydrate formation kinetics using a semi-batch stirred tank

reactor at nominal temperatures of 274, 276 and 278 K and at pressures ranging from 1.59 to 2.79 MPa.[74] The used a kinetic model based on the crystallization theory coupled with the two-film theory for gas absorption in liquid phase, that was developed by Englezos *et al*. and considered the growth of a hydrate crystals as a two step process based on a fugacity driving force as given by Eqs. (2-8) to (2-13) below.[89] It was assumed that the particles were spherical, with the outside surface of the surrounding layers being equal to the inside surface layer and that there was no accumulation in the diffusion layer. Malegaonkar *et al*. modified the model equations[89] by considering the particle size as the particle diameter consistently for the solubility of carbon dioxide in water.[74] The rate of growth per particle was given by:

$$\left(\frac{dn_{\text{gas}}}{dt}\right)_{\text{p}} = K_{\text{form}} A_{\text{p}} \left(f - f_{\text{eq}}\right) \tag{2-8}$$

where n_{gas} is moles of gas consumed, t is reaction time, ($f - f_{\text{eq}}$) is the difference in the fugacity of the dissolved gas and its fugacity at the three phase equilibrium, defines the overall driving force. K_{form} is an overall rate constant for the formation and A_{p} is the surface area between bulk fluid and hydrate phases of each particles. The global reaction rate for all the particles, $R_y(t)$, is given by:

$$R_y(t) = \int_0^{\infty} \left(\frac{dn_{\text{gas}}}{dt}\right)_{\text{p}} \phi\left(d_{\text{p}}, t\right) dd_{\text{p}} \tag{2-9}$$

where $\phi(d_{\text{p}}, t)$ is the particle size distribution, d_{p} is particle diameter. The second moment of the particle, μ_2, is given by:

$$\mu_2 = \int_0^{\infty} d_{\text{p}}^2 \phi\left(d_{\text{p}}, t\right) dd_{\text{p}} \tag{2-10}$$

Eq. (2-11) can be developed from Eq. (2-9) by using Eqs. (2-8) and (2-10).

$$R_y(t) = \pi K_{\text{form}} \mu_2 \left(f - f_{\text{eq}} \right) \tag{2-11}$$

Assuming quasi steady state conditions, diffusion and reaction in the liquid film are given by Eq.(2-12):

$$D_{\text{F}} \frac{d^2 c}{dy^2} = \pi K_{\text{form}} \mu_2 \left(f - f_{\text{eq}} \right) \tag{2-12}$$

where D_{F} is Fick's diffusion coefficient of the gas, c is the concentration of gas in liquid water and y is the distance from the gas-liquid interface. Following the development of Englezos *et al*.,[89] the dynamic behavior of the process is described by Eq.(2-13):

$$\frac{dn_{\text{gas}}}{dt} = \left(\frac{D^* \gamma A_{(\text{g-l})}}{y_L} \right) \frac{\left(\left(f_{\text{g}} - f_{\text{eq}} \right) \cosh\gamma - \left(f_{\text{bulk}} - f_{\text{eq}} \right) \right)}{\sinh\gamma} \tag{2-13}$$

where $A_{(\text{g-l})}$ is the gas-liquid interfacial area, y_L is the film thickness, and f_{g} and f_{bulk} are fugacities of the reactor gas phase and that of the bulk of the liquid phase, respectively. Hatta number, γ, and D^* are given by Eqs. (2-14) and (2-15):

$$\gamma = y_L \sqrt{\frac{\pi K_{\text{form}} \mu_2}{D_F^*}} \tag{2-14}$$

$$D_{\text{F}}^* = D_{\text{F}} \left(\frac{c_{\text{eq}} + c_{\text{w0}}}{H - f_{\text{eq}}} \right) \tag{2-15}$$

where H is Henry's constant, c_{eq} is the concentration of gas in liquid water at the three phase equilibrium conditions and c_{w0} is the initial concentration of water. The definition of D_{F}^* was modified from the Englezos *et al*. model[89] for the solubility of carbon dioxide as Eq.(2-15). In this model, the kinetic rate constants, K_{form}, obtained for methane and carbon dioxide could be used to

simulate hydrate formation from their mixtures,[90] or to describe the kinetics of hydrate formation in aqueous electrolyte solutions.[91] The K_{form} obtained for carbon dioxide hydrate formation (0.49×10^{-3} mol/(m·s·MPa) at 274 K) determined from Eq. (2-13) are higher than those for methane hydrate (0.31×10^{-4} mol/(m·s·MPa) at 274 K).[74] However, these values are much higher than previous values, for which K_{form} for methane hydrate formation obtained by Englezos *et al*. was 0.65×10^{-5} mol/(m·s·MPa) at 274 K[89] and that for carbon dioxide hydrate formation obtained by Chun and Lee were in the range from 0.69 to 0.71 $\times10^{-5}$ mol/(m·s·MPa) at temperatures range from 275 to 279 K.[92] Malegaonkar *et al*.[74] considered that the values were higher due to corrections incorporated in the model according to the particle size in the derivation of the model equations. In addition, it appears that Chun and Lee[92] did not take into account the increase in the solution temperature during the turbidity time and subsequently during hydrate growth to calculate f_{eq}. The turbidity time is the time during a stable critical size hydrate nuclei that appears in a catastrophic manner.[74] Malegaonkar *et al*.[74] took as zero time, the time after the turbidity time in the measurement of isotherm the gas consumption rate under isothermal conditions. The temperature dependence of the rate constants for CO_2 hydrate formation is not strong and thus, the activation energy for CO_2 hydrate formation is generally not reported in the literature.[74] The temperature dependence of the rate constant for CO_2 hydrate formation can be observed after improving the estimation of surface area and this has been reported for the case of using *in-situ* particle size analysis,[68,74] however, the differences are small. The above researchers have reported a minimum value for the reaction rate constant in presence of several hydrate formers around 277 K.[68,74,89] The water density at this temperature is the highest for the liquid state, however, the

change in water density is not significant over the temperature interval investigated. This trend, for which the reaction rate constant around 277 K was the smallest among 273 – 280 K,[68,74,89] could be attributed to the hydrate formation kinetics model based on a fugacity driving force and the two-film theory.

Bergeron and Servio chose to use temperature and pressure conditions for investigating CO_2 hydrate formation kinetics using a semibatch stirred-tank reactor incorporating a closed-loop particle size analyzer.[66] Reaction rate constants were determined using a kinetic model that assumed that the mole fraction of the gas hydrate former in the bulk-liquid phase remained constant during hydrate growth as given by Eqs. (2-16) and (2-17), which are independent of dissolution rate at the vapor-liquid water interface.[93] As for μ_2(t) given by Eq.(2-16), it can be obtained either experimentally, using the particle-size analyzer or using a population balance, which is a semitheoretical approach given by Eq.(2-17):

$$\frac{dn}{dt} = \frac{V_L \rho_w}{MW_w} \frac{\left(x^l - x^{H-L}\right)}{1/\pi\mu_2(t) k_r} \tag{2-16}$$

$$\frac{dn}{dt} = \frac{V_L \rho_w}{MW_w} \frac{\left(x^l - x^{H-L}\right)}{1/\pi\left(\mu_0^0 G^2 t^2 + 2 d_c \mu_0^0 G t + d_c^2 \mu_0^0\right) k_r} \tag{2-17}$$

where V_L is volume of liquid, ρ_w and MW_w are density of and molecular weight of water, x^l is mole fraction of the gas hydrate former in the bulk liquid and $x^{H\text{-}L}$ is solubility of the gas hydrate former under hydrate-liquid water equilibrium, μ_0^0 is the initial number of hydrate particles, G is growth rate, d_c is critical nuclei diameter, and k_r is the reaction rate constant. The obtained experimental and semi-theoretical reaction rate constants were 4.5 and 4.1 $\times 10^{-8}$ m/s at 277.5 K, these values

depended on the method used. Hashemi *et al.*[94] determined intrinsic kinetic rate constant of CO_2 hydrate formation from the experimental data of Clarke and Bishnoi [68] using a concentration driving force and the model of Englezos *et al.*[89] The reaction rate constants of CO_2 hydrate formation reported by Bergeron and Servio[66] were in relatively good agreement with the value (1.2×10^{-8} m/s) reported by Hashemi *et al.*[94] using a population balance at 277.15 K. The reaction rate constants reported by Bergeron and Servio increased with increasing temperature and their trend with temperature followed an Arrhenius-type relationship,[66] which differs from previous literature.[74] However, the activation energy estimated by Arrhenius plot is *ca*. 402 kJ/mol, which is remarkably larger than estimated previously values (20 – 54 kJ/mol).[68,72,74] This means that the assumption of hydrate crystal growth process had a significant influence on the temperature dependence on the reaction rate constants. The model of Bergeron and Servio[66] assumed a concentration driving force and independence of dissolution rate at the vapor-liquid water interface, which is different from the fugacity driving force and the diffusion in the liquid film in the model of Malegaonkar *et al.*.[74] On the other hand, the model of Hashemi *et al.*[94] did not discuss temperature dependence on the intrinsic kinetic rate constant, which assumed a concentration driving force and the diffusion in the liquid film. Thus, the temperature dependence on the driving force of the intrinsic kinetic rate constant for CO_2 hydrate formation can be discussed by comparing the models of Malegaonkar *et al.*[74] and Hashemi *et al.*[94] and the assumption of diffusion in the liquid film can be discussed by comparing the models of Bergeron and Servio[66] and Hashemi *et al.*[94] If the influence of the driving force is negligibly small, the influence of the dissolution rate at the vapor-liquid water interface should be reconsidered. Furthermore the mechanism can probably be understood directly

in terms of the physical chemistry.

The effect of additives on CO_2 hydrate formation kinetics has been studied in several works. Use of NaCl solution inhibits the formation kinetics,[72] while use of porous silica gel and sodium dodecyl sulfate (SDS) promotes formation rates.[69] Kinetic data obtained under various SDS concentrations show a promotion of rates even when the SDS concentration is chosen to be less than the critical micelle concentration (CMC). This behavior implies that characteristic hydrate formation is probably dominated by the solubility of the promoter rather than the CMC of the surfactant.[95,96] Activation energy analyses for these additive effects are not available.

2.4.2.2 Formation of clathrate hydrates from ice particles

Although the above-mentioned CO_2 hydrate formation kinetics study focused on temperature conditions above the ice point, some reports have appeared for measurements below the ice point.[75,76] Takeya *et al*. conducted *in-situ* observations of CO_2 hydrate growth from ice particles using high-energy X-ray at high pressures.[75] By assuming a two-stage kinetic model with a diffusion-limited reaction that proceeds with a pressure driving force as given by Eqs. (2-18) and (2-19), diffusion coefficients of CO_2 and H_2O molecules could be estimated at temperatures between 233 K and 272.5 K. The growth rate in Stage (1), υ_I can be described using a pressure difference relative to the dissociation pressure, $p - p_d(T)$,[97]

$$\upsilon_I = K_I\left(p - p_d(T)\right) \tag{2-18}$$

where K_I is the reaction rate constant and p_d (T) is dissociation pressure of CO_2 hydrate at temperature T. The volume change of ice in Stage (2) can be written according to a diffusion

equation as given by Eq. (2-19),[98]

$$\frac{dV_i}{dt} = -4\pi D \frac{r_i r_h}{r_h - r_i}\left(\frac{p - p_d(T)}{p}\right)\frac{\rho_{hw}}{\rho_i} \qquad (2\text{-}19)$$

where t is reaction time, V_i is the volume of ice, D is the inter-diffusion coefficient. The r_i and r_h in Eq. (2-19) are the radii of the ice particle and hydrate particle, respectively. In Eq. (2-19), ρ_i is the ice density (918 kg/m^3) and ρ_{hw} is the water density of the hydrate (785 kg/m^3). The diffusion constants rapidly increase above *ca.* 263 K where the reaction seems to proceed in the quasi-liquid layer (QLL) existing on the surface of the ice particles. Temperature dependence of the reaction constants below 263 K had an activation energy of *ca.* 20 kJ/mol. In comparison with the literature,[85] this value was not equal to the activation energy of diffusion of H_2O molecule in hexagonal ice (*ca.* 59 kJ/mol), but was close to that in the QLL (*ca.* 24 kJ/mol). Therefore, the nucleation and growth of hydrate on the ice surface might be determined by migration of H_2O molecules on the ice surface. The inter-diffusion coefficient for CO_2 hydrate (*ca.* 8 $\times 10^{-16}$ m^2/s at 263 K)[75] was one to two orders smaller than that of air hydrate (*ca.* 2 ~ 4 $\times 10^{-14}$ m^2/s at 263 K).[98] Between 238 K and 263 K, the diffusion activation energy for CO_2 hydrate was *ca.* 39 kJ/mol,[75] which is comparable with that for air hydrate (30 ~ 50 kJ/mol).[98] This result implies that the diffusion coefficient is determined by the diffusion of H_2O molecules.

Henning *et al*. used time-of-flight neutron powder diffraction for analyzing CO_2 hydrate formation kinetics at temperatures ranging from 230 to 263 K in the presence of a CO_2 gas phase.[76] Experimental data were correlated with a shrinking core diffusion model as given by Eq.(2-20):

$$(1-\alpha_r)^{1/3} = \left(\frac{-(2k_D)^{1/2}}{r_0}\right)(t-t*)^{1/2} + (1-\alpha_r^*)^{1/3} \quad (2\text{-}20)$$

where k_D and r_0 are the diffusion constant and the original radius of the particles, and α_r and α_r^* are degrees of reactions at times t and t^*, respectively. The term t* is indicates the time where the conversion process is initially dominated by the diffusion of CO_2 molecules through the hydrate layer. For each temperature, a straight line is obtained plotting $(1 - \alpha_r)^{1/3}$ as a function of $(t - t^*)^{1/2}$ according to Eq.(2-20). Since t* corresponds to ~ 20 % conversion for each temperature, after approximately 20 % conversion, the rate-limiting step of the process is the diffusion of CO_2 molecules through the layer of hydrate. This is in agreement with the suggestion that the slower growth rate of CO_2 hydrates in a water drop covered with a thin film of CO_2 hydrate may cause the slow transport of CO_2 molecules across the growing solid hydrate layer.[99] The temperature dependence of the diffusion constants gave an activation energy of 27.3 kJ/mol,[76] which is also close to the activation energy of diffusion of H_2O molecules in the QLL (*ca.* 24 kJ/mol[85]). This result shows that the formation of the hydrate is through a reaction between CO_2 and water molecules in the QLL.

For clathrate hydrates, many formation and dissociation phenomena have been studied. However, investigations on the formation phenomena the semi-clathrate hydrates are presently insufficient for understanding how these solids can be used in gas separation and gas storage processes.

2.4.3 Formation kinetics of semi-clathrate hydrates with gases

Trueba et al. investigated formation kinetics of H_2-TBAB semi-clathrate hydrate[100] or H_2 and CO_2-TBAF semi-clathrate hydrate.[101] The influence of pressure (1.5 – 16 MPa), TBA salt concentration (1.8 – 3.7 mol%) and formation method (*T*-cycle method and *T*-constant method) on the induction time, the formation rate and the amount of gas storage were determined. The induction time were favored at higher pressures and higher TBA salt concentrations due to the increase in supersaturation.[102] The difference between the induction time of H_2-TBAF-water system (150 – 250 min at pressure range of 5.0 – 13.0 MPa) and CO_2-TBAF-water system (90 – 150 min at pressure range of 1.6 – 2.3 MPa) at 3.4 mol% TBAF and similar temperature (H_2: 294 K, CO_2: 293 K) was thought to be due to the supersaturation of CO_2 in the liquid phase being reached faster than the supersaturation of H_2 because CO_2 hydrates are stable at higher temperatures and lower pressures than H_2 hydrates. Namely, the subcooling of the CO_2 system is larger than that of the H_2 system.[101] The rate of hydrate formation was calculated as the ratio of gas storage from the turbidity point to the stationary point over the formation time. The gas storage amount was calculated from the (*p*-*T*) data using the Peng-Robinson equation of state.[103] In H_2-TBAB[100] and H_2-TBAF[101] semi-clathrate hydrates, an increase in pressure and TBA salt concentration results in an increase in the formation rate (9.1×10^{-2} mmol/min at 3.4 mol% TBAF; 3.3×10^{-2} mmol/min at 1.8 mol% TBAF at 13 MPa) and the H_2 storage amount (12.0 mmol at 3.4 mol% TBAF; 4.5 mmol at 1.8 mol% TBAF at 13 MPa). Results obtained from both formation methods (*T*-cycle method and *T*-constant method) for semi-clathrate hydrate formation rates and H_2 storage amounts were similar and did not depend on the method. The reason for this is that the formation rate is

proportional to the driving force (supersaturation),[90] which increases with increasing H_2 pressure and TBA salt concentration. On the other hand, the salient dependence of TBAF concentration for formation rate and CO_2 storage amount for CO_2-TBAF semi-clathrate hydrate was not observed, and so only its CO_2 pressure dependence could be obtained (5.8×10^{-2} mmol/min at 3.1 MPa and 1.8 mol% TBAF; 2.2×10^{-2} mmol/min at 1.8 mol% TBAF at 2.3 MPa; 1.3×10^{-2} mmol/min at 3.4 mol% TBAF at 2.2 MPa).[101] Thus, the supersaturation of CO_2 seems to increase with pressure.

Fan et al. investigated the effect of TBAB and TBAF on the semi-clathrate hydrate formation rate and separation efficiency for CO_2 (16.6 mol%) and N_2 systems.[104] The TBAB and TBAF concentration were 0.293 mol%. The time to reach equilibrium with TBAF (*ca*. 0.25 h at 278 K) was about one-half that of TBAB (0.5 – 1 h at 278 K)[104] and one-fourth that of THF (1 – 2 h at 273 K and 0.5 – 1.5 mol% THF).[105] Thus, TBAB and TBAF seem to possibly accelerate hydrate formation. The semi-clathrate hydrate formation rate was quantitatively analyzed with a kinetic model given by Eq. (2-21).[104] The chemical potential difference was used as the driving force and the apparent gas storage rate ($-dn/dt = r_f$) was expressed as:[89,106]

$$r_f = aK^* \left(\mu_g - \mu_{eq} \right) \tag{2-21}$$

where a is the interfacial area, K^* is the overall kinetic constant, μ_g and μ_{eq} are chemical potentials of the guest molecule in the gas phase and in the hydrate phase, respectively. The mass transfer was assumed to be fast enough compared with crystal growth in the agitated the reactor, since semi-clathrate hydrate formation rate can be expressed by:

$$r_f = ak_f RT \ln \frac{f_g}{f_{eq}} \tag{2-22}$$

$$r_{\mathrm{f}} = \frac{V_{\mathrm{g}}}{RT}\frac{\left(f_{\mathrm{g}} - f_{\mathrm{eq}}\right)}{\Delta t} \tag{2-23}$$

where k_{f} is the crystal growth constant, f_{g} and f_{eq} are the fugacity of the gas phase and the hydrate phase at equilibrium conditions, respectively. The V_{g} is the volume of the gas phase and Δt is the time to reach equilibrium storage. Thus, the hydrate rate constant, ak_{f}, is expressed as:

$$ak_{\mathrm{f}} = \frac{V_{\mathrm{g}}}{\left(RT\right)^2}\frac{\left(f_{\mathrm{g}} - f_{\mathrm{eq}}\right)}{\Delta t \ln\left(f_{\mathrm{g}}/f_{\mathrm{eq}}\right)} \tag{2-24}$$

The ak_{f} increased with increasing feed pressure, and under the same feed pressure, the ak_{f} with TBAF (ak_{f} =8.26 $\times 10^{-7}$ mol^2/(s·J) at 6.8 MPa) was much higher than that with TBAB (ak_{f} =2.82 $\times 10^{-7}$ mol^2/(s·J) at 7.31 MPa). In addition, it was found that the CO_2 recovery was about 50 % with TBAF or TBAB, and the optimum CO_2 separation factor with TBAF was 37. This value was higher than the CO_2 separation factor with TBAB (9.8),[104] with THF (7.6)[105] or with pure water (13).[107] Therefore, TBAF semi-clathrate can be considered to be a possible gas capture, membrane or separation material.

2.5 Conclusions

For semi-clathrate hydrates, there are many structural and physical property data that are available. Although semi-clathrate hydrates seem to be feasible for use as H_2 storage materials, the H_2 storage amount with semi-clathrate hydrates is lower than that for clathrate hydrates. Nevertheless, semi-clathrate hydrates have high potential for gas capture and separation because of their stability and their favorable hydrate formation kinetics. For practical realization of the gas

separation technologies with semi-clathrate hydrate, it is important that their structure, phase equilibria and formation kinetics for guest molecules such as H_2 or CO_2 are studied in detail.

In this thesis, the objectives are to understand the gas inclusion phenomena in terms of crystal structure, phase equilibria, equilibrium gas storage amount and gas adsorption rate for gas separation method development in H_2 purification process from biomass. Therefore, in Chapter 3, the phase equilibria of gases + TBA salt + water system were measured, and a model for clathrate hydrate equilibria was developed. In Chapters 4 and 5, gas adsorption rates for clathrate hydrate and semi-clathrate hydrate particles are measured. A kinetic model for gas adsorption is developed in Chapter 4 that allows description of gas adsorption rate of clathrate hydrates.[108] The model is extended to semi-clathrate hydrates in Chapter 5. The theories and data for adsorption of H_2 and CO_2 with semi-clathrate particles are used to propose separation processes though simulation. The simulations are confirmed with experimental measurements of gas mixtures with semi-clathrate hydrates in Chapter 5. Conclusions and areas for future work are given in Chapter 6.

2.6 References

1. McMullan R, Jeffrey GA. Hydrates of the tetra-*n*-butyl and tetra-*i*-amyl quaternary ammonium salts. J Chem Phys. 1959;31:1231-1234.
2. McMullan RK, Jeffrey GA, Panke D. Polyhedral clathrate hydrates .XVI. structure of isopropylamine octahydrate. J Chem Phys. 1970;53:3568-3577.
3. McMullan RK, Jeffrey GA, Bonamico M. Polyhedral clathrate hydrates .V. structure of tetra-*n*-butyl ammonium fluoride hydrate. J Chem Phys. 1963;39:3295-3310.
4. Solodovnikov SF, Polianskaia TM, Alexeev VI, Diadin IA, Bakakin VV. Crystal-structure of

clathrate hydrate of tetraisoamylphosphonium bromide (i-$C_5H_{11})_4$ Pbr.$32H_2O$. Dokl Akad Nauk Sssr. 1979;247:357-360.

5. Lipkowski J, Suwinska K, Rodionova TV, Udachin KA, Dyadin YA. Phase and X-ray study of clathrate formation in the tetraisoamylammonium fluoride-water system. J Inclusion Phenom Mol. 1994;17:137-148.
6. Alekseev VI, Gatilov YV, Polyanskaya TM, Bakakin VV, Dyadin YA, Gaponenko LA. Characteristic features of the production of the hydrate framework around the hydrophobic-hydrophilic unit in the crystal-structure of the clathrate tri-*n*-butylphosphine oxide 34.5-hydrate. J Struct Chem. 1982;23:395-399.
7. Dyadin YA, Terekhova IS, Polyanskaya TM, Aladko LS. Clathrate hydrates of tetrabutylammonium fluoride and oxalate. J Struct Chem. 1976;17:566-571.
8. Komarov VY, Rodionova TV, Terekhova IS, Kuratieva NV. The cubic superstructure-I of tetrabutylammonium fluoride $(C_4H_9)_4NF\cdot 29.7H_2O$ clathrate hydrate. J Inclusion Phenom Macro. 2007;59:11-15.
9. Rodionova T, Komarov V, Villevald G, Aladko L, Karpova T, Manakov A. Calorimetric and structural studies of tetrabutylammonium chloride ionic clathrate hydrates. J Phys Chem B. 2010;114:11838-11846.
10. Lipkowski J, Komarov VY, Rodionova TV, Dyadin YA, Aladko LS. The structure of tetrabutylammonium bromide hydrate $(C_4H_9)_4NBr\cdot 2^1/_3H_2O$. J Supramol Chem. 2002;2:435-439.
11. Gaponenko LA, Solodovnikov SF, Dyadin YA, Aladko LS, Polyanskaya TM. Crystallographic study of tetra-*n*-butylammonium bromide polyhydrates. J Struct Chem. 1984;25:157-159.
12. Shimada W, Shiro M, Kondo H, Takeya S, Oyama H, Ebinuma T, Narita H. Tetra-*n*-butylammonium bromide-water (1/38). Acta Crystallogr C. 2005;61:O65-O66.
13. Davidson DW. *Water - A Comprehensive Treatise*. Vol 2.Plenum Press; New York. 1973.
14. Oyama H, Shimada W, Ebinuma T, Kamata Y, Takeya S, Uchida T, Nagao J, Narita H. Phase diagram, latent heat, and specific heat of TBAB semiclathrate hydrate crystals. Fluid Phase Equilib. 2005;234:131-135.
15. Dyadin YA, Udachin KA. Clathrate formation in water-peralkylonium salts systems. J Inclusion Phenom. 1984;2:61-72.
16. Dyadin YA, Gaponenko LA, Aladko LS, Bogatyryova SV. Clathrate hydrates of tetrabutylammonium carboxylates and dicarboxylates. J Inclusion Phenom. 1984;2:259-266.
17. Beurskens G, Jeffrey GA, Mcmullan RK. Polyhedral clathrate hydrates .VI. lattice type and ion

distribution in some new peralkyl ammonium, phosphonium, and sulfonium salt hydrates. J Chem Phys. 1963;39:3311-3315.

18. Mao WL, Mao HK, Goncharov AF, Struzhkin VV, Guo QZ, Hu JZ, Shu JF, Hemley RJ, Somayazulu M, Zhao YS. Hydrogen clusters in clathrate hydrate. Science. 2002;297:2247-2249.
19. Tsuda T, Ogata K, Hashimoto S, Sugahara T, Moritoki M, Ohgaki K. Storage capacity of hydrogen in tetrahydrothiophene and furan clathrate hydrates. Chem Eng Sci. 2009;64:4150-4154.
20. Komatsu H, Yoshioka H, Ota M, Sato Y, Watanabe M, Smith RL, Peters CJ. Phase equilibrium measurements of hydrogen-tetrahydrofuran and hydrogen-cyclopentane binary clathrate hydrate systems. J Chem Eng Data. 2010;55:2214-2218.
21. Florusse LJ, Peters CJ, Schoonman J, Hester KC, Koh CA, Dec SF, Marsh KN, Sloan ED. Stable low-pressure hydrogen clusters stored in a binary clathrate hydrate. Science. 2004;306:469-471.
22. Cruz Duarte AR, Peters CJ, Zevenbergen JF. Kinetics of formation and dissociation of sII hydrogen clathrate hydrates. Paper presented at: The 6th International Conference on Gas Hydrates; July 6-10, 2008; Vancouver, British Columbia, Canada.
23. Cruz Duarte AR, Shariati A, Zevenbergen JF, Florusse LJ, Peters CJ. Hydrogen storage in clathrate hydrates: phase equilibria, thermodynamics and kinetics. Paper presented at: The 6th International Conference on Gas Hydrates; July 6-10, 2008; Vancouver.
24. Duarte ARC, Shariati A, Peters CJ. Phase equilibrium measurements of structure sH hydrogen clathrate hydrates with various promoters. J Chem Eng Data. 2009;54:1628-1632.
25. Imai S, Okutani K, Ohmura R, Mori YH. Phase equilibrium for clathrate hydrates formed with difluoromethane + either cyclopentane or tetra-*n*-butylammonium bromide. J Chem Eng Data. 2005;50:1783-1786.
26. Hashimoto S, Murayama S, Sugahara T, Sato H, Ohgaki K. Thermodynamic and Raman spectroscopic studies on H_2+tetrahydrofuran + water and H_2+tetra-*n*-butyl ammonium bromide + water mixtures containing gas hydrates. Chem Eng Sci. 2006;61:7884-7888.
27. Hashimoto S, Sugahara T, Moritoki M, Sato H, Ohgaki K. Thermodynamic stability of hydrogen + tetra-*n*-butyl ammonium bromide mixed gas hydrate in nonstoichiometric aqueous solutions. Chem Eng Sci. 2008;63:1092-1097.
28. Arjmandi M, Chapoy A, Tohidi B. Equilibrium data of hydrogen, methane, nitrogen, carbon dioxide, and natural gas in semi-clathrate hydrates of tetrabutyl ammonium bromide. J Chem

Eng Data. 2007;52:2153-2158.

29. Duc NH, Chauvy F, Herri JM. CO_2 capture by hydrate crystallization - A potential solution for gas emission of steelmaking industry. Energ Convers Manage. 2007;48:1313-1322.
30. Lin W, Delahaye A, Fournaison L. Phase equilibrium and dissociation enthalpy for semi-clathrate hydrate of CO_2 plus TBAB. Fluid Phase Equilib. 2008;264:220-227.
31. Sun ZG, Jiang CM, Xie NL. Hydrate equilibrium conditions for tetra-*n*-butyl ammonium bromide. J Chem Eng Data. 2008;53:2375-2377.
32. Sun ZG, Sun L. Equilibrium conditions of semi-clathrate hydrate dissociation for methane + tetra-*n*-butyl ammonium bromide. J Chem Eng Data. 2010;55:3538-3541.
33. Li DL, Du JW, Fan SS, Liang DQ, Li XS, Huang NS. Clathrate dissociation conditions for methane plus tetra-*n*-butyl ammonium bromide (TBAB) plus water. J Chem Eng Data. 2007;52:1916-1918.
34. Zhong DL, Ye Y, Yang C. Equilibrium conditions for semiclathrate hydrates formed in the CH_4 + N_2 + O_2 + tetra-*n*-butyl ammonium bromide systems. J Chem Eng Data. 2011;56:2899-2903.
35. Li XS, Xia ZM, Chen ZY, Yan KF, Li G, Wu HJ. Equilibrium hydrate formation conditions for the mixtures of CO_2 + H_2 + tetrabutyl ammonium bromide. J Chem Eng Data. 2010;55:2180-2184.
36. Mohammadi AH, Richon D. Phase equilibria of semi-clathrate hydrates of tetra-*n*-butylammonium bromide + hydrogen sulfide and tetra-*n*-butylammonium bromide + methane. J Chem Eng Data. 2010;55:982-984.
37. Mohammadi AH, Eslamimanesh A, Belandria V, Richon D. Phase equilibria of semiclathrate hydrates of CO_2, N_2, CH_4, or H_2 + tetra-*n*-butylammonium bromide aqueous solution. J Chem Eng Data. 2011;56:3855-3865.
38. Mohammadi AH, Eslamimanesh A, Belandria V, Richon D, Naidoo P, Ramjugernath D. Phase equilibrium measurements for semi-clathrate hydrates of the (CO_2 + N_2 + tetra-*n*-butylammonium bromide) aqueous solution system. J Chem Thermodyn. 2012;46:57-61.
39. Mohammadi AH, Eslamimanesh A, Richon D. Semi-clathrate hydrate phase equilibrium measurements for the CO_2+H_2/CH_4+tetra-*n*-butylammonium bromide aqueous solution system. Chem Eng Sci. 2013;94:284-290.
40. Wang S, Danner M, Kuchling T, Clarke MA. Measurement of the three-phase (vapour + liquid + solid) equilibrium conditions of semi-clathrates formed from mixtures of CO_2, CO and H_2. J Chem Thermodyn. 2013;56:149-152.

41. Li SF, Fan SS, Wang JQ, Lang XM, Wang YH. Semiclathrate hydrate phase equilibria for CO_2 in the presence of tetra-*n*-butyl ammonium halide (bromide, chloride, or fluoride). J Chem Eng Data. 2010;55:3212-3215.

42. Deschamps J, Dalmazzone D. Dissociation enthalpies and phase equilibrium for TBAB semi-clathrate hydrates of N_2, CO_2, N_2 + CO_2 and CH_4 + CO_2. J Therm Anal Calorim. 2009;98:113-118.

43. Deschamps J, Dalmazzone D. Hydrogen storage in semiclathrate hydrates of tetrabutyl ammonium chloride and tetrabutyl phosphonium bromide. J Chem Eng Data. 2010;55:3395-3399.

44. Chapoy A, Gholinezhad J, Tohidi B. Experimental clathrate dissociations for the hydrogen + water and hydrogen + tetrabutylammonium bromide + water systems. J Chem Eng Data. 2010;55:5323-5327.

45. Lee S, Lee Y, Park S, Seo Y. Phase equilibria of semiclathrate hydrate for nitrogen in the presence of tetra-*n*-butylammonium bromide and fluoride. J Chem Eng Data. 2010;55:5883-5886.

46. Lee S, Park S, Lee Y, Lee J, Lee H, Seo Y. Guest gas enclathration in semiclathrates of tetra-*n*-butylammonium bromide: stability condition and spectroscopic analysis. Langmuir. 2011;27:10597-10603.

47. Sun QA, Guo XQ, Liu AX, Liu B, Huo YS, Chen GY. Experimental study on the separation of CH_4 and N_2 via hydrate formation in TBAB solution. Ind Eng Chem Res. 2011;50:2284-2288.

48. Kim SM, Lee JD, Lee HJ, Lee EK, Kim Y. Gas hydrate formation method to capture the carbon dioxide for pre-combustion process in IGCC plant. Int J Hydrogen Energ. 2011;36:1115-1121.

49. Meysel P, Oellrich L, Bishnoi PR, Clarke MA. Experimental investigation of incipient equilibrium conditions for the formation of semi-clathrate hydrates from quaternary mixtures of (CO_2 + N_2 + TBAB + H_2O). J Chem Thermodyn. 2011;43:1475-1479.

50. Acosta HY, Bishnoi PR, Clarke MA. Experimental measurements of the thermodynamic equilibrium conditions of tetra-*n*-butylammonium bromide semiclathrates formed from synthetic landfill gases. J Chem Eng Data. 2011;56:69-73.

51. Park S, Lee S, Lee Y, Seo Y. CO_2 capture from simulated fuel gas mixtures using semiclathrate hydrates formed by quaternary ammonium salts. Environ Sci Technol. 2013;47:7571-7577.

52. Fan SS, Li Q, Nie JH, Lang XM, Wen YG, Wang YH. Semiclathrate hydrate phase equilibrium for CO_2/CH_4 gas mixtures in the presence of tetrabutylammonium halide (bromide, chloride, or

fluoride). J Chem Eng Data. 2013;58:3137-3141.

53. Godishala KK, Sangwai JS, Sami NA, Das K. Phase stability of semiclathrate hydrates of carbon dioxide in synthetic sea water. J Chem Eng Data. 2013;58:1062-1067.

54. Makino T, Yamamoto T, Nagata K, Sakamoto H, Hashimoto S, Sugahara T, Ohgaki K. Thermodynamic stabilities of tetra-*n*-butyl ammonium chloride + H_2, N_2, CH_4, CO_2, or C_2H_6 semiclathrate hydrate systems. J Chem Eng Data. 2010;55:839-841.

55. Mayoufi N, Dalmazzone D, Furst W, Delahaye A, Fournaison L. CO_2 enclathration in hydrates of peralkyl-(ammonium/phosphonium) salts: Stability conditions and dissociation enthalpies. J Chem Eng Data. 2010;55:1271-1275.

56. Sakamoto J, Hashimoto S, Tsuda T, Sugahara T, Inoue Y, Ohgaki K. Thermodynamic and Raman spectroscopic studies on hydrogen + tetra-*n*-butyl ammonium fluoride semi-clathrate hydrates. Chem Eng Sci. 2008;63:5789-5794.

57. Mohammadi A, Manteghian M, Mohammadi AH. Dissociation data of semiclathrate hydrates for the systems of tetra-*n*-butylammonium fluoride (TBAF) + methane + Water, TBAF + carbon dioxide + water, and TBAF + nitrogen + water. J Chem Eng Data. 2013;58:3545-3550.

58. Mayoufi N, Dalmazzone D, Delahaye A, Clain P, Fournaison L, Furst W. Experimental data on phase behavior of simple tetrabutylphosphonium bromide (TBPB) and mixed CO_2 + TBPB semiclathrate hydrates. J Chem Eng Data. 2011;56:2987-2993.

59. Fujisawa Y, Tsuda T, Hashimoto S, Sugahara T, Ohgaki K. Thermodynamic stability of hydrogen + tetra-*n*-butyl phosphonium bromide mixed semi-clathrate hydrate. Chem Eng Sci. 2012;68:660-662.

60. Suginaka T, Sakamoto H, Iino K, Sakakibara Y, Ohmura R. Phase equilibrium for ionic semiclathrate hydrate formed with CO_2, CH_4, or N_2 + tetrabutylphosphonium bromide. Fluid Phase Equilib. 2013;344:108-111.

61. Shi LL, Liang DQ, Li DL. Phase equilibrium data of tetrabutylphosphonium bromide + carbon dioxide or nitrogen semiclathrate hydrates. J Chem Eng Data. 2013;58:2125-2130.

62. Du JW, Liang DQ, Li DL, Chen YF, Li XJ. Phase equilibrium conditions of tetrabutyl ammonium nitrate + CO_2, N_2, or CH_4 semiclathrate hydrate systems. Ind Eng Chem Res. 2011;50:11720-11723.

63. Shi LL, Liang DQ, Li DL. Phase equilibrium conditions for simulated landfill gas hydrate formation in aqueous solutions of tetrabutylammonium nitrate. J Chem Thermodyn. 2014;68:322-326.

64. Hughes TJ, Marsh KN. Methane semi-clathrate hydrate phase equilibria with tetraisopentylammonium fluoride. J Chem Eng Data. 2011;56:4597-4603.

65. Ogata K, Tsuda T, Amano S, Hashimoto S, Sugahara T, Ohgaki K. Hydrogen storage in trimethylamine hydrate: Thermodynamic stability and hydrogen storage capacity of hydrogen + trimethylamine mixed semi-clathrate hydrate. Chem Eng Sci. 2010;65:1616-1620.

66. Bergeron S, Servio P. Reaction rate constant of CO_2 hydrate formation and verification of old premises pertaining to hydrate growth kinetics. AIChE J. 2008;54:2964-2970.

67. Clarke M, Bishnoi PR. Determination of the activation energy and intrinsic rate constant of methane gas hydrate decomposition. Can J Chem Eng. 2001;79:143-147.

68. Clarke MA, Bishnoi PR. Determination of the intrinsic kinetics of CO_2 gas hydrate formation using in situ particle size analysis. Chem Eng Sci. 2005;60:695-709.

69. Kang SP, Lee JW. Kinetic behaviors of CO_2 hydrates in porous media and effect of kinetic promoter on the formation kinetics. Chem Eng Sci. 2010;65:1840-1845.

70. Kim HC, Bishnoi PR, Heidemann RA, Rizvi SSH. Kinetics of methane hydrate decomposition. Chem Eng Sci. 1987;42:1645-1653.

71. Komai T, Kang SP, Yoon JH, Yamamoto Y, Kawamura T, Ohtake M. In situ Raman spectroscopy investigation of the dissociation of methane hydrate at temperatures just below the ice point. J Phys Chem B. 2004;108:8062-8068.

72. Lee JW, Chun MK, Lee KM, Kim YJ, Lee H. Phase equilibria and kinetic behavior of CO_2 hydrate in electrolyte and porous media solutions: Application to ocean sequestration CO_2. Korean J Chem Eng. 2002;19:673-678.

73. Liang MY, Chen GJ, Sun CY, Yan LJ, Liu J, Ma QL. Experimental and modeling study on decomposition kinetics of methane hydrates in different media. J Phys Chem B. 2005;109:19034-19041.

74. Malegaonkar MB, Dholabhai PD, Bishnoi PR. Kinetics of carbon dioxide and methane hydrate formation. Can J Chem Eng. 1997;75:1090-1099.

75. Takeya S, Hondoh T, Uchida T. In situ observation of CO_2 hydrate by X-ray diffraction. Ann NY Acad Sci. 2000;912:973-982.

76. Henning RW, Schultz AJ, Thieu V, Halpern Y. Neutron diffraction studies of CO_2 clathrate hydrate: Formation from deuterated ice. J Phys Chem A. 2000;104:5066-5071.

77. Kamath VA, Holder GD. Dissociation heat-transfer characteristics of methane hydrates. AIChE J. 1987;33:347-350.

78. Kamath VA, Mutalik PN, Sira JH, Patil SL. Experimental study of brine injection and depressurization methods for dissociation of gas hydrates. SPE Form Eval. 1991;6:477-484.

79. Clarke M, Bishnoi PR. Determination of the intrinsic rate of ethane gas hydrate decomposition. Chem Eng Sci. 2000;55:4869-4883.

80. Kamath VA, Holder GD, Angert PF. Three phase interfacial heat transfer during the dissociation of propane hydrates. Chem Eng Sci. 1984;39:1435-1442.

81. Kamath VA, Patil SL. Analogy between effect of inhibitors on hydrate equilibrium thermodynamics and hydrate decomposition kinetics. Ann NY Acad Sci. 1994;715:463-467.

82. Circone S, Stern LA, Kirby SH. The role of water in gas hydrate dissociation. J Phys Chem B. 2004;108:5747-5755.

83. Takeya S, Shimada W, Kamata Y, Ebinuma T, Uchida T, Nagao J, Narita H. In situ X-ray diffraction measurements of the self-preservation effect of CH_4 hydrate. J Phys Chem A. 2001;105:9756-9759.

84. Takeya S, Ebinuma T, Uchida T, Nagao J, Narita H. Self-preservation effect and dissociation rates of CH_4 hydrate. J Cryst Growth. 2002;237:379-382.

85. Mizuno Y, Hanafusa N. Studies of surface properties of ice using nuclear magnetic resonance. J Phys Colloq C1. 1987;48:511-517.

86. Shepherd TD, Koc MA, Molinero V. The quasi-liquid layer of ice under conditions of methane clathrate formation. J Phys Chem C. 2012;116:12172-12180.

87. He YY, Rudolph ESJ, Zitha PLJ, Golombok M. Kinetics of CO_2 and methane hydrate formation: An experimental analysis in the bulk phase. Fuel. 2011;90:272-279.

88. Englezos P. Nucleation and growth of gas hydrate crystals in relation to "kinetic inhibition". Rev Inst Fr Petrol. 1996;51:789-795.

89. Englezos P, Kalogerakis N, Dholabhai PD, Bishnoi PR. Kinetics of formation of methane and ethane gas hydrates. Chem Eng Sci. 1987;42:2647-2658.

90. Englezos P, Kalogerakis N, Dholabhai PD, Bishnoi PR. Kinetics of gas hydrate formation from mixtures of methane and ethane. Chem Eng Sci. 1987;42:2659-2666.

91. Dholabhai PD, Englezos P, Kalogerakis N, Bishnoi PR. Equilibrium conditions for methane hydrate formation in aqueous mixed electrolyte-solutions. Can J Chem Eng. 1991;69:800-805.

92. Chun MK, Lee H. Kinetics of formation of carbon dioxide clathrate hydrates. Korean J Chem Eng. 1996;13:620-626.

93. Bergeron S, Servio P. CO_2 and CH_4 mole fraction measurements during hydrate growth in a

semi-batch stirred tank reactor and its significance to kinetic modeling. Fluid Phase Equilib. 2009;276:150-155.

94. Hashemi S, Macchi A, Servio P. Gas hydrate growth model in a semibatch stirred tank reactor. Ind Eng Chem Res. 2007;46:5907-5912.

95. Okutani K, Kuwabara Y, Mori YH. Surfactant effects on hydrate formation in an unstirred gas/liquid system: Amendments to the previous study using HFC-32 and sodium dodecyl sulfate. Chem Eng Sci. 2007;62:3858-3860.

96. Watanabe K, Imai S, Mori YH. Surfactant effects on hydrate formation in an unstirred gas/liquid system: An experimental study using HFC-32 and sodium dodecyl sulfate. Chem Eng Sci. 2005;60:4846-4857.

97. Uchida T, Hondoh T, Mae S, Duval P, Lipenkov VY. Effects of temperature and pressure on the transformation rate from air bubbles to air-hydrate crystals in ice sheets. Ann Glaciol. 1994;20:143-147.

98. Salamatin AN, Hondoh T, Uchida T, Lipenkov VY. Post-nucleation conversion of an air bubble to clathrate air-hydrate crystal in ice. J Cryst Growth. 1998;193:197-218.

99. Uchida T, Ebinuma T, Kawabata J, Narita H. Microscopic observations of formation processes of clathrate-hydrate films at an interface between water and carbon dioxide. J Cryst Growth. 1999;204:348-356.

100. Trueba AT, Radovic IR, Zevenbergen JF, Kroon MC, Peters CJ. Kinetics measurements and in situ Raman spectroscopy of formation of hydrogen-tetrabutylammonium bromide semi-hydrates. Int J Hydrogen Energ. 2012;37:5790-5797.

101. Trueba AT, Radovic IR, Zevenbergen JF, Peters CJ, Kroon MC. Kinetic measurements and in situ Raman spectroscopy study of the formation of TBAF semi-hydrates with hydrogen and carbon dioxide. Int J Hydrogen Energ. 2013;38:7326-7334.

102. Natarajan V, Bishnoi PR, Kalogerakis N. Induction phenomena in gas hydrate nucleation. Chem Eng Sci. 1994;49:2075-2087.

103. Peng D, Robinson DB. A new two-constant equation of state. Ind Eng Chem Fund. 1976;15:59-64.

104. Fan SS, Li SF, Wang JQ, Lang XM, Wang YH. Efficient capture of CO_2 from simulated flue gas by formation of TBAB or TBAF semiclathrate hydrates. Energ Fuel. 2009;23:4202-4208.

105. Linga P, Adeyemo A, Englezos P. Medium-pressure clathrate hydrate/membrane hybrid process for postcombustion capture of carbon dioxide. Environ Sci Technol. 2008;42:315-320.

106. Daimaru T, Yamasaki A, Yanagisawa Y. Effect of surfactant carbon chain length on hydrate formation kinetics. J Petrol Sci Eng. 2007;56:89-96.

107. Linga P, Kumar RN, Englezos P. Gas hydrate formation from hydrogen/carbon dioxide and nitrogen/carbon dioxide gas mixtures. Chem Eng Sci. 2007;62:4268-4276.

108. Komatsu H, Ota M, Sato Y, Watanabe M, Smith RL. Multiple adsorption resistance model for constituent molecular effects of hydrogen clathration-kinetics in clathrate hydrate particles. Chem Eng Sci. 2014;108:270-282.

Chapter 3

Measurement and correlation of phase equilibria of semi-clathrate hydrates with H_2 and CO_2

3.1 Introduction

Quaternary ammonium salts (QAS), such as tetra-*n*-butyl ammonium (TBA) salts, form semi-clathrate hydrates by replacing of water molecules in the crystal structure with the cation and anion of the QAS. The crystal structures of semi-clathrate hydrates vary greatly according to the type of QAS that is added.[1-5] The *P*-*T* diagram for gas + QAS semi-clathrate hydrate is related to the crystal structure and affects gas inclusion behavior. Therefore, phase behavior as a function of temperature, pressure or composition is important for understanding the practical use of semi-clathrate hydrates.

In this chapter, phase equilibria of gas + tetra-*n*-butyl ammonium (TBA) salt semi-clathrate hydrates are reported. Gases studied are hydrogen (H_2), carbon dioxide (CO_2) and mixtures H_2 and CO_2. TBA salts studied are tetra-*n*-butyl ammonium bromide (TBAB), tetra-*n*-butyl

ammonium chloride (TBAC) and tetra-*n*-butyl ammonium fluoride (TBAF). The effect of crystal structure and anion of the TBA salt on the phase equilibria are investigated. Experimental data with pure gas systems are correlated with a modified van der Waals and Platteeuw model. The H_2 and CO_2 inclusion behavior is discussed in terms of the experimentally determined phase equilibria and in terms of the model correlation.

3.2 Experimental

3.2.1 Materials

High-purity water obtained from a distillation unit (Advantec Toyo Kaisha, Ltd., RFD250NB) that had an electrical conductivity below 5.5 μS/m was used in the experiments. Hydrogen gas (99.99%), carbon dioxide (99.99%), a hydrogen-carbon dioxide gas mixture (H_2 (99.99999%): *ca.* 80 vol%, CO_2 (99.995 %): *ca.* 20 vol%), tetra-*n*-butyl ammonium bromide (≥98.0%, Wako Pure Chemical Industries, Ltd.), tetra-*n*-butyl ammonium chloride (>98.0%, Tokyo Chemical Industry Co., Ltd.) and tetra-*n*-butyl ammonium fluoride trihydrate (≥97.0%, Sigma-Aldrich Co.) salts were used without further purification. H_2-CO_2 gas mixture cylinder was made in a similar way with that in Chapter 5, thus H_2 composition in Chapter 3 was assumed to be the same as that in Chapter 5 (H_2/CO_2 = 3.4). The quaternary ammonium salts are referred to as TBAB, TBAC and TBAF for bromide, chloride and fluoride anions, respectively.

3.2.2 Experimental apparatus

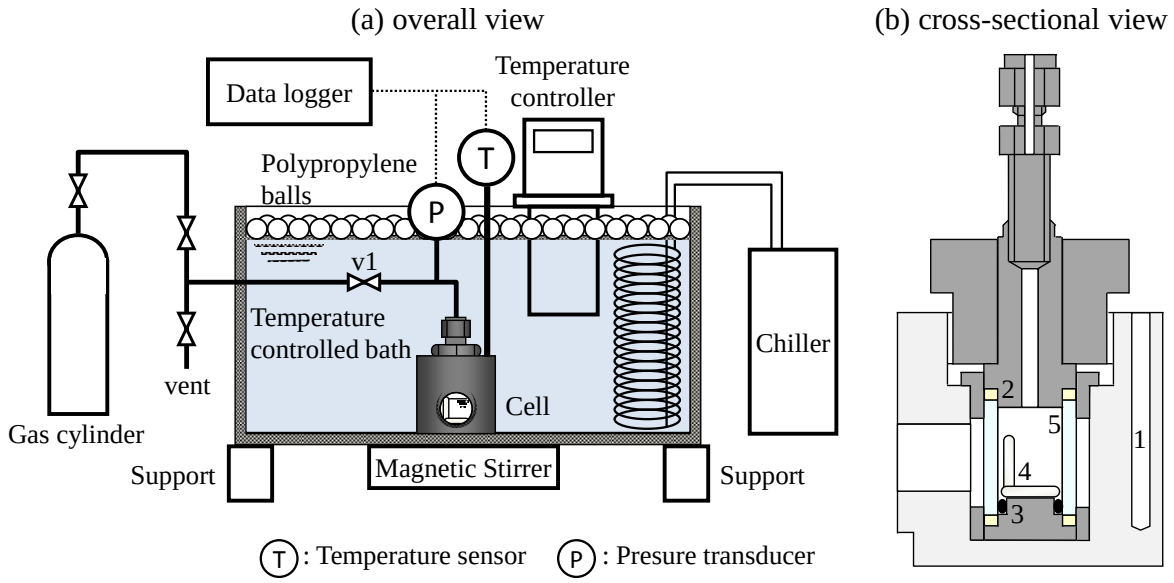

Figure 3-1. Schematic diagram of the experimental apparatus. (a): overall view of the apparatus, (b): cross-section is taken at 90° to allow view of the thermowell. 1: thermowell, 2: O-ring made from polytetrafluoroetylene (PTFE), 3: O-ring made from nitrile butadiene rubber (NBR), 4: L-shape stirrer bar, 5: sapphire tube.

Figure 3-1 (a) shows a schematic diagram of the experimental apparatus and Figure 3-1 (b) shows a cross-sectional view of the cell. The inner volume of the cell (Figure 3-1 b) was 1.3 cm^3 and its maximum was pressure 15 MPa. The cell was fabricated out of 304 stainless steel and consisted of a seven piece assembly that included a sapphire tube (14.0 mm o.d., 10.0 mm i.d., length 17.7 mm, Ogura Jewel Industry Co., Ltd., Tokyo) which was held internally with two O-rings (PTFE) used on the outer lips of the tube and one O-ring (NBR, JIS class 1B) used on the inner surface of the tube (Figure 3-1 b). The sapphire tube was maintained in a vertical position by a lower support and upper support gland nut that were held in an outer housing. The outer housing (Figure 3-1 b) had two diametrically opposed view ports (10 mm diameter) that allowed for

visual observation of the cell contents. A stirrer was made by wrapping and pressing a 1.58 mm diameter stainless tube (1/16 inch 316 stainless steel) around a teflon stirring bar (3 mm diameter × 8 mm long, rare-earth magnet, *ca.* 0.4 kG) into a coiled L-shape (8.95 × 9.40 mm). The stirrer was interfaced to a magnetic stirrer (RP-1AR, Matsuura Seisakusyo, Ltd., Tokyo) that was outside of the temperature-controlled bath. The entire cell assembly was thermally-insulated with Aeroflex sheet (Aeroflex, U.S.A) and immersed in a temperature-controlled ethylene glycol-water (*ca.* 24 mol% ethylene glycol) bath. The volume of gas space (Figure 3-1 a) between the cell and the valve (v1) along with volume of the pressure transducer was *ca.* 2.57 cm^3 and was kept in the thermally-controlled bath. The temperature of the bath was controlled with a refrigerated circulator controller (Model MB, Julabo, Germany) and a chiller (CA-1112 type, Tokyo Rika Kikai Co., Ltd.). The bath was thermally insulated on the sides and bottom with Aeroflex sheet (Aeroflex, U.S.A) and on the top with polypropylene balls (diameter, 10 mm, Matsuura Seisakusyo, Ltd., Tokyo) such that the temperature of the cell could be controlled to within ±17 mK at 273.6 K. The system temperature was measured with a platinum resistance temperature sensor (Pt 100 Ω, 3.17 mm diameter (1/8 inch), NR-350, 4-wire type, Netsushin) calibrated against a standard temperature probe (GE Kaye IRTD-400, accuracy ±25 mK) that had a stated accuracy of 44 mK (Appendix A), and was inserted into a hole in the cell assembly wall. The system pressure was measured by a sealed gauge pressure transducer (20 MPa F.S., PTX621-0, GE Sensing Japan) calibrated against a dead weight tester (Druck Pressurements M2200-5, stated accuracy ±0.015%) that had a stated accuracy of 4.5 kPa (Appendix B).

3.2.3 Experimental procedure

For the measurement of phase equilibria of gases with TBA salts and water, a TBA salt aqueous solution was charged into the cell that would give a TBAB mole fraction of 0.6 or 3.7 mol%, a TBAC mole fraction of 3.3 mol%, or a TBAF mole fraction of 3.0 or 3.3 mol% which corresponded to literature data[6,7] or stoichiometric compositions for TS-I (Table 5-1). The cell was purged with H_2, CO_2 or H_2 and CO_2 mixture five times at 4 MPa to reduce the air concentration to trace, and was then pressurized to 12 MPa with H_2, 5 MPa with CO_2 or 8 MPa with H_2 and CO_2 mixture gas. The system temperature was maintained at 294 K (TBAB or TBAC systems) or 305 K (TBAF systems) for 6 h as the solution was stirred. The temperature was lowered to about 274 K (TBAB or TBAC added systems) or 291 K (TBAF added systems), to initiate semi-clathrate hydrate formation. For CO_2 systems, however, the temperature was not lowered below 283 K since it was necessary to avoid liquefaction of CO_2. For TBAC or TBAF added systems, the temperature was increased to the semi-clathrate hydrate dissociation temperature so that the semi-clathrate hydrates would be in a liquid state and gas inclusion could be increased. The semi-clathrate hydrate became solid by lowering the system temperature to below the dissociation temperature. The system temperature was held constant until the system pressure stabilized.

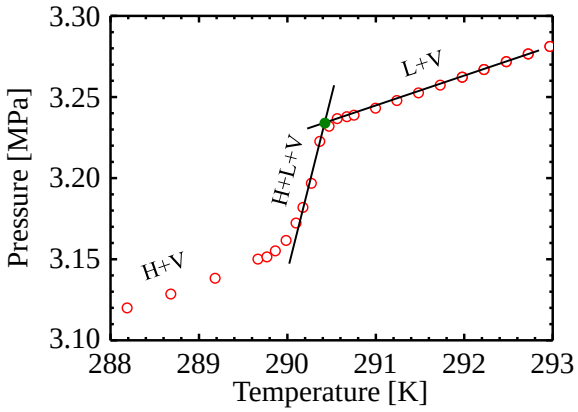

Figure 3-2. Typical pressure – temperature working plot for determining the hydrate dissociation pressure for the CO_2 + TBAB + water system. Red circles are experimental data point, green filled circle shows the dissociation temperature and pressure determined from the intersection of the H-L-V equilibrium line with the L-V equilibrium curve. H: hydrate phase, L: liquid phase, V: vapor phase.

In a typical set of measurements (Figure 3-2), the cell was heated in steps by gradually increasing the temperature and allowing the pressure to stabilize. The system temperature and pressure stabilized rapidly and typically required three minutes, however, longer equilibration times (ca. > 3 h) were used as noted below. The step-size of the temperature increase was typically 0.1 K. After each temperature increase, pressure was allowed to equilibrate and to remain stable for at least 3 h and in the vicinity of the hydrate dissociation temperature, the equilibration time used was typically 17 h. Points were noted on the hydrate-vapor (H-V), hydrate-liquid-vapor (H-L-V) and liquid-vapor (L-V) equilibrium curves as shown in Figure 3-2. The point of the hydrate dissociation was taken as the point at the intersection of the liquid-vapor (L-V) line and the hydrate-liquid-vapor (H-L-V) line as shown in Figure 3-2. The temperature of hydrate dissociation was defined as the point of hydrate equilibria[8] and was determined from the intersection of the H-L-V equilibrium line with the L-V equilibrium curve. Visual observations

from the cell window were used to confirm the phase equilibria.

3.3 Results and discussion

3.3.1 Experimental results

Figure 3-3 show phase equilibria measurement and literature results of (a) H_2-TBAB-water, H_2-TBAC-water, (b) CO_2 + TBAB or TBAC + water systems, Table 3-1 summarizes phase equilibrium data of the gases + TBA salt + water system measured in this work.

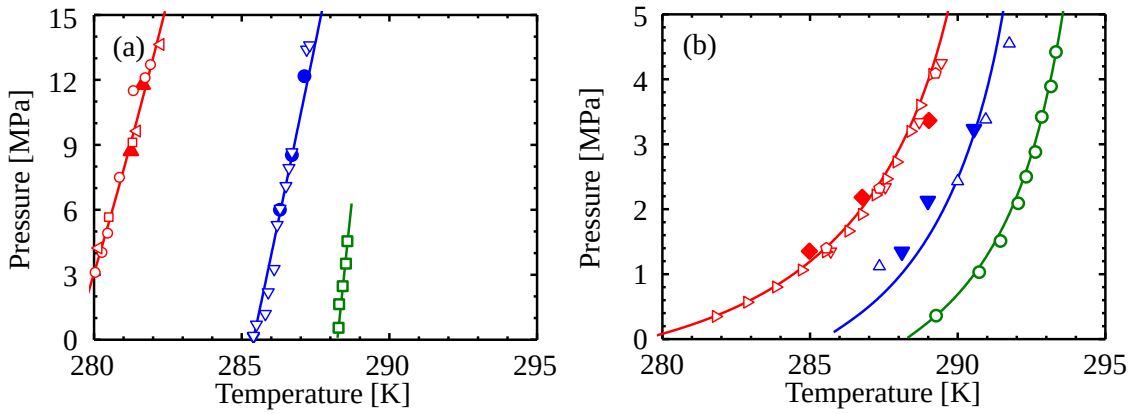

Figure 3-3. Phase diagram of (a) H_2 + TBAB or TBAC + water systems and (b) CO_2 + TBAB or TBAC + water systems. Continuous lines are correlation results. Red symbols (H_2:▲this work,[9] ◁,[10] □,[11] and ○.[12] CO_2: ◆this work,[9] ▷,[13] ▽[14] and ⬠ [10]) refer to 0.6 mol% TBAB systems. Blue symbols (H_2:●this work[9] and ▽.[12] CO_2:▼this work[9] and △[14]) refer to 3.7 mol% TBAB systems. Green symbols (H_2: □. [6] CO_2: ○[6]) refer to 3.3 mol% TBAC systems.

The phase equilibria data measured in this work were compared with literature data[10-15] (Figure 3-3) and were in agreement so that the experimental methods used could be confirmed.

Figure 3-4 show phase equilibria measurement and literature results of (a) H_2 + TBAF + water systems, (b) CO_2 + TBAF + water systems.

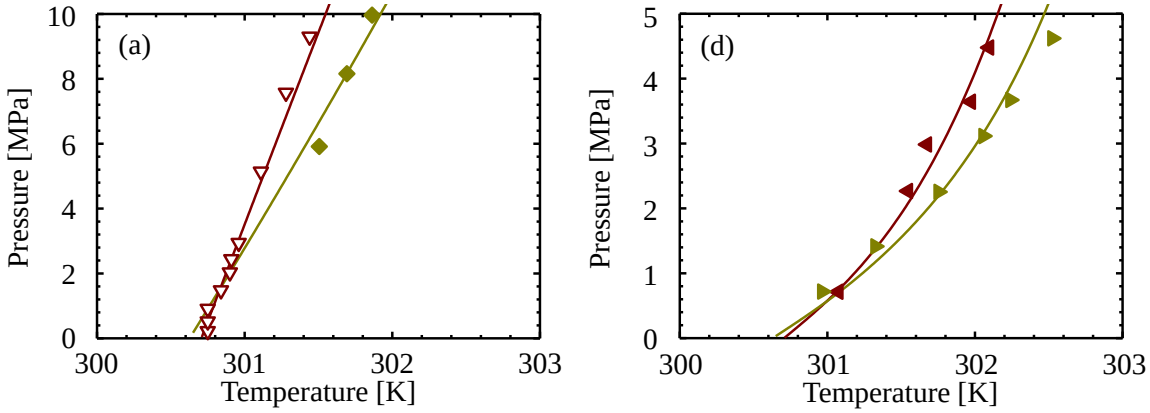

Figure 3-4. Phase diagram of (a) H_2 + TBAF + water systems and (b) CO_2 + TBAF + water systems. Continuous lines are correlation results. Olive symbols (H_2:◆this work, CO_2: ▶this work) refer to 3.0 mol% TBAF systems. Brown symbol (H_2: ▽[7] CO_2:◀this work[9]) refer to 3.3 mol% TBAF systems.

For H_2 and CO_2 systems, dissociation temperatures were in the order of (largest to smallest) 3.0 mol% TBAF, 3.3 mol% TBAF, 3.3 mol% TBAC, 3.7 mol% TBAB and 0.6 mol% TBAB. The 3.0 mol% TBAF semi-clathrate hydrate was most stable among the TBA salt systems studied (Figures 3-3 and 3-4). The order of the system stabilities corresponded to the order of their dissociation temperatures at atmospheric pressure.[7,16,17] Although 3.0 mol% TBAF semi-clathrate hydrate had a comparable dissociation temperature at atmospheric pressure with that of 3.3 mol% TBAF semi-clathrate,[7] the dissociation temperatures of 3.0 mol% TBAF semi-clathate hydrate were higher than those of 3.3 mol% TBAF semi-clathrate hydrates above 1 MPa (Figure 3-4).

Table 3-1. Phase equilibrium data (H + L + V) for gases + tetra-*n*-butyl ammonium (TBA) salt + water systems measured in this work. H: hydrate phase, L: liquid phase, V: vapor phase.

Gas	TBA salt	*T* [K]	*P* [MPa]
H_2	0.6 mol% TBAB[9]	281.25	8.715
		281.65	11.774
	3.7 mol% TBAB[9]	286.29	6.003
		286.70	8.523
		287.13	12.170
	3.0 mol% TBAF	301.51	5.914
		301.69	8.157
		301.86	9.966
CO_2	0.6 mol% TBAB[9]	284.98	1.353
		286.76	2.184
		289.02	3.366
	3.7 mol% TBAB[9]	288.11	1.345
		288.99	2.127
		290.55	3.233
	3.0 mol% TBAF	300.97	0.717
		301.33	1.414
		301.75	2.255
		302.06	3.114
		302.24	3.671
		302.52	4.621
	3.3 mol% TBAF	301.07	0.715
		301.55	2.267
		301.67	2.985
		301.97	3.643
		302.10	4.479
H_2/ CO_2 = 3.4	0.6 mol% TBAB[9]	282.72	3.360
		283.41	5.041
		283.44	4.993
	3.7 mol% TBAB[9]	286.58	1.460
		287.19	3.332
		287.63	5.369
		287.69	5.928
		287.89	7.690
	3.3 mol% TBAC	289.31	1.281
		289.90	2.706
		290.50	3.961
		290.99	5.407
	3.0 mol% TBAF	301.32	4.547
		301.61	6.090
		301.77	6.979

TBAB : tetra-*n*-butyl ammonium bromide, TBAC: tetra-*n*-butyl ammonium chloride, TBAF: tetra-*n*-butyl ammonium fluoride.

For TBAF semi-clathrate hydrate, TS-I and SCS-I structures have been reported.[4,5] The number of S-cages included with gas per H_2O molecule for TS-I and SCS-I were 0.06 (=10/162) and 0.05 (16/344) (Table 5-1), respectively, which means that the gas inclusion capacity of TS-I structure is higher than that of SCS-I structure. The high stability of 3.0 mol% TBAF semi-clathrate hydrate at high pressure can probably be attributed to the amount of included gas because 3.0 mol% TBAF probably form TS-I structure and 3.3 mol% TBAF probably forms SCS-I structure at these conditions. On the other hand, below 1 MPa, the dissociation temperature of 3.3 mol% TBAF semi-clathrate hydrate was higher than that of 3.0 mol% TBAF semi-clathrate hydrate (Figure 3-3 d). This trend implies that gas inclusion behavior and structure formation at high pressure are different from those at low pressure.

Figure 3-5 shows phase equilibria measurements and literature results for H_2 + TBAF + water and CO_2 + TBAF + water systems.

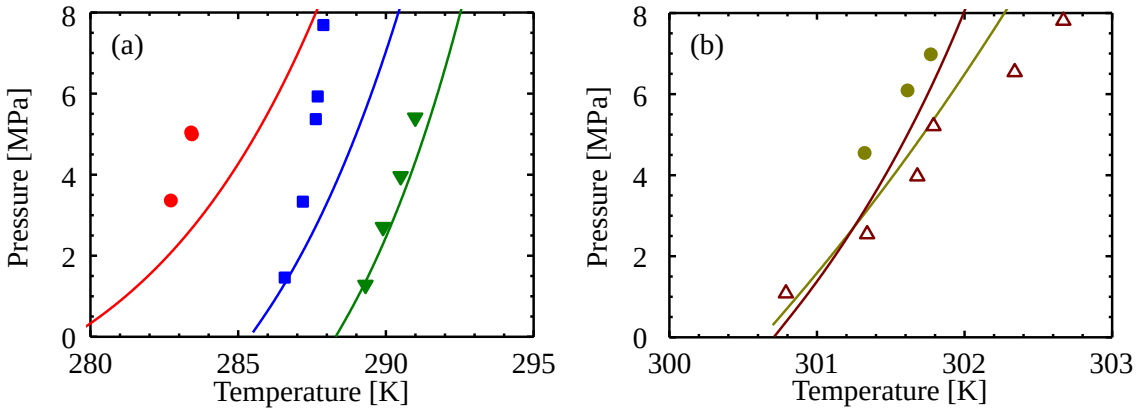

Figure 3-5. Phase diagram of H_2-CO_2 gas mixture + TBA salt + water systems. Continuous lines were correlation results. ●: H_2+CO_2 (H_2/CO_2 = 3.4) + 0.6 mol% TBAB + water systems, ■: H_2+CO_2 (H_2/CO_2 = 3.4) + 3.7 mol% TBAB + water systems, ▼: H_2+CO_2 (H_2/CO_2 = 3.4) + 3.3 mol% TBAC + water systems, ●: H_2+CO_2 (H_2/CO_2 = 3.4) + 3.0 mol% TBAF + water systems and △: H_2+CO_2 (H_2/CO_2 = 1.5) + 3.3 mol% TBAF + water systems.[18]

For H_2 + CO_2 (H_2/CO_2 = 3.4) systems, the *dP*/*dT* of 3.7 mol% TBAB semi-clathrate hydrate was clearly larger than that of 0.6 mol% TBAB and 3.3 mol% TBAC semi-clathrate hydrate (Figure 3-5 a). The *dP/dT* of H_2 + CO_2 (H_2/CO_2 = 1.5) + 3.3 mol% TBAF semi-clathrate hydrate was comparable with that for H_2 + CO_2 (H_2/CO_2 = 3.4) + 3.0 mol% TBAF semi-clathrate hydrate despite the high CO_2 composition (Figure 3-5b). The crystal structure and anion of TBA salt seem to affect gas inclusion behavior.

3.3.2 Thermodynamic model for semi-clathrate hydrate phase equilibira

The phase equilibrium model for gas clathrate hydrates by Parrich and Prausnitz[19] that is based on the clathrate hydrate model by van der Waals-Platteeuw[20] was modified to allow description of semi-clathrate hydrates. In this thesis, the structure and thermal parameters prepared (section 3.3.2.1) and the definition of the L-cage was changed (sections 2.2.2 and 3.3.2.2). The proposed model follows the fundamental assumptions of Parrich and Prausnitz and van der Waals-Platteeuw, which are given as follows:[19]

1. The host molecules contribution to the free energy is independent of their occupation in the cages. This assumption implies that included guest molecules do not distort the cage.
2. Each cage can contain at most one guest molecule, which cannot diffuse from the cage.
3. There are no interactions of the solute molecules, such as the energy of each included guest molecule; each guest molecule is independent of the number and types of other solute molecules.
4. No quantum effects are present and classical statistics are valid.

The hydrate is considered to form from liquid water as a hypothetical empty hydrate structure and

then guest molecules are included into the hydrate cages. Phase equilibria is considered to exist when the chemical potential difference between the liquid phase μ_W^L and the empty hydrate phase μ_W^β in Eq. (3-1) are equal to the chemical potential difference of clathrate hydrate phase μ_W^H and the empty hydrate μ_W^β in Eq. (3-2) as:

$$\Delta\mu_W^L = \mu_W^\beta - \mu_W^L \quad (3\text{-}1)$$

$$\Delta\mu_W^H = \mu_W^\beta - \mu_W^H \quad (3\text{-}2)$$

so that

$$\Delta\mu_W^L = \Delta\mu_W^H \quad (3\text{-}3)$$

3.3.2.1 Chemical potential difference of the liquid phase

The chemical potential difference of the liquid phase is determined from Eq. (3-4):

$$\frac{\Delta\mu_W^L}{RT} = \frac{\Delta\mu_W^0}{RT_0} - \int_{T_0}^{T} \frac{\Delta h_W^L}{RT^2} dT + \int_{P_0}^{P} \frac{\Delta v_W^L}{RT} dP - \ln\left(a_W\right) \quad (3\text{-}4)$$

where, $\Delta\mu_W^0$ is the differential chemical potential between water of empty hydrate structure and pure liquid water at reference conditions (T_0 = 273.15 K, P_0 = 0.1 MPa), and Δv_W^L is the molar volume difference between water of empty hydrate structure and pure liquid water. The $a_{W,salt}$ is an activity of water in liquid phase as described by Eq.(3-5): [21]

$$\ln a_W = \ln a_{W,salt} + \ln a_{W,gas} \quad (3\text{-}5)$$

The $a_{W,salt}$ and $a_{W,gas}$ are activity of water in TBA salt aqueous solution and in the presence of dissolved in pure water, respectively. The Δh_W^L is the enthalpy difference between water of the empty hydrate structure and pure liquid water, which is calculated from Eqs.(3-6) and (3-7) as:

$$\Delta h_{\mathrm{W}}^{\mathrm{L}} = \Delta h_{W,0}^{\mathrm{L}} + \int_{T_0}^{T} \Delta C_{\mathrm{pw}} dT \tag{3-6}$$

$$\Delta C_{\mathrm{pw}} = \Delta C_{\mathrm{pw},0} + q\left(T - T_0\right) \tag{3-7}$$

where ΔC_{pw} is thermal capacity differences between water of the empty hydrate structure and pure liquid water. The q is a correction for the difference of the reference temperature (T_0 = 273.15 K). The $\Delta\mu_{\mathrm{W}}^{0}$, $\Delta C_{\mathrm{pw},0}$ and q values used were those for structure I,[19] namely, $\Delta\mu_{\mathrm{W}}^{0}$ =1247 J·mol^{-1}, $\Delta C_{\mathrm{pw},0}$ = -38.13 J·mol^{-1}·K^{-1} and q = 0.141 J·mol^{-1}·K^{-2}. These values were used for all semi-clathrate hydrates. It is important to note that thermal properties, $\Delta h_{\mathrm{W},0}^{\mathrm{L}}$, can be estimated from differential scanning calorimeter (DSC) analysis which is considered in this thesis (Appendix 3-1). The $\Delta\nu_{\mathrm{W}}^{\mathrm{L}}$ for each crystal structure were estimated from liquid water molar volume (18.02 cm^3/mol) and water molar volume for TBAB semi-clathrate hydrate, which was calculated (Appendix 3-2) from Eq. (3-8) as:

$$\nu_W^H = \frac{N_A}{N_{H_2O}^*}\left(a \times b \times c\right) \times 10^{-24} \tag{3-8}$$

The activity of water in TBA salt aqueous solution, $a_{\mathrm{W,salt}}$ was calculated from Eq. (3-9) as:

$$\ln\left(a_{\mathrm{W,salt}}\right) = -\frac{mM_{\mathrm{W}}\phi\left(\upsilon_{\mathrm{c}} + \upsilon_{\mathrm{a}}\right)}{1000} \tag{3-9}$$

where m, ϕ, υ_{c} and υ_{a} are molar mass concentration, osmotic coefficient, and the valences of the cation and the anion, respectively. The ϕ were taken from literature data for each TBA salts (Appendix 3-3).[22-24] The activity of water in the presence of dissolved in pure water, $a_{\mathrm{W,gas}}$ can be estimated assuming that the gas is dissolved in pure water as described by Eq. (3-10):[25]

$$a_{\text{gas}} = 1 - x_{\text{gas}}^{\text{L}} = 1 - \frac{f_{\text{gas}}^{\text{V}}}{H_{\text{gw}} \exp\left(\frac{v_{\text{gas}}^{\infty} P}{RT}\right)} \tag{3-10}$$

where $x_{\text{gas}}^{\text{L}}$ is the gas mole fraction in water, $f_{\text{gas}}^{\text{V}}$ is the fugacity of the chemical species in the vapor phase, H_{gw} is Henry's constant of gas in water[26] and v_{gas}^{∞} is molar volume of the gas at infinite dilution conditions.[27] The estimation technique used for $x_{\text{gas}}^{\text{L}}$ is described in Appendix 3-4.

3.3.2.2 Chemical potential difference of the hydrate phase

The chemical potential difference of the hydrate phase, $\Delta\mu_{\text{W}}^{\text{H}}$ was determined by:

$$\Delta\mu_{\text{W}}^{\text{H}} = -RT\sum_i v_i \ln\left(1 - \sum_j \theta_{ij}\right) \tag{3-11}$$

Eq. (3-11) assumes that the volume of unit cell of the clathrate hydrate and clathrate empty hydrate are equal. In Eq. (3-11), the v_i is number of cages *i* per water molecule and θ_{ij} is the occupancy of cage *i* by gas *j*, which is calculated from:

$$\theta_{ik} = \frac{C_{ik} f_k}{1 + \sum_j C_{ij} f_j} \tag{3-12}$$

where C_{ik} and f_k are the Langmuir constant of gas *k* in cage-*i* and fugacity of gas *k*, respectively. The gas fugacity was calculated with the Peng-Robinson equation of state.[28] Determination of the H_2-CO_2 interaction parameters is described in Appendix C. Combining Eqs. (3-11) and (3-12) gives:

$$\Delta\mu_{\mathrm{W}}^{\mathrm{H}} = RT\sum_i v_i \ln\left(1+\sum_j C_{ij} f_j\right) \tag{3-13}$$

The theoretical formulas for HS-I, TS-I and SCS-I structures are 2TBA salt·$76H_2O$, 5TBA salt·$162H_2O$ and 12TBA salt·$344H_2O$ for which the unit cells are $6(5^{12})\cdot4(5^{12}6^2)\cdot4(5^{12}6^3)$, $10(5^{12})\cdot16(5^{12}6^2)\cdot4(5^{12}6^3)$ and $16(5^{12})\cdot48(5^{12}6^2)$.[3] Gas molecules are included in the 5^{12} cage, and the TBA salt is included in four cages that have combinations of $5^{12}6^2$ and $5^{12}6^3$, which are defined as the S-cage and the QL-cage, respectively (Figure 2-2). Applying Eq. (3-13) gives Eq. (3-14) as:

$$\Delta\mu_{\mathrm{W}}^{\mathrm{H}} = RT\left[v_{\mathrm{S}}\ln\left(1+\sum_j C_{\mathrm{S}j} f_j^{\mathrm{V}}\right) + v_{\mathrm{QL}}\ln\left(1+C_{\mathrm{QL,TBA\,salt}} f_{\mathrm{TBA\,salt}}^{\mathrm{L}}\right)\right] \tag{3-14}$$

where $f_{\mathrm{TBA\,salt}}^{\mathrm{L}}$ is the fugacity of the TBA salt in the aqueous solution, which is calculated from Eq. (3-15) as:

$$f_{\mathrm{TBA\,salt}}^{\mathrm{L}} = x_{\mathrm{TBA\,salt}}^{\mathrm{L}}\gamma_{\mathrm{TBA\,salt}}P_{\mathrm{TBA\,salt}}^{\mathrm{sat}}\exp\left(\frac{V_{\mathrm{TBA\,salt}}^{\mathrm{L}}\left(P-P_{\mathrm{TBA\,salt}}^{\mathrm{sat}}\right)}{RT}\right) \tag{3-15}$$

where $x_{\mathrm{TBA\,salt}}^{\mathrm{L}}$, $\gamma_{\mathrm{TBA\,salt}}$, $P_{\mathrm{TBA\,salt}}^{\mathrm{sat}}$ and $V_{\mathrm{TBA\,salt}}^{\mathrm{L}}$ are the mole fraction of TBA salt in the liquid phase, the activity coefficient of the TBA salt, the saturation pressure of the TBA salt aqueous solution and the molar volume of the aqueous solution (Appendix 3-5), respectively. The $P_{\mathrm{TBA\,salt}}^{\mathrm{sat}}$ was assumed to be equal to the saturation pressure of water as described Eq.(3-16): [29]

$$P_{\mathrm{TBA\,salt}}^{\mathrm{sat}} = P_{\mathrm{w}}^{\mathrm{sat}} = 10^{-6}\exp\left(73.649-\frac{7258.2}{T}-7.3037\ln\left(T\right)+4.1653\times10^{-6}T^2\right) \tag{3-16}$$

The $\gamma_{\mathrm{TBA\,salt}}$ values were calculated from the eNRTL model[24] that was fitted to literature data for each TBA salt (Appendix 3-6).[22-24] The $x_{\mathrm{TBA\,salt}}^{\mathrm{L}}$ values were calculated with consideration for the

gas solubility (Appendix 3-7).

Langmuir constants were calculated from the Du-Gue model [30] as:

$$C_{\mathrm{S,H_2}} = \frac{a_{\mathrm{H_2}}}{T}\exp\left(\frac{b_{\mathrm{H_2}}}{T}\right) \tag{3-17}$$

$$C_{\mathrm{S,CO_2}} = \frac{c_{\mathrm{CO_2}}}{T}\exp\left(\frac{d_{\mathrm{CO_2}}}{T}\right) \tag{3-18}$$

$$C_{\mathrm{QL,TBA\,salt}} = \left(\frac{A_{\mathrm{TBA\,salt}}}{T}\exp\left(\frac{B_{\mathrm{TBA\,salt}}}{T}\right)\right)\left(1+\frac{C_{\mathrm{TBA\,salt}}}{m}\right) \tag{3-19}$$

where $a_{\mathrm{H_2}}$, $b_{\mathrm{H_2}}$, $c_{\mathrm{CO_2}}$, $d_{\mathrm{CO_2}}$, $A_{\mathrm{TBA\,salt}}$, $B_{\mathrm{TBA\,salt}}$ and $C_{\mathrm{TBA\,salt}}$ are fitting parameters. For TBAF systems, $C_{\mathrm{TBA\,salt}}$ was set equal to zero due to the lack of phase equilibrium data at different TBA salt concentrations. The initial values of $b_{\mathrm{H_2}}$, $d_{\mathrm{CO_2}}$ and $B_{\mathrm{TBA\,salt}}$ were set by reference to literature values.[9,30,31] Then, the values of $a_{\mathrm{H_2}}$, $c_{\mathrm{CO_2}}$ and $A_{\mathrm{TBA\,salt}}$ were initialized in such a way that the calculated curves gave the trends of the experimental data. Then, all fitting parameters for the same TBA salt and crystal structure systems were determined by using all experimental data of H_2 + TBA salt + water system and CO_2 + TBA salt + water system fixed TBA salt species and crystal structure.

3.3.3 Correlation of phase equilibrium data

Figures 3-3 and 3-4 show correlation results for H_2 or CO_2 + TBAB, TBAC or TBAF + water systems. Table 3-2 summarizes the fitting parameters and the average relative deviation (ARD) for each phase equilibrium system, where ARD is defined as:

$$\mathrm{ARD}\,\% = \frac{100}{N_{\mathrm{data}}} \sum_{i} \left| \frac{P_{\mathrm{exp}}(i) - P_{\mathrm{calc}}(i)}{P_{\mathrm{exp}}(i)} \right| \tag{3-20}$$

As shown in Figure 3-5 and Table 3-2, although the ARD of pressure for 3.7 mol% TBAB system is large, the modified thermodynamic model could describe the phase equilibria of H_2 or CO_2 + TBA salt + water systems well.

Table 3-2. Langmuir expression fitting parameters, Eqs. (3-17) to (3-19), for H_2, CO_2 and tetra-*n*-butyl ammonium (TBA) salts determined.

TBA salt	a_{H_2} [$\times 10^{-8}$ K·Pa^{-1}]	b_{H_2} [$\times 10^{3}$ K]	c_{CO_2} [$\times 10^{-6}$ K·Pa^{-1}]	d_{CO_2} [$\times 10^{3}$ K]	$A_{\text{TBA salt}}$ [$\times 10^{-6}$ K·Pa^{-1}]	$B_{\text{TBA salt}}$ [$\times 10^{4}$ K]	$C_{\text{TBA salt}}$ [mol/kg]	ARD %
0.6 mol% TBAB	5.639	1.335	2.282	1.400	3.691	1.129	-0.069	9.31
3.7 mol% TBAB	2.416	1.391	8.119	0.926	3.082	1.100	-0.832	16.9
3.3 mol% TBAC	2.997	1.131	2.609	1.230	2.929	1.115	-0.405	6.44
3.0 mol% TBAF	3.140	1.546	3.653	0.824	3.793	1.205	0	8.76
3.3 mol% TBAF	1.199	1.317	4.000	0.815	3.100	1.108	0	8.97

TBAB : tetra-*n*-butyl ammonium bromide, TBAC: tetra-*n*-butyl ammonium chloride, TBAF: tetra-*n*-butyl ammonium fluoride.

Figure 3-6 shows the temperature dependence of the Langmuir constants of H_2 and CO_2 for each TBA salt.

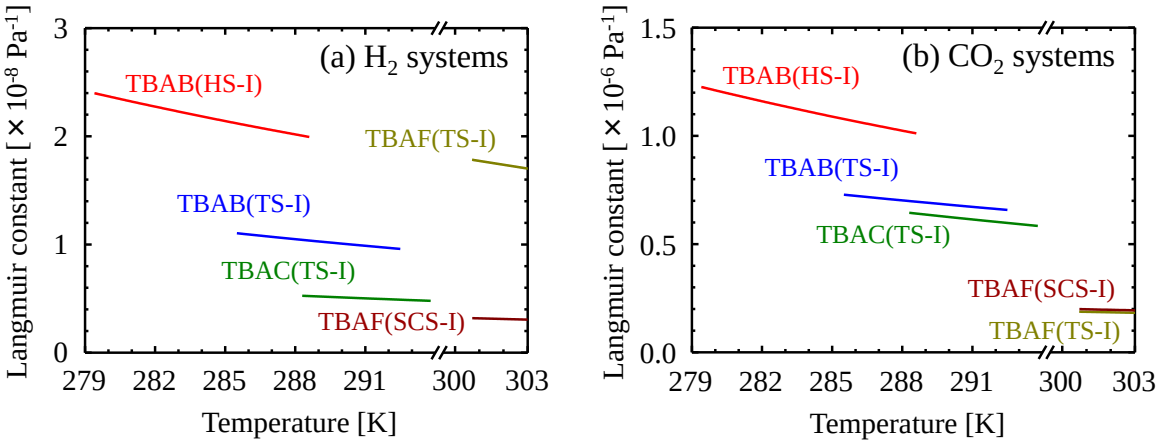

Figure 3-6. Calculated Langmuir constants of (a) H_2 and (b) CO_2 for each tetra-*n*-butyl ammonium (TBA) salt and crystal structure of semi-clathrate hydrate with Eqs. (3-17) and (3-18). Continuous lines show TBA salt and structure of semi-clathrate hydrate. Lines: red, 0.6 mol% TBAB (HS-I); blue, 3.7 mol% TBAB (TS-I); green, 3.3 mol% TBAC (TS-I); olive, 3.0 mol% TBAF (TS-I); brown, 3.3 mol% TBAF (SCS-I).

The Langmuir constants of H_2 (*ca.* 10^{-8} Pa^{-1}) were smaller than those of CO_2 (*ca.* 10^{-6} Pa^{-1}). The reason for this is that the molecular size of H_2 is smaller than that of CO_2. For H_2 and CO_2 of both systems, Langmuir constants for the HS-I structure were largest and those for the SCS-I structure were the smallest. The crystal structure dependence of Langmuir constant in the H_2 system was in accord with that in the CO_2 system. On the other hand, Langmuir constants of H_2 for the TS-I structure increased in order of TBAF > TBAB > TBAC, and those of CO_2 increased in order of TBAB > TBAC > TBAF. Thus, the TBAF semi-clathrate hydrate for the TS-I structure of Langmuir constant in H_2 systems was different from that in CO_2 systems. Therefore, gas inclusion

appears to vary according to both the anion of the TBA salt and the crystal structure of the semi-clathrate hydrate that is related to the size of the gas molecule, the electrophilicity of the anion[32] and the gas capture cage size.

3.3.4 Occupancy for mixed gas systems

Phase equilibrium diagram of the mixed gas system, H_2 + CO_2 + TBA salt + water systems, was calculated from the previously obtained fitting parameters (Section 3.3.3). Figure 3-5 shows the results. The model provides qualitative description of the phase equilibria of H_2-CO_2 (H_2/CO_2 = 3.4)-3.3 mol% TBAC-water systems and H_2-CO_2 (H_2/CO_2 = 1.5)-3.3 mol% TBAF-water systems. From the trends, it can be concluded that mixture gas inclusion behavior changes according to TBA salt and gas composition

Figure 3-7 shows P-y_{H2} and P-x_{H2} diagram for each semi-clathrate hydrate. The mole fractions of the vapor phase (y_{H2}) and liquid phase (x_{H2}) are calculated on an H_2O-free and TBA salt-free basis. The x_{H2} were calculated from the gas occupancy in the S-cage as:

$$x_{H_2} = \frac{\theta_{eq.,H_2}}{\theta_{eq.,H_2} + \theta_{eq.,CO_2}} \tag{3-21}$$

The H_2/CO_2 selectivity S_{H_2/CO_2} was calculated from Eq.(3-22):

$$S_{H_2/CO_2} = \frac{y_{H_2} / x_{H_2}}{y_{CO_2} / x_{CO_2}} \tag{3-22}$$

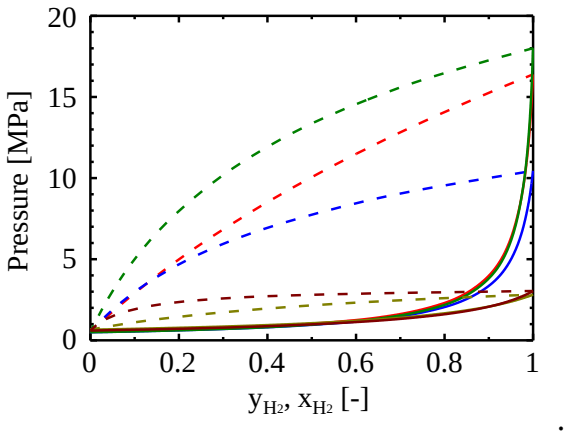

Figure 3-7. Phase equilibria for H_2–CO_2 with each semi-clathrate hydrate, where y_{H2} is the composition of H_2 the vapor phase and x_{H2} is the H_2 composition without H_2O and tetra-*n*-butyl ammonium (TBA) salt in the hydrate phase. Continuous and dashed lines show y_{H2} and x_{H2}, respectively. Lines show TBA salt and dissociation temperature. Lines: red, 0.6 mol% TBAB (HS-I), 282.7 K; blue, 3.7 mol% TBAB (TS-I), 287.0 K; green, 3.3 mol% TBAC (TS-I), 289.7 K; olive, 3.0 mol% TBAF (TS-I), 301 K; brown, 3.3 mol% TBAF (SCS-I), 301 K.

The S_{H_2/CO_2} increased with increasing H_2 composition in the vapor phase. The S_{H_2/CO_2} (H_2/CO_2 = 3.4) were in the order of (largest to smallest) 3.3 mol% TBAC at 289.7 K (S_{H_2/CO_2} = 123), 3.3 mol% TBAF at 301.0 K (S_{H_2/CO_2} = 63), 3.7 mol% TBAB at 287.0 K (S_{H_2/CO_2} = 67), 0.6 mol% TBAB at 282.7 K (S_{H_2/CO_2} = 51) and 3.0 mol% TBAF at 301.0 K (S_{H_2/CO_2} = 11). The S_{H_2/CO_2} was high for 3.3 mol% TBAC, because the S_{H_2/CO_2} is greatly affected by the TBA salt and crystal structure. Especially, the S_{H_2/CO_2} for 3.0 mol% TBAF at 301 K was small. From the results of the calculations, the TBAF semi-clathrate hydrates were the most stable among the TBA salts examined. However, the gas selectivity of 3.0 mol% TBAF semi-clathrate hydrates is probably greatly reduced close to the equilibrium temperature due to decreasing differences between H_2 and CO_2 included amounts. Therefore, the crystal structure is important for gas separation applications.

3.4 Conclusions

In this chapter, the phase equilibria of H_2 and CO_2 + tetra-*n*-butyl ammonium (TBA) salt + water systems were measured. The TBA salts used were tetra-*n*-butyl ammonium bromide (TBAB), tetra-*n*-butyl ammonium chloride (TBAC) and tetra-*n*-butyl ammonium fluoride (TBAF). The apparatus and procedures in this work were confirmed to be sufficient for obtaining reliable data by comparison with literature data for TBAB semi-clathrate hydrate systems.

For TBAF semi-clathrate hydrates, dissociation temperatures varied according to TBAF concentration, in which 3.0 mol% TBAF semi-clathrate hydrate was found to be more stable than 3.3 mol% TBAF semi-clathrate hydrate above 1 MPa. Thus, it was confirmed that 3.0 mol% TBAF semi-clathrate hydrates form a different structure from that of 3.3 mol% TBAF semi-clathrate hydrate because the equilibrium gas inclusion amounts of 3.0 mol% TBAF semi-clathrate were larger than those of the 3.0 mol% TBAF semi-clathrate hydrate.

A phase equilibrium model was developed for semi-clathrate hydrates by using parameters for the QL-cage combined $5^{12}6^2$ cage and $5^{12}6^3$ cage, and estimating $\Delta\nu_W^L$ from the molar volume of water for TBAB semi-clathrate hydrate. The model could describe the phase equilibria of H_2 or CO_2-TBA salt-water binary systems well, but could only provide qualitative agreement for mixture systems. The inclusion behavior of mixture gases is most likely different from that of pure gases and it seems to depend on the TBA salt. The gas selectivity of semi-clathrate hydrates is affected by the crystal structure and the TBA salt. Although the TBAF semi-clathrate hydrate can be readily applied because its high dissociation temperature, its selectivity for 3.0 mol% TBAF is probably low at temperatures close to its dissociation temperature.

3.5 References

1. Davidson DW. *Water - A Comprehensive Treatise.* Vol 2.Plenum Press; New York. 1973.
2. Shimada W, Shiro M, Kondo H, Takeya S, Oyama H, Ebinuma T, Narita H. Tetra-*n*-butylammonium bromide-water (1/38). Acta Crystallogr C. 2005;61:O65-O66.
3. Rodionova T, Komarov V, Villevald G, Aladko L, Karpova T, Manakov A. Calorimetric and structural studies of tetrabutylammonium chloride ionic clathrate hydrates. J Phys Chem B. 2010;114:11838-11846.
4. Dyadin YA, Terekhova IS, Polyanskaya TM, Aladko LS. Clathrate hydrates of tetrabutylammonium fluoride and oxalate. J Struct Chem. 1976;17:566-571.
5. Komarov VY, Rodionova TV, Terekhova IS, Kuratieva NV. The cubic superstructure-I of tetrabutylammonium fluoride $(C_4H_9)_4NF \cdot 29.7H_2O$ clathrate hydrate. J Inclusion Phenom Macro. 2007;59:11-15.
6. Makino T, Yamamoto T, Nagata K, Sakamoto H, Hashimoto S, Sugahara T, Ohgaki K. Thermodynamic stabilities of tetra-*n*-butyl ammonium chloride + H_2, N_2, CH_4, CO_2, or C_2H_6 semiclathrate hydrate systems. J Chem Eng Data. 2010;55:839-841.
7. Sakamoto J, Hashimoto S, Tsuda T, Sugahara T, Inoue Y, Ohgaki K. Thermodynamic and Raman spectroscopic studies on hydrogen + tetra-*n*-butyl ammonium fluoride semi-clathrate hydrates. Chem Eng Sci. 2008;63:5789-5794.
8. Mooijer-van den Heuvel MM, Peters CJ, Arons JD. Influence of water-insoluble organic components on the gas hydrate equilibrium conditions of methane. Fluid Phase Equilib. 2000;172:73-91.
9. Hayasaka A. [M.S. Thesis]: Chemical Engneering Department, Tohoku; 2012.
10. Arjmandi M, Chapoy A, Tohidi B. Equilibrium data of hydrogen, methane, nitrogen, carbon dioxide, and natural gas in semi-clathrate hydrates of tetrabutyl ammonium bromide. J Chem Eng Data. 2007;52:2153-2158.
11. Mohammadi AH, Eslamimanesh A, Belandria V, Richon D. Phase equilibria of semiclathrate hydrates of CO_2, N_2, CH_4, or H_2 + tetra-*n*-butylammonium bromide aqueous solution. J Chem Eng Data. 2011;56:3855-3865.
12. Hashimoto S, Murayama S, Sugahara T, Sato H, Ohgaki K. Thermodynamic and Raman spectroscopic studies on H_2+tetrahydrofuran + water and H_2+tetra-*n*-butyl ammonium bromide + water mixtures containing gas hydrates. Chem Eng Sci. 2006;61:7884-7888.

13. Ye N, Zhang P. Equilibrium data and morphology of tetra-*n*-butyl ammonium bromide semiclathrate hydrate with carbon dioxide. J Chem Eng Data. 2012;57:1557-1562.
14. Lee S, Park S, Lee Y, Lee J, Lee H, Seo Y. Guest gas enclathration in semiclathrates of tetra-*n*-butylammonium bromide: stability condition and spectroscopic analysis. Langmuir. 2011;27:10597-10603.
15. Hashimoto S, Sugahara T, Moritoki M, Sato H, Ohgaki K. Thermodynamic stability of hydrogen + tetra-*n*-butyl ammonium bromide mixed gas hydrate in nonstoichiometric aqueous solutions. Chem Eng Sci. 2008;63:1092-1097.
16. Oyama H, Shimada W, Ebinuma T, Kamata Y, Takeya S, Uchida T, Nagao J, Narita H. Phase diagram, latent heat, and specific heat of TBAB semiclathrate hydrate crystals. Fluid Phase Equilib. 2005;234:131-135.
17. Aladko LS, Dyadin YA. Clathrate formation in the Bu_4NCl-NH_4Cl-H_2O system. Mendeleev Commun. 1996:198-200.
18. Park S, Lee S, Lee Y, Seo Y. CO_2 capture from simulated fuel gas mixtures using semiclathrate hydrates formed by quaternary ammonium salts. Environ Sci Technol. 2013;47:7571-7577.
19. Parrish WR, Prausnit.Jm. Dissociation pressures of gas Hydrates formed by gas-mixtures. Ind Eng Chem Proc Dd. 1972;11:26-35.
20. van der Waals JH, Platteeuw JC. Clathrate Solutions. Adv Chem Phys. 1959;2:1-57.
21. Shabani MM, Nydal OJ, Larsen R. A proposed thermodynamic model for gas hydrate equilibrium in electrolyte solutions. Heat Transfer Eng. 2011;32:168-175.
22. Lindenbaum S, Boyd GE. Osmotic + activity coefficients for symmetrical tetraalkyl ammonium halides in aqueous solution at 25 ºC. J Phys Chem-Us. 1964;68:911-917.
23. Wen WY, Saito S, Lee CM. Activity and osmotic coefficients for four symmetrical tetraalkylammonium fluroides in aqueous solutions at 25 ºC. J Phys Chem-Us. 1966;70:1244-1248.
24. Chen CC, Britt HI, Boston JF, Evans LB. Local composition model for excess gibbs energy of electrolyte systems .1. single solvent, single completely dissociated electrolyte systems. AIChE J. 1982;28:588-596.
25. Tumba K, Reddy P, Naidoo P, Ramjugernath D, Eslamimanesh A, Mohammadi AH, Richon D. Phase equilibria of methane and carbon dioxide clathrate hydrates in the presence of aqueous solutions of tributylmethylphosphonium methylsulfate ionic liquid. J Chem Eng Data. 2011;56:3620-3629.

26. Klauda JB, Sandler SI. Phase behavior of clathrate hydrates: a model for single and multiple gas component hydrates. Chem Eng Sci. 2003;58:27-41.

27. Moore JC, Battino R, Rettich TR, Handa YP, Wilhelm E. Partial molar volumes of gases at infinite dilution in water at 298.15 K. J Chem Eng Data. 1982;27:22-24.

28. Peng D, Robinson DB. A new two-constant equation of state. Ind Eng Chem Fund. 1976;15:59-64.

29. Daubert TE, Danner RP. *DIPPR Data Compilation Tables of Properties of Pure Compounds*.AIChE New York. 1985.

30. Du YH, Guo TM. Prediction of hydrate formation for systems containing methanol. Chem Eng Sci. 1990;45:893-900.

31. Eslamimanesh A, Mohammadi AH, Richon D. Thermodynamic modeling of phase equilibria of semi-clathrate hydrates of CO_2, CH_4, or N_2+tetra-*n*-butylammonium bromide aqueous solution. Chem Eng Sci. 2012;81:319-328.

32. Chattaraj PK, Duley S. Electron affinity, electronegativity, and electrophilicity of atoms and ions. J Chem Eng Data. 2010;55:1882-1886.

Chapter 4

Hydrogen adsorption behavior in clathrate hydrates and development of kinetic models

4.1 Introduction

Gas adsorption rates of clathrate hydrates are important for their practical use. There has been considerable research on hydrogen adsorption with clathrate hydrates that contain guest additives.[1-5] For example, hydrogen adsorption kinetic models have been proposed for clathrate hydrates that contain guest additive tetrahydrofuran (THF).[2,4,5] Although formation kinetics have been reported for other guest additives such as furan and tetrahydrothiophene (THT), hydrogen diffusion behavior in furan and THT clathrate hydrate particles is different from that in THF clathrate hydrate particles,[6] and these have not been analyzed with kinetic models yet. Hydrogen adsorption behavior in THF clathrate hydrates (D_2O)[7] and cyclopentane (CP) clathrate hydrates[7-9] which exist at higher temperatures than THF clathrate hydrates have not been reported yet. Further, kinetic models that describe adsorption behavior for guest additive clathrate hydrates might

be expected to be applicable to gas adsorption with semi-clathrate hydrate particles, which is considered in Chapter 5 of this thesis.

In this chapter, the objectives are to develop a H_2 adsorption kinetic model that is applicable to a wide range of guest additives. Guest additives considered are hydrophilic additives (THF and THF-d8) and hydrophobic additives (furan, CP and THT). The kinetic model is assessed with adsorption data for clathrate hydrate particle through comparison with literature adsorption models.

4.2 Experimental

4.2.1 Materials

High-purity water was obtained from Advantec Toyo Kaisha, Ltd., RFD250NB with an electrical conductivity below 5.5 μS/m was used in the experiments. H_2 gas (99.99 %), tetrahydrofuran without stabilizer (99.5 %, Wako Pure Chemical, Inc.), D_2O (Deuterated rate: 99.8 %, Kanto Chemical), tetradrofuran-d8 (Deuterated rate: 99.5 %, Kanto Chemical), cyclopentane (≥ 99 %, Aldrich), furan with stabilizer (BHT) (≥ 99 %, Tokyo Chemical Industry), tetrahydrothiophene (≥ 99 %, Tokyo Chemical Industry), acetone-d6 (Deuterated rate: 99.9 %, Merck) were used without further purification.

4.2.2 Clathrate hydrate preparation

Batches of clathrate hydrate particles were made by loading water (or D_2O) and THF (or THF-d8, CP, furan, THT) into a perfluoroalkoxyethylene vessel in such a way that the concentration

of organic liquids were 5.56 mol% with the contents being weighed to a precision of 1 mg with a balance (Mettler Toledo AX504) that was followed by cooling of the solution to 274 K with a low temperature-controlled bath while stirring. The molar concentration chosen for the guest additive was the stoichiometric concentration for full occupancy of the guest additive in all L-cages for structure II (sII). The formed clathrate hydrates were cooled to 253 K in a freezer for at least 6 hours. The solids were crushed with a mortar and pestle at liquid nitrogen temperatures and graded with stainless steel-type 316 sieves while being kept in the freezer at 253 K. Particle size ranges of 500 – 600 μm were used in the experiments. Formation of clathrate hydrates were confirmed at room temperature and atmospheric pressure with a laser Raman spectrometer (JASCO, NR-2000) that had a holographic grating, CCD (Princeton Instruments, Inc.) (Appendix 4-1). The existence of ice in clathrate hydrate particles was determined with X-ray diffraction (Rigaku, type Ultima III) using the CuKα radiation (40 kV, 40 mA) at 123 K, and the lattice constants of the clathrate hydrates were calculated with RIETAN-2000 program. The proportion of ice to hydrate was estimated with ^{1}H NMR (AV-400, Bruker BioSpin K.K.) spectroscopy.

4.2.3 *Experimental apparatus*

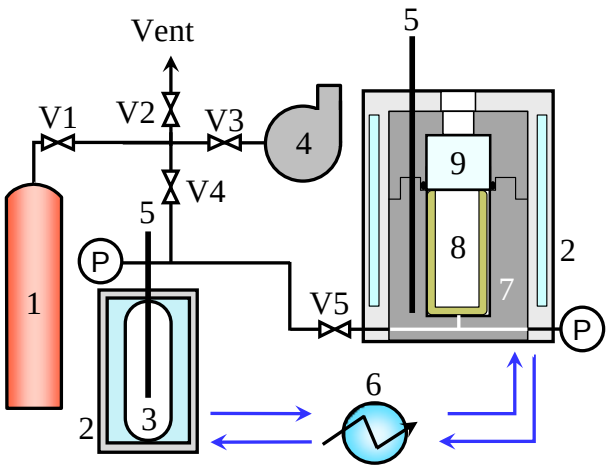

Figure 4-1. Schematic diagram of the apparatus for hydrogen adsorption experiments. Labels, 1: H_2 cylinder, 2: glycol jacket, 3: reservoir tank, 4: vacuum pump, 5: Pt 4-wire thermometer, 6: chiller, 7: hydrate formation cell, 8: inner cell, 9: window for *in-situ* Raman measurements.

Figure 4-1 shows a schematic diagram of the experimental apparatus. The reservoir tank system was designed to be separated from the equilibrium cell during the loading of the reservoir tank with H_2. In the hydrate formation cell, the window was held externally with a O-ring (IIR-70°, Morisei Kako Co.) and the inner cell was made of brass. The hydrate formation cell was maintained at the temperature of interest (265 to 273 K) to within ± 0.02 K by an integral cooling aluminum jacket that was cooled by a circulator (F32-HE, Julabo Co., Ltd.). The reservoir tank was volume calibrated with nitrogen over a range of temperatures (265 – 273 K) and pressures (1.1 – 5.6 MPa) and found to have an average volume of 304.67 cm^3 from 11 independent trials (σ = 0.158 cm^3) (Appendix D). The hydrate formation cell was volume calibrated with nitrogen over a range of temperatures (269 – 273 K) and pressures (2.5 – 8.9 MPa) and found to have an average volume of 26.324 cm^3 from 6 independent trials (σ = 0.133 cm^3) (Appendix D). The temperature

of the reservoir tank could be controlled to within ± 0.05 K by an integral cooling glycol jacket that was cooled by a circulator (F25-MP, Julabo Co., Ltd.). The system temperature was measured with two platinum resistance temperature sensors (Pt 100 Ω, 3.17 mm diameter (1/8 in.), NR-350, four-wire type, Netsushin) calibrated against a standard temperature probe (GE Kaye IRTD-400, stated uncertainty ±25 mK). The temperature sensors that inserted into a hole in the cell assembly wall had the uncertainty of ±29 (Appendix A). The system pressure was measured by two sealed gauge pressure transducers (the cell: 14 MPa F.S. PMP4015, GE sensing Japan, the tank: 14 MPa F.S. PMP5013, GE sensing Japan) calibrated against a dead weight tester (Druck Pressurements M2200-5, stated uncertainty ±0.015 %). The two pressure gauges on the cell and the tank had the uncertainty of ±1.7 and ±2.3 kPa, respectively (Appendix B).

4.2.4 Experimental procedure

When the hydrate formation cell and the reservoir tank were cooled to 265 – 273 K, about 3 – 5 g of the clathrate hydrate particles were loaded. As soon as the system was briefly evacuated for 3 s by a vacuum pump (Hitachi Koki Co., VR16L), V5 was closed. After the reservoir tank was sufficiently evacuated by the vacuum pump, H_2 gas was pressurized to about 4.3 – 11.2 MPa in the reservoir tank. When temperature and pressure of the reservoir tank stabilized, H_2 gas was loaded into the formation cell over a period of about 5 s. The analysis method was based on the pressure decay method with material balances for H_2 in both the formation cell and reservoir tank as in previous work, [2] however, the contribution of porosity is considered in this chapter. The amount of H_2 gas loaded $n_{H_2,\,load}$, was calculated by the difference in the H_2 concentration before and after

loading of the reservoir tank by using Eq. (4-1) and the virial EoS that was correlated to NIST Chemistry WebBook (Appendix E).[10]

$$n_{\mathrm{H_2,\ load}} = n_{\mathrm{H_2,\ R,initial}} - n_{\mathrm{H_2,\ R,final}} \tag{4-1}$$

The amount of H_2 in the hydrate phase was calculated from relationships below.

Volume of gas phase:

$$V_{\mathrm{Gas}} = \frac{n_{\mathrm{H_2,load}}}{C_{\mathrm{H_2,Gas}}\left(t=0\right)} \tag{4-2}$$

Moles of free H_2 gas:

$$n_{\mathrm{H_2,Gas}}\left(t\right) = \frac{C_{\mathrm{H_2,Gas}}\left(t=0\right)V_{\mathrm{Gas}}}{M_{\mathrm{H_2}}} \tag{4-3}$$

Moles of H_2 in hydrate phase by material balance:

$$n_{\mathrm{H_2,Hyd}}\left(t\right) = n_{\mathrm{H_2,load}} - n_{\mathrm{H_2,Gas}}(t) \tag{4-4}$$

The volume of hydrate phase calculated from Eq. (4-5) was different from that of hydrate phase calculated from Eq. (4-6) using theoretical water density in the hydrate phase; Eq. (4-7).

Volume of hydrate phase:

$$V_{\mathrm{Hyd}} = V_{\mathrm{cell}} - V_{\mathrm{H_2,\ Gas}} \tag{4-5}$$

Volume of theoretical clathrate hydrate:

$$V_{\mathrm{Theor}} = \frac{n_{\mathrm{H_2O,\ Hyd}} M_{\mathrm{H_2O}}}{\rho_{\mathrm{H_2O,\ Theor}}} \tag{4-6}$$

Water density in the theoretical clathrate hydrate:

$$\rho_{\mathrm{H_2O,\ Theor}} = \frac{N^*_{\mathrm{H_2O}} M_{\mathrm{H_2O}}}{N_{\mathrm{A}} a^3} \tag{4-7}$$

Since pores exist in clathrate hydrate particles,[11] the theoretical volume of the clathrate hydrate was corrected using the porosity ε:

$$V_{\mathrm{Hyd}} = \frac{V_{\mathrm{Theor}}}{1-\varepsilon} \tag{4-8}$$

where the theoretical number of water molecules per unit cell $N^*_{\mathrm{H_2O}}$ was taken to be 136 based on sII structure. The lattice constant a was calculated from observed full diffraction pattern by XRD by using RIETAN-2000 program. The ε was calculated from Eqs. (4-5), (4-6) and (4-8). For the clathrate hydrates in the hydrophobic guest additive systems, the mole ratio of the guest additive molecule to water was analyzed using ^{1}H NMR spectroscopy. Before each H_2 adsorption experiment, hydrate powders were dissolved into acetone-d8 (Ac-d8), and the solutions were analyzed. The ratio between guest additive molecule and water molecule was calculated from the relationship between peak area of ^{1}H NMR, $A_{^1\mathrm{H}}$ and proton number, $N_{^1\mathrm{H}}$ corresponding to each molecule as given by Eq. (4-9):

$$\frac{n_{\mathrm{Guest}}}{n_{\mathrm{H_2O}}} = \frac{A_{^1\mathrm{H,\,Guest}} \Big/ N_{^1\mathrm{H,\,Guest}}}{\dfrac{A_{^1\mathrm{H,\,H_2O}}}{N_{^1\mathrm{H,\,H_2O}}} - \dfrac{A_{^1\mathrm{H,\,Ac\text{-}d8}}}{N_{^1\mathrm{H,\,Ac\text{-}d8}}} \dfrac{A^*_{^1\mathrm{H,\,H_2O}} \Big/ N_{^1\mathrm{H,\,H_2O}}}{A^*_{^1\mathrm{H,\,Ac\text{-}d8}} \Big/ N_{^1\mathrm{H,\,Ac\text{-}d8}}}} C_{\mathrm{apparatus}} \tag{4-9}$$

where $A^*_{^1\mathrm{H}}$ is the peak area given by ^{1}H NMR analysis of the pure Ac-d8 liquid and $C_{\mathrm{apparatus}}$ is the apparatus constant for ^{1}H NMR, that is the slope of the calibration curve with ordinate, loaded

composition, and abscissa, estimated composition, from the ^{1}H NMR. The clathrate hydrate mass (weight) was calculated from the following relationships by assuming that all L-cages of the clathrate hydrates were occupied by guest additive molecules as given by Eq. (4-10) – (4-12).

Mass (weight) of guest additive molecule:

$$W_{\mathrm{Guest}} = \frac{\dfrac{n_{\mathrm{Guest}}}{n_{\mathrm{H_2O}}}\dfrac{M_{\mathrm{Guest}}}{M_{\mathrm{H_2O}}}}{1+\dfrac{n_{\mathrm{Guest}}}{n_{\mathrm{H_2O}}}\dfrac{M_{\mathrm{Guest}}}{M_{\mathrm{H_2O}}}} W_{\mathrm{Total}} \tag{4-10}$$

Mass (weight) of H_2O in hydrate phase:

$$W_{\mathrm{H_2O,\ Hyd}} = \left(\frac{100}{C_{\mathrm{Stoich}}} - 1 \right) W_{\mathrm{Guest}} \tag{4-11}$$

where C_{Stoich} is the stoichiometric concentration when all L-cages are occupied by guest additive molecules (sII structure: 5.6 mol%).

Mass (weight) of clathrate hydrate:

$$W_{\mathrm{Hyd}} = W_{\mathrm{H_2O,\ Hyd}} + W_{\mathrm{Guest}} \tag{4-12}$$

Mass (weight) of ice:

$$W_{\mathrm{Ice}} = W_{\mathrm{Total}} - W_{\mathrm{Hyd}} \tag{4-13}$$

4.3 Results and discussion

4.3.1 X-ray diffractometer analysis

Figure 4-2 shows the XRD pattern of (a) THF clathrate hydrates, (b) CP clathrate hydrate as an example of the solids formed in this chapter. For hydrophilic solvent systems (THF clathrate hydrate, THF clathrate hydrate (D_2O), THF-d8 clathrate hydrate), the peaks showed the existence of clathrate hydrates (Appendix 4-2(a)) and almost a complete absence of ice peaks, so that the yield of clathrate hydrate for these samples was over 99%. On the other hand, for hydrophobic guest additive systems (CP clathrate hydrate, furan clathrate hydrate, THT clathrate hydrate), ice peaks were observed (Appendix 4-2(b)).

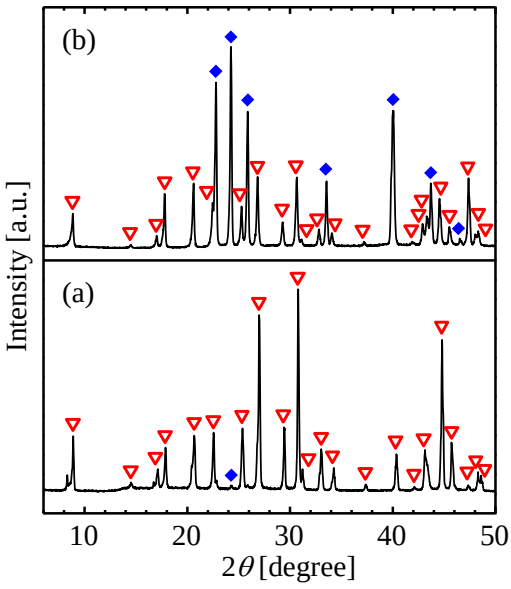

Figure 4-2. X-ray diffraction pattern of (a) tetrahydrofuran (THF) clathrate hydrate, (b) cyclopentane (CP) clathrate hydrate at 123 K. Down-pointing triangles and diamonds show clathrate hydrate structure II (sII) and ice, respectively.

In the clathrate hydrate formation process of hydrophobic guest additive systems, the agitation of samples became progressively difficult due to increased viscosity of the mixtures. Water and the

hydrophobic guest additives become separated and ice forms without the addition of a compound such as a surface-active agent. For hydrophobic guest additive systems, due to their XRD pattern and the availability of the structure parameters for only THF clathrate hydrate,[12] the rates of the clathrate hydrate in the samples were estimated with ^{1}H NMR spectroscopy.

4.3.2 Hydrogen adsorption rate measurements

Table 4-1 summarizes the experimental runs made and the lattice constants determined. Figure 4-3 shows H_2 adsorption as a function of time for clathrate hydrates of hydrophilic systems (runs 2, 13 and 19). The occupancy of the S-cage, θ_S was calculated from Eq. (4-14) on the assumption that a single H_2 molecule occupies the S-cage of the clathrate hydrate (Appendix 4-3).

$$\theta_S = \frac{W_{H_2,Hyd}}{M_{H_2}} \frac{M_{H_2O} N^*_{H_2O}}{W_{H_2O,Hyd} N_{\theta_S}} \tag{4-14}$$

Gas adsorption rates for clathrate hydrates were assessed by the time required to reach half the equilibrium gas occupancy in the S-cage, t_{half}. A small t_{half} implies a fast adsorption rate. The t_{half} of H_2 + THF-8 hydrate was shorter than that of H_2 + THF clathrate hydrate (D_2O) and H_2 + THF clathrate hydrate (Table 4-2). The deuteration effect of the host molecule was larger than that of the guest additive molecule for phase equilibria, which has been observed for H_2 + THF + D_2O, D_2 + THF + H_2O and H_2 + THF-d8 + H_2O systems.[7] However, the H_2 adsorption rate showed that the deuteration effect of the guest molecule was only slightly larger than that of the guest molecule (Table 4-2).

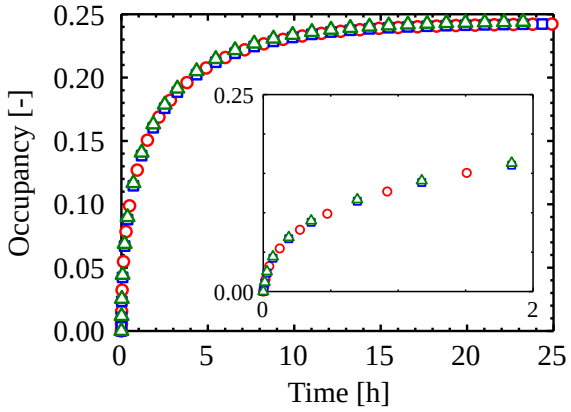

Figure 4-3. H_2 adsorption as a function of time in the clathrate hydrates of hydrophilic solvent system (d = 500 – 600 mm, T = 269 K, $P_{initial}$ = 8 MPa). Red circles, blue squares and green triangles show tetrahydrofuran (THF), THF (D_2O) and THF-d8 clathrate hydrate particles, respectively. Inset: expanded view at 0 – 2 h.

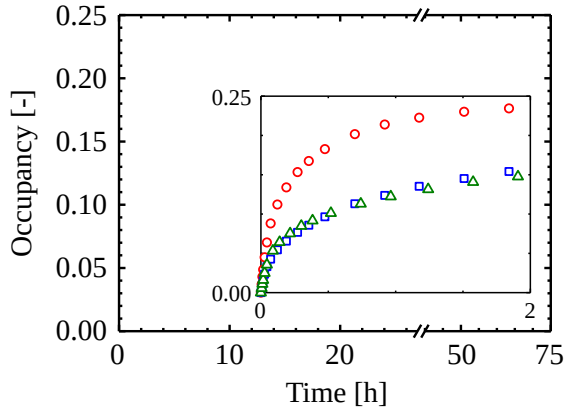

Figure 4-4. H_2 adsorption as a function of time in the clathrate hydrates of hydrophobic guest additive system (d = 500 – 600 μm, T = 269 K, $P_{initial}$ = 8 MPa). Red circles, blue squares and green triangles show furan, cyclopentane (CP) and tetrahydrothiophene (THT) clathrate hydrate particles, respectively. Inset: expanded view at 0 – 2 h.

Table 4-1. H_2 clathrate hydrate inclusion conditions and measured lattice constants.

Run	Host Molecule	Guest Molecule	Conc. [mol%]	T [K]	$P_{initial}$ [MPa]	W_{Hyd} [g]	W_{Ice} [g]	a [Å]
1	H_2O	THF	5.6	265.1	8.10	2.90	-	17.147
2				269.1	8.13	4.18	-	
3				273.0	8.14	4.62	-	
4				269.2	3.98	4.61	-	
5				269.3	10.22	4.80	-	
6			6.2	265.1	8.10	3.21	-	
7				269.2	8.17	4.52	-	
8				272.9	8.10	2.89	-	
9			4.4	269.3	8.18	3.89	0.90	
10			5.0	269.2	8.16	4.55	0.45	
11			6.8	269.1	8.12	4.32	-	
12	D_2O	THF	5.6	265.1	8.19	5.22	-	17.157
13				269.1	8.19	5.01	-	
14				273.0	8.13	4.01	-	
15			6.2	265.1	8.19	5.24	-	
16				269.1	8.21	4.82	-	
17				273.0	8.18	5.16	-	
18	H_2O	THF-d8	5.6	265.1	8.17	4.57	-	17.160
19				269.2	8.16	3.77	-	
20				273.0	8.16	4.18	-	
21	H_2O	furan	6.6	265.4	8.05	2.22	1.12	17.133
22				269.1	8.08	1.92	1.57	
23				272.3	8.11	2.14	2.06	
24	H_2O	CP	6.0	265.1	8.15	5.03	0.00	17.238
25				269.1	8.14	4.13	0.09	
26				273.0	8.09	4.10	0.13	
27	H_2O	THT	5.6	269.1	8.15	2.83	0.90	17.247

T: temperature, $P_{initial}$: initial pressure, W_{Hyd}: mass (weight) of hydrate in product .particles, W_{Ice}: mass (weight) of ice in product particles, a: hydrate lattice constant.

Table 4-2. Results derived from H_2 clathrate hydrate formation experiments.

Run	Host molecule	Guest molecule	Conc. [mol%]	T [K]	P_{final} [MPa]	t_{half} [h]	θ_{eq} [-]	$C_{H_2,\,S}$ [$\times 10^{-2}$ MPa^{-1}]	Average S-cage diameter [Å]
1	H_2O	THF	5.6	265.1	7.68	0.48	0.257	4.293	7.730
2				269.1	7.53	0.83	0.244	4.077	
3				273.0	7.49	0.61	0.231	3.833	
4				269.2	3.64	0.79	0.130	4.008	
5				269.3	9.36	0.79	0.288	4.077	
6			6.2	265.1	7.64	0.61	0.264	4.469	
7				269.2	7.53	0.44	0.242	4.052	
8				272.9	7.71	0.38	0.243	3.977	
9			4.4	269.3	7.65	0.38	0.222	3.561	
10			5.0	269.2	7.50	0.56	0.236	3.933	
11			6.8	269.1	7.50	0.24	0.242	4.043	
12	D_2O	THF	5.6	265.1	7.46	0.88	0.254	4.356	7.734
13				269.1	7.52	0.83	0.243	4.076	
14				273.0	7.63	0.70	0.230	3.723	
15			6.2	265.1	7.46	0.61	0.257	4.436	
16				269.1	7.58	0.44	0.243	4.032	
17				273.0	7.54	0.36	0.224	3.651	
18	H_2O	THF-d8	5.6	265.1	7.50	0.96	0.256	4.370	7.736
19				269.2	7.63	0.79	0.245	4.057	
20				273.0	7.60	0.70	0.228	3.714	
21	H_2O	furan	6.6	265.4	7.72	0.14	0.256	4.241	7.724
22				269.1	7.81	0.16	0.247	3.991	
23				272.3	7.85	0.12	0.199	3.018	
24	H_2O	CP	6.0	265.1	7.35	1.01	0.260	4.554	7.771
25				269.1	7.54	0.92	0.247	4.150	
26				273.0	7.47	0.48	0.245	4.138	
27	H_2O	THT	5.6	269.1	7.77	0.79	0.231	3.681	7.775

P_{final}: pressure at experimental finished, t_{half}: time for consumption of half of H_2 gas, θ_{eq}: equilibrium occupancy, C_S: Langmuir constants of H_2 in S-cage.

Figure 4-4 shows H_2 adsorption as a function of time in the clathrate hydrate of hydrophobic guest additive systems. The t_{half} of H_2 were in the order (shortest to longest) of H_2 + furan clathrate hydrate, H_2 + CP clathrate hydrate, H_2 + THT clathrate hydrate in the early stages of formation (Figure 4-4), but the t_{half} of H_2 + THT clathrate hydrate was shorter than that of H_2 + CP clathrate hydrate (Table 4-2). This was considered to be due to the formation processes of the H_2 + guest additive clathrate hydrate being different in the early stage and in the later stage of formation. Tsuda et al. reported that H_2 adsorption is much faster in furan and THT clathrate hydrates than in THF clathrate hydrates at 275.1 K,[6] which differs from the H_2 adsorption rates found for the THT clathrate hydrates in this chapter. The differences in rates are probably related to the formation of ice that occurs at low temperatures. Therefore, it is necessary to consider the method of forming clathrate hydrates, which has an effect on H_2 adsorption rates.

Table 4-2 summarizes H_2 clathrate hydrate experimental results. The Langmuir constant for S-cage, C_S was calculated from Eq. (4-15).

$$C_S = \frac{\theta_{S,eq}}{\left(1-\theta_{S,eq}\right) f_{H_2,eq}} \tag{4-15}$$

The Langmuir constant is a parameter that indicates the occupied capacity of H_2 in the S-cage. It was confirmed that the Langmuir constant had a similar value (0.041 MPa^{-1} at 269 K) for each initial pressure, runs 2, 4 and 5 (Appendix 4-4, Table 4-2). This value was comparable to the calculated Langmuir constant (~0.04 MPa^{-1} at 280 K) of H_2 molecules in the S-cage in H_2-THF phase equilibria.[13] Thus, the obtained Langmuir constants from H_2 adsorption experiments were comparable with literature values. The average S-cage diameters were calculated from the lattice

constants and oxygen atomic coordinate of water for H_2S + THF clathrate hydrate.[14] The interactions between host and H_2 molecules as judged by the Langmuir constants became stronger as the Langmuir constant increased. The Langmuir constants decreased slightly with an increase in the S-cage diameter (Table 4-2), which means that the difference of S-cage size has a slight effect on the interactions between host and H_2 molecules. However, this effect is small since H_2 has a small molecular size compared with the S-cage size. The Langmuir constant is related to the interaction energy between guest molecule and the hydrate cage. The size ratio of the guest molecule in the hydrate cage can be considered as a factor that is related to the interaction energy. For example, the Langmuir constant of methane is large (~6 MPa^{-1} at 280 K)[13] because the molecular size of methane is large, while molecules having very large Langmuir constants, such as THF (~1.5×10^6 MPa^{-1}), probably have the effect of stretching the cage size due to strong interactions with water molecules.

4.3.3 Kinetic models

4.3.3.1 Correlation of hydrogen adsorption data

Theoretical description of gas adsorption in hydrate particles can be grouped into two categories: (i) hydrogen delocalization (one-step) models and (ii) hydrogen inclusion – diffusion (two-step) models. In the hydrogen delocalization model, it is assumed that hydrogen rapidly delocalizes into hydrate particles from the particle surface and is expressed by Eq. (4-16):

$$\frac{dn_{H_2}}{dt} = KA_{p,\text{total}} n_{H_2O} \left(f_{\text{Gas}} - f_{\text{eq}} \right) \tag{4-16}$$

where K is a kinetic constant for binary clathrate hydrate formation, $A_{\mathrm{p,\,total}}$ is the total surface area of the clathrate hydrate particles and $n_{\mathrm{H_2O}}$ is the amount of H_2O molecules of H_2 non-inclusion clathrate hydrate particles. Kawamura et al. [15] assumed that the area of active surface did not change with the reaction time for CO_2 clathrate hydrate formation process on ice particles. Nagai et al. improved the model of Kawamura et al., Eq. (4-16), by allowing the surface area to be variable so that the H_2 consumption rate was proportional to the remaining amount of H_2O, $n_{\mathrm{H_2O}}$ as Eq. (4-17):[2]

$$n_{\mathrm{H_2O}} = n_{\mathrm{H_2O,\,0}}\left(1 - \frac{\theta_{\mathrm{S}}}{\theta_{\mathrm{S,\,eq}}}\right) \tag{4-17}$$

where $n_{\mathrm{H_2O,\,0}}$ is the initial H_2O moles of H_2 non-included hydrate particles.

Hydrogen inclusion – diffusion (two step) models have been developed based on the shrinking core model. The hydrogen hydrate phase diffusion (HHPD) model [2,4] assumes that H_2 molecules are included and diffuse with the driving force for mass transfer being the difference between the hydrogen fugacity at the bulk and equilibrium conditions. The fugacity gradient in the diffusion step is assumed as linear so that the H_2 adsorption rate is expressed by Eq. (4-18) as:

$$\frac{dn_{\mathrm{H_2}}}{dt} = 1\Bigg/\left(\frac{1}{k_{\mathrm{a}}A_{\mathrm{c,\,total}}} + \frac{L'}{D'_{\mathrm{H_2}}A_{\mathrm{c,\,total}}}\right)\left(f_{\mathrm{Gas}} - f_{\mathrm{eq}}\right) \tag{4-18}$$

where k_{a} and $D'_{\mathrm{H_2}}$ are constants for H_2 adsorption and effective diffusion coefficient, respectively. The L' and $A_{\mathrm{c,\,total}}$ are the H_2 diffusion distance (Eq. (4-19)) and interfacial area for the H_2 inclusion step (Eq. (4-20)), respectively:

$$L' = r_p - \left\{ \frac{3V_{Hyd,\,total}}{4\pi N_p} \left(1 - \frac{\theta_S}{\theta_{S,\,eq}} \right) \right\}^{\frac{1}{3}} \tag{4-19}$$

$$A_{c,\,total} = 4\pi N_p \left(r_p - L' \right)^2 \tag{4-20}$$

where $V_{Hyd,\,total}$ and N_p are total hydrate particle volume and particle number, respectively.

Hashimoto et al. [5] proposed a hydrogen absorption model and assumed that H_2 molecules are included and diffuse with a driving force for mass transfer being the H_2 molar concentration in gas phase. The concentration gradient in the H_2 occupying layer was calculated by integrating the equation for H_2 consumption rate in the diffusion step, so that the H_2 absorption rate is expressed as:

$$\frac{dn_{H_2}}{dt} = \frac{4\pi N_p}{V_{gas}} \frac{n_{H_2,0,gas} - n_{H_2,hyd}}{\frac{1}{D_e}\left(\frac{1}{r_c} - \frac{1}{r_p} \right) + \frac{1}{k_c}\frac{1}{r_c^2}} \tag{4-21}$$

where V_{gas}, $n_{H_2,0,gas}$, $n_{H_2,hyd}$, r_c, k_c and D_e are the volume in the gas phase, initial molar quantity of H_2 in the gas phase, molar quantity of H_2 in the hydrate phase, radius of H_2 non-included core, rate constant of inclusion at the interface of the H_2 non-included core and effective diffusion coefficient of H_2, respectively. The kinetic models are summarized in Table 4-3.

Figure 4-5 shows correlation results for H_2 adsorption rates in THF clathrate hydrates (run 2) and CP clathrate hydrates (run 25) with models given by Eqs. (4-16), (4-18) and (4-21). The HHPD model could describe the H_2 adsorption process of the THF clathrate hydrate system (Figure 4-5 a and c). However, the model could not describe the initial adsorption process in the CP clathrate hydrate system (Figure 4-5 b and d). Models based on shrinking core theory tend to give qualitative description of the H_2 adsorption rate in THF clathrate hydrate particles, but cannot describe the H_2 adsorption rate in CP clathrate hydrate particles (Figure 4-5, continuous line: H_2

absorption model[5] and dash line: HHPD model[2,4]) probably because there are several adsorption processes occurring, and those processes differ depending on the occupying guest additive molecule.

Table 4-3. Summary of kinetic models and their parameters for describing H_2 inclusion in clathrate hydrates.

Kinetic model	Delocalized state	Shrinking core state	Parameters
H_2 delocalization model [2]	$\frac{dn_{H_2}}{dt} = KA_{p,total} n_{H_2O} \left(f_{Gas} - f_{eq} \right)$		K
HHPD model [2,4]		$\frac{dn_{H_2}}{dt} = 1 \Big/ \left(\frac{1}{k_a A_{c,total}} + \frac{L'}{D'_{H_2} A_{c,total}} \right) \left(f_{Gas} - f_{eq} \right)$	k_a D'_{H_2}
H_2 absorption model[5]		$\frac{dn_{H_2}}{dt} = \frac{4\pi N_P}{V_{gas}} \frac{n_{H_2,0,gas} - n_{H_2,hyd}}{\frac{1}{D_e}\left(\frac{1}{r_c} - \frac{1}{r_p} \right) + \frac{1}{k_c} \frac{1}{r_c^2}}$	k_c D_e
MAR model	$\left(\frac{dn_{H_2,B1}}{dt} \right)_p = \left(V_{B1} \right)_p \left(1 - \frac{\theta_{S,B1}}{\theta_{S,eq}} \right) K_a C_{H_2,bulk}$ $\left(\frac{dn_{H_2,B2}}{dt} \right)_p = \left(V_{B2} \right)_p \left(1 - \frac{\theta_{S,B2}}{\theta_{S,eq}} \right) K_a N_{GCC} C_{H_2,bulk}$	$\left(\frac{dn_{H_2,B3}}{dt} \right)_p = \frac{4\pi r_c^2 \left(1 - \frac{\theta_{S,B3}}{\theta_{S,eq}} \right)^{\frac{2}{3}} \theta_{S,eq} k_c C_{H_2,core}}{1 + \left(1 - \frac{\theta_{S,B3}}{\theta_{S,eq}} \right)^{\frac{2}{3}} \frac{\theta_{S,eq} k_c r_c}{\left(1 - \theta_{S,eq} \right) D_a} \left(1 - \frac{r_c}{r_{B3}} \right)}$	L K_a k_c D_a

HHPD model: hydrogen hydrate phase diffusion model, MAR model: multiple adsorption resistance model

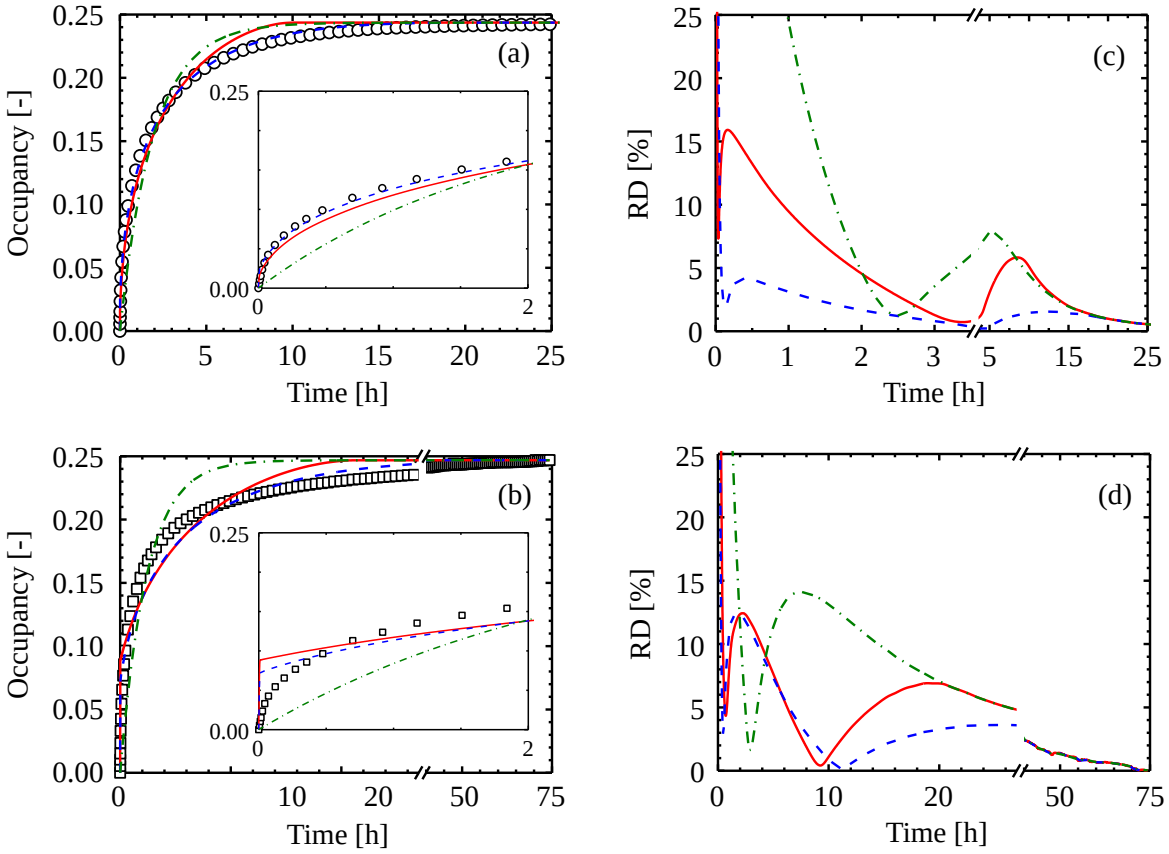

Figure 4-5. Correlation of H_2 adsorption rates in (a) tetrahydrofuran (THF) (run 2) and (b) cyclopentane (CP) (run 25) clathrate hydrate particles at 269 K and 8 MPa with a hydrogen delocalization model (Eq. (4-16)),[2] the hydrogen hydrate phase diffusion (HHPD) model (Eq. (4-18))[2] and the hydrogen absorption model (Eq. (4-21)).[5] Hydrophilic solvent system (a): H_2 adsorption as a function of time in THF clathrate hydrate (circles). Hydrophobic guest additives system (b): H_2 adsorption as a function of time in CP clathrate hydrate (squares). (c) and (d) show model deviations in THF and CP clathrate hydrate particles, respectively. Continuous line (red), dashed line (blue) and dashed-dotted line (green) show the hydrogen absorption model,[5] hydrogen hydrate phase diffusion (HHPD) model[2] and delocalization model[2] with inset: expanded view at 0 – 2 h.

In fact, the above kinetic models do not consider that pores exist on the clathrate hydrate particle surface.[11] Compositional variations of included gases molecules in the reformed clathrate hydrate particle are also not considered.[16] Therefore, a kinetic model that allows variation of the adsorption processes would be helpful to study some of the differences in the data.

4.3.3.2 Development of multiple adsorption resistance model

This section describes in the development of a new model for adsorption in clathrate hydrates. The H_2 adsorption process in a clathrate hydrate particle is assumed to consist of a delocalized state and a shrinking core state that have different adsorption resistances. The H_2 adsorption in clathrate hydrate particles is assumed to proceed according to an H_2 molar concentration driving force and one H_2 molecular inclusion in the S-cage. Figure 4-6 shows a schematic diagram of the proposed multiple adsorption resistance (MAR) model that assumes three boundaries of differential H_2 adsorption system. The three resistances for the H_2 adsorption are (i) the clathrate hydrate framework, (ii) the guest included cage and (iii) the H_2 adsorbed shell. The H_2 adsorption in all boundaries is affected by the hydrate framework characteristics such as cage size and number of possible inclusion cages.

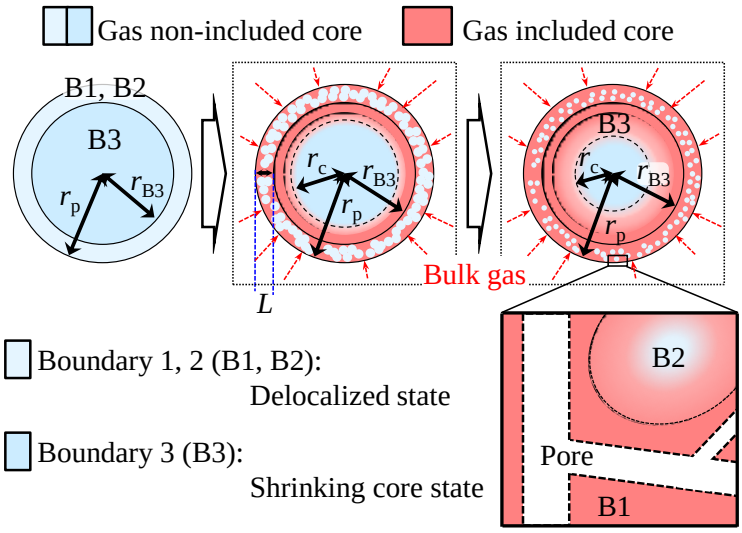

Figure 4-6. Schematic diagram of the multiple adsorption resistance (MAR) model. Blue color indicates hydrogen non-included regions. Pink color indicates hydrogen included regions. The symbols r_p, r_{B3} and r_c refer to particle radius, interface in shrinking core state (boundary 3) radius and non-included solid core radius, respectively.

In boundary 1 and 2 of Figure 4-6, H_2 molecules adsorb in a delocalized state near the surface of the clathrate hydrate particle because pores exist on clathrate hydrate particle surface.[11] The H_2 adsorption rate to empty S-cage ratio depends on the volume of the sorbable clathrate hydrate in boundary 1. The ratio between the volume of sorbable clathrate hydrate $V_{\mathrm{B1,sorbable}}$ and total clathrate hydrate V_{B1} in boundary 1 (B1) is assumed to be given by Eq. (4-22) as:

$$\left(\frac{V_{\mathrm{B1,\,sorbable}}}{V_{\mathrm{B1}}}\right)_{\mathrm{p}} = \left(1-\frac{\theta_{\mathrm{S,B1}}}{\theta_{\mathrm{S,eq}}}\right) \tag{4-22}$$

Then, the H_2 adsorption rate in boundary 1 is expressed as Eq. (4-23):

$$\begin{aligned}\left(\frac{dn_{\mathrm{H_2,B1}}}{dt}\right)_{\mathrm{p}} &= \left(V_{\mathrm{B1,sorbable}}\right)_{\mathrm{p}} K_{\mathrm{a}} C_{\mathrm{H_2,bulk}} \\ &= \left(V_{\mathrm{B1}}\right)_{\mathrm{p}} \left(1-\frac{\theta_{\mathrm{S,B1}}}{\theta_{\mathrm{S,eq}}}\right) K_{\mathrm{a}} C_{\mathrm{H_2,bulk}}\end{aligned} \tag{4-23}$$

where K_{a} and $C_{\mathrm{H_2,bulk}}$ are adsorption rate constant in delocalization adsorbed layer and H_2 molar concentration in bulk (gas) phase.

Boundary 2 was assumed to have H_2 adsorbed molecules in the sorbable S-cages with no access to the pores in the delocalized state. Thus, the H_2 molecules pass inward through the S-cage because the L-cage is occupied by a guest additive molecule. The H_2 hydrogen adsorption rate was assumed to depend on the number of gas capture cavities (S-cage) per host molecule, N_{GCC},[17] and expressed by Eq. (4-24).

$$\left(\frac{dn_{\mathrm{H_2,B2}}}{dt}\right)_{\mathrm{p}} = \left(V_{\mathrm{B2}}\right)_{\mathrm{p}} \left(1-\frac{\theta_{\mathrm{S,B2}}}{\theta_{\mathrm{S,eq}}}\right) K_{\mathrm{a}} N_{\mathrm{GCC}} C_{\mathrm{H_2,bulk}} \tag{4-24}$$

The volume rate between boundary 1 and boundary 2 was assumed to depend on N_{GCC} as given by Eq. (4-25).

$$\frac{V_{\mathrm{B1}}}{V_{\mathrm{B2}}} = 1 - 2N_{\mathrm{GCC}} \tag{4-25}$$

The volume of boundary 1 and total delocalization adsorbed layer V_{delocal} were calculated by Eq. (4-26) and Eq. (4-27), respectively as:

$$V_{\mathrm{B1}} = \frac{1 - 2N_{\mathrm{GCC}}}{2\left(1 - N_{\mathrm{GCC}}\right)} V_{\mathrm{delocal}} \tag{4-26}$$

$$V_{\mathrm{delocal}} = \frac{4}{3}\pi\left(r_{\mathrm{p}}^3 - r_{\mathrm{B3}}^3\right) \tag{4-27}$$

where $r_{\mathrm{B3}}\left(= r_{\mathrm{p}} - L\right)$ is the ratio of boundary 3, and L is the thickness of the delocalized shell.

In boundary 3, the shrinking of non-included solid core was assumed to be the rate-limiting step. The H_2 adsorption rate was assumed to be described by an H_2 diffusion process in H_2 adsorbed shell and an H_2 adsorption process near the interfacial boundary of the non-included solid core. In the diffusion process, an H_2 molecule diffuses as the H_2 concentration gradient is the driving force, and the diffusion rate depends on the number of non-sorbable S-cages of a particle[5] as shown by Eq. (4-28):

$$\left(\frac{dn_{\mathrm{H_2,B3}}}{dt}\right)_{\mathrm{p}} = 4\pi r_{\mathrm{c}}^2\left(1 - \theta_{\mathrm{S,eq}}\right) D_{\mathrm{a}}\left(\frac{dC_{\mathrm{H_2}}}{dr}\right) \tag{4-28}$$

where D_{a} is the apparent diffusion coefficient, $D_{\mathrm{a}} = D_{\mathrm{e}} \Big/ \left(1 - \theta_{\mathrm{S,eq}}\right)$ which is related to the effective diffusion coefficient by the occupancy at equilibrium. The ratio between the volume of non-inclusion core V_{c} and total hydrate V_{B3} in boundary 3 (B3) is assumed as Eq. (4-29), and

then the ratio of non-included solid core in boundary 3, r_c is expressed as Eq. (4-30):

$$\left(\frac{V_c}{V_{B3}}\right)_p = \left(1 - \frac{\theta_{S,B3}}{\theta_{S,eq}}\right) \tag{4-29}$$

$$\begin{aligned} \frac{\frac{4}{3}\pi r_c^3}{\frac{4}{3}\pi r_{B3}^3} &= \left(1 - \frac{\theta_{S,B3}}{\theta_{S,eq}}\right) \\ r_c &= r_{B3}\left(1 - \frac{\theta_{S,B3}}{\theta_{S,eq}}\right)^{\frac{1}{3}} \end{aligned} \tag{4-30}$$

In the adsorption process, the H_2 adsorption rate depends on the equilibrium occupancy,[5] and depends on the sorbable area of interface of non-included solid core in boundary 3 because the unreacted core shrinks with the compositional gradient as shown by Eq. (4-31).

$$\left(\frac{dn_{H_2,B3}}{dt}\right)_p = A_{c,sorbable}\theta_{S,eq}k_c C_{H_2,c} \tag{4-31}$$

Since the outside clathrate hydrate particle becomes large as gases are included,[16] the ratio between the sorbable and total area on interface of non-included solid core in boundary 3 is assumed as Eq. (4-32).

$$\begin{aligned} \left(\frac{A_{c,sorbable}}{A_c}\right)_p &= \left(1 - \frac{\theta_{S,B3}}{\theta_{S,eq}}\right)^{\frac{2}{3}} \\ \left(A_{c,sorbable}\right)_p &= 4\pi r_c^2\left(1 - \frac{\theta_{S,B3}}{\theta_{S,eq}}\right)^{\frac{2}{3}} \end{aligned} \tag{4-32}$$

Then, Eq. (4-31) is designated as Eq. (4-33).

$$\left(\frac{dn_{\mathrm{H_2,B3}}}{dt}\right)_{\mathrm{p}} = 4\pi r_{\mathrm{c}}^2 \left(1-\frac{\theta_{\mathrm{S,B3}}}{\theta_{\mathrm{S,eq}}}\right)^{\frac{2}{3}} \theta_{\mathrm{S,eq}} k_{\mathrm{c}} C_{\mathrm{H_2,c}} \tag{4-33}$$

At equilibrium conditions or at the quasi-equilibrium conditions, the left-hand side of Eq. (4-28) equals to that of Eq. (4-33). Then, by eliminating $C_{\mathrm{H_2,c}}$, which is the H_2 concentration at the near the interfacial boundary of the non-included solid core, Eq. (4-34) results:

$$\left(\frac{dn_{\mathrm{H_2,B3}}}{dt}\right)_{\mathrm{p}} = \frac{4\pi r_{\mathrm{c}}^2 \left(1-\frac{\theta_{\mathrm{S,B3}}}{\theta_{\mathrm{S,eq}}}\right)^{\frac{2}{3}} \theta_{\mathrm{S,eq}} k_{\mathrm{c}} C_{\mathrm{H_2,core}}}{1+\left(1-\frac{\theta_{\mathrm{S,B3}}}{\theta_{\mathrm{S,eq}}}\right)^{\frac{2}{3}} \frac{\theta_{\mathrm{S,eq}} k_{\mathrm{c}} r_{\mathrm{c}}}{\left(1-\theta_{\mathrm{S,eq}}\right) D_{\mathrm{a}}} \left(1-\frac{r_{\mathrm{c}}}{r_{\mathrm{B3}}}\right)} \tag{4-34}$$

The H_2 adsorbs inward from the interface at boundary 3 under quasi-equilibrium conditions, thus the H_2 concentration at the interface between delocalized state and shrinking core state, $C_{\mathrm{H_2,core}}$ is calculated from Eq. (4-35) as:

$$C_{\mathrm{H_2,core}} = \frac{N_{\theta_{\mathrm{S}}} \theta_{\mathrm{S,eq}}}{N_{\mathrm{A}} a^3} \tag{4-35}$$

The H_2 occupancy of S-cage in each boundary i, $\theta_{\mathrm{S,B}i}$, the equilibrium H_2 occupancy of S-cage $\theta_{\mathrm{S,eq}}$ and the radius of non-included solid core r_{c} are calculated from Eq. (4-36) and Eq. (4-37), respectively as:

$$\theta_{\mathrm{S,B}i} = \frac{n_{\mathrm{H_2,B}i} N_{\mathrm{A}} a^3}{V_{\mathrm{p,B}i} N_{\mathrm{p}} \left(1-\varepsilon\right)} \qquad \left(i = 1,2,3\right) \tag{4-36}$$

$$\theta_{\mathrm{S,eq}}\left(t\right) = \frac{C_{\mathrm{H_2,S}} f_{\mathrm{H_2}}\left(t\right)}{1+C_{\mathrm{H_2,S}} f_{\mathrm{H_2}}\left(t\right)} \tag{4-37}$$

The equilibrium H_2 occupancy $\theta_{S,eq}$ changes due to pressure drop according to the H_2 consumed. The $\theta_{S,eq}$ is calculated from the H_2 fugacity at a given time, which means that $\theta_{S,eq}$ at early H_2 adsorption times is larger than that at latter H_2 adsorption times. When $\theta_{S,B1\text{ and }B2}$ is larger than $\theta_{S,eq}$, the adsorption H_2 amount in each boundary changes so as to become equal, namely $\theta_{S,Bi} = \theta_{S,eq}$ because the time-to-equilibrium of $\theta_{S,B1\text{ and }B2}$ is faster than that of $\theta_{S,B3}$. The amount of adsorbed H_2 in each phase can be calculated from Eq. (4-38) by using Eqs. (4-23), (4-24) and (4-34).

$$n_{H_2,Bi}\left(t_{n+1}\right) = n_{H_2,Bi}\left(t_n\right) + \left(\frac{dn_{H_2,Bi}\left(t_{n+1}\right)}{dt}\right)_p N_p dt \qquad \left(i = 1,2,3\right) \tag{4-38}$$

Fitting parameters in the model are the thickness of delocalized state, L ($= r_p - r_{B3}$), the adsorption rate constant in delocalized state, K_a, the inclusion rate constant on interface of H_2 non-included solid core, k_c and the apparent diffusion coefficient, D_a. The model was correlated with the experimental data to minimize the average deviation (AD) defined as:

$$\text{AD} = \frac{10^6}{N_{data}} \sum_i \left| n_{H_2,\,exp}\left(i\right) - n_{H_2,\,calc}\left(i\right) \right| \tag{4-39}$$

where N_{data} is the number of data points.

Figure 7 shows correlation results for H_2 adsorption rates for all hydrates at 269 K and 8 MPa with the MAR model given by Eqs. (4-23) – (4-38). Table 4-4 summarizes the vapor pressure,[18] S-cage diameter, the fitting parameters and the resulting average relative deviation (ARD) defined as:

$$\mathrm{ARD}\,\% = \frac{100}{N_{\mathrm{data}}} \sum_{i} \left| \frac{n_{\mathrm{H_2,\,exp}}(i) - n_{\mathrm{H_2,\,calc}}(i)}{n_{\mathrm{H_2,\,exp}}(i)} \right| \qquad (4\text{-}40)$$

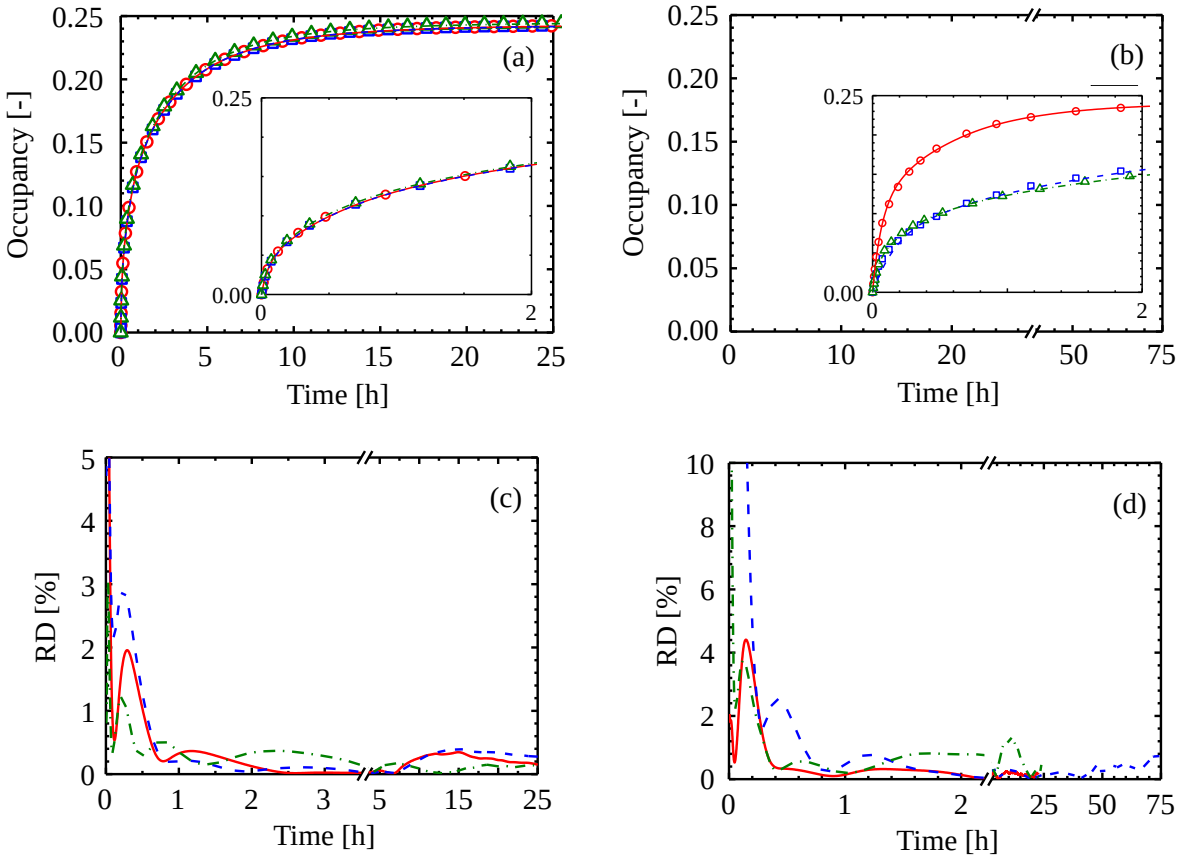

Figure 4-7. Correlation of H_2 adsorption rate at 269 K and 8 MPa. (a): hydrophilic solvents systems. Red circles (continuous line), blue squares (dashed line) and green triangles (dashed-dotted line) show tetrahydrofuran (THF) clathrate hydrate, THF clathrate hydrate (D_2O) and THF-d8 clathrate hydrate, respectively. (b): hydrophobic guest additive systems. Red circles (continuous line), blue squares (dashed line) and green triangles (dashed-dotted line) show cyclopentane (CP) clathrate hydrate, tetrahydrothiophene (THT) clathrate hydrate and furan clathrate hydrate, respectively. (c) and (d) show model deviations in hydrophilic solvent systems and hydrophobic guest additive systems, respectively. Inset: expanded view at 0 – 2 h.

As shown in Figure 4-7 and Table 4-4, the MAR model could describe the formation process for the clathrate hydrate particles well.

Table 4-4. Correlation of H_2 adsorption rate for each clathrate hydrate system.

Run	Host Molecule	Guest Molecule	Conc. [mol%]	T [K]	$P_{initial}$ [MPa]	$P_{vapor,\ guest}$ [MPa]	Average S-cage diameter [Å]	L [μm]	K_a [$\times 10^{-4}$ s^{-1}]	k_c [$\times 10^{-9}$ ms^{-1}]	D_a [$\times 10^{-13}$ m^2s^{-1}]	ARD [%]
1	H_2O	THF	5.6	265.1	8.10	5.06	7.730	55.0	21.98	37.43	13.79	1.07
2				269.1	8.13			32.2	25.06	42.70	17.27	0.56
3				273.0	8.14			35.4	29.54	53.38	20.57	0.85
4				269.2	3.98			27.0	30.25	106.5	6.232	0.80
5				269.3	10.22			30.1	28.66	40.67	13.60	0.48
6			6.2	265.1	8.10			47.1	20.99	38.69	27.99	1.18
7				269.2	8.17			47.2	23.37	48.30	31.79	0.25
8				272.9	8.10			49.6	29.06	54.06	35.33	0.66
9			4.4	269.3	8.18			43.2	24.07	103.2	11.03	1.01
10			5.0	269.2	8.16			39.2	23.96	65.67	8.571	0.26
11			6.8	269.1	8.12			62.9	25.75	72.96	48.59	0.61
12	D_2O	THF	5.6	265.1	8.19		7.734	33.3	22.15	36.41	9.070	0.74
13				269.1	8.19			29.5	25.86	47.24	11.71	0.75
14				273.0	8.13			30.5	29.81	60.40	13.76	0.35
15			6.2	265.1	8.19			35.0	23.89	53.99	18.32	0.28
16				269.1	8.21			38.8	26.52	69.35	20.76	0.61
17				273.0	8.18			41.8	30.66	88.41	24.07	0.93
18	H_2O	THF-d8	5.6	265.1	8.17		7.736	27.8	26.35	41.21	9.042	0.49
19				269.2	8.16			29.0	31.60	51.38	11.17	0.31
20				273.0	8.16			25.2	36.66	74.86	13.53	2.24
21	H_2O	furan	6.6	265.4	8.05	22.65	7.724	185	16.90	10.34	101.0	2.33
22				269.1	8.08			172	18.91	12.41	121.9	0.48
23				272.3	8.11			176	20.52	15.28	140.7	0.49
24	H_2O	CP	6.0	265.1	8.15	11.60	7.771	85.9	4.513	4.513	18.87	1.56
25				269.1	8.14			82.0	6.259	7.695	35.64	2.16
26				273.0	8.09			120	7.210	12.57	70.07	1.60
27	H_2O	THT	5.7	269.1	8.15	0.419	7.775	27.2	28.79	115.7	2.487	1.42

P_{vapor}: Vapor pressure at 269 K.[18] L : thickness of delocalized state. K_a : adsorption rate constant in delocalized state. k_c : inclusion rate constant on interface of H_2 non-included solid core. D_a : apparent diffusion coefficient. ARD : average relative deviation.

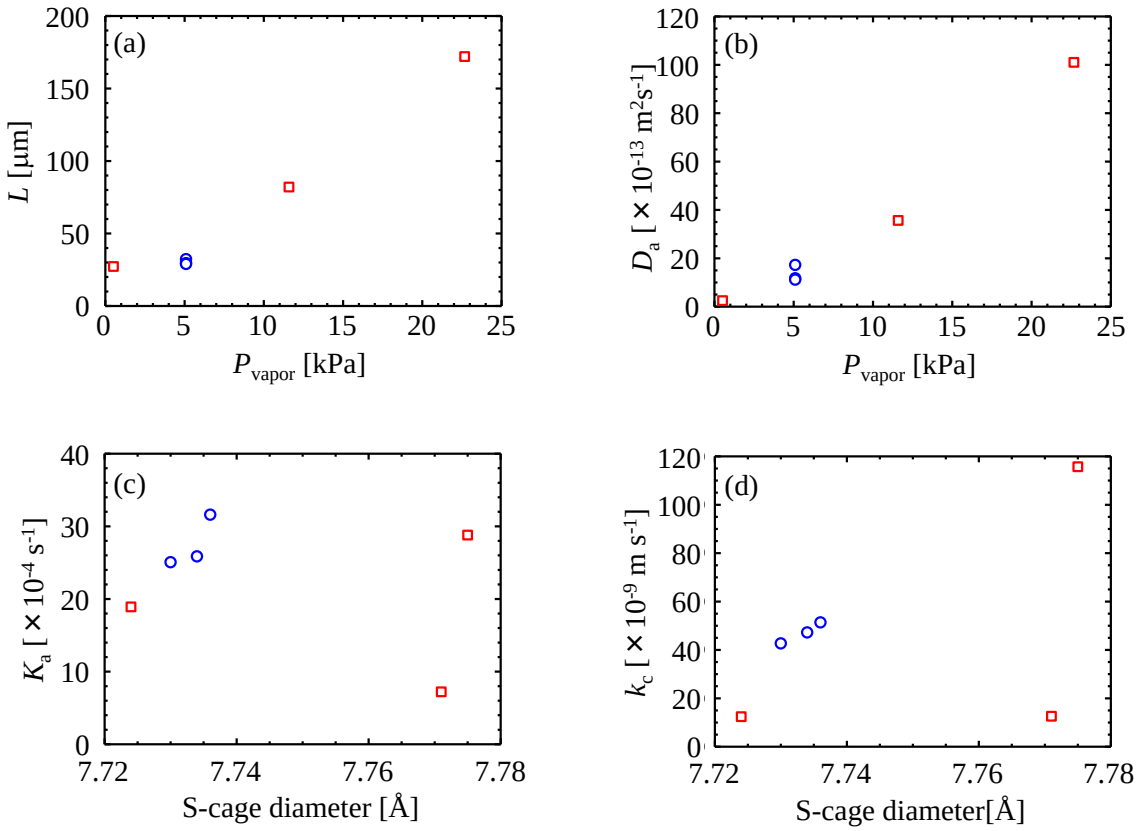

Figure 4-8. Fitting parameters of each hydrate particles at 269 K and 8 MPa. Blue circles were hydrophilic solvent systems, red squares was hydrophobic solvent systems. (a): L and (d): D_a versus vapor pressure[18] at 269 K, (b): K_a and (c): k_c versus lattice constant.

The L and D_a depend on the vapor pressure of the additive guest molecules while the K_a and k_c depended on the S-cage size of each clathrate hydrate in hydrophilic solvent systems (269 K and 8 MPa, Table 4-4 and Figure 4-8). The L and D_a were found to be directly proportional to the vapor pressure of the guest additive molecule, which implies that the pores readily form near the particle surface and at the grain boundaries from inside of the particle where non-included guest additive molecules volatilize. Therefore, the vapor pressure of the guest additive molecule is important in the H_2 adsorption kinetics. In furan clathrate hydrates, the H_2 adsorption amount in the delocalization state (boundary 1 and 2) was 95% of the total H_2 adsorption amount, so that the

observed formation of furan clathrate hydrate being the fastest in this work was most likely due to delocalized adsorption behavior. The more that the S-cage size increased, the more that K_a and k_c increased in hydrophilic solvent systems as can be concluded without considering the thermodynamic stability of clathrate hydrates[7] although the changes were small. This dependency probably means that the H_2 molecules were included in the hydrate cage without translation of water molecules.

On the other hand, the trends found for hydrophobic guest additive systems were not observed for hydrophilic solvent systems. In hydrophobic guest additive systems, there is the presence of ice, non-included guest additive molecules and water molecules, all of which have a large influence on the H_2 adsorption phenomenon.

Correlation results for H_2 adsorption rate in each concentration THF hydrate are given in Figure 4-9 and Table 4-4. Although K_a does not seem to depend on THF concentration (Figure 4-10), L, k_c and D_a, on the other hand, show concentration dependence (Figure 4-10). The L and k_c in the stoichiometric (5.6 mol%) THF were smallest, and L and D_a in 6.8 mol% THF were highest at these concentrations. Ice and non-included THF seemed to deform the hydrate cages and promote formation of pores in the clathrate hydrate particles. The effect of non-included THF was higher than that of ice. It is considered that non-included THF promoted the diffusion rate of H_2 by reducing the crystallinity of clathrate hydrate through the formation of grain boundaries. However, the existence of ice or non-included guest additive molecules had a negligible effect on K_a and k_c for CP hydrate. In other words, interactions between CP and H_2O or CP and H_2 probably inhibited the inclusion of H_2 molecules in the clathrate hydrate cages.

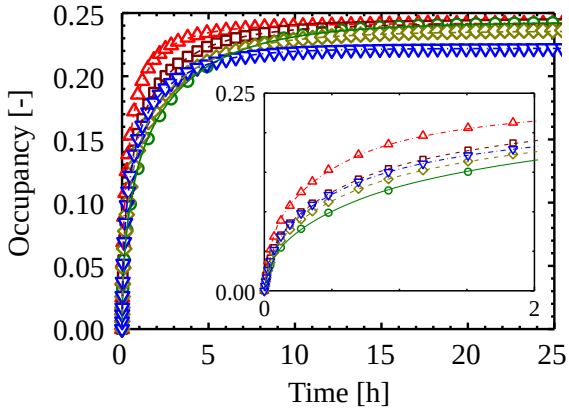

Figure 4-9. Correlation of H_2 adsorption rates in tetrahydrofuran (THF) clathrate hydrate particles at 269 K with multiple adsorption resistant (MAR) model. Red up-pointing triangles (dashed-dotted line), brown squares (dashed line), green circles (continuous line), olive diamonds (dashed line) and blue down-pointing triangles (dashed-dotted line) show 6.8 (run 11), 6.2 (run 7), 5.6 (run 2), 5.0 (run 10) and 4.4 (run 9) mol% THF clathrate hydrate particles, respectively. Inset: expanded view at 0 – 2 h.

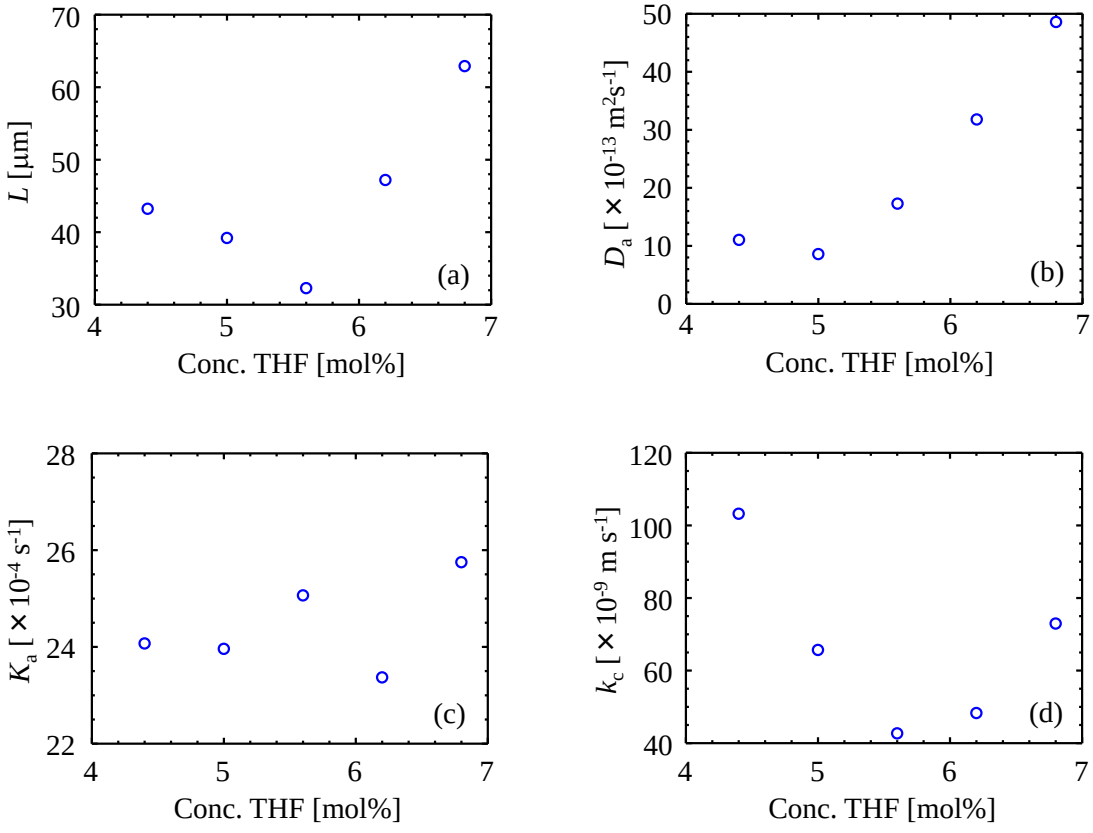

Figure 4-10. Fitting parameters of each concentration THF hydrate particles at 269 K and 8 MPa. (a): L, (b): K_a, (c): k_c, (d): D_a.

4.3.4 Activation energy

Correlated results for H_2 adsorption rate in each clathrate hydrate particles at 265 – 273 K are given in Table 4 (Appendix 4-5). Arrhenius plots were made by for each parameter (Figure 4-8) to determine activation energies from Eqs. (4-41) – (4-43):

$$K_{\mathrm{a}} = K_{\mathrm{a}}^{*} \exp\left(\frac{-\Delta E_{K_{\mathrm{a}}}}{RT}\right) \tag{4-41}$$

$$k_{\mathrm{c}} = k_{\mathrm{c}}^{*} \exp\left(\frac{-\Delta E_{k_{\mathrm{c}}}}{RT}\right) \tag{4-42}$$

$$D_{\mathrm{a}} = D_{\mathrm{a}}^{*} \exp\left(\frac{-\Delta E_{D_{\mathrm{a}}}}{RT}\right) \tag{4-43}$$

Tables 4-5 and 4-6 summarize constituent molecule dependencies of the activation energies for each parameter and the activation energies of formation rate for gas clathrate hydrate systems in previous studies, respectively. The temperature dependence of each parameter was confirmed because most R^2 values were near unity. The activation energies of hydrogen adsorption reaction $\Delta E_{K_{\mathrm{a}}}$ were 17 to 25 kJ/mol. This implies that the H_2 adsorbs at surface of hydrate particles by a similar mechanism for either hydrate particle. The activation energies of hydrogen inclusion reaction $\Delta E_{k_{\mathrm{c}}}$ in each hydrate other than CP clathrate hydrate were 26 to 45 kJ/mol. Previous studies for CH_4 and CO_2 systems reported the following: CH_4 clathrate hydrate (61.5 kJ/mol,[19] 39.7 kJ/mol,[11] 92.8 kJ/mol[20]), CH_4 clathrate hydrate (D_2O) (33.9 kJ/mol [11]), CO_2 clathrate hydrate (27.2 kJ/mol [21]) and CO_2 clathrate hydrate (D_2O) (42.3 kJ/mol [22]).

Table 4-5. Activation energy ΔE of adsorption (ΔE_{K_a}), inclusion (ΔE_{k_c}), and apparent diffusion (ΔE_{D_a}) for H_2 systems studied in this thesis.

Host molecule	Guest molecule	ΔE_{K_a} [kJ/mol]	R^2	ΔE_{k_c} [kJ/mol]	R^2	ΔE_{D_a} [kJ/mol]	R^2
H_2O	5.6 mol% THF	22.59	0.9930	27.08	0.9723	30.65	0.9973
H_2O	6.2 mol% THF	24.87	0.9488	25.90	0.9775	17.97	0.9997
D_2O	5.6 mol% THF	22.61	0.9999	38.59	0.9999	31.79	0.9883
D_2O	6.2 mol% THF	19.03	0.9869	37.69	0.9998	20.83	0.9949
H_2O	5.6 mol% THF-d8	25.25	0.9987	45.47	0.9714	30.79	0.9999
H_2O	Furan	16.84	0.9988	33.75	0.9913	28.79	0.9994
H_2O	CP	24.15	0.9985	78.24	0.9999	100.1	0.9985

Table 4-6. Activation energy ΔE of formation ($\Delta E_{K_{\text{form.}}}$) and effective diffusion (ΔE_{D_e}) for gas clathrate hydrate systems in experimented and simulation studies.

Experimental values				
Target	Particle type	$\Delta E_{K_{\text{form.}}}$ [kJ·mol^{-1}]	ΔE_{D_e} [kJ·mol^{-1}]	Reference
H_2	THF hydrate	-28	52 – 64	Yoshioka et al.[4]
		58	30	Hashimoto et al.[5]
	THF-d8 hydrate (D_2O)		3 ± 1	Okuchi et al[1]
CH_4	Ice	61.5		Wang et al.[19]
		39.7		Staykova et al.[11]
		92.8	52.1	Kuhs et al.[20]
	Ice (D_2O)	33.9	59.8	Staykova et al.[11]
CO_2	Ice	27.2		Henning et al.[21]
			38.6	Takeya et al.[23]
		42.3	54.6	Genov et al[22]
Molecular dynamics (MD) simulation values				
Target	Particle type	Barrier energy [kJ/mol]	ΔE_{D_e} [kJ/mol]	Reference
H_2	Hydrate structure		32.3	Frankcombe and Kroes[24]
	Hexagonal face (L-cage)	23.8 and 27.6		
		24 – 27		Alavi and Ripmeester[25]
	Pentagonal face (S-cage)	Over 200		Frankcombe and Kroes [24]
		99 – 118		Alavi and Ripmeester [25]

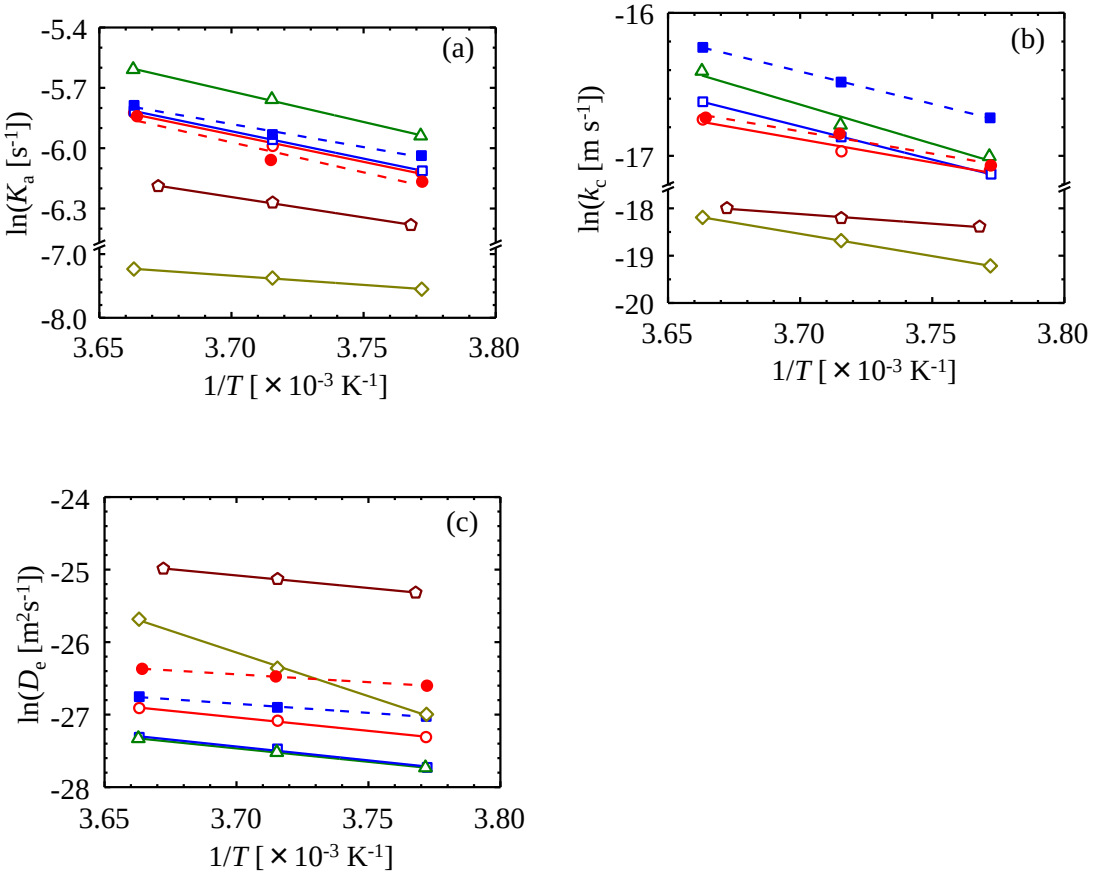

Figure 4-8. Arrhenius plots for (a): the adsorption rate in delocalized state, K_a, (b): the interface of non-included solid core, k_c and (c): the H_2 diffusion rate in H_2 included shell, D_a in each hydrate particles. Red circles (continuous line), filled red circle (dashed line), blue squares (continuous line), filled blue squares (dashed line), green triangles (continuous line), blown pentagons (continuous line) and olive diamonds (continuous line) were 5.6 mol% tetrahydrofuran (THF), 6.2 mol% THF, 5.6 mol% THF (D_2O), 6.2 mol% THF (D_2O), 5.6 mol% THF-d8, furan, cyclopentane (CP) clathrate hydrate, respectively.

The ΔE_{k_c}, other than CP clathrate hydrate in this chapter agreed with values of previous studies [11,21,22] and this means that the molecular inclusion process is similar regardless of the gas. In H_2 systems, Yoshioka et al. reported that the activation energy of adsorption in THF clathrate hydrate particle had a negative value of -28 kJ/mol [4]. The negative value is probably due to the enthalpy

of adsorption reaction according to the van't Hoff equation because the clathrate hydrate formation reaction is exergonic. The H_2 adsorption and dissociation reactions are reversible so that the adsorption rate constant in the HHPD model possibly allows one to estimate the equilibrium constant of the adsorption process, which is the ratio between adsorption and dissociation rate constants under quasi-equilibrium conditions. Hashimoto et al. reported an activation energy of H_2 adsorption in THF clathrate hydrate particle as being +58 kJ/mol,[5] which is higher than the value in this work. Hashimoto et al. estimated the actual H_2 adsorption rate constant with the relationship between the obtained H_2 adsorption rate constant from correlation with Eq. (4-21) and the equilibrium H_2 occupancy at the end of the experiment.[5] In this experiment, the equilibrium H_2 occupancy decreased with time because pressure decreased with H_2 adsorption. Thus, the effect of occupancy of H_2 on adsorption process is dynamically considered in the MAR model. As a consequence, the temperature dependence of the adsorption rate constant for MAR model was smaller than that for the H_2 absorption model.[5] In CP clathrate hydrates, the activation energy for k_c was higher than other clathrate hydrates. The ΔE_{k_c} for CP clathrate hydrate (79 kJ/mol) was close to the CH_4 clathrate hydrate formation value from ice particles (61.5 kJ/mol[19] and 92.8 kJ/mol[20]). This is probably because very little ice exists inside the CP clathrate hydrate particles which reacts with non-included CP molecules to form a new CP clathrate hydrate.

The activation energies of hydrogen diffusion in each clathrate hydrate were 29 to 32 kJ/mol in 5.6 mol% THF clathrate hydrate, 5.6 mol% THF clathrate hydrate (D_2O), THF-d8 clathrate hydrate and furan clathrate hydrate. These values were lower than those of previous reports for CH_4 clathrate hydrate (52.1 kJ/mol[20]), CH_4 clathrate hydrate (D_2O) (59.8 kJ/mol [11]), CO_2 clathrate

hydrate (38.6 kJ/mol[23]), CO_2 clathrate hydrate (D_2O) (54.6 kJ/mol[22]) and H_2-THF clathrate hydrate (52 to 64 kJ/mol[4] and were comparable to H_2-THF clathrate hydrate 30 kJ/mol[5]). These results are considered to be due to the small molecular size of H_2. Okuchi et al.[1] reported 3 ± 1 kJ/mol in H_2-THF-d8 clathrate hydrate (D_2O), which was lower than the above values. Their measurements were based on the principle of diffusion-ordered spectroscopy [26] with NMR. The observed diffusion pathway is probably different between NMR and the differential methods. Alavi and Ripmeester reported that the energies required for the H_2 molecule to migrate through a hexagonal face of the L-cage were 24 to 27 kJ/mol and through pentagonal faces were 99 to 118 kJ/mol with molecular dynamics (MD) simulation.[25] Frankcombe and Kroes reported that the activation energy was 32.3 kJ/mol, which was similar to the calculated barrier energies for migration through hexagonal faces (L-cage) (27.6 and 23.8 kJ/mol) in H_2 clathrate hydrate with MD simulation.[24] The barrier energies for migration through pentagonal face (S-cage) is more than 200 kJ/mol.[24] Mizuno and Hanafusa reported that the activation energy of diffusion of H_2O molecule in ice was 58 kJ/mol.[27] In agreement with the literature, the results in this work support that H_2 molecules diffuse through some of the S-cages and L-cages along with H_2O translation. On the other hand, the activation energies of H_2 diffusion process were 19 to 21 kJ/mol for 6.2 mol% THF clathrate hydrates, which were lower than these in stoichiometric concentration (5.6 mol%) THF clathrate hydrates. This implies that non-included THF molecules promote formation of a grain boundary and a quasi-liquid layer (QLL) because the activation energy of diffusion of H_2O molecule in QLL was 23.5 kJ/mol (253.2 to 271.7K).[27] In CP clathrate hydrate, the activation energy of H_2 diffusion process was 100 kJ/mol, which was similar to the energy barrier of H_2 migration through

pentagonal faces (S-cage) (99 – 118 kJ/mol [25]), which implies that the H_2 molecule diffuses only through S-cages. Therefore, the H_2 diffusion pathway in hydrate particles depends on the guest additive molecule.

4.4 Conclusions

In this chapter, the formation clathrate hydrate particles were analyzed by Raman spectra and XRD and the lattice constants of the clathrate hydrates were calculated with RIETAN-2000 program. The H_2 adsorption rates were measured in the clathrate hydrate particles with pressure decay method at 265 – 273 K and 4 – 10 MPa. The clathrate hydrate particles consisted of host molecule (H_2O and D_2O) and guest additive molecule (THF, THF-d8, furan, CP and THT) so that the effect of the constituent molecule of clathrate hydrate on H_2 adsorption rate in the clathrate hydrate particle could be investigated. For hydrophobic guest additive systems (furan, CP and THT), the spectra of ice with clathrate hydrate was observed by using XRD. The effect of ice or non-included guest additive molecules on H_2 adsorption rate was investigated. The H_2 adsorption rates in furan and 6.8 mol% THF clathrate hydrates were fastest among the systems studied in this chapter.

The multiple adsorption resistance (MAR) model model was constructed by assuming three boundaries of differential H_2 adsorption system. The three resistances in the MAR model for H_2 adsorption are (i) the clathrate hydrate framework, (ii) the guest included cage and (iii) the H_2 adsorbed shell. In boundary 1 and 2, H_2 molecules adsorb in a delocalized state near the surface of the clathrate hydrate particles due to existence of pores. Especially, H_2 molecules are included in

the gas capture cage (S-cage) near pores in boundary 1, H_2 molecules are included in S-cages distant from the pores in boundary 2. In boundary 3, the shrinking of non-adsorbed core is assumed to be rate-limiting, so that the H_2 adsorption rate is described by H_2 diffusion in the H_2 adsorbed layer and the H_2 adsorption process near the interfacial boundary of the non-included solid core. The H_2 concentrations in boundary 1 and 2 were as the concentration in bulk phase due to H_2 delocalization adsorption. The H_2 concentration at interface of boundary 3 was calculated from the number of S-cage and the equilibrium H_2 occupancy due to the quasi-equilibrium adsorbed conditions. The thickness of the delocalized state L, the adsorption rate in delocalized state K_a and the interface of non-included solid core k_c, and the H_2 diffusion rate in H_2 included shell D_e can be analyzed with the MAR model.

The L and D_a in the model depend on the vapor pressure of the guest additive molecule and concentration of THF. This means that non-included guest molecules promote formation of the pore and grain boundary when clathrate hydrate particles are formed. On the other hand, K_a and k_c depend on the S-cage size of each clathrate hydrate in hydrophilic solvent systems without considering the thermodynamic stability of clathrate hydrate. In hydrophilic systems of THF clathrate hydrates, H_2 molecules become included in the clathrate hydrate cage without translation of water molecules. However, this phenomena does not seem to occur according to analyses with the proposed model of hydrophobic guest additive of CP clathrate hydrates. In CP clathrate hydrate, the activation energies of k_c and D_a were 78 and 100 kJ/mol, respectively, which were higher than those of other clathrate hydrates studied in this work. The activation energy for k_c was similar to those for CH_4 clathrate hydrate formation from ice, so this implies that little ice

exists inside CP clathrate hydrates. The activation energy of D_a was similar to the energy barrier of H_2 migration through pentagonal faces (S-cage), so this implies that diffusion of H_2 molecules through the L-cage is difficult. Therefore, it can be concluded that the H_2 diffusion pathway in clathrate hydrate particles depends on the guest additive molecules and these affect the possible resistances in different ways for hydrophilic and hydrophobic guest additive systems.

In Chapter 5, semi-clathrate hydrate systems are considered for which gas adsorption and diffusion characteristics are complicated because guest additive salts and clathrate structures both affect gas adsorption behavior. The MAR model can be applied to analyze H_2 adsorption behavior for a variety of clathrate hydrate systems which have the different pathways of diffusion for the H_2 molecules in the clathrate hydrate particle and so the MAR model will be used to study gas adsorption behavior in semi-clathrate hydrate systems.

4.5 Nomenclature

A	=	area	[m^2]
$A_{^1H}$	=	peak area of ^1H NMR	[-]
$A^*_{^1H}$	=	peak area of ^1H NMR when analyzed pure acetone-d8 liquid	[-]
AD	=	average deviation	[mol]
ARD	=	average relative deviation	[%]
a	=	lattice constant of hydrate structure II	[Å]
$C_{apparatus}$	=	apparatus constant	[-]
C_{H_2}	=	hydrogen concentration	[mol/m^3]
C_S	=	Langmuir constant of S-cage	[Pa^{-1}]
C_{stoich}	=	stoichiometric concentration	[wt%]
D_e	=	effective diffusion coefficient in models based on shrinking core model	[m^2/s]
D_a	=	apparent diffusion coefficient in models based on shrinking core model	[m^2/s]
D^*_a	=	frequency factor for D_a	[m^2/s]
D'_{H_2}	=	effective diffusion coefficient in hydrogen hydrate phase diffusion model	[$mol/(Pa \cdot s \cdot m)$]
f	=	fugacity	[Pa]
K	=	kinetic constant in hydrogen delocalization model	[$(Pa \cdot s \cdot m^2)^{-1}$]
K_a	=	adsorption rate constant in delocalized state	[s^{-1}]
K^*_a	=	frequency factor for K_a	[s^{-1}]
k_a	=	kinetic constant in hydrogen adsorption in hydrogen hydrate phase diffusion model	[$mol/(Pa \cdot s \cdot m^2)$]
k_c	=	inclusion rate constant on interface of H_2 non-included solid core	[m/s]
k^*_c	=	frequency factor for k_c	[m/s]
L	=	thickness of delocalized state	[m]
L'	=	phase thickness of hydrogen included clathrate hydrate	[m]
M	=	molecular weight	[kg/mol]
N	=	number	[-]
$N_{^1H}$	=	proton number	[-]

N_A	=	Avogadro constant	[mol^{-1}]
$N^*_{H_2O}$	=	theoretical number of water molecules per unit cell	[-]
n	=	mole number	[mol]
n_{H_2O}	=	amount of H_2O molecules of H_2 non-inclusion clathrate hydrate particle	[mol]
r	=	radius	[m]
t	=	time	[s]
V	=	volume	[m^3]
W	=	mass weight	[kg]

Greek letters

ΔE_{K_a}	=	activation energy for K_a	[J/mol]
ΔE_{k_c}	=	activation energy for k_c	[J/mol]
ΔE_{D_e}	=	activation energy for D_e	[J/mol]
ε	=	porosity	[-]
θ_S	=	occupancy in S-cage	[-]
ρ	=	density	[kg/m^3]

Subscripts

0	=	initial
B	=	Boundary
bulk	=	bulk phase
c	=	interface of non-included solid core
calc	=	calculation
cell	=	hydrate formation cell
data	=	data point
delocal	=	delocalized state
eq	=	equilibrium state
exp	=	experiment

Gas = gas phase

GCC = gas capture cavity

Guest = guest additive molecule

H_2 = hydrogen

H_2O = water

half = half of the equilibrium occupancy for H_2 molecule

Hyd = hydrate phase

Ice = ice phase

load = loading

p = particle

R,initial = before loading of reservoir tank

R,final = after loading of reservoir tank

core = interface between delocalized state and shrinking core state

sorbable = sorbable state

Theor = theoretical hydrate

Total = total loaded sample particle

4.6 References

1. Okuchi T, Moudrakovski IL, Ripmeester JA. Efficient storage of hydrogen fuel into leaky cages of clathrate hydrate. Appl Phys Lett. 2007;91:171903.
2. Nagai Y, Yoshioka H, Ota M, Sato Y, Inomata H, Smith RL. Binary hydrogen-tetrahydrofuran clathrate hydrate formation kinetics and models. AIChE J. 2008;54:3007-3016.
3. Ogata K, Hashimoto S, Sugahara T, Moritoki M, Sato H, Ohgaki K. Storage capacity of hydrogen in tetrahydrofuran hydrate. Chem Eng Sci. 2008;63:5714-5718.
4. Yoshioka H, Ota M, Sato Y, Watanabe M, Inomata H, Smith RL, Peters CJ. Decomposition kinetics and recycle of binary hydrogen-tetrahydrofuran clathrate hydrate. AIChE J. 2011;57:265-272.
5. Hashimoto S, Yamamoto K, Tsuda T, Inoue Y. Modeling on hydrogen absorption in

tetrahydrofuran hydrate. J Chem Eng Jpn. 2012;45:444-451.

6. Tsuda T, Ogata K, Hashimoto S, Sugahara T, Moritoki M, Ohgaki K. Storage capacity of hydrogen in tetrahydrothiophene and furan clathrate hydrates. Chem Eng Sci. 2009;64:4150-4154.
7. Peters CJ. Hydrogen storage in gas clathrate hydrates. Paper presented at: 5th International Symposium of Molecular Thermodynamics and Molecular Simulation2009; Kanagawa.
8. Komatsu H, Yoshioka H, Ota M, Sato Y, Watanabe M, Smith RL, Peters CJ. Phase equilibrium measurements of hydrogen-tetrahydrofuran and hydrogen-cyclopentane binary clathrate hydrate systems. J Chem Eng Data. 2010;55:2214-2218.
9. Du JW, Liang DQ, Li DL, Li XJ. Experimental determination of the equilibrium conditions of binary gas hydrates of cyclopentane + oxygen, cyclopentane + nitrogen, and cyclopentane + hydrogen. Ind Eng Chem Res. 2010;49:11797-11800.
10. NIST Chemistry WebBook. http://webbook.nist.gov/chemistry/. Accessed March, 2013.
11. Staykova DK, Kuhs WF, Salamatin AN, Hansen T. Formation of porous gas hydrates from ice powders: Diffraction experiments and multistage model. J Phys Chem B. 2003;107:10299-10311.
12. Jones CY, Marshall SL, Chakoumakos BC, Rawn CJ, Ishii Y. Structure and thermal expansivity of tetrahydrofuran deuterate determined by neutron powder diffraction. J Phys Chem B. 2003;107:6026-6031.
13. Strobel TA, Koh CA, Sloan ED. Thermodynamic predictions of various tetrahydrofuran and hydrogen clathrate hydrates. Fluid Phase Equilib. 2009;280:61-67.
14. Mak TCW, McMullan RK. Polyhedral clathrate hydrates .X. structure of double hydrate of tetrahydrofuran and hydrogen sulfide. J Chem Phys. 1965;42:2732-2737.
15. Kawamura T, Komai T, Yamamoto Y, Nagashima K, Ohga K, Higuchi K. Growth kinetics of CO_2 hydrate just below melting point of ice. J Cryst Growth. 2002;234:220-226.
16. Murshed MM, Schmidt BC, Kuhs WF. Kinetics of methane-ethane gas replacement in clathrate-hydrates studied by time-resolved neutron diffraction and raman spectroscopy. J Phys Chem A. 2010;114:247-255.
17. Komatsu H, Hayasaka A, Ota M, Sato Y, Watanabe M, Smith RL. Measurement of pure hydrogen and pure carbon dioxide adsorption equilibria for THF clathrate hydrate and tetra-*n*-butyl ammonium bromide semi-clathrate hydrate. Fluid Phase Equilib. 2013;357:80-85.
18. Yaws CL. *Chemical properties handbook: Physical , thermodynamic, environmental , transport,*

safery, and health related properties for organic and inorganic chemicals. 1st ed.McGraw-Hill; New York. 1999.

19. Wang XP, Schultz AJ, Halpern Y. Kinetics of methane hydrate formation from polycrystalline deuterated ice. J Phys Chem A. 2002;106:7304-7309.
20. Kuhs WF, Staykova DK, Salamatin AN. Formation of methane hydrate from polydisperse ice powders. J Phys Chem B. 2006;110:13283-13295.
21. Henning RW, Schultz AJ, Thieu V, Halpern Y. Neutron diffraction studies of CO_2 clathrate hydrate: Formation from deuterated ice. J Phys Chem A. 2000;104:5066-5071.
22. Genov G, Kuhs WF, Staykova DK, Goreshnik E, Salamatin AN. Experimental studies on the formation of porous gas hydrates. Am Mineral. 2004;89:1228-1239.
23. Takeya S, Hondoh T, Uchida T. In situ observation of CO_2 hydrate by X-ray diffraction. Ann NY Acad Sci. 2000;912:973-982.
24. Frankcombe TJ, Kroes GJ. Molecular dynamics simulations of type-sII hydrogen clathrate hydrate close to equilibrium conditions. J Phys Chem C. 2007;111:13044-13052.
25. Alavi S, Ripmeester JA. Hydrogen-gas migration through clathrate hydrate cages. Angew Chem Int Edit. 2007;46:6102-6105.
26. Johnson Jr CS. Diffusion ordered nuclear magnetic resonance spectroscopy: Principles and applications. Prog Nucl Magn Reson Spectrosc. 1999;34:203-256.
27. Mizuno Y, Hanafusa N. Studies of surface properties of ice using nuclear magnetic resonance. J Phys Colloq C1. 1987;48:511-517.

Chapter 5

Gas adsorption and diffusional characteristics of semi-clathrate hydrates for gas separation processes

5.1 Introduction

In Chapter 3, the phase equilibria of tetra-*n*-butyl ammonium (TBA) salt semi-clathrate with H_2 and CO_2 was shown to vary greatly according to the type of TBA salt that was added and this implied that the gas inclusion behavior was affected by the additive TBA salt. The gas adsorption behavior must depend on different factors, many of which have not been elucidated yet. A better understanding of the role of quaternary ammonium salt (QAS) in semi-clathrate hydrate applications can be obtained by varying some of the anions systematically, so that characteristics of the particles formed can be related to gas adsorption behavior.

In this chapter, the effect of anion (Br^-, Cl^- and F^-) of TBA salt on the H_2 and CO_2 adsorption characteristics of semi-clathrate hydrate for the purpose of gas separations is investigated. Gas adsorption mechanisms in semi-clathrate hydrate are investigated quantitatively with a

newly-developed model that is referred to as multiple adsorption resistance (MAR) model (Chapter 4). The separation potential of TBA salts semi-clathrate hydrates was estimated for H_2 and CO_2 mixture gases with the MAR model. Validities of the simulation results are demonstrated by H_2-CO_2 mixture gas adsorption measurements with characterized semi-clathrate hydrate particles.

5.2 Experimental

5.2.1 Materials

High-purity water was obtained from Advantec Toyo Kaisha, Ltd., RFD250NB with an electrical conductivity below 5.5 μS/m was used in the experiments. Helium gas (99.99%,), argon gas (99.99%,), hydrogen gas (99.99%), carbon dioxide (99.99%), hydrogen-carbon dioxide mixture gas (H_2 (99.99999%): *ca.* 80 vol%, CO_2 (99.995 %): *ca.* 20 vol%), tetra-*n*-butyl ammonium bromide (≥98.0%, Wako Pure Chemical Industries, Ltd.), tetra-*n*-butyl ammonium chloride (>98.0%, Tokyo Chemical Industry Co., Ltd.) and tetra-*n*-butyl ammonium fluoride trihydrate (≥ 97.0%, Sigma-Aldrich Co.) salts were used without further purification. Tetra-*n*-butyl ammonium salts are referred to as TBAB, TBAC and TBAF, for bromide, chloride and fluoride compounds, respectively.

5.2.2 Semi-clathrate hydrate preparation and characterization

Batches of semi-clathrate hydrate particles were made by loading water (*ca*. 15 g) and TBA salts (TBAB, TBAC, and TBAF) into a perfluoroalkoxyethylene vessel in such a way that the concentration of TBA salts were 2.6 – 3.7 mol% and then the contents were weighed to a precision

of 1 mg with a balance (Mettler Toledo AX504) that was followed by cooling of the solution to a predefined temperature (274 – 295 K) with low temperature-controlled bath (LP-50P, Nippon Medical & Chemical Ins. Co., Ltd.) while stirring with a hand-made stirring bar attachment that promoted mixing throughout the vessel.

For TBAB semi-clathrate hydrates, the effect of formation temperature on the formation structure was confirmed. For TBAC semi-clathrate hydrates, the effect of the concentration of TBAC on the formation structure was confirmed. For TBAF semi-clathrate hydrates, the effect of the concentration of TBAF and formation temperature on the formation structure was confirmed. The formed semi-clathrate hydrates were cooled to 253 K in a freezer for at least six hours. The solids were crushed with a mortar and pestle at liquid nitrogen temperatures and then graded with stainless steel-type 316 sieves while being kept in the freezer at 253 K. Particle size ranges of 106-150 or 250-355 μm were used in the experiments. The H_2 equilibrium adsorption amount was measured as with experimental methods and apparatus used in Chapter 4. The formation of hydrates was confirmed with differential scanning calorimetry (DSC-6100, SII Ltd.) and laser Raman spectroscopy (NRS-5100, JASCO, Tokyo) with experimental methods described in Appendix 5-4. Table 5-1 summarizes the preparation conditions and characterization of the semi-clathrate hydrates.

Table 5-1. Description of semi-clathrate hydrate structures, hexagonal structure-I (HS-I), tetragonal structure-I (TS-I) and superlattice of cubic structure-I (SCS-I). Lattice constants are typical for each structure and tetra-*n*-butyl ammonium (TBA) salt as compiled from the literature.

Crystal system (abbreviation)	N_{H_2O} (N_{ideal,H_2O})	$N_{TBA\ salt}$	N_S	TBA salt	Hydration number	$N^*_{H_2O}$	Lattice constants [Å]			Ref.
							a	*b*	*c*	
Orthorhombic (HS-I)	76 (80)	2	6	TBAB	38	76	21.06	12.643	12.018	Shimada (2005)[1]
Tetragonal (TS-I)	162 (172)	5	10	TBAB	32.8	164	23.57		12.3	Davidson (1973)[2]
				TBAC	30.4	152	23.582		12.415	Rodionva (2010)[3]
				TBAF	32.8	164	23.52		12.3	Dyadin (1976)[4]
Cubic (SCS-I)	344 (368)	12	16	TBAF	29.7	356.8	24.375			Komarov (2007)[5]

TBAB : tetra-*n*-butyl ammonium bromide, TBAC: tetra-*n*-butyl ammonium chloride, TBAF: tetra-*n*-butyl ammonium fluoride.

N_{ideal,H_2O} : ideal number of water molecules per unit cell, N_{H_2O} : number of non-replaced water molecules as host molecule by cation and anion of TBA salt per unit cell, $N^*_{H_2O}$: reported number of water molecules per unit cell, $N_{TBA\ salt}$: number of included TBA salt molecules in semi-clathrate hydrate structure per unit cell, N_S : number of S-cage of semi-clathrate hydrate per unit cell.

5.2.3 Experimental apparatus

The experimental apparatus consisted of a hydrate formation cell and a reservoir tank as described in Chapter 4. The reservoir tank system was designed to be separated from the equilibrium cell during the loading of the reservoir tank with gas. In the hydrate formation cell, the window was held externally with an O-ring (IIR-70°, Morisei Kako Co. (H_2 systems) or KEF Co. (CO_2 systems)) and the inner cell was made of brass. In CO_2 systems, CO_2 is soluble in the O-ring used in H_2 systems thus an O-ring (IIR-70°, KEF Co.) that had low CO_2 gas solubility was developed. The inner volumes of the hydrate formation cell and reservoir tank were 304.7 and 26.3 cm^3, respectively (Appendix D). The cell and the tank were maintained to within ± 0.02 K and ± 0.05 K, respectively. Two temperature sensors that were inserted into a hole in the cell assembly wall and into the reservoir tank had uncertainties of ±29 and ±78 mK, respectively (Appendix A). Two pressure gauges on the cell and the tank had uncertainties of ±1.7 and ±2.3 kPa, respectively (Appendix B). Detailed specifications of the apparatus, such as temperature control system, temperature sensor and pressure gauges have been described in Chapter 4.

5.2.4 Experimental procedure

The experimental procedure was similar to that used in Chapter 4 and is briefly described here. When the hydrate formation cell and the reservoir tank were cooled to 269 K, about 4 g of the TBA salt semi-clathrate hydrate particles was loaded. As soon as the hydrate formation cell and the reservoir tank were evacuated for 5 s by a vacuum pump (Hitachi Koki Co., VR16L), the valve between the hydrate formation cell and the reservoir tank was closed. After the reservoir tank was

sufficiently evacuated by the vacuum pump, H_2 gas was pressurized to about 4.3 MPa, CO_2 gas was pressurized to about 0.9 MPa, or H_2-CO_2 mixture gas was pressurized to about 4.9 MPa in the reservoir tank. The CO_2 and H_2-CO_2 mixture pressures were set so as to not form pure CO_2 clathrate hydrate that are known to be ice-hydrate-vapor phase equilibrium at conditions of 268.9 K and 0.924 MPa.[6] The H_2 pressure was set to be about four times the initial CO_2 pressure value on the assumption of the theoretical reactions of the reforming of CH_4 and water gas shift ($CH_4 + 2H_2O \rightarrow 4H_2 + CO_2$).[7] When temperature and pressure of the reservoir tank stabilized, the gas was loaded into the formation cell over a period of about 5 s (H_2) or 10 s (CO_2 or H_2-CO_2). The analysis method was based on the pressure decay method with material balances being used in the formation cell and reservoir tank as in Chapter 4. The amount of gas loaded $n_{\text{gas, load}}$, was calculated by the difference in the gas density before and after loading of the reservoir tank (Eq.(5-1)) with the virial EoS calibrated to NIST correlations(Appendix E).[8] The second and third virial coefficients of H_2 were estimated from the molar volume at temperatures of 240 – 300 K and at pressures of 0.05 – 14 MPa, and those for CO_2 were estimated from the saturated pressure at temperatures from 217 to 303 K. The second and third mixture virial coefficients of the virial equation of state were estimated from liquid-vapor equilibria of H_2-CO_2 systems (Appendix E).[9-12]

$$n_{\text{gas, load}} = n_{\text{gas, R, initial}} - n_{\text{gas, R, final}} \tag{5-1}$$

The amount of gas in the hydrate phase was calculated from the relationships below.

Volume of vapor phase:

$$V_{\text{vapor}} = \frac{n_{\text{gas, load}} M_{\text{gas}}}{\rho_{\text{gas, vapor}}\left(t = 0\right)} \tag{5-2}$$

Moles of free gas in vapor phase:

$$n_{\text{gas, vapor}}\left(t\right) = \frac{\rho_{\text{gas, vapor}}\left(t\right)V_{\text{vapor}}}{M_{\text{gas}}} \tag{5-3}$$

Moles of gas in hydrate phase by material balance:

$$n_{\text{gas, Hyd}}\left(t\right) = n_{\text{gas, load}} - n_{\text{gas, vapor}}(t) - n_{\text{gas, leak}}(t) \tag{5-4}$$

where the leak rate in Eq. (5-4) was assumed to be constant. The leak rates of H_2 and CO_2 were (6.2 $\pm$ 0.9) $\times$ 10^{-4} mmol/h and (1.30 $\pm$ 0.10) $\times$ 10^{-3} mmol/h, respectively, which corresponds to a pressure drop rate of 0.05 – 0.11 kPa/h. The experiment for the run was judged to have reached the equilibrium adsorption amount when the leak rate for the run was close to that for a system without sample according to values noted above. The leak amount of gas from the O-ring, $n_{\text{gas, leak}}(t)$ was calculated by using the leak rate at the end of the experiment. The volume of hydrate phase was calculated from Eq. (5-5) and that of the hydrate phase was calculated from Eq. (5-6) using the theoretical water density in the hydrate phase (Eq. (5-7)) as given below.

Volume of hydrate phase:

$$V_{\text{Hyd}} = V_{\text{cell}} - V_{\text{vapor}} \tag{5-5}$$

Volume of theoretical hydrate phase:

$$V_{\text{Theor Hyd}} = \frac{n_{\text{H}_2\text{O, Hyd}}M_{\text{H}_2\text{O}}}{\rho_{\text{H}_2\text{O, Theor Hyd}}} \tag{5-6}$$

Theoretical water density in the hydrate phase is:

$$\rho_{\text{H}_2\text{O, Theor Hyd}} = \frac{N_{\text{H}_2\text{O}}M_{\text{H}_2\text{O}}}{\left(a \times b \times c\right)N_{\text{A}}} \tag{5-7}$$

Because pores exist in the hydrate particles,[13] the difference was corrected using the porosity, ε, as in Eq.(5-8):

$$V_{\mathrm{Hyd}} = \frac{V_{\mathrm{Theor\ Hyd}}}{1-\varepsilon} \tag{5-8}$$

where $N_{\mathrm{H_2O}}$ is the theoretical number of water molecules per unit cell. The lattice constants *a*, *b* and *c* were taken from the literature.[1-5] Table 5-1 summarizes $N_{\mathrm{H_2O}}$ and lattice constants for each semi-clathrate hydrate. In H_2-CO_2 mixture systems, the gas composition of the vapor phase was analyzed with gas chromatography (GC) (INFICON 3000 Micro Gas Chromatograph, Agilent Technologies, Inc.) with a two column systems and a thermal conductivity detector (TCD). In the MolSieve 5A PLOT (10 m) backflush column system, the carrier was argon gas, injection time was 20 ms and back flash time was 15 s. In the PLOT Q (8 m) column system, the carrier was helium gas and injection time was 100 ms. In both columns, temperatures in the injector and column, and pressure of carrier gas were 323 K, 323 K and 172 kPa, respectively. The amount of sample gas in the cell was diluted by 1:6 by volume with Ar gas to increase its volume. Similarly, the sample gas in the tank was analyzed after dilution with Ar gas to standardize the sample gas conditions. The H_2 composition of sample gas in vapor phase, $y_{\mathrm{H_2}}$ was calculated from the peak area of GC, $A_{\mathrm{GC,gas}}$ corresponding to each gas as given by Eq. (5-9):

$$y_{\mathrm{H_2}} = \frac{A_{\mathrm{GC,H_2}} \Big/ A^{*}_{\mathrm{GC,H_2}}}{\dfrac{A_{\mathrm{GC,H_2}}}{A^{*}_{\mathrm{GC,H_2}}} + \dfrac{A_{\mathrm{GC,CO_2}}}{A^{*}_{\mathrm{GC,CO_2}}}} \tag{5-9}$$

where $A^{*}_{\mathrm{GC,gas}}$ is the peak area given by GC analysis of the pure gas, which was measured for run numbers 16 – 20. These data reported represent the average of three values. The uncertainly of

the selectively was estimated from error analysis of the H_2 composition (Appendix 5-1).

5.3 Results and Discussion

5.3.1 Assessment of semi-clathrate hydrate particles

Figure 5-1 shows typical DSC curves of TBA salt semi-clathrate hydrates for differential formation conditions and Table A5-1 (Appendix 5-2) summarizes their characterization. Figure A5-1 (Appendix 5-2) shows all DSC curves in Chapter 5 In TBAB systems (Figure 5-1 a and b), the dissociation temperature was similar to literature values[14] for each structure and a single DSC peak derived from TBAB semi-clathrate hydrate was observed. Thus, it can be concluded that 2.6 mol% TBAB semi-clathrate hydrate was mainly HS-I hydrate and 3.7 mol% TBAB semi-clathrate hydrate was mainly TS-I hydrate. The ice in the prepared particles for the 2.6 mol% TBAB semi-clathrate hydrates was neglected (272.5 K) because the peak was small. In TBAC systems (Figure 5-1 c, Figure A5-1 c – f), the dissociation temperatures were similar to literature values[15] for all formation conditions and a single DSC peak derived from TBAC semi-clathrate hydrate was confirmed. A peak corresponding to ice was observed for TBAC concentrations other than 3.2 mol% (Figure A5-1 c – f). The reason for ice formation in 3.7 mol% TBAC system is considered to be that non-included TBAC became hydrated separately from the semi-clathrate hydrate. Therefore, it was confirmed in this work that 3.2 mol% TBAC system can form TBAC semi-clathrate hydrate without forming ice (Figure 5-1 c). In TBAF systems (Figure 5-1 d and e, Figure A5-1 g – j), the dissociation temperatures were similar to literature values[16] and a single DSC peak derived from the TBAF semi-clathrate hydrate was observed for all formation conditions

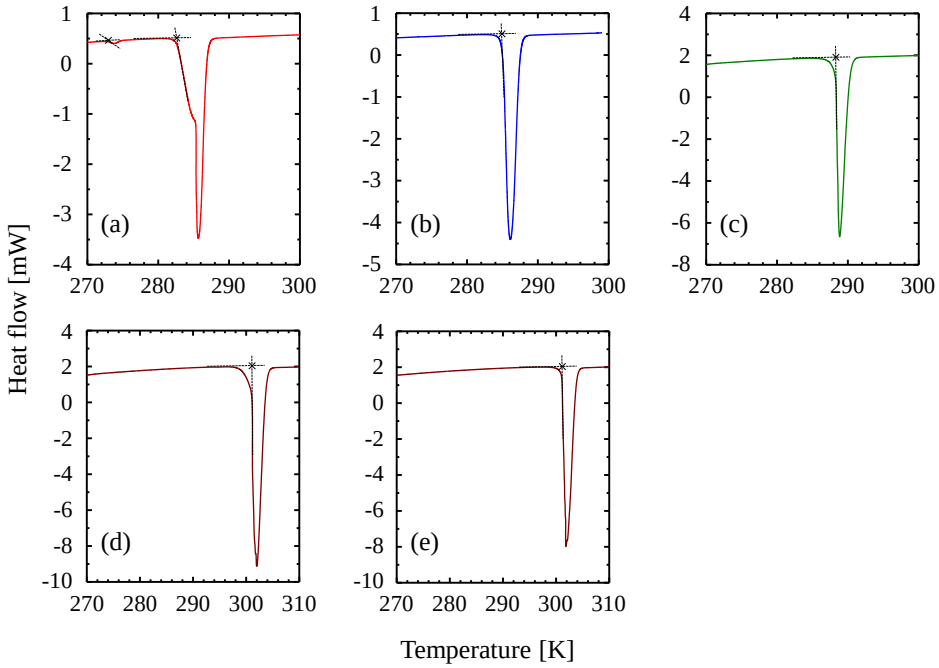

Figure 5-1. DSC curves of tetra-*n*-butyl ammonium (TBA) salt semi-clathrate hydrates at atmospheric pressure for a heating rate of 1 K/min. Symbol:×: decomposition temperature. TBAB semi-clathrate hydrates were formed at (a) 2.6 mol% TBAB and 274 K (red line), (b) 3.7 mol% TBAB and 283 K (blue line). TBAC semi-clathrate hydrates were formed at (c) 3.2 mol% TBAC and 276 K (green line). TBAF semi-clathrate hydrates were formed at (d) 3.0 mol% TBAF and 296 K (brown line), (e) 3.3 mol% TBAF and 296 K (brown line).

5.3.2 Raman analysis

Figure 5-2 shows typical Raman spectra for the TBA salt semi-clathrate hydrates for each formation condition. Figure A5-2 (Appendix 5-3) shows Raman spectra of all semi-clathrate hydrates studied in this chapter. Raman peaks at around 700 – 1500 cm^{-1} and 2800 – 3100 cm^{-1} correspond to the TBAB molecules,[17] TBAC molecules or TBAF molecules.[16,18] Broad peaks at 3200 – 3400 cm^{-1} corresponding to O-H vibration of the H_2O molecules. Hashimoto et al. reported that the Raman peak around 1134 cm^{-1} for the TBAB semi-clathrate hydrate in HS-I structure was not observed for HS-I structure.[17] The effect of formation temperature on the

structure of 2.6 mol% TBAB semi-clathrate hydrate was obtained (Appendix 5-4). the peak around 1134 cm^{-1} was hardly observed for 2.6 mol% TBAB semi-clathrate hydrate formed at 274 K, which indicates that 2.6 mol% TBAB semi-clathrate hydrate is mainly HS-I structure. However, changes in specific Raman peaks were not observed for other TBA salt semi-clathrate hydrates. The semi-clathrate hydrate structures were assessed for their H_2 equilibrium storage amount.

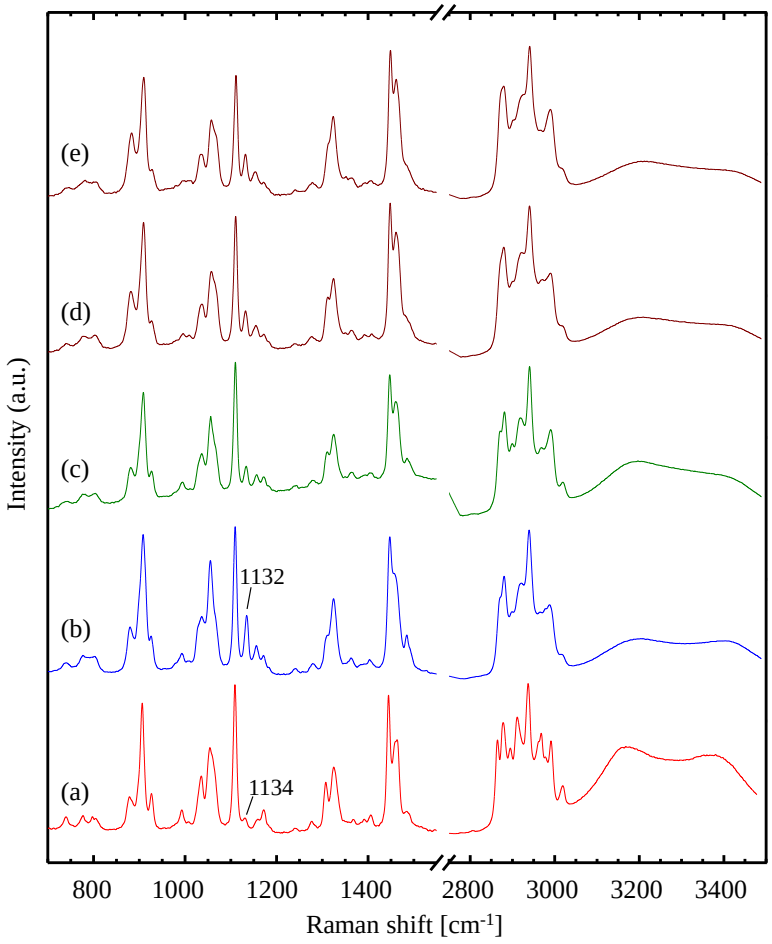

Figure 5-2. Raman spectra for tetra-*n*-butyl ammonium (TBA) salts systems at room temperature and atmospheric pressure. TBAB semi-clathrate hydrates were formed at (a) 2.6 mol% TBAB and 274 K (red line), (b) 3.7 mol% TBAB and 283 K (blue line). TBAC semi-clathrate hydrates were formed at (c) 3.2 mol% TBAC and 276 K (green line). TBAF semi-clathrate hydrates were formed at (d) 3.0 mol% TBAF and 296 K (brown line), (e) 3.3 mol% TBAF and 296 K (brown line). The Raman peak around 1134 cm^{-1} depends on TBAB semi-clathrate hydrate structure.[17]

5.3.3 Equilibrium hydrogen storage

Figure 5-3 shows H_2 equilibrium storage amount in TBAB, TBAC or TBAF semi-clathrate hydrates and Table 5-2 and 5-3 summarizes experimental conditions and results. The H_2 equilibrium storage amounts with respect to the sample (hydrate and ice), $X_{\mathrm{eq.,H_2}}$ were calculated from Eq. (5-10):

$$X_{\mathrm{eq.,H_2}} = \frac{n_{\mathrm{eq.,H_2,Hyd}}}{n_{\mathrm{H_2O,\,load}} + n_{\mathrm{TBA\,salt,\,load}}} \tag{5-10}$$

where $n_{\mathrm{H_2O,\,load}}$ and $n_{\mathrm{TBA\,salt,\,load}}$ are the amount of H_2O and TBA salt contained in the sample powder, respectively. The $X_{\mathrm{eq.,H_2}}$ greatly depended on the semi-clathrate hydrate structure, but did not seem to be affected by the presence of ice. The $X_{\mathrm{eq.,H_2}}$ for the 2.6 mol% TBAB semi-clathrate that had HS-I structure (Sections 5.3.1 and 5.3.2) exhibit the highest values for H_2 solubility (*ca.* 7 $\mathrm{mmol_{-H2}}$ /$\mathrm{mol_{-H2O+TBA\,salt}}$) among the semi-clathrate hydrates (Table 5-4, runs 1 – 10). The $X_{\mathrm{eq.,H_2}}$ for the TBAC semi-clathrate hydrate systems and the 3.0 mol% TBAF semi-clathrate hydrate systems were about the same (*ca.* 3 $\mathrm{mmol_{-H2}}$ /$\mathrm{mol_{-H2O+TBA\,salt}}$). The $X_{\mathrm{eq.,H_2}}$ for 3.3 mol% TBAF semi-clathrate hydrate system values (*ca.* 2 $\mathrm{mmol_{-H2}}$ /$\mathrm{mol_{-H2O+TBAF}}$) were lower those that for other semi-clathrate hydrate systems (Table 5-4, runs 1 – 10). This change in the $X_{\mathrm{eq.,H_2}}$ implies some differences in the semi-clathrate hydrate structures.

For TBAC semi-clathrate hydrates, the H_2 equilibrium storage amounts (Figure 5-3 and Table 5-3, runs 3 – 6) were in order of (largest to smallest) 3.2 mol% TBAC (run 5), 3.0 mol% TBAC (run 4), 3.7 mol% TBAC (run 6), and 2.6 mol% TBAC (run 3). The reason that the H_2 equilibrium storage amount for 3.2 mol% TBAC semi-clathrate hydrate was the highest among the

concentrations examined is probably due to the formation of ice (Figure A5-1 c – f). Since H_2 equilibrium storage amount given by in Eq.(5-10) is lowered by the existence of ice, some TBAC essentially had no contribution to hydrate formation due to the standardized loading amounts of the salts used. However, the H_2 equilibrium storage amount did not change greatly among the TBAC semi-clathrate hydrates and those values were close to those for 3.7 mol% TBAB semi-clathrate hydrate of TS-I structure (Table 5-3, run 2). These results are evidence that TBAC semi-clathrate hydrate had TS-I structure independent of the TBAC concentration.

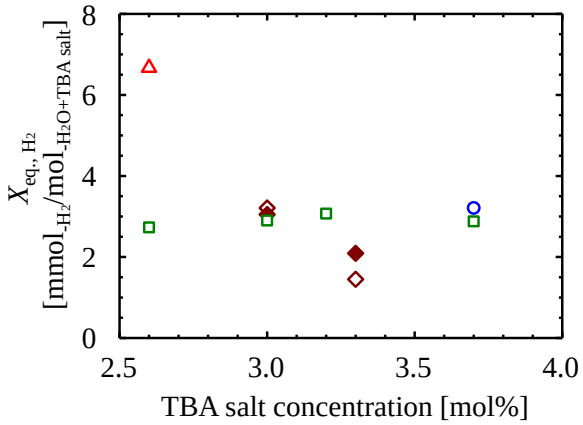

Figure 5-3. Hydrogen equilibrium storage amount tetra-*n*-butyl ammonium bromide (TBAB), chloride (TBAC) or fluoride (TBAF) semi-clathrate hydrates (d_p = 250 – 355 μm, T = 269 K, $P_{initial}$ = 4.0 MPa). Symbols show semi-clathrate hydrate formation temperatures. Red triangle, TBAB, 274 K; blue circle, TBAB, 283 K; green squares, TBAC, 276 K; brown diamonds, TBAF, 297 K; filled brown diamonds, TBAF, 276 K.

For TBAF semi-clathrate hydrate in Table 5-3, the H_2 equilibrium storage amount for 3.3 mol% TBAF (run 10) was lower than half of that for 3.0 mol% TBAF (run 8). Thus, the effect of TBAF concentration on the H_2 equilibrium storage amount for TBAF semi-clathrate hydrates was larger than that for TBAC semi-clathrate hydrates (Figure 5-3 and Table 5-3). The difference in H_2

equilibrium storage amounts for 3.0 mol% TBAF semi-clathrate hydrates and 3.3 mol% TBAF semi-clathrate hydrates formed near the dissociation temperature (ΔT = 5 K) was larger than that for TBAF semi-clathrate hydrates formed at 276 K (ΔT = 25 K). These results imply that semi-clathrate hydrates of different structures are formed between 3.0 mol% TBAF and 3.3 mol% TBAF, and these two structures probably formed at the same time for the given set of conditions in which there was a large degree of supercooling (ΔT). The H_2 equilibrium storage amount for 3.0 mol% TBAF semi-clathrate hydrate formed at ΔT equal to 5 K (Table 5-2, run 8) was close to that for 3.7 mol% TBAB semi-clathrate hydrate of TS-I structure (Table 5-3, run 2), thus it can be concluded that the TBAF semi-clathrate hydrate (Table 5-3, run 8) is TS-I structure rich. The 3.3 mol% TBAF semi-clathrate hydrate formed at ΔT equal to 5 K (Table 5-2, run 10) for which the H_2 equilibrium storage amount was lowest (Table 5-3) is most likely SCS-I structure rich. The TS-I structure seemed to readily form for 3.0 mol% TBAF and the SCS-I structure seemed to readily form for 3.3 mol% TBAF.

Table 5-2. Gas adsorption experimental conditions for semi-clathrate hydrate particles (T = 269.2 K). Particle sizes for H_2 systems were 250 – 355 μm and those for CO_2 system were 106 – 150 μm.

Run	Gas	TBA salt	Conc. [mol%]	ΔT [K]	$P_{initial}$ [MPa]	W_{Hyd} [g]
1	H_2	TBAB	2.6	9	4.02	4.369
2			3.7	2	3.99	5.217
3		TBAC	2.6	12	4.07	7.501
4			3.0	12	4.05	7.319
5			3.2	12	4.05	8.192
6			3.7	12	4.05	8.795
7		TBAF	3.0	25	4.02	7.324
8			3.0	5	4.05	5.368
9			3.3	25	4.12	7.213
10			3.3	5	4.02	6.609
11	CO_2	TBAB	2.6	9	0.82	2.389
12			3.7	2	0.84	2.862
13		TBAC	3.2	12	0.85	3.380
14		TBAF	3.0	5	0.84	4.349
15			3.3	5	0.83	3.789
16	H_2/CO_2 = 3.4	TBAB	2.6	9	4.50	4.054
17			3.7	2	4.49	3.791
18		TBAC	3.2	12	4.51	3.782
19		TBAF	3.0	5	4.49	4.257
20			3.3	5	4.51	4.570

TBAB : tetra-*n*-butyl ammonium bromide, TBAC: tetra-*n*-butyl ammonium chloride, TBAF: tetra-*n*-butyl ammonium fluoride.

ΔT: degree of supercooling, T: temperature, $P_{initial}$: initial pressure, W_{Hyd}: mass (weight) of hydrate in product particles

Table 5-3. Results derived from gas adsorption in semi-clathrate hydrates experiments. Time at completion of experiment was 4.0 h (runs: 16 – 20)

Run	Pure gas	TBA salt	Conc. [mol%]	ΔT [K]	P_{final} [MPa]	t_{half} [h]	$X_{eq.,\,gas}$ $\left[\frac{mmol_{gas}}{mol_{H_2O+TBA\,salt}}\right]$	$\theta_{eq.,\,gas,\,S}$ [-]	$C_{gas,\,S}$ [$\times 10^{-1}$ MPa^{-1}]
1	H_2	TBAB	2.6	9	3.90	0.79	6.67	0.087	0.238
2			3.7	2	3.93	0.74	3.21	0.052	0.136
3		TBAC	2.6	12	3.97	0.15	2.73	0.045	0.117
4			3.0	12	3.94	0.22	2.90	0.048	0.126
5			3.2	12	3.93	0.94	3.07	0.051	0.134
6			3.7	12	3.93	0.48	2.88	0.048	0.126
7		TBAF	3.0	25	3.91	0.27	3.05	0.051	0.134
8			3.0	5	3.97	0.31	3.21	0.054	0.140
9			3.3	25	4.04	0.52	2.09	0.046	0.118
10			3.3	5	3.97	0.15	1.45	0.032	0.081
11	CO_2	TBAB	2.6	9	0.56	3.24	35.58	0.413	13.15
12			3.7	2	0.68	13.1	14.02	0.236	4.991
13		TBAC	3.2	12	0.60	14.1	19.40	0.325	8.341
14		TBAF	3.0	5	0.55	4.24	16.93	0.283	7.504
15			3.3	5	0.65	14.0	9.82	0.218	4.489
	Gas mixture					X_{H_2}	X_{CO_2}	$\theta_{H_2,\,S}$	$\theta_{CO_2,\,S}$
16		TBAB	2.6	9	4.21	2.97	17.68	0.039	0.230
17			3.7	2	4.40	1.70	5.63	0.029	0.095
18	H_2/CO_2	TBAC	3.2	12	4.40	1.43	7.07	0.024	0.118
19		TBAF	3.0	5	4.35	1.02	8.02	0.017	0.133
20			3.3	5	4.44	0.96	3.82	0.021	0.085

H_2/CO_2: H_2 + CO_2 mixture gas (H_2/CO_2=3.4). TBAB : tetra-*n*-butyl ammonium bromide, TBAC: tetra-*n*-butyl ammonium chloride, TBAF: tetra-*n*-butyl ammonium fluoride.

P_{final}: pressure at experimental finished, t_{half} : time to reach half the equilibrium gas occupancy in S-cage, X_{gas}: gas mole number in semi-clathrate hydrate phase by H_2O and TBA salt molecules in samples, θ_{eq}: equilibrium occupancy, C_S: Langmuir constants of gas in S-cage.

5.3.4 Characteristics of gas occupancy

Table 5-2 and 5-3 summarize experimental conditions and results for the gas adsorption experiments. Figure 5-4 shows gas occupancy in the S-cages as a function of time for the TBA salt semi-clathrate hydrates for either H_2 or CO_2. The gas occupancy in the S-cage, $\theta_{\text{gas, S}}$ was calculated from Eq. (5-11) based on the assumption of single occupancy in the S-cage:

$$\theta_{\text{gas, S}} = \frac{n_{\text{gas, Hyd}} N_{\text{H}_2\text{O}}}{n_{\text{H}_2\text{O, load}} N_{\text{S}}} \tag{5-11}$$

where N_{S} is the number of S-cages according to the unit cell. When $\theta_{\text{H}_2\text{, S}}$ is 1, all S-cages are occupied with H_2 molecules. In Eq. (5-11), water molecules are assumed to not occupy the S-cage for simplicity. It should be noted, however, that different occupancies for H_2O molecules have been reported for the SCS-I structure of the TBAF semi-clathrate hydrate.[4,5] This point is considered in a later section. Gas adsorption rates for semi-clathrate hydrates were assessed by the time required to reach half the equilibrium gas occupancy in the S-cage, t_{half}. A low t_{half} value means that the adsorption rate is high and that adsorption occurs fast. The t_{half} for H_2 systems (Table 5-3) were in order of (shortest to longest) 3.3 mol% TBAF (run 10), 3.0 mol% TBAF (run 8), 3.7 mol% TBAB (run 2), 2.6 mol% TBAB (run 1), and 3.2 mol% TBAC (run 5). The t_{half} for H_2 systems were influenced more by the anion of the TBA salt than the structure of the semi-clathrate hydrate and were in order of (shortest to longest) TBAF, TBAB and TBAC.

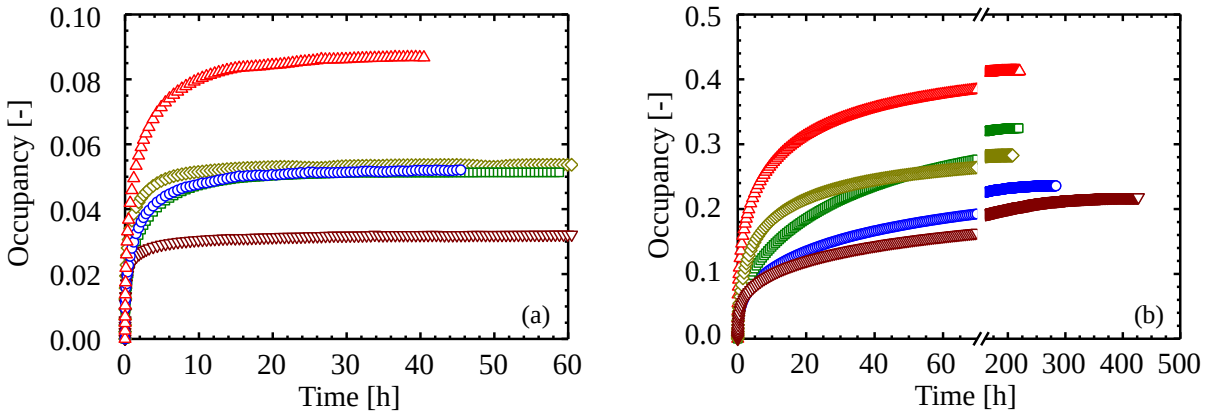

Figure 5-4. Experimental results of H_2 or CO_2 occupancy as a function of time in S-cages of the semi-clathrate hydrates at 269 K. (a): H_2 adsorption systems (d_p = 250 – 355 μm, $P_{initial}$ = 4.0 MPa). (b): CO_2 adsorption systems (d_p = 106 – 150 μm, $P_{initial}$ = 0.8 MPa). Symbols show tetra-*n*-butyl ammonium (TBA) salt and structure of semi-clathrate hydrate. Symbols: red up-pointing triangles, 2.6 mol% TBAB (HS-I); blue circles, 3.7 mol% TBAB (TS-I); green squares, 3.2 mol% TBAC (TS-I); olive diamonds, 3.0 mol% TBAF (TS-I); brown down-pointing triangles, 3.3 mol% TBAF (SCS-I).

The t_{half} for CO_2 systems (Table 5-3) were in order of (shortest to longest) 2.6 mol% TBAB, (run 11), 3.0 mol% TBAF (run 14), 3.7 mol% TBAB (run 12), 3.3 mol% TBAF (run 15), and 3.2 mol% TBAC (run 13). The t_{half} for CO_2 systems depended not only on the anion of the TBA salt, but also on the semi-clathrate hydrate structures. Considering the TBA anion and clathrate structure, the t_{half} for CO_2 systems were in order of (shortest to longest) TBA salt (TBAF, TBAB and TBAC) and semi-clathrate hydrate structure (HS-I, TS-I and SCS-I). The effect of the TBA anion on t_{half} for CO_2 systems corresponded to that for H_2 systems. This implies that the area of the crystal grain boundary, A_{gb} for the semi-clathrate hydrates increases in order of $A_{gb,TBAF} > A_{gb,TBAB} > A_{gb,TBAC}$. In fact, TBAF semi-clathrate hydrates could be easily crushed when the hydrate particles were prepared (Section 5.2.2). The effect of clathrate structure on t_{half} for CO_2

systems seems to be in correspondence with the hydration number (Table 5-1). Low hydration numbers of TBA salts ($N_{\mathrm{H_2O}} \big/ N_{\mathrm{TBA\ salt}}$, Table 5-1) tended to have high anion compositions as the host molecule. This means that the anion of host molecule inhibited the gas adsorbed into the semi-clathrate hydrate. The inner diameter of the S-cage with the anion is probably smaller than that of other S-cages because the anion radius[19] is larger than that of water.[20] Therefore, the dependence of the CO_2 adsorption rate on semi-clathrate hydrate structure implies that the anion as host molecule physically inhibits CO_2 adsorption due to the CO_2 molecular size being close to the S-cage size. Especially for the TS-I structure, the t_{half} for the TBAF semi-clathrate hydrate was significantly shorter than that for the TBAB and TBAC semi-clathrate hydrate because the ionic radius of F^- (1.71 Å) is much smaller than that of Cl^- (2.23 Å) and Br^- (2.35 Å).[19]

The H_2 equilibrium occupancies in the S-cage, $\theta_{\mathrm{eq.,\ H_2,S}}$ (Table 5-3) were in order of (largest to smallest) for the semi-clathrate hydrates: 2.6 mol% TBAB (run 1), 3.0 mol% TBAF (run 8), 3.7 mol% TBAB (run 2), 3.2 mol% TBAC (run 5), and 3.3 mol% TBAF (run 10). The effect of the anion on the $\theta_{\mathrm{eq.,\ H_2,S}}$ for TS-I structure (Table 5-3, runs 8, 2 and 5) was small but seemed to correspond to the size of the unit cell for TS-I structure (Table 5-1), since the $\theta_{\mathrm{S,\ H_2,\ eq}}$ increased as the size of unit cell decreased. Thus, this result implies that van der Waals interactions between H_2 and H_2O increase as the size of the S-cage becomes smaller. On the other hand, the $\theta_{\mathrm{eq.,\ H_2,S}}$ seemed to be more strongly influenced by the semi-clathrate hydrate structure (Table 5-3, runs 1, 5 and 10). This trend implies that the S-cage was occupied by H_2O molecules, because the occupancy of H_2 decreases with the introduction of other guest molecules as Eq. (5-12):

$$\theta_{\mathrm{eq.,\,H_2,\,S}} = \frac{C^*_{\mathrm{H_2,\,S}} f_{\mathrm{H_2}}}{1 + C^*_{\mathrm{H_2,\,S}} f_{\mathrm{H_2}}} \left(1 - \theta_{\mathrm{eq.,\,other,\,S}}\right) \tag{5-12}$$

where $C^*_{\mathrm{H_2,\,S}}$ and f are the actual Langmuir constant and fugacity, respectively. The occupancy of H_2O probably depended on the number of anions of TBA salt as host molecule regardless of the anion species of the TBA salt. For the case of occupied H_2O as a guest molecule, the $\theta_{\mathrm{eq.,\,H_2,S}}$ changes slightly because the $\theta_{\mathrm{eq.,\,H_2,S}}$ calculated from Eq. (5-11) changes from $N_{\mathrm{H_2O}}$ to $N^*_{\mathrm{H_2O}}$. The $C^*_{\mathrm{H_2,\,S}}$ was calculated from Eqs. (5-13) and (5-14) by considering the number of H_2O molecules occupied in the S-cage per unit cell, $N_{\mathrm{Occ,\,H_2O}}$ as follows:

$$\theta^*_{\mathrm{eq.,\,H_2,\,S}} = \frac{n_{\mathrm{eq.,\,H_2,\,Hyd}} \left(N_{\mathrm{H_2O}} + N_{\mathrm{Occ,\,H_2O}}\right)}{n_{\mathrm{H_2O,\,load}} \left(N_{\mathrm{S}} - N_{\mathrm{Occ,\,H_2O}}\right)} \tag{5-13}$$

$$C^*_{\mathrm{H_2,\,S}} = \frac{\theta^*_{\mathrm{eq.,\,H_2,\,S}}}{f_{\mathrm{H_2}} \left(1 - \theta^*_{\mathrm{eq.,\,H_2,\,S}}\right)} \tag{5-14}$$

where $\theta^*_{\mathrm{eq.,\,H_2,\,S}}$ is the equilibrium occupancy of H_2 in the S-cage non-occupied with H_2O. The $C^*_{\mathrm{H_2,\,S}}$ was assumed to be equal to that for clathrate hydrates of sII structure, because the effect of distortion of the S-cage on $C^*_{\mathrm{H_2,\,S}}$ is small in the sII structure due to the small molecular size of H_2.[21] The Langmuir constant for H_2 in the S-cage for sII structure, $C^*_{\mathrm{H_2,\,S}}$ was 0.04 $\mathrm{MPa^{-1}}$ at 269 K from the measurements in Chapter 4, thus $\theta^*_{\mathrm{eq.,\,H_2,\,S}}$ was 0.14 at 4 MPa. The $N_{\mathrm{Occ,\,H_2O}}$ was estimated by using the $\theta^*_{\mathrm{eq.,\,H_2,\,S}}$, structure parameters ($N_{\mathrm{H_2O}}$ and N_{S}) and experimental results ($n_{\mathrm{H_2O,\,load}}$ and $n_{\mathrm{eq.,\,H_2,\,Hyd}}$) in Eq. (5-13). The $N_{\mathrm{Occ,\,H_2O}}$ for HS-I, TS-I and SCS-I structures were taken to be 2.1, 6.0 and 12.2, respectively. These values correspond to the number of included TBA salt molecules per unit cell, $N_{\mathrm{TBA\,salt}}$ (Table 5-1) and implies that the number of included H_2O

molecules are strongly related to the number of included TBA salt species. In these results, the occupancy of H_2O molecules in the S-cage were about 0.35, 0.6 and 0.76 for HS-I, TS-I and SCS-I structures, respectively. Komarov et al. reported that the occupancy of H_2O molecules in the S-cage was 0.8 for the SCS-I structure of TBAF semi-clathrate hydrate,[5] so that results in this work are in accordance with the literature.[5] From these results, it can be implied that gas adsorption capacities can be increased if the occupancy of H_2O molecules can be inhibited.

The CO_2 equilibrium occupancy in the S-cage, $\theta_{S,\,CO_2,\,eq}$ for semi-clathrate hydrates (Table 5-3) were in order of (largest to smallest) 2.6 mol% TBAB (run 11), 3.2 mol% TBAC (run 13), 3.0 mol% TBAF (run 14), 3.7 mol% TBAB (run 12), and 3.3 mol% TBAF (run 15). The $\theta_{eq.,\,CO_2,S}$ depended not only on the structure, but also on the anion of the TBA salt in contrast to the H_2 systems. The $\theta_{eq.,\,CO_2,S}$ for TBAC semi-clathrate hydrate (Run 13) was highest among TS-I structures (Runs 12 – 15) regardless of the order of ion radii (F^-: 1.71 Å, Cl^-: 2.23 Å and Br^-: 2.35 Å).[19] This result implies that the size of the S-cage of TBAC semi-clathrate hydrate is optimum for CO_2 molecule.

5.3.5 Analysis of gas adsorption behavior with MAR model

The multiple adsorption resistance (MAR) model described in Chapter 4 was applied to results in this work. For semi-clathrate hydrates, three resistances for gas adsorption are (i) the semi-clathrate hydrate framework, (ii) the anion of the TBA salt, (iii) the guest included cage and (iv) the gas adsorbed shell in Chapter 4, in addition, one resistance is (iv) the anion of the TBA salt. The MAR model has the assumptions for the three boundaries of differential gas adsorption. In

boundaries 1 and 2 (B1 and B2), gas molecules adsorb in a delocalized state near the surface of the semi-clathrate hydrate particle in which pores exist. Boundary 2 (B2) is a domain with no access to the pores in the delocalized state. Boundary 3 (B3) is an inner core of semi-clathrate hydrate particle for which the shrinking of the non-included gas solid core was assumed to be the rate-limiting step. Gas adsorption in semi-clathrate hydrate particles in boundaries B1 and B2 were assumed to proceed according to a gas molar concentration in the bulk phase, $C_{\text{gas, bulk}}$ driving force and one gas molecular inclusion in the S-cage without regard to occupancy by H_2O molecules. The gas adsorption rate in each boundary was expressed as Eq. (5-15) – (5-19).

$$\left(\frac{dn_{\text{gas, B1}}}{dt}\right)_{\text{p}} = \left(V_{\text{B1}}\right)_{\text{p}} \left(1 - \frac{\theta_{\text{S, B1}}}{\theta_{\text{S, eq}}}\right) K_{\text{a}} C_{\text{gas, bulk}} \tag{5-15}$$

$$\left(\frac{dn_{\text{gas, B2}}}{dt}\right)_{\text{p}} = \left(V_{\text{B2}}\right)_{\text{p}} \left(1 - \frac{\theta_{\text{S, B2}}}{\theta_{\text{S, eq}}}\right) K_{\text{a}} N_{\text{GCC}} C_{\text{gas, bulk}} \tag{5-16}$$

$$V_{\text{B1}} + V_{\text{B2}} = \frac{4}{3}\pi\left(r_{\text{p}}^3 - \left(r_{\text{p}} - L\right)^3\right) \tag{5-17}$$

where V_{B1}, V_{B2}, K_{a}, and L are the volume of boundary 1 and 2, the gas adsorption rate constant in the delocalized adsorbed shell, the thickness of the delocalized adsorbed shell and the number of gas capture cavities (S-cage), respectively. The $N_{\text{GCC}}\left(= N_{\text{S}} \big/ N_{\text{ideal, H}_2\text{O}}\right)$ in Eq.(5-16) is defined as number of S-cage of the unit cell, N_{S}, per number of ideal host molecules of the unit cell $N_{\text{ideal, H}_2\text{O}}$.[22] The gas adsorption rate in boundary B3 was assumed to proceed according to the molar concentration of gas in the solid particle expressed as:

$$\left(\frac{dn_{\text{gas, B3}}}{dt}\right)_{\text{p}} = \frac{4\pi r_{\text{c}}^2 \left(1-\frac{\theta_{\text{S, B3}}}{\theta_{\text{S, eq}}}\right)^{\frac{2}{3}} \theta_{\text{S, eq}} k_{\text{c}} C_{\text{gas, core}}}{1+\left(1-\frac{\theta_{\text{S, B3}}}{\theta_{\text{S, eq}}}\right)^{\frac{2}{3}} \frac{\theta_{\text{S, eq}} k_{\text{c}} r_{\text{c}}}{\left(1-\theta_{\text{S, eq}}\right) D_{\text{a}}} \left(1-\frac{r_{\text{c}}}{r_{\text{B3}}}\right)} \tag{5-18}$$

$$C_{\text{gas, core}} = \frac{N_{\text{S}} \theta_{\text{S, eq}}}{N_{\text{A}} \left(a \times b \times c\right)} \tag{5-19}$$

The r_{p}, r_{B3} and r_{c} are the radius of particle, boundary 3 and gas non-included solid core in boundary 3, respectively and the k_{c} is the inclusion rate constant on interface of gas non-included solid core, and D_{a} is the apparent diffusion coefficient. The $C_{\text{gas, core}}$ is the gas molar concentration at interface between the delocalized gas-adsorbed outer shell and the localized gas-adsorbed inner core. Fitting parameters in this model are L, K_{a}, k_{c} and D_{a}. Figure 5-5 shows the relationship between a schematic diagram of the MAR model and fitting parameters. The model was correlated with the experimental data in such a way that average deviation (AD) was minimized as:

$$\text{AD} = \frac{10^6}{N_{\text{data}}} \sum_i \left| n_{\text{gas, exp}}\left(i\right) - n_{\text{gas, calc}}\left(i\right) \right| \tag{5-20}$$

where N_{data} is the number of data points.

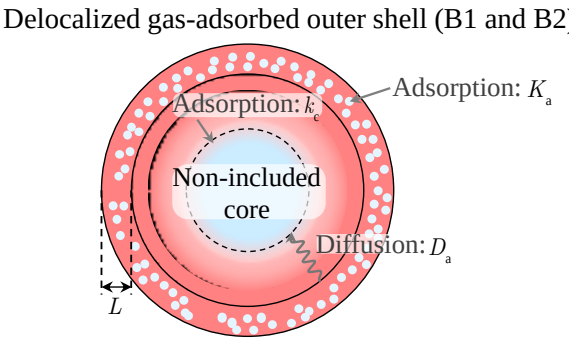

Figure 5-5. Schematic diagram of the multiple adsorption resistance (MAR) model and its fitting parameters. L: thickness of the delocalized adsorbed shell, K_a: gas adsorption rate constant in the delocalized gas-adsorbed shell, k_c: inclusion rate constant on interface of gas non-included solid core and D_a: apparent diffusion coefficient. Blue area, the non-included gas solid; red area, gas-included solid.

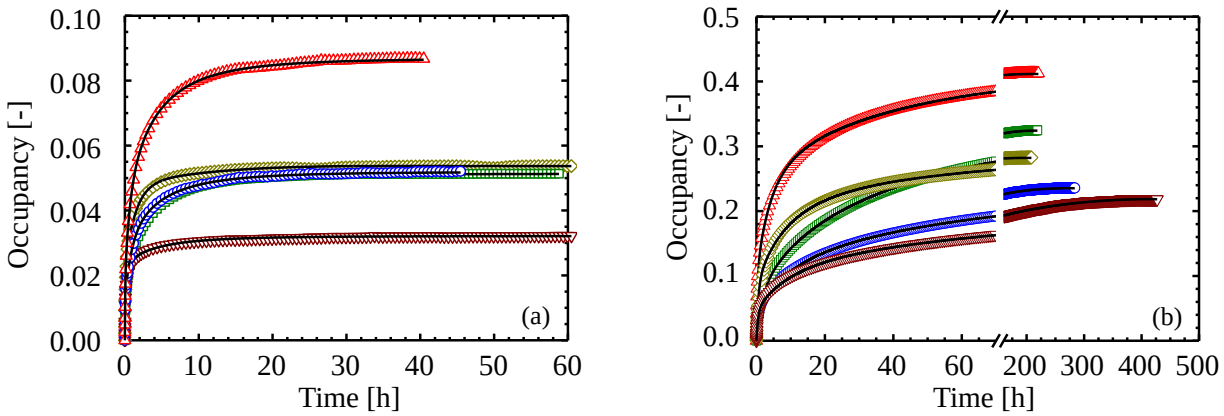

Figure 5-6. Correlation results of H_2 or CO_2 occupancy as a function of time in S-cages of the semi-clathrate hydrates at 269 K with multiple adsorption resistant (MAR) model. (a): H_2 adsorption systems (d_p = 250 – 355 μm, $P_{initial}$ = 4.0 MPa). (b): CO_2 adsorption systems (d_p = 106 – 150 μm, $P_{initial}$ = 0.8 MPa). Continuous lines are correlation results. Symbols show tetra-*n*-butyl ammonium (TBA) salt and structure of semi-clathrate hydrate. Symbols: red up-pointing triangles, 2.6 mol% TBAB (HS-I); blue circles, 3.7 mol% TBAB (TS-I); green squares, 3.2 mol% TBAC (TS-I); olive diamonds, 3.0 mol% TBAF (TS-I); brown down-pointing triangles, 3.3 mol% TBAF (SCS-I).

Table 5-4. Correlation results of gas adsorption rates for semi-clathrate hydrate particles.

Run	Gas	TBA salt	Conc. [mol%]	ΔT [K]	L [μm]	K_a [$\times 10^{-4}$ s^{-1}]	k_c [$\times 10^{-9}$ ms^{-1}]	D_a [$\times 10^{-13}$ m^2s^{-1}]	ARD %
1	H_2	TBAB	2.6	9	28.2	9.116	34.89	15.76	0.69
2			3.7	2	33.2	4.094	52.34	5.127	1.74
3		TBAC	2.6	12	38.1	14.60	285.6	12.18	6.05
4			3.0	12	42.9	7.756	104.2	19.59	3.07
5			3.2	12	20.0	7.630	87.55	1.934	2.17
6			3.7	12	27.9	5.656	145.0	6.949	7.02
8		TBAF	3.0	5	78.2	2.560	10.89	20.03	1.47
10			3.3	5	56.1	5.000	60.81	18.96	1.98
11	CO_2	TBAB	2.6	9	10.7	35.09	0.706	0.0238	1.58
12			3.7	2	5.11	6.170	1.642	0.0073	1.83
13		TBAC	3.2	12	3.70	3.445	2.313	0.0111	2.49
14		TBAF	3.0	5	11.4	10.59	1.264	0.0122	1.42
15			3.3	5	6.91	5.907	10.36	0.0034	0.95

TBAB: tetra-*n*-butyl ammonium bromide, TBAC: tetra-*n*-butyl ammonium chloride, TBAF: tetra-*n*-butyl ammonium fluoride.

ΔT: degree of supercooling, L: thickness of delocalized state, K_a: adsorption rate constant in delocalized state, k_c: inclusion rate constant on interface of gas non-included solid core, D_a: apparent diffusion coefficient, ARD: average relative deviation.

Figure 5-6 shows correlation results for H_2 and CO_2 adsorption in semi-clathrate hydrate particles with the MAR model (Table 3, H_2: runs 1, 2, 5, 8, 10, CO_2: runs 11 – 15). Table 5-4 summarizes fitting parameters and average relative deviation (ARD) of the model, where ARD is defined as:

$$\mathrm{ARD}\,\% = \frac{100}{N_{\mathrm{data}}} \sum_i \left| \frac{n_{\mathrm{gas,\,exp}}(i) - n_{\mathrm{gas,\,calc}}(i)}{n_{\mathrm{gas,\,exp}}(i)} \right| \tag{5-21}$$

As shown in Figure 5-6 and Table 5-4, the MAR model could describe the gas adsorption process for both CO_2 and H_2 well.

The L in the MAR model is the thickness of the delocalized gas-adsorbed outer shell, which is probably related to the area of the crystal grain boundary. Clathrate hydrate particles for which L is large have many cracks and pores. In the TS-I structure, the L values were in order of (largest to smallest) TBAF, TBAB and TBAC, and thus this implies that the area of the crystal grain boundary was in order of (largest to smallest) TBAF, TBAB and TBAC. The adsorption rate constants K_a for the CO_2 systems (3.4 – 35 $\times 10^{-4}$ s^{-1}) had the trend of being larger than those for the H_2 systems (2.6 – 9.1 $\times 10^{-4}$ s^{-1}), which implies that the stable gas in the S-cage is rapidly adsorbed from vapor phase. In contrast, the inclusion rate constant k_c for H_2 systems (11 – 88 $\times 10^{-9}$ $m \cdot s^{-1}$) were larger than those for CO_2 systems (0.7 – 10 $\times 10^{-9}$ $m \cdot s^{-1}$). On the interface of the non-included gas solid core, the gas is included from the gas included shell. Thus, the stable gas in the S-cage probably transfers with difficulty from the gas included shell. In the gas included shell, a gas molecule diffuses through an empty S-cage or grain boundary. The diffusion coefficients D_a for H_2 systems (1.9 – 21 $\times 10^{-13}$ $m^2 \cdot s^{-1}$) were larger than those for CO_2 systems (0.3 – 2.4 $\times 10^{-15}$ $m^2 \cdot s^{-1}$) as should be expected, because the molecular size of CO_2 is much larger than that of H_2. The MAR model provides trends in accordance with general physics.

Table 5-5 summarizes the effect of TBA salt and structure on fitting parameters (K_a, k_c and D_a). In H_2 systems, the K_a, k_c for TS-I structure were in order of (largest to smallest) TBAC, TBAB and TBAF (run 5, 2 and 8) in Table 5-4, which corresponds to descending order of the lattice constant or S-cage size (TBAC, TBAB and TBAF) in Table 5-1. This dependence for the S-cage

size was observed for H_2-additive binary clathrate hydrates[21] and means that H_2 molecules were included in the S-cage of semi-clathrate hydrates without translation of water molecules as for H_2-additive binary clathrate hydrates.[21] The cause of this is thought to be that H_2 adsorption is difficult to be inhibited by the QAS anion due to the small molecular size of H_2. The D_a for TS-I structures were in order of (largest to smallest) TBAF, TBAB and TBAC in Table 5-4, which corresponds to ascending order of the area of the crystal grain boundary inferred from the relative values of L. Thus H_2 molecules probably diffuse through the grain boundaries of semi-clathrate hydrate particles.

In CO_2 systems, the k_c for TS-I structure were in order of (largest to smallest) TBAC, TBAB and TBAF (Table 5-4, runs 12 – 14) and these had similar trends for k_c in H_2 systems (Table 5-4, runs 2, 5 and 8). However, the K_a for TS-I structure were in order of (largest to smallest) TBAF, TBAB and TBAC in contrast to H_2 systems, which corresponds to ascending order of the area of the crystal grain boundary. Thus, the K_a in CO_2 systems were strongly influenced by the diffusivity of CO_2. The D_a for TS-I structure were in order of (largest to smallest) TBAF, TBAC and TBAB, which corresponds to ascending order of the ionic radii of the anions. This result implies that the diffusion of CO_2 molecules was physically inhibited by the anion, and that the relationship between the size of the gas molecule, the anion and the S-cage is important for this inhibition effect.

Table 5-5. Effect of tetra-*n*-butyl ammonium (TBA) salts and clathrate structures on fitting parameters.

Parameter	Order	Involved properties	Relationship
	H_2 systems		
K_a	TBAC > TBAB > TBAF	S-cage size	P
	HS-I > TS-I < SCS-I	Distortion of hydrate cage	P
k_c	TBAC > TBAB > TBAF	S-cage size	P
	SCS-I > TS-I > HS-I	Number density of S-cage	P
D_a	TBAF > TBAB > TBAC	Area of crystal grain boundary	P
	HS-I > TS-I > SCS-I	Number density of S-cage	P
	CO_2 systems		
K_a	TBAF > TBAB > TBAC	Area of crystal grain boundary	P
	HS-I > TS-I > SCS-I	Area of crystal grain boundary	P
k_c	TBAC > TBAB > TBAF	S-cage size	P
	SCS-I > TS-I > HS-I	Number density of S-cage	InvP
D_a	TBAF > TBAC > TBAB	Ionic radius of anion	InvP
	HS-I > TS-I > SCS-I	Number density of S-cage	P
		Number density of anion	InvP

K_a: adsorption rate constant in delocalized state, k_c: inclusion rate constant on interface of gas non-included solid core, D_a: apparent diffusion coefficient, P : proportional, InvP: inversely proportional. HS-I: hexagonal structure-I, TS-I: tetragonal structure-I, SCS-I: superlattice of cubic structure-I.

The effect of semi-clathrate hydrate structure on K_a, k_c and D_a is best discussed for a given TBA salt semi-clathrate hydrate. Specifically, TS-I structures are compared with HS-I structures for TBAB systems, and TS-I structures are compared with SCS-I structures for TBAF systems. However HS-I structures cannot be compared directly with the SCS-I structures due to the lack of the common TBA salt semi-clathrate hydrate. In H_2 systems, K_a for the TS-I structure were larger than those values for the HS-I structure (Table 5-4, runs 1 and 2) and for the

SCS-I structure (Table 5-4, runs 8 and 10). It is probable that lattice defects of the semi-clathrate hydrate HS-I and SCS-I structures were larger than those for the TS-I structure. For the HS-I structure, other crystals such as ice probably formed in the formation process. Water molecules in the HS-I structure are affected by that of ice, so that lattice defects in the HS-I structure probably occur. For the SCS-I structure, the number of anions as host molecules seems to be related to the distortion of the hydrate cages. The lattice defect of semi-clathrate hydrate cages are probably distorted by the ionic size and attracted H_2O molecules to the anion as host molecule. The number of the anions as host molecules for the SCS-I structure was largest among those structures (Table 5-1). Thus, the distortion of the hydrate cage for the SCS-I structure was probably larger than that for the TS-I structure. The k_c for each structure were in order of (largest to smallest) SCS-I, TS-I and HS-I, which corresponds to ascending order for the number of S-cages per ideal number of water molecules of the unit cell (Table 5-1). On the other hand, the D_a for each structure were in order of (largest to smallest) HS-I, TS-I and SCS-I, which corresponds to descending order for the number of S-cages per ideal number of water molecules of unit cell (Table 5-1). The relationship between the k_c, the D_a and the number density of S-cages of the semi-clathrate hydrates exhibited similar dependencies with occupancy of the S-cage as that observed for H_2-THF clathrate hydrates.[23] Therefore, it can be implied that the H_2 adsorption rate is faster as the number density of sorbable sites decreases.

In CO_2 systems, the K_a for each structure were in order of (largest to smallest) HS-I, TS-I and SCS-I, which corresponds to descending order of the L parameter that is related to the area of the crystal grain boundary (Table 5-4, runs 11, 12, 14 and 15) as well as the anions (Table 5-4, runs

12 – 14). The k_c for each structure were in order of (largest to smallest) SCS-I, TS-I and HS-I, and the D_a for each structure were in order of (largest to smallest) HS-I, TS-I and SCS-I as with H_2 systems. Therefore, the relationship between CO_2 adsorption or diffusion rate and the number density of sorbable sites are the same as that for H_2 systems. In CO_2 systems, the descending order of the D_a for each structure corresponds to the ascending order of the number density of the anions in semi-clathrate hydrates, because the diffusion of CO_2 molecules is inhibited by the anion as a host molecule.

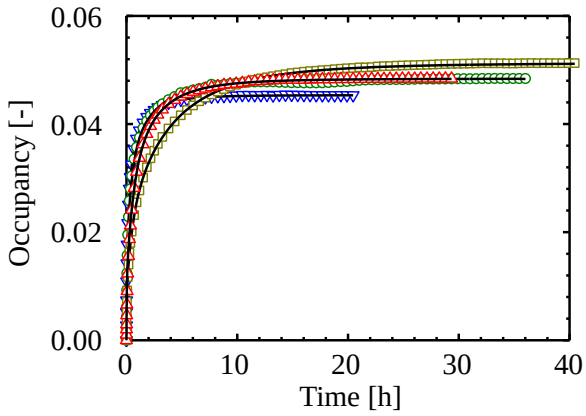

Figure 5-7. Correlation of H_2 adsorption rates in tetra-*n*-butyl ammonium chloride (TBAC) semi-clathrate hydrate particles with multiple adsorption resistant (MAR) model (d_p = 250 – 355 μm, T = 269 K, $P_{initial}$ = 4.0 MPa). Symbols show TBAC concentration. Symbols: red up-pointing triangles, 3.7 mol% (Run 11); olive squares, 3.2 mol% (Run 7); green circles, 3.0 mol% (Run 2); blue down-pointing triangles, 2.6 mol% (Run 10).

Figure 5-7 shows correlation results for H_2 adsorption for each concentration of TBAC semi-clathrate hydrate particles with MAR model (Run 3 – 6). Table 5-4 summarizes fitting parameters and average relative deviations (ARD) for H_2 adsorption. The K_a for each TBAC concentration were in order of (largest to smallest) 2.6, 3.0, 3.2 and 3.7 mol%, which implies that the non-included TBAC inhibited H_2 adsorption and diffusion. The k_c for each TBAC concentration were in order of (largest to smallest) 2.6, 3.7, 3.0 and 3.2 mol%, which implies that

ice was present and that TBAC deformed the S-cages in the TS-I structure, assuming that the k_c is related to the distortion of the S-cage as well as the structure dependence of the k_c in H_2 systems. The D_a for each TBAC concentration were in order of (largest to smallest) 3.0, 2.6, 3.7 and 3.2 mol%, which corresponds to the descending order of the L as well as the anion dependency of D_a and L for TS-I structure in H_2 systems. This implies that the ice and the non-included TBAC increased the area of the crystal grain boundary, but also that the ice and the non-included TBAC caused large resistance to H_2 diffusion.

5.3.6 Measurement and simulation of H_2/CO_2 selectivity of hydrate particles

Mixture gas (H_2 and CO_2) adsorption behavior was simulated by using the correlated values from the gas adsorption measurements with MAR model to estimate H_2/CO_2 selectivities. The conditions of the simulation were assumed to be those of the experimental conditions as summarized in Table 5-2 (runs 16 – 20). The Langmuir constant and the parameters for MAR model in Tables 5-3 and 5-4 were used (runs 1, 2, 5, 8, and 10 – 15). The parameter L is the semi-clathrate hydrate particle property, thus the L values used for mixture gas adsorption simulation were same as those used at CO_2 adsorption experiments because particle diameter for mixture gas adsorption experiment was the same as that in the CO_2 adsorption experiments.

Figure 5-8 shows experimental and calculated H_2/CO_2 selectivities for TBA salt semi-clathrate hydrates with results being summarized in Table 5-6. In the simulation results (Table 5-6), the equilibrium H_2/CO_2 selectivities S_{H_2/CO_2} for the semi-clathrate hydrates were in order of (largest to smallest) 3.2 mol% TBAC, 2.6 mol% TBAB, 3.0 mol% TBAF semi-clathrate hydrate, 3.3 mol%

TBAF and 3.7 mol% TBAB. The H_2/CO_2 selectivity for 3.2 mol% TBAC semi-clathrate hydrate was highest among the semi-clathrate hydrates. The S_{H_2/CO_2} in each semi-clathrate hydrate were higher than the S_{H_2/CO_2} by gas clathrate hydrate formation without additive guest molecules (T = 273 K, $P_{initial}$ = 3.8 MPa, n_{H2}/n_{CO2} = 1.6).[24]

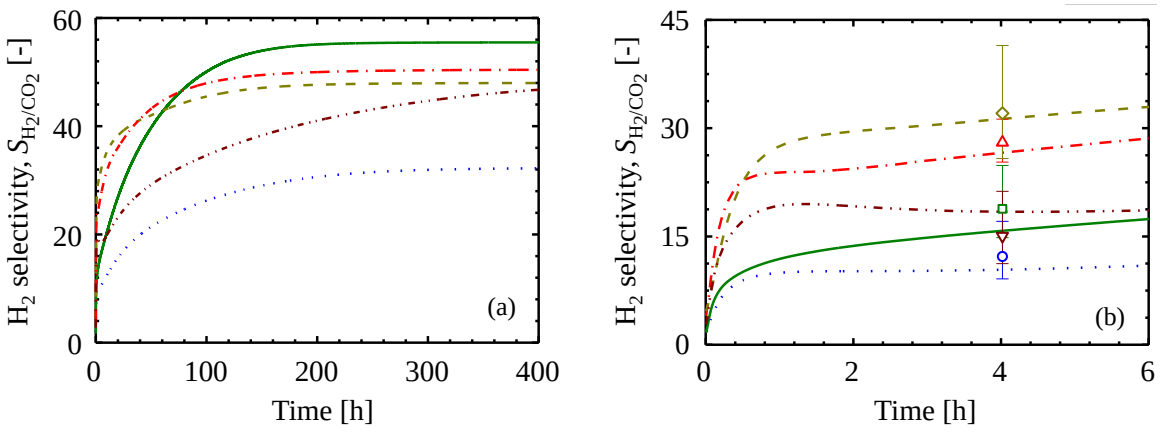

Figure 5-8. H_2 selectivity for CO_2 as a function of time for semi-clathrate hydrate particles (d_p = 128 μm, T = 269 K, $P_{initial}$ (H_2/CO_2 = 3.4) = 4.5 MPa). (a): long time-scale and (b): short time-scale. Lines show the simulation results with the multiple adsorption resistance (MAR) model. Symbols show tetra-*n*-butyl ammonium (TBA) salt and structure of semi-clathrate hydrate. Symbols: red up-pointing triangle (dashed-dotted line), 2.6 mol% TBAB (HS-I); blue circle (dotted line), 3.7 mol% TBAB (TS-I); green square (continuous line), 3.2 mol% TBAC (TS-I); olive diamond (dashed line), 3.0 mol% TBAF (TS-I); brown down-pointing triangle (dashed-two dotted line), 3.3 mol% TBAF (SCS-I). Langmuir constants and fitting parameters of MAR model for each gas and semi-clathrate hydrate are given in Tables 5-4 and 5-5.

The rate of increase in the S_{H_2/CO_2} at the early stages of adsorption were in order of (largest to smallest) 3.0 mol% TBAF, 2.6 mol%, 3.3 mol% TBAF, 3.2 mol% TBAC and 3.7 mol% TBAB semi-clathrate hydrate according to the simulation. In the experimental results (Table 5-6), the H_2/CO_2 selectivities S_{H_2/CO_2} for the semi-clathrate hydrates at 4 h were in order of (largest to smallest) 3.0 mol% TBAF (run 19), 2.6 mol% TBAB (run 16), 3.2 mol% TBAC semi-clathrate

hydrate (run 18), 3.3 mol% TBAF (run 20) and 3.7 mol% TBAB (run 17). The S_{H_2/CO_2} of the simulation results were close to those of the experimental results as shown in Figure 5-8 and Table 5-6. Therefore, 3.0 mol% TBAF semi-clathrate hydrate is considered to be applicable as separation media for H_2/CO_2 systems in pressure swing adsorption (PSA) processes. Because the cycle time of the gas adsorption and desorption is generally on the order of minutes, high selectivity at short contact times is required. In this section, the structure of semi-clathrate hydrates as separation media is unified as much as possible. However, the gas adsorption rate increases with increasing area of crystal grain boundaries so that by mixing other crystals, such as TBAC semi-clathrate hydrates it may be possible to create more favorable systems (Figure 5-7). The gas selectivity and adsorption rate of semi-clathrate hydrates can possibly be improved by combining semi-clathrate hydrates with additive salts and considering the structures.

Table 5-6. H_2/CO_2 selectivity semi-clathrate hydrates obtained from experiment and by simulation with the multiple adsorption resistance (MAR) model.

Run	TBA salt semi-clathrate	Time [h]	H_2/CO_2 selectivity, $S_{H2/CO2}$ [-]	
			Experiment	Simulation
16	2.6 mol% TBAB	4	28.0	26.8
		400		50.4
17	3.7 mol% TBAB	4	12.2	10.4
		400		32.2
18	3.2 mol% TBAC	4	18.8	15.9
		400		55.5
19	3.0 mol% TBAF	4	32.1	31.4
		400		48.0
20	3.3 mol% TBAF	4	15.1	18.4
		400		46.8

TBAB : tetra-*n*-butyl ammonium bromide, TBAC: tetra-*n*-butyl ammonium chloride, TBAF: tetra-*n*-butyl ammonium fluoride.

5.3.7 Simulation of H_2/CO_2 selectivity with hydrate membrane

Theoretical selectivity with polymeric membranes to separate a gas mixture can be calculated from the solubility and diffusivity of the species.[25] The theoretical selectivity α_{H_2/CO_2} with hydrate membranes is calculated from Eq. (5-22) as:

$$\alpha_{H_2/CO_2} = \frac{p_{H_2}}{p_{CO_2}} = \frac{C_{H_2,S}}{C_{CO_2,S}} \frac{D_{H_2}}{D_{CO_2}} \tag{5-22}$$

where p is the species permeability. However, the apparent diffusion coefficient depends on occupancy,[23] which means that the diffusion coefficient depends on the partial pressure of the gas, P_{gas}. Thus, the gas permeability is calculated from Eqs. (5-23) – (5-26) with Langmuir constants and apparent diffusion coefficients as:

$$p_{gas} = \frac{d_m F_{gas}}{A_m \left(P_{gas,inlet} - P_{gas,outlet} \right)} \tag{5-23}$$

$$F_{gas} = D_{e,gas} A_m \frac{R T_0}{P_0} \frac{\left(C_{gas,m,inlet} - C_{gas,m,outlet} \right)}{d_m} \tag{5-24}$$

$$D_{e,gas} = \left(1 - \theta_{S,gas} \right) D_{a,gas} \tag{5-25}$$

$$C_{gas,m,inlet} = \frac{N_S}{N_A V_{unit\ cell}} \left(\frac{C_{gas,S} f_{gas,inlet}}{1 + C_{H_2,S} f_{H_2,inlet} + C_{CO_2,S} f_{CO_2,inlet}} \right) \tag{5-26}$$

where A_m, d_m, F, $C_{gas,m,inlet}$, θ_S and $C_{gas,S}$ are the membrane area, membrane thickness, gas permeate flow rate, supply side gas concentration, S-cage occupancy and Langmuir constant for the gas in the S-cage, respectively. The effective diffusion coefficient, $D_{e,gas}$ in Eq.(5-25) is related to the apparent diffusion coefficient, $D_{a,gas}$ by the occupancy in the S-cage. Figure 5-9 shows the

pressure dependence of H_2 and CO_2 permeability.

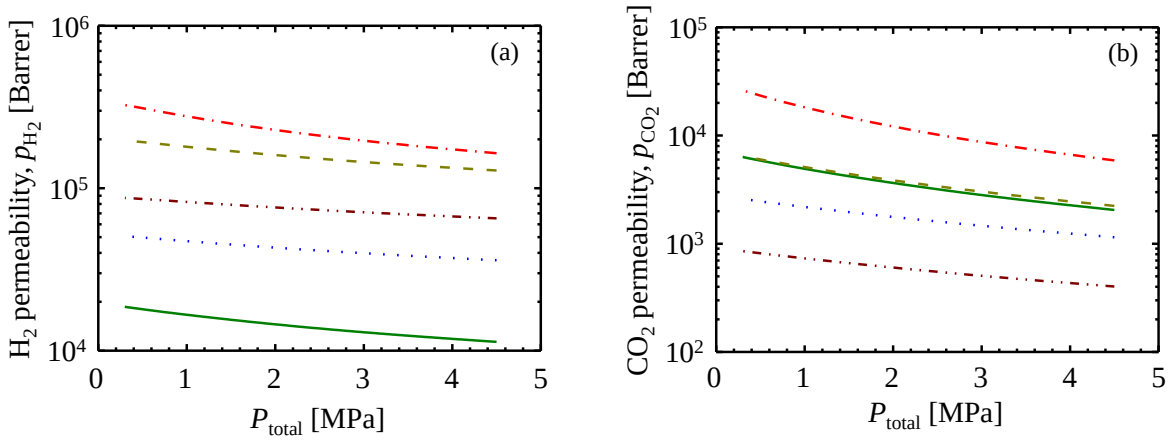

Figure 5-9. Effect of pressure on gas permeability for semi-clathrate hydrate membrane at 269 K and initial H_2/CO_2 = 3.4. (a): H_2 permeability and (b) CO_2 permeability. Lines show tetra-*n*-butyl ammonium (TBA) salt and crystal structure of semi-clathrate hydrate. Lines: red dashed-dotted line, 2.6 mol% TBAB (HS-I); blue dotted line, 3.7 mol% TBAB (TS-I); green continuous line, 3.2 mol% TBAC (TS-I); olive dashed line, 3.0 mol% TBAF (TS-I); brown dashed-two dotted line, 3.3 mol% TBAF (SCS-I).

As the total pressure increases, the H_2 and CO_2 permeability decreases for all semi-clathrate hydrates. As the gas partial pressure increases, the adsorption amount of the gas increases. However, as the occupancy of the gas increases, the effective diffusion coefficient decreases as Eq.(5-25). Therefore, this trend is due to the decrease in the ratio of gas diffusion rate being larger than the increase in the ratio of the gas adsorption amount. Figure 5-10 shows the pressure dependence of H_2/CO_2 selectivity versus H_2 permeability. As the H_2 permeability increases, H_2/CO_2 selectivity decreases for all semi-clathrate hydrates. This reason for this is thought to be due to the decreasing ratio of CO_2 permeability for partial pressures larger than that of H_2

permeability (Figure 5-9) because the CO_2 occupancy of the S-cage is larger than the H_2 occupancy of the S-cage. This trend is different from the separation characteristics of materials such as polymeric membranes.[25] For semi-clathrate hydrate membranes, as pressure increases, H_2/CO_2 selectivity increases. The SCS-I structure TBAF semi-clathrate hydrate seems to be most favorable for use as a hydrate membrane among the semi-clathrate hydrates since it can be used at conditions close to ambient temperature. Therefore, it is probable that gas selectivity of semi-clathrate hydrates can be made high for QAS that lower the permeability of large size molecules or by control of the clathrate structure. Based on the above results, the semi-clathrate hydrates examined in this work are favorable for applications in membrane separation due to their high selectivity and mild operating conditions. Further research is needed on membrane support materials for semi-clathrate hydrates and on conditions for semi-clathrate hydrate thin film formation.

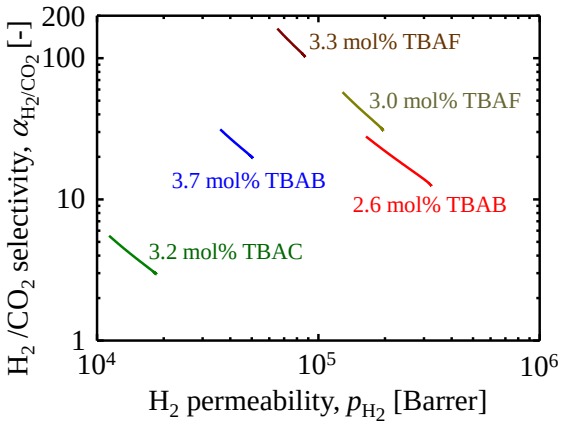

Figure 5-10. Relationship between H_2 permeability and H_2/CO_2 selectivity at 269 K and initial H_2/CO_2 = 3.4. Lines show tetra-*n*-butyl ammonium (TBA) salt and structure of semi-clathrate hydrate. Lines: red, 2.6 mol% TBAB (HS-I); blue, 3.7 mol% TBAB (TS-I); green, 3.2 mol% TBAC (TS-I); olive, 3.0 mol% TBAF (TS-I); brown, 3.3 mol% TBAF (SCS-I).

5.4 Conclusions

In this chapter, the formation tetra-*n*-butyl ammonium (TBA) salt semi-clathrate hydrate particles were analyzed by differential scanning calorimetry, Raman spectroscopy and by consideration of the equilibrium H_2 storage amounts for understanding of the role of quaternary ammonium salt (QAS) in semi-clathrate hydrate. The TBA salts used were tetra-*n*-butyl ammonium bromide (TBAB), tetra-*n*-butyl ammonium chloride (TBAC) and tetra-n-butyl ammonium fluoride (TBAF). TBAC semi-clathrate hydrate formed TS-I structure regardless of TBAC concentration, and 3.2 mol% TBAC semi-clathrate hydrate formed without forming ice. TBAF semi-clathrate hydrate formed TS-I structure for 3.0 mol% TBAF and SCS-I structure for 3.3 mol% TBAF at small degrees of supercooling.

The H_2 or CO_2 adsorption rates with the semi-clathrate hydrate particles were measured with a pressure decay method. The time for half of the equilibrium consumption, t_{half}, strongly depended on the anion of TBA salt for H_2 systems, whereas H_2 adsorption was not a strong function of the semi-clathrate hydrate structure. The t_{half} in CO_2 systems depended not only on the anion of the TBA salt, but also on the semi-clathrate hydrate structure, and this is attributed to the size of the CO_2 molecule. The equilibrium H_2 occupancy in the S-cage $\theta_{\mathrm{S,\,H_2,\,eq}}$ strongly depended on the semi-clathrate hydrate structure rather than on the anion of the TBA salt, which might also be affected by some S-cages being occupied by H_2O molecules. The equilibrium CO_2 occupancy in S-cage $\theta_{\mathrm{S,\,CO_2,\,eq}}$ depended not only on the semi-clathrate structure but also on the TBA salt for TS-I structure. The size of S-cage of TBAC semi-clathrate hydrate is optimum for CO_2 molecule because the $\theta_{\mathrm{S,\,CO_2,\,eq}}$ for TBAC semi-clathrate hydrate was highest among TS-I structures.

From the analysis results made with the multiple adsorption resistance (MAR) model in this chapter, it is implied that the gas in the S-cage is rapidly adsorbed from the vapor phase, since the adsorption rate constants K_a of H_2 were larger than those of CO_2 for the same semi-clathrate hydrate systems. On the other hand, the gas in the S-cage transfers with difficulty in the more stable hydrate phase as can be concluded from the simulation results. Namely, the inclusion rate constants k_c and the apparent diffusion coefficients D_a for H_2 systems were larger than those for CO_2 systems. The adsorption and diffusion rate for both H_2 and CO_2 systems were proportional to crystal grain boundary and the number density of S-cages. The reason for this is that gas molecules could probably penetrate into the inside of the particles and increase the diffusion pathway. The k_c increased for both H_2 and CO_2 systems with increasing the number density of S-cages. In contrast, the D_a for both H_2 and CO_2 systems decreased with increasing the number density of S-cages. Therefore, the gas adsorption rate became faster as the number density of sorbable sites decreased, and the gas diffusion rate became faster as the number density of sorbable site increased. In addition, the D_a for CO_2 systems decreased with increasing the number density of the anions. This means that the diffusion of CO_2 molecules is inhibited by anion as host molecule.

The H_2/CO_2 selectivities S_{H_2/CO_2} for TBA salt semi-clathrate hydrates were obtained from MAR model simulations with Langmuir constants obtained from experiments. In the simulation results, the S_{H_2/CO_2} for 3.2 mol% TBAC semi-clathrate hydrate was highest among TBA salt semi-clathrate hydrates. On the other hand, the S_{H_2/CO_2} for 3.0 mol% TBAF semi-clathrate hydrate in the early stages of gas adsorption was the highest among TBA salt semi-clathrate

hydrates. Therefore 3.0 mol% TBAF semi-clathrate hydrate is considered to be appropriate as separation media for H_2/CO_2 systems in pressure swing adsorption processes among the semi-clathrate hydrate systems studied in this paper. The H_2/CO_2 selectivities for semi-clathrate hydrates can probably be improved by using additive salts to control the structure.

The H_2/CO_2 selectivities α_{H_2/CO_2} for TBA salt semi-clathrate hydrates were calculated from Langmuir constants and apparent diffusion coefficients. The α_{H_2/CO_2} for 3.3 mol% TBAF semi-clathrate hydrate was highest among TBA salt semi-clathrate hydrates, which was more than 100. Thus, the applicability of semi-clathrate hydrates as membrane separation media is confirmed. For semi-clathrate hydrates, the α_{H_2/CO_2} increased with decreasing gas permeability. Therefore, the characteristics required for semi-clathrate hydrate membranes are different from semi-clathrate hydrate particles that might be used for a pressure swing adsorption process. In either separation process, however, the adsorption and diffusion characteristics of the larger molecules can be controlled by choice of the QAS and the use of conditions to form appropriate semi-clathrate hydrate structures.

5.5 Nomenclature

A_{GC}	=	peak area of gas chromatography (GC)	[-]
A^*_{GC}	=	peak area given by GC analysis for the pure gas	[-]
A_m	=	membrane area	[m^2]
AD	=	average deviation	[mol]
ARD	=	average relative deviation	[%]
a, b, c	=	lattice constants	[Å]

C_{gas}	=	gas concentration	[mol/m^3]
C_S	=	Langmuir constant of S-cage	[Pa^{-1}]
C_S^*	=	actual Langmuir constant of S-cage	[Pa^{-1}]
D_a	=	apparent diffusion coefficient	[m^2/s]
D_e	=	effective diffusion coefficient	[m^2/s]
d_m	=	membrane thickness	[m]
F	=	gas permeate flow rate	[m^3(STP)/s]
f	=	fugacity	[Pa]
K_a	=	adsorption rate constant in delocalized state	[s^{-1}]
k_c	=	inclusion rate constant on interface of H_2 non-included solid core	[m/s]
L	=	thickness of delocalized gas-adsorbed outer shell	[m]
M	=	molecular weight	[g/mol]
N	=	number	[-]
N_A	=	Avogadro constant	[mol^{-1}]
$N^*_{H_2O}$	=	theoretical number of water molecules per unit cell	[-]
N_{ideal,H_2O}	=	number of water molecules per unit cell of structure non-replaced H_2O	[-]
N_{Occ,H_2O}	=	number of occupied water molecules in S-cage per unit cell	[-]
n	=	mole number	[mol]
p	=	permeability [m^3(STP)m/(m^2·s·Pa)] ×1.33×10^{17}	[Barrer]
r	=	radius	[m]
S_{H_2/CO_2}	=	equilibrium H_2/CO_2 selectivity for semi-clathrate hydrate particles	[-]
t	=	time	[h]
V	=	volume	[m^3]
X	=	storage amount with respect to the hydrates	[mmol$_{\text{-gas}}$/mol$_{\text{-H}_2\text{O+TBA salt}}$]
y	=	composition in vapor phase	[-]

Greek letters

α_{H_2/CO_2}	=	H_2/CO_2 selectivity for semi-clathrate hydrate membrane	[-]
ΔT	=	degree of supercooling	[K]
ε	=	porosity	[-]
θ_S	=	occupancy in S-cage	[-]
θ_S^*	=	occupancy in S-cage non-occupied with H_2O	[-]
ρ	=	density	[g/m^3]

Subscripts

B	=	Boundary
bulk	=	bulk phase
CO_2	=	carbon dioxide
c	=	interface of non-included solid core
calc	=	calculation
cell	=	hydrate formation cell
core	=	interface between delocalized gas-adsorbed outer shell and localized gas-adsorbed inner core
data	=	data point
eq	=	equilibrium state
exp	=	experiment
Gas	=	gas molecule
GCC	=	gas capture cavity
gb	=	grain boundary
H_2	=	hydrogen
H_2O	=	water
Hyd	=	hydrate phase
half	=	half of the equilibrium occupancy for gas molecule
inlet	=	supply side
load	=	loading
m	=	membrane
other	=	other guest molecule

outlet = permeation side

p = particle

R, initial = before loading of reservoir tank

R, final = after loading of reservoir tank

S = S-cage

TBAB = tetra-*n*-butyl ammonium bromide

TBAC = tetra-*n*-butyl ammonium chloride

TBAF = tetra-*n*-butyl ammonium fluoride

TBA salt = tetra-*n*-butyl ammonium salt

Theor Hyd = theoretical hydrate

vapor = vapor phase

leak = leak of gas molecule

5.6 References

1. Shimada W, Shiro M, Kondo H, Takeya S, Oyama H, Ebinuma T, Narita H. Tetra-*n*-butylammonium bromide-water (1/38). Acta Crystallogr C. 2005;61:O65-O66.
2. Davidson DW. *Water - A Comprehensive Treatise*. Vol 2.Plenum Press; New York. 1973.
3. Rodionova T, Komarov V, Villevald G, Aladko L, Karpova T, Manakov A. Calorimetric and structural studies of tetrabutylammonium chloride ionic clathrate hydrates. J Phys Chem B. 2010;114:11838-11846.
4. Dyadin YA, Terekhova IS, Polyanskaya TM, Aladko LS. Clathrate hydrates of tetrabutylammonium fluoride and oxalate. J Struct Chem. 1976;17:566-571.
5. Komarov VY, Rodionova TV, Terekhova IS, Kuratieva NV. The cubic superstructure-I of tetrabutylammonium fluoride $(C_4H_9)_4NF \cdot 29.7H_2O$ clathrate hydrate. J Inclusion Phenom Macro. 2007;59:11-15.
6. Sloan ED, Koh CA. *Clathrate hydrates of natural gases, 3rd Ed.*CRC Press; Boca Raton. 2007.
7. Onstot WJ, Minet RG, Tsotsis TT. Design aspects of membrane reactors for dry reforming of methane for the production of hydrogen. Ind Eng Chem Res. 2001;40:242-251.
8. NIST Chemistry WebBook. http://webbook.nist.gov/chemistry/. Accessed March, 2013.

9. Spano JO, Heck CK, Barrick PL. Liquid-vapor equilibria of hydrogen-carbon dioxide system. J Chem Eng Data. 1968;13:168-171.

10. Yorizane M, Yoshimura S, Masuoka H. Vapor liquid equilibrium at high pressure (N_2-CO_2, H_2-CO_2 system). Kagaku Kogaku. 1970;34:953 - 957.

11. Tsang CY, Streett WB. Phase equilibria in the H_2/CO_2 system at temperatures from 220 K to 290 K and pressures to 172 MPa. Chem Eng Sci. 1981;36:993-1000.

12. Bezanehtak K, Combes GB, Dehghani F, Foster NR, Tomasko DL. Vapor-liquid equilibrium for binary systems of carbon dioxide plus methanol, hydrogen plus methanol, and hydrogen plus carbon dioxide at high pressures. J Chem Eng Data. 2002;47:161-168.

13. Staykova DK, Kuhs WF, Salamatin AN, Hansen T. Formation of porous gas hydrates from ice powders: Diffraction experiments and multistage model. J Phys Chem B. 2003;107:10299-10311.

14. Oyama H, Shimada W, Ebinuma T, Kamata Y, Takeya S, Uchida T, Nagao J, Narita H. Phase diagram, latent heat, and specific heat of TBAB semiclathrate hydrate crystals. Fluid Phase Equilib. 2005;234:131-135.

15. Aladko LS, Dyadin YA. Clathrate formation in the Bu_4NCl-NH_4Cl-H_2O system. Mendeleev Commun. 1996:198-200.

16. Sakamoto J, Hashimoto S, Tsuda T, Sugahara T, Inoue Y, Ohgaki K. Thermodynamic and Raman spectroscopic studies on hydrogen + tetra-*n*-butyl ammonium fluoride semi-clathrate hydrates. Chem Eng Sci. 2008;63:5789-5794.

17. Hashimoto S, Sugahara T, Moritoki M, Sato H, Ohgaki K. Thermodynamic stability of hydrogen + tetra-*n*-butyl ammonium bromide mixed gas hydrate in nonstoichiometric aqueous solutions. Chem Eng Sci. 2008;63:1092-1097.

18. Trueba AT, Radovic IR, Zevenbergen JF, Peters CJ, Kroon MC. Kinetic measurements and in situ Raman spectroscopy study of the formation of TBAF semi-hydrates with hydrogen and carbon dioxide. Int J Hydrogen Energ. 2013;38:7326-7334.

19. Joung IS, Cheatham TE. Determination of alkali and halide monovalent ion parameters for use in explicitly solvated biomolecular simulations. J Phys Chem B. 2008;112:9020-9041.

20. Sloan ED. Fundamental principles and applications of natural gas hydrates. Nature. 2003;426:353-359.

21. Komatsu H, Ota M, Sato Y, Watanabe M, Smith RL. Multiple adsorption resistance model for constituent molecular effects of hydrogen clathration-kinetics in clathrate hydrate particles.

Chem Eng Sci. 2014;108:270-282.

22. Komatsu H, Hayasaka A, Ota M, Sato Y, Watanabe M, Smith RL. Measurement of pure hydrogen and pure carbon dioxide adsorption equilibria for THF clathrate hydrate and tetra-*n*-butyl ammonium bromide semi-clathrate hydrate. Fluid Phase Equilib. 2013;357:80-85.
23. Hashimoto S, Yamamoto K, Tsuda T, Inoue Y. Modeling on hydrogen absorption in tetrahydrofuran hydrate. J Chem Eng Jpn. 2012;45:444-451.
24. Kumar R, Linga P, Ripmeester JA, Englezos P. Two-Stage Clathrate Hydrate/Membrane Process for Precombustion Capture of Carbon Dioxide and Hydrogen. J Environ Eng-Asce. 2009;135:411-417.
25. Lin HQ, Van Wagner E, Freeman BD, Toy LG, Gupta RP. Plasticization-enhanced hydrogen purification using polymeric membranes. Science. 2006;311:639-642.

Chapter 6

Conclusions and future work

6.1 Summary and conclusions

In this thesis, the phase equilibria, the equilibrium adsorption and the adsorption rates of H_2 and CO_2 + tetra-*n*-butyl ammonium (TBA) salts semi-clathrate hydrate were measured. The TBA salts studied were TBA bromide (TBAB), TBA chloride (TBAC) and TBA fluoride (TBAF). A phase equilibrium model was modified to describe the phase equilibria of H_2 and CO_2 + TBA salt + water systems. A gas adsorption kinetics model was developed to describe the H_2 and CO_2 adsorption behavior in guest additive clathrate hydrates or TBA salt semi-clathrate hydrates. The H_2/CO_2 selectivity was estimated with experimentally determined Langmuir constants and fitted diffusion coefficients for semi-clathrate hydrate particles or membranes.

Phase equilibria of H_2 and CO_2 + TBA salt semi-clathrate hydrate (Chapter 3)

The phase quilibria of H_2 and CO_2 + TBA salt + water systems were measured. For CO_2 + TBAF semi-clathrate hydrates, dissociation temperatures vary according to TBAF concentration, in which 3.0 mol% TBAF semi-clathate hydrate was found to be more stable than 3.3 mol% semi-clathrate hydrate above 1 MPa. This finding is evidence that the crystal structure of 3.0 mol% TBAF semi-clathrate hydrate is different from that of 3.0 mol% TBAF semi-clathrate hydrate. A phase equilibrium prediction model was developed for semi-clathrate hydrates by using parameters for the QL-cage that combines $5^{12}6^2$ cage with $5^{12}6^3$ cage, and by estimating $\Delta\nu_{W}^{L}$ from the molar volume of water for TBAB semi-clathrate hydrate. The model could describe the phase equilibria of binary mixtures H_2 + TBA salt or CO_2 + TBA salt semi-clathrate hydrate + water systems quantitatively, but could only describe ternary mixture H_2 + CO_2 + TBA salt semi-clathrate hydrate equilibria qualitatively. The inclusion behavior of mixture gas is most likely different from that of pure gases and it depends on the TBA salt. Although the TBAF semi-clathrate hydrate can be readily applied because its high dissociation temperature (*ca*. 301 K), its selectivity for 3.0 mol% TBAF is probably low at temperatures close to its dissociation temperature.

Development of H_2 adsorption kinetic model (Chapter 4)

The multiple adsorption resistance (MAR) model model was constructed by assuming three boundaries of differential H_2 adsorption system. The three resistances in the MAR model for H_2 adsorption are the clathrate hydrate framework, the guest included cage and the H_2 adsorbed shell. In boundary 1 and 2, H_2 molecules adsorb in a delocalized state near the surface of the clathrate

hydrate particles due to existence of pores. Especially, H_2 molecules are included in the gas capture cage (S-cage) near pores in boundary 1, H_2 molecules are included in S-cages distant from the pores in boundary 2. In boundary 3, the shrinking of non-adsorbed core is assumed to be rate-limiting, so that the H_2 adsorption rate is described by H_2 diffusion in the H_2 adsorbed layer and the H_2 adsorption process near the interfacial boundary of the non-included solid core. The H_2 concentrations in boundary 1 and 2 are assumed to be the same as the concentration in bulk phase due to H_2 delocalization adsorption. The H_2 concentration at the interface of boundary 3 is calculated from the number of S-cages and the equilibrium H_2 occupancy due to the quasi-equilibrium adsorbed conditions. The MRA model is able to describe the H_2 adsorption behavior in guest additive clathrate hydrate particles well. Based on the activation energies of diffusion, the H_2 diffusion pathway in hydrate particles depends on the clathrate hydrate formation process and the interactions between guest additive molecule and the host molecule.

Gas adsorption and diffusional characteristics with semi-clathrate hydrates (Chapter 5)

The equilibrium adsorption amounts of H_2 depend on the crystal structure of the semi-clathrate hydrate. On the other hand, the equilibrium adsorption amounts of CO_2 depend not only on the anion of the TBA salt, but also on the semi-clathrate hydrate structure. The adsorption and diffusion characteristic of large molecules such as CO_2 probably depend on the anion of TBA salt much more so than small molecules such as H_2.

The H_2/CO_2 selectivity S_{H_2/CO_2} for 3.2 mol% TBAC semi-clathrate hydrate was highest among the TBA salt semi-clathrate hydrates. However, the S_{H_2/CO_2} for 3.0 mol% TBAF semi-clathrate

hydrate in the early stages of gas adsorption was the highest among TBA salt semi-clathrate hydrates. Therefore, 3.0 mol% TBAF semi-clathrate hydrate is considered to be appropriate as separation media for H_2/CO_2 systems that use pressure swing adsorption (PSA) processes for gas separations. On the other hand, the H_2/CO_2 selectivity α_{H_2/CO_2} for 3.3 mol% TBAF semi-clathrate hydrate was highest among the TBA salt semi-clathrate hydrates exauined and had a value greater than 100. Thus, the applicability of semi-clathrate hydrates as possible membrane separation media is confirmed through results in this thesis.

6.2 Future work

There are a number of topics that are listed below for future work:

1. In this thesis, it was determined that semi-clathrate hydrates exhibit selectivity for different gases. The detailed mechanism on why this selectivity occurs is presently not known. Further experiments on mixed gases, H_2 and CO_2 are needed to understand not only the adsorption kinetics but also the equilibrium of mixed gases with semi-clathrate hydrates.

2. In this thesis, it was determined that the structure of the semi-clathrate hydrate affects both the adsorption kinetics and equilibrium, especially for CO_2. It is likely that other structures can be manipulated to tailor the structure to accomodate more of a particular gas or to improve the kinetics of adsorption. Therefore, new studies are needed that explore structural changes of the semi-clathrate hydrates possibly through the use of mixed guest additives or through the use of particle formation techniques.

3. In this thesis, the practical application of H_2 and CO_2 gas separation was studied. It would be interesting and beneficial to construct small-scale membrane or pressure-swing adsorption apparatus to check aspects of cycling the semi-clathrate hydrates including heat transfer. The study of these processes would also help to develop the necessary thermodynamic models required in engineering.

4. The thermodynamic model developed in this thesis was effective for binary gas + semi-clathrate systems, however, it was only qualitative for gas mixtures. One assumption in the model is that the bulk gas concentration is equal to the delocalized concentration on the surface of the hydrate particle. This assumption needs to be studied in detail with short time-scale experiments or theoretical simulations to develop a mechanism for gas mixtures.

5. The gas mixture studied in this thesis was CO_2 + H_2. However, the study of other gas mixtures needs to be made. For example, semi-clathrate hydrates can possibly be used in natural gas processing to remove H_2S and other gases. There are also many other gas mixtures for which semi-clathrate hydrates could be used advantageously.

Appendices

General appendices

Appendix A Calibration of temperature sensor

Three platinum resistance temperature sensors (Pt 100 W, 3.17 mm diameter (1/8 in), NR-350, four-wire type, Netsushin) that were used in Chapters 3 – 5 were calibrated against a standard temperature probe (GE Kaye IRTD-400, stated uncertainty ± 25 mK). The temperature sensor in the reservoir tank was calibrated only at the ice point. Reported temperatures are corrected with Eq. (A-1):

$$T_{\text{calc}} = a T_{\text{raw}} + b \tag{A-1}$$

Table A-1. Parameters of Eq. (A-1) and uncertainty of each platinum resistance temperature sensor. The uncertainty is calculated as 25 mK plus two times the standard deviation.

Apparatus	*a*	*b*	Uncertainty [mK]
Phase equilibria cell	0.99678	0.16871	±44
Hydrate formation cell	0.99885	0.04954	±29
Reservoir tank	1	-0.4652	-

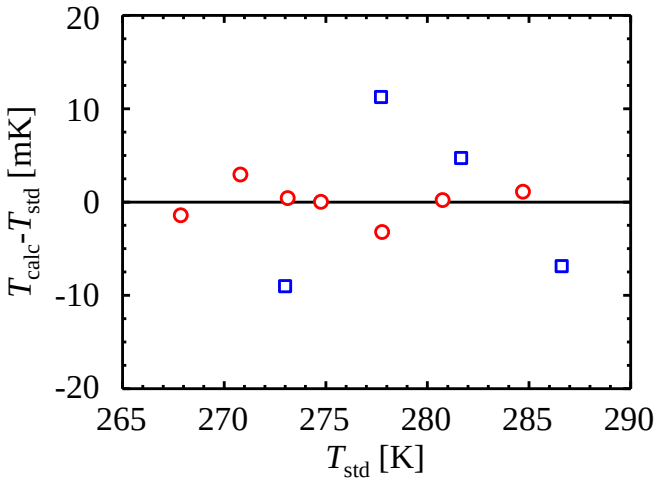

Figure A-1. Deviation of calculation values for each platinum resistance temperature sensor. Symbols: blue square, phase equilibrium cell; red circles, hydrate formation cell.

Appendix B Calibration of pressure gauge

A sealed gauge pressure transmitter (20 MPa F.S., PTX621-0, GE Sensing Japan) that were used in Chapter 3 and two sealed gauge pressure transducers (hydrate formation cell: 14 MPa F.S. PMP4015, GE sensing Japan, reservoir tank: 14 MPa F.S. PMP5013, GE sensing Japan) that were used in Chapters 4 and 5 were calibrated against a dead weight tester (Druck Pressurements M2200-5, stated uncertainty ±0.015%, Figure A-2).

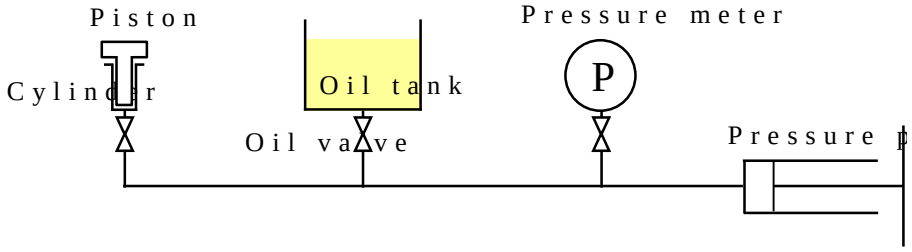

Figure A-2. Schematic diagram of the dead weight tester.

Calibration curve of the sealed gauge pressure transmitter:

$$P_{\text{calc}} = dA_{\text{DC}} + h \tag{A-2}$$

where A_{DC} is current in units of mA, and d and h are given in Table A-2.

Calibration curve of the sealed gauge pressure transducers:

$$P_{\text{calc}} = f_{\text{a}}V_{\text{DC}}^2 + f_{\text{b}}V_{\text{DC}} + f_{\text{c}} \tag{A-3}$$

$$f_{\text{a}} = aT + b \tag{A-4}$$

$$f_{\text{b}} = cT + d \tag{A-5}$$

$$f_{\text{c}} = eT^2 + gT + h \tag{A-6}$$

where V_{DC} is the direct-current voltage and T is the surrounding temperature of pressure gauge.

Parameters in Eqs. (A-4) – (A-6) are given in Table A-2.

Table A-2. Calibration curve parameters and uncertainty of each pressure gauge. The uncertainty is calculated as two times the standard deviation.

Apparatus	$a\times10^{-6}$	$b\times10^{-3}$	$c\times10^{-4}$	d	$e\times10^{-6}$	$g\times10^{-3}$	h	Uncertainty [kPa]
Equilibria cell	-	-	-	1249	-	-	-4.881	±4.5
Formation cell	4.796	-2.590	-2.348	2.874	-4.238	2.537	-0.293	±1.7
Reservoir tank	-	-	1.247	2.762	-	-2.032	0.682	±2.3

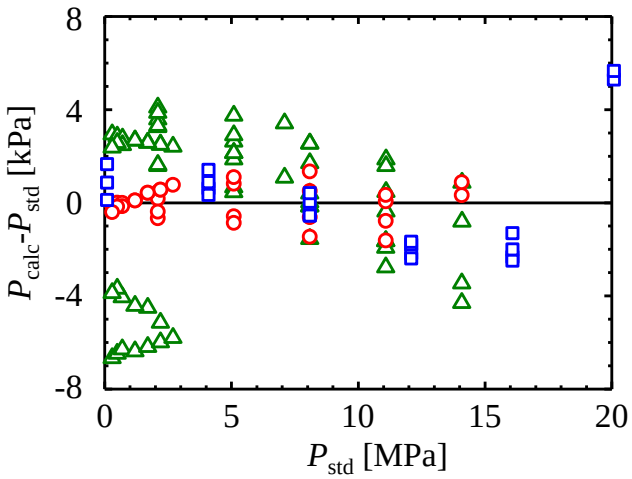

Figure A-3. Deviation of calculation values for each pressure gauge taken with the high-pressure range dead weight piston. Symbols: blue square, phase equilibrium cell at room temperature; red circles, hydrate formation cell at 273 K; green triangles, reservoir tank at 273 K. Green symbols ($P_{calc} - P_{std} < -3$) at low pressure P < 3 MPa are data based on the low-pressure range dead weight piston.

Appendix C Peng-Robinson equation of state (PR-EoS)

PR-EoS is described by Eqs. (A-7) – (A-11):

$$P = \frac{RT}{\nu - b} - \frac{a}{\nu\left(\nu + b\right) + b\left(\nu - b\right)} \tag{A-7}$$

$$\ln\left(\frac{f}{P}\right) = Z - 1 - \ln\left(Z - B\right) - \frac{A}{2\sqrt{2}B}\ln\left\{\frac{Z + \left(\sqrt{2}+1\right)B}{Z - \left(\sqrt{2}-1\right)B}\right\} \tag{A-8}$$

$$Z^3 - \left(1 - B\right)Z^2 + \left(A - 3B^2 - 2B\right)Z - \left(AB - B^2 - B^3\right) = 0 \tag{A-9}$$

$$A = \frac{aP}{R^2T^2} \tag{A-10}$$

$$B = \frac{bP}{RT} \tag{A-11}$$

where R is the universal gas constant, P is the pressure, T is the temperature, v is the molar volume, f is the fugacity and Z is the compressibility factor. The a is a function of T, $a(T)$ and the b is a constant as described by Eqs. (A-12) – (A-15):

$$a\left(T\right) = a\left(T_{\mathrm{c}}\right)\cdot\alpha\left(T_{\mathrm{r}},\omega\right) \tag{A-12}$$

$$a\left(T_{\mathrm{c}}\right) = 0.45724\frac{R^2{T_{\mathrm{c}}}^2}{P_{\mathrm{c}}} \tag{A-13}$$

$$\alpha\left(T_{\mathrm{r}},\omega\right) = \left\{1 + \left(0.37464 + 1.54226\omega - 0.26992\omega^2\right)\left(1 - \sqrt{T_{\mathrm{r}}}\right)\right\}^2 \tag{A-14}$$

$$b\left(T_{\mathrm{c}}\right) = 0.07780\frac{RT_{\mathrm{c}}}{P_{\mathrm{c}}} \tag{A-15}$$

where T_{c} is the critical temperature, $T_{\mathrm{r}} = T/T_{\mathrm{c}}$, P_{c} is critical pressure, ω is acentric factor. Table A-3 summarizes the critical properties of H_2 and CO_2.

Table A-3. Critical properties of each molecule.[1]

Molecule	M_w [g/mol]	T_c [K]	P_c [MPa]	ω [-]
H_2	2.016	32.98	1.293	-0.2170
CO_2	44.01	304.20	7.383	0.2240

Fugacity of *i* component in the mixture, $\hat{f}_k$, is described by Eqs. (A-16) – (A-20):

$$\ln\left(\frac{\hat{f}_k}{x_k P}\right)=\frac{b_k^{*}}{b_{\mathrm{mix}}}(Z-1)-\ln(Z-B_{\mathrm{mix}})-\frac{A_{\mathrm{mix}}}{2\sqrt{2}B_{\mathrm{mix}}}\left(\frac{a_k^{*}}{a_{\mathrm{mix}}}-\frac{b_k^{*}}{b_{\mathrm{mix}}}\right)\ln\left\{\frac{Z+\left(\sqrt{2}+1\right)B_{\mathrm{mix}}}{Z-\left(\sqrt{2}-1\right)B_{\mathrm{mix}}}\right\} \quad \text{(A-16)}$$

$$A_{\mathrm{mix}}=\frac{a_{\mathrm{mix}}P}{R^2T^2} \quad \text{(A-17)}$$

$$B_{\mathrm{mix}}=\frac{b_{\mathrm{mix}}P}{RT} \quad \text{(A-18)}$$

$$a_k^{*}=2\sum_i x_i a_{ik} \quad \text{(A-19)}$$

$$b_k^{*}=2\sum_i x_i b_{ik}-b_{\mathrm{mix}} \quad \text{(A-20)}$$

where *x* is the composition. The vdW2 mixing rule is described by Eqs. (A-21) – (A-24):

$$a_{\mathrm{mix}}=\sum_i\sum_j x_i x_j a_{ij} \quad \text{(A-21)}$$

$$a_{ij}=\left(1-k_{ij}\right)\sqrt{a_{ii}a_{jj}} \quad \text{(A-22)}$$

$$b_{\mathrm{mix}}=\sum_i\sum_j x_i x_j b_{ij} \quad \text{(A-23)}$$

$$b_{ij}=\left(1-l_{ij}\right)\frac{b_{ii}+b_{jj}}{2} \quad \text{(A-24)}$$

The interaction parameter, k_{ij}, is considered to be function of temperature as shown in Eq. (A-25) and l_{ij} is considered to be independent of temperature.

$$k_{ij}=k_c+k_T * T \quad \text{(A-25)}$$

The correlations in this thesis used H_2 + CO_2 vapor-liquid equilibria from the literature.[2-5] The experimental conditions were 220 – 290 K and 1 – 20 MPa. The fitting parameters were k_c, k_T and l_{ij}. The ARD described by Eq. (A-26):

$$\text{ARD \%} = \frac{1}{N}\sum_{i}^{N}\left|\frac{x_{\text{exp}} - x_{\text{calc}}}{x_{\text{exp}}}\right| \times 100 \qquad \text{(A-26)}$$

Table A-4 summarizes the interaction parameters and ARD, and Figure A-4 shows correlation results for H_2-CO_2 vapor-liquid equilibria.

Table A-4. Interaction parameters and ARD of correlation results for H_2-CO_2 vapor-liquid equilibria.

k_c [-]	k_T [$\times 10^3$ K^{-1}]	l_{ij} [-]	ARD %
-0.5704	2.657	-0.0417	7.63

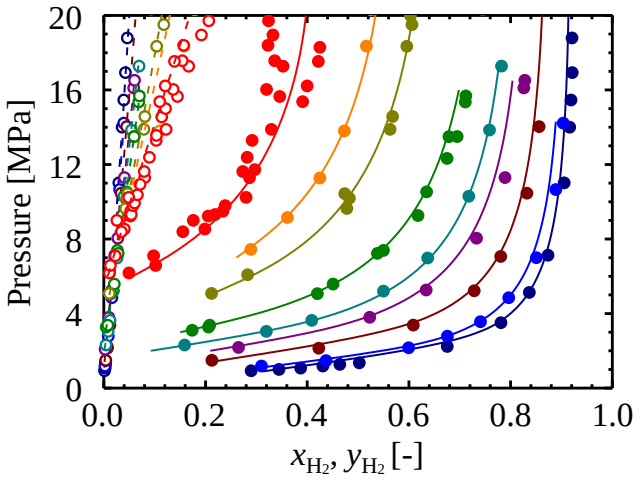

Figure A-4. Correlation results for H_2-CO_2 vapor-liquid equilibria. The continuous lines and dash lines show correlation results for vapor phase (y_{H_2}) and liquid phase (x_{H_2}), respectively. The filled symbols and unfilled symbols show experimental results for vapor phase (y_{H_2}) and liquid phase (x_{H_2}), respectively. Colors show temperature: red, 290 K; orange, 280 K; olive, 273 K; green, 260 K; blue green, 250 K; purple, 245 K; brown, 235 K; blue, 225 K; navy blue, 220 K.

Appendix D Calibration of tank and cell volumes

The reservoir tank and the hydrate formation cell were volume calibrated with nitrogen and water (Chapters 4 and 5).

Figure A-5 shows experimental set up for inner volume calibration of the reservoir tank.

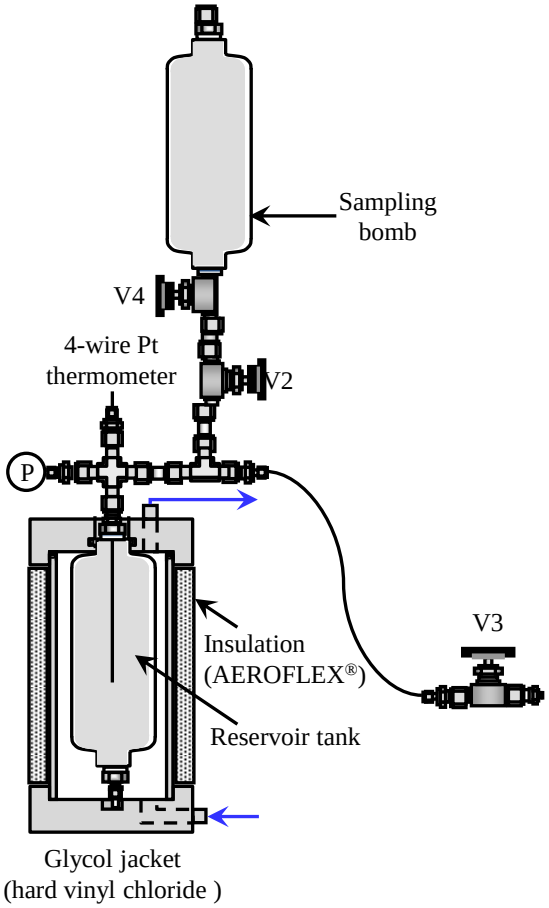

Figure A-5. Experimental apparatus of inner volume calibration of reservoir tank.

The inner volume between valve 2 (V2, Figure A-5) and valve 4 (V4, Figure A-5) was calibrated with pressurized water supplied by a high performance liquid chromatography (HPLC) pump (PU-1580, JASCO Co.). The inner volume between V2 and the reservoir tank was calibrated by subtracted the weight of N_2 between V2 and V4 from that between V4 and the reservoir tank. Tables A-5 and A-6 summarize volume calibration results.

Table A-5. Calibration results for volume between V2 and V4 (Figure A-5)

Run	T [K]	P [MPa]	W_{H_2O}[g]	ρ_{H_2O} [g/cm^3]	$V_{V2\text{-}V4}$ [cm^3]	Deviation [cm^3]
1	293.7	12.7	1.721	1.0038	1.715	-0.021
2	293.5	14.3	1.717	1.0045	1.709	-0.026
3	294.2	12.4	1.767	1.0035	1.761	0.025
4	294.7	13.9	1.757	1.0041	1.750	0.015
5	294.8	16.3	1.751	1.0051	1.742	0.007

Average: 1.735 cm^3, uncertainty: 0.022 cm^3.

Table A-6. Calibration results for volume between V2 and reservoir tank (Figure A-5)

Run	T [K]	P [MPa]	W_{N_2} [g]	ρ_{N_2} [$\times 10^{-2}$ g/cm^3]	$V_{V2\text{-}tank}$ [cm^3]	Deviation [cm^3]
1	265.00	2.412	9.453	3.1037	304.579	-0.093
2	264.99	5.175	20.477	6.7186	304.778	0.106
3	264.98	1.208	4.708	1.5458	304.578	-0.093
4	264.99	2.586	10.138	3.3292	304.508	-0.163
5	264.88	5.554	22.007	7.2207	304.772	0.100
6	269.12	2.344	9.029	2.9647	304.562	-0.109
7	269.11	5.028	19.534	6.4093	304.773	0.101
8	269.15	1.102	4.224	1.3863	304.698	0.026
9	269.15	2.343	9.028	2.9631	304.691	0.019
10	269.02	4.976	19.347	6.3445	304.936	0.265
11	273.11	4.814	18.365	6.3011	304.512	-0.160

Average: 304.672 cm^3, uncertainty: 0.136 cm^3.

The reservoir tank was volume calibrated with nitrogen over a range of temperatures (265 – 273 K) and pressures (1.1 – 5.6 MPa) and was found to have an average volume of 304.67 cm^3 from 11 independent trials. Total uncertainty was estimated as 0.022 cm^3 (Table A-5) + 0.136 cm^3 (Table A-6) for a total uncertainty of 0.158 cm^3.

Figure A-6 shows experimental apparatus used for volume calibration of the hydrate formation cell.

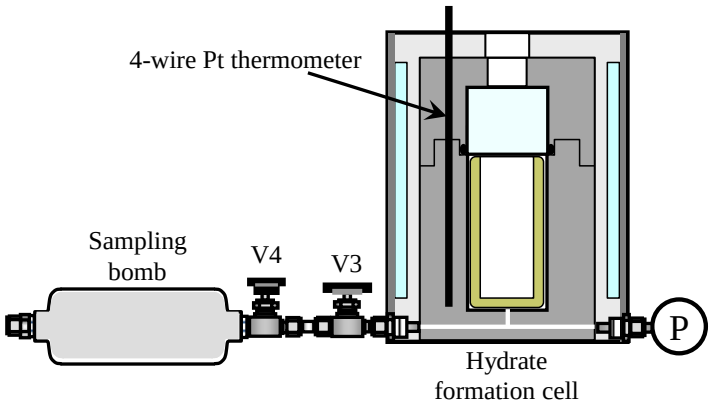

Figure A-6. Experimental apparatus for volume calibration of hydrate formation cell.

The inner volume between valve 3 (V3, Figure A-6) and valve 4 (V4, Figure A-6) was calibrated with pressurized water by HPLC pump (PU-1580, JASCO Co.). The inner volume between V3 and the hydrate formation cell was calibrated by subtracting the weight of N_2 between V3 and V4 from that between V4 and the hydrate formation cell. Tables A-7 and A-8 summarize volume calibration results for the hydrate formation cell.

Table A-7. Calibration results for volume between V2 and V4 (Figure A-5)

Run	T [K]	P [MPa]	W_{H_2O}[g]	ρ_{H_2O} [g/cm^3]	$V_{V3\text{-}V4}$ [cm^3]	Deviation [cm^3]
1	294.2	17.3	3.597	1.0057	3.577	0.036
2	293.6	10.6	3.598	1.0029	3.588	0.047
3	293.7	9.9	3.545	1.0025	3.536	-0.004
4	293.7	12.9	3.526	1.0039	3.512	-0.028
5	295.4	9.4	3.497	1.0019	3.490	-0.050
6	295.3	15.7	3.541	1.0047	3.524	-0.016

Average: 3.541 cm^3, uncertainty: 0.041 cm^3.

Table A-8. Calibration results for volume between V3 and hydrate formation cell (Figure A-6)

Run	T [K]	P [MPa]	W_{N_2} [g]	ρ_{N_2} [$\times 10^{-2}$ g/cm^3]	$V_{V3\text{-}cell}$ [cm^3]	Deviation [cm^3]
1	269.19	8.270	2.784	10.568	26.342	0.018
2	269.17	6.166	2.062	7.872	26.196	-0.128
3	269.18	2.456	0.815	3.107	26.227	-0.097
4	269.18	4.656	1.563	5.928	26.367	0.043
5	273.21	8.872	2.936	11.126	26.389	0.065
6	273.20	3.848	1.271	4.809	26.421	0.098

Average: 26.324 cm^3, uncertainty: 0.091 cm^3.

The reservoir tank was volume calibrated with nitrogen over a range of temperatures (269 – 273 K) and pressures (2.5 – 8.9 MPa) and was found to have an average volume of 26.324 cm^3 from 6 independent trials. Total uncertainty was estimated as 0.041 cm^3 (Table A-7) + 0.091 cm^3 (Table A-8) for a total uncertainty of 0.133 cm^3.

Appendix E Virial equation of state (Virial-EoS)

Virial-EoS is described by Eqs. (A-27) – (A-30):

$$P = \frac{RT}{v} + \frac{RTB}{v^2} + \frac{RTC}{v^3} \tag{A-27}$$

$$\ln\left(\frac{f}{P}\right) = \frac{2\alpha B}{Z} + \frac{3\alpha^2 C}{2Z^2} - \ln Z \tag{A-28}$$

$$Z^3 - Z^2 - \alpha BZ - \alpha^2 C = 0 \tag{A-29}$$

$$\alpha = \frac{P}{RT} \tag{A-30}$$

where R is the universal gas constant, P is the pressure, T is the temperature, v is the molar volume, f is the fugacity and Z is the compressibility factor. The B and C are the second and third virial coefficient, respectively, and are only a function of temperature as described by Eqs. (A-31) and (A-32):

$$B = aT^2 + bT + c \tag{A-31}$$

$$C = dT^2 + eT + g \tag{A-32}$$

where a, b, c, d, e and g are fitting parameters. Virial coefficients for H_2 were estimated from the molar volume at temperatures of 240 – 300 K and at pressures of 0.05 – 14 MPa,[6] and those for CO_2 were estimated from the saturated pressure at temperatures from 217 to 303 K[6] with Deiters method.[7] Table A-9 summarizes the fitting parameters determined.

Table A-9. Fitting parameters determined for second and third virial coefficients of H_2 and CO_2.

Molecule	$a \times 10^{-10}$ [$m^3/(mol \cdot K^2)$]	$b \times 10^{-7}$ [$m^3/(mol \cdot K)$]	$c \times 10^{-6}$ [m^3/mol]	$d \times 10^{-15}$ [$m^6/(mol^2 \cdot K^2)$]	$e \times 10^{-12}$ [$m^6/(mol^2 \cdot K)$]	$g \times 10^{-10}$ [m^6/mol^2]
H_2	-1.379	1.022	-3.793	1.847	-1.715	7.116
CO_2	-27.03	31.37	-815.4	-365.6	123.8	0.8041

Fugacity of *i* component in the mixture, $\hat{f}_k$, is described by Eqs. (A-33) – (A-36):

$$\ln\left(\frac{\hat{f}_k}{x_k P}\right) = \frac{2\alpha B_k^{*}}{Z_{\text{mix}}} + \frac{3\alpha^2 C_k^{*}}{2Z_{\text{mix}}^2} - \ln Z_{\text{mix}} \tag{A-33}$$

$$Z_{\text{mix}}^3 - Z_{\text{mix}}^2 - \alpha B_{\text{mix}} Z_{\text{mix}} - \alpha^2 C_{\text{mix}} = 0 \tag{A-34}$$

$$B_k^{*} = \sum_i x_i B_{ki} \tag{A-35}$$

$$C_k^{*} = \sum_i \sum_j x_i x_j C_{kij} \tag{A-36}$$

Mixing rules for B and C are described by Eqs. (A-37) – (A-41):

$$B_{\text{mix}} = \sum_i \sum_j x_i x_j B_{ij} \tag{A-37}$$

$$C_{\text{mix}} = \sum_i \sum_j \sum_k x_i x_j x_k C_{ijk} \tag{A-38}$$

$$C_{ijk} = \left(C_{ij} + C_{jk} + C_{ik}\right)^{1/3} \tag{A-39}$$

$$B_{ij} = \frac{B_T}{T} + B_{\text{c}} \tag{A-40}$$

$$C_{ij} = \frac{C_T}{T} + C_{\text{c}} \tag{A-41}$$

The fitting parameters are B_T, B_c, C_T and C_c in Eqs. (A-37) – (A-41). These parameters were determined by using H_2 + CO_2 binary equilibria data from the literature[2-5] and the ARD described by Eq. (A-26). The experimental conditions were 245 – 290 K and 2 – 26 MPa. Figure A-7 shows correlation results for H_2-CO_2 vapor-liquid equilibria[2-5] and Table A-10 summarizes the second and third cross virial coefficients parameters and ARD.

Table A-10. Second and third cross virial coefficients parameters and ARD of correlation results for H_2-CO_2 vapor-liquid equilibria.

B_c [×10^{-5} m^3/mol]	B_T [×10^{-3} K·m^3/mol]	C_c [×10^{-9} m^6/mol^2]	C_T [×10^{-7} K·m^6/mol^2]	ARD %
2.484	-7.390	-1.271	9.003	9.17

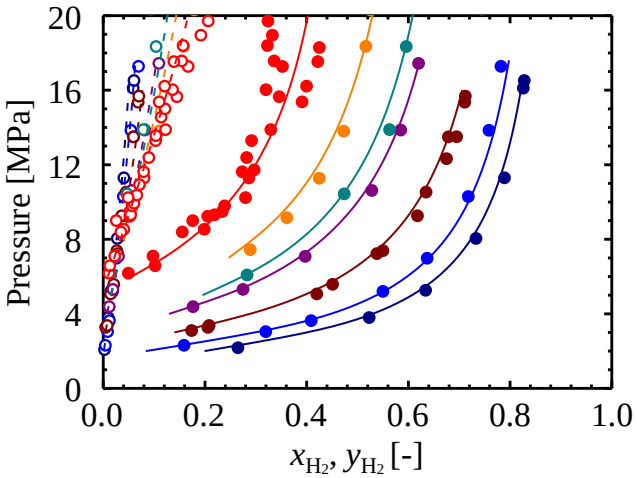

Figure A-7. Correlation results for H_2-CO_2 vapor-liquid equilibria. The continuous lines and dash lines show correlation results for vapor phase (y_{H_2}) and liquid phase (x_{H_2}), respectively. The filled symbols and unfilled symbol show experimental result for vapor phase (y_{H_2}) and liquid phase (x_{H_2}), respectively. Colors show temperature: red, 290 K; orange, 280 K; blue green, 273 K; purple, 270 K; brown, 260 K; blue, 250 K; navy blue, 245 K.

Chapter appendices

Appendix 3-1 Thermal properties

The enthalpy difference between water of the empty hydrate structure and pure liquid water, $\Delta h^{\mathrm{L}}_{\mathrm{W},0}$, was estimated from differential scanning calorimeter (DSC) analysis. The $\Delta h^{\mathrm{L}}_{\mathrm{W},0}$ was assumed to depend only on the crystal structure, namely hexagonal structure-I (HS-I), tetragonal structure-I (TS-I) and superlattice of cubic structure-I (SCS-I). Results for tetra-*n*-butyl ammonium bromide (TBAB) semi-clathrate hydrate were used ($\Delta h^{\mathrm{L}}_{\mathrm{W},0} = -\Delta h^{\mathrm{dis}}_{\mathrm{TBAB,structure}}$) because dehydration free energy for bromide was smallest among the anions.[8] However, TBAB semi-clathrate hydrate cannot form SCS-I so that the $\Delta h^{\mathrm{dis}}_{\mathrm{TBAB,SCS\text{-}I}}$ was estimated from the relationship between the dehydration free energy of anions (Br^- and F^-) and the dissociation enthalpy of crystal structures (TS-I and SCS-I) as described by Eq. (A3-1):

$$\Delta h^{\mathrm{dis}}_{\mathrm{TBAB,SCS\text{-}I}} = \Delta h^{\mathrm{dis}}_{\mathrm{TBAF,SCS\text{-}I}} + \frac{\Delta h^{\mathrm{dis}}_{\mathrm{TBAB,TS\text{-}I}} - \Delta h^{\mathrm{dis}}_{\mathrm{TBAF,TS\text{-}I}}}{E_{\mathrm{Dehyd},Br^-} - E_{\mathrm{Dehyd},F^-}} \left(E_{\mathrm{Dehyd},Br^-} - E_{\mathrm{Dehyd},F^-} \right) \qquad \text{(A3-1)}$$

where $\Delta h^{\mathrm{dis}}_{\mathrm{TBA\ salt,structure}}$ is the dissociation enthalpy of TBA salt semi-clathrate hydrate for the crystal structure, $E_{\mathrm{Dehyd,anion}}$ is the dehydration free energy of the anion. Table A3-1 summarizes the dehydration energy of anion and the dissociation enthalpy of TBA salt semi-clathrate hydrates.

Table A3-1. Dehydration energy of anion and dissociation enthalpy of tetra-*n*-butyl ammonium (TBA) salt semi-clathrate hydrates

TBA salt	E_{Dehyd} [kJ/mol][8]	HS-I		TS-I		SCS-I	
		Δh^{dis} [J/g]	[kJ/mol$_{\text{-}H_2O}$]	Δh^{dis} [J/g]	[kJ/mol$_{\text{-}H_2O}$]	Δh^{dis} [J/g]	[kJ/mol$_{\text{-}H_2O}$]
TBAB	346.0	172	4.581	153	4.300	-	3.841
TBAF	501.2	-	-	238	6.241	212	5.782

Appendix 3-2 Volume change due to dehydration

The molar volume difference between water in the empty hydrate structure and pure liquid water, $\Delta\nu_{\mathrm{W}}^{\mathrm{L}}$, for each crystal structure was estimated from liquid molar volume of water (18.02 cm^3/mol) and volume of the water in TBAB semi-clathrate hydrate per mole of pure water, $\nu_{\mathrm{W}}^{\mathrm{H}}$ because dehydration energy for bromide was smallest for bromide, chloride and fluoride anion.[8] The $\Delta\nu_{\mathrm{W}}^{\mathrm{L}}$ was assumed to depend on only the crystal structure, namely hexagonal structure-I (HS-I), tetragonal structure-I (TS-I) and superlattice of cubic structure-I (SCS-I). However, TBAB semi-clathrate hydrate cannot form SCS-I. Thus, the $\nu_{\mathrm{W,TBAB,SCS\text{-}I}}^{\mathrm{H}}$ was estimated from the relationship between the dehydration energy of anions (Br^- and F^-) and the water molar volume for the crystal structures (TS-I and SCS-I) as described by Eq. (A3-2):

$$\nu_{\mathrm{W,TBAB,SCS\text{-}I}}^{\mathrm{H}} = \nu_{\mathrm{W,TBAF,SCS\text{-}I}}^{\mathrm{H}} + \frac{\nu_{\mathrm{W,TBAB,TS\text{-}I}}^{\mathrm{H}} - \nu_{\mathrm{W,TBAF,TS\text{-}I}}^{\mathrm{H}}}{E_{\mathrm{Dehyd,Br^-}} - E_{\mathrm{Dehyd,F^-}}}\left(E_{\mathrm{Dehyd,Br^-}} - E_{\mathrm{Dehyd,F^-}}\right) \qquad \text{(A3-2)}$$

The $\nu_{\mathrm{W}}^{\mathrm{H}}$ were calculated from Eq. (3-7) and the structure parameters (Table 5-1). Table 3-2 summarizes the dehydration energy of anion and the $\nu_{\mathrm{W}}^{\mathrm{H}}$ and $\Delta\nu_{\mathrm{W}}^{\mathrm{L}}$ for TBA salt semi-clathrate hydrates.

Table A3-2. Dehydration energy of anion and volume of the water in tetra-*n*-butyl ammonium (TBA) salt semi-clathrate hydrate per mole pure water, $\nu_{\mathrm{W}}^{\mathrm{H}}$ and molar volume difference between water in the empty hydrate structure and pure liquid water, $\Delta\nu_{\mathrm{W}}^{\mathrm{L}}$ for each crystal structure.

		HS-I		TS-I		SCS-I	
TBA salt	E_{Dehyd} [kJ/mol][8]	$\nu_{\mathrm{W}}^{\mathrm{H}}$ [$cm^3/mol_{\text{-}H_2O}$]	$\Delta\nu_{\mathrm{W}}^{\mathrm{L}}$ [$cm^3/mol_{\text{-}H_2O}$]	$\nu_{\mathrm{W}}^{\mathrm{H}}$ [$cm^3/mol_{\text{-}H_2O}$]	$\Delta\nu_{\mathrm{W}}^{\mathrm{L}}$ [$cm^3/mol_{\text{-}H_2O}$]	$\nu_{\mathrm{W}}^{\mathrm{H}}$ [$cm^3/mol_{\text{-}H_2O}$]	$\Delta\nu_{\mathrm{W}}^{\mathrm{L}}$ [$cm^3/mol_{\text{-}H_2O}$]
TBAB	346.0	25.36[9]	7.34	25.40[10]	7.38	25.50	7.48
TBAF	501.2	-	-	25.25[11]	7.23	25.35[12]	7.33

Appendix 3-3 Osmotic coefficient

Osmotic coefficient, ϕ, for TBA salt is described by Eq. (A3-3):

$$\phi = 1 + am^{1/2} + bm + cm^{3/2} + dm^2 + em^{5/2} + gm^3 \quad \text{(A3-3)}$$

where m is molality. The fitting parameters in Eq, (A3-3) are *a*, *b*, *c*, *d*, *e* and g. Figure A3-1 shows correlation results of the osmotic coefficient for tetra-*n*-butyl ammonium bromide (TBAB) (*m*: 0.1 – 3 mol/kg),[13] tetra-*n*-butyl ammonium chloride (TBAC) (*m*: 0.1 – 2.5 mol/kg)[13] and tetra-*n*-butyl ammonium fluoride (TBAF) (*m*: 0.1 – 1.6 mol/kg),[14] and Table A3-3 summarizes the fitting parameters and ARD. The ARD was calculated with Eq. (A3-4):

$$\text{ARD \%} = \frac{1}{N}\sum_{i}^{N}\left|\frac{\phi_{\text{exp}} - \phi_{\text{calc}}}{\phi_{\text{exp}}}\right| \times 100 \quad \text{(A3-4)}$$

Table A3-3. Fitting parameters for osmotic coefficient (Eq. (A3-3)) of tetra-*n*-butyl ammonium (TBA) salt determined from literature data.[13,14]

TBA salt	*a* [(kg/mol)$^{1/2}$]	*b* [kg/mol]	*c* [(kg/mol)$^{3/2}$]	*d* [(kg/mol)^2]	*e* [(kg/mol)$^{5/2}$]	*g* [m(kg/mol)^3]	ARD %
TBAB	-0.518	0.478	-0.360	0.136	-0.023	0.0015	0.91
TBAC	-0.399	0.554	-0.484	0.452	-0.212	0.0257	0.35
TBAF	-0.140	0.573	0.002	0.020	-0.001	-0.0032	0.43

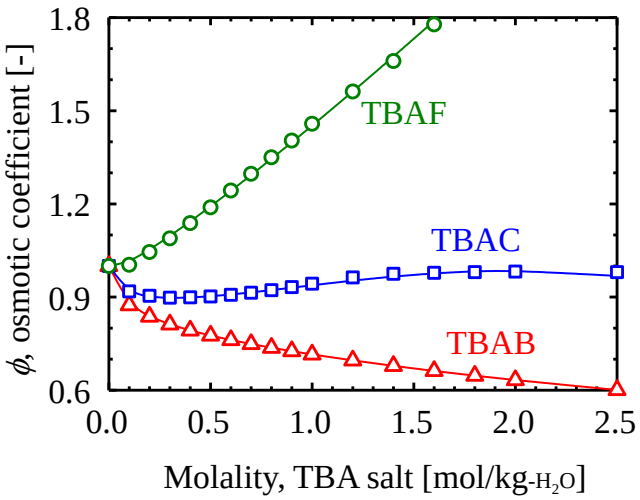

Figure A3-1. Correlation results for the osmotic coefficient of tetra-*n*-butyl ammonium (TBA) salts. The lines showed correlation results and symbols show experimental data.[13,14] Colors show anion: red, bromide;[13] blue, chloride;[13] green, fluoride.[14]

Appendix 3-4 Gas mole fraction in water

Gas mole fraction in water, $x_{\text{gas}}^{\text{L}}$ is described by Eq. (A3-5) using the Krichevsky-Kasarnovsky equation: [15]

$$x_{\text{gas}}^{\text{L}} = \frac{f_{\text{gas}}^{\text{V}}}{H_{\text{gw}} \exp\left(\frac{\nu_{\text{gas}}^{\infty} P}{RT}\right)} \tag{A3-5}$$

where $f_{\text{gas}}^{\text{V}}$ is the fugacity of the chemical species in the vapor phase, $\nu_{\text{gas}}^{\infty}$ is molar volume of gas at infinite dilution conditions, and H_{gw} is Henry's constant of gas in water as described by Eq. (A3-6) in units of Pa^{-1}:

$$H_{\text{gw}} = 101325 \times \exp\left\{-\left(H_{\text{gw}}^{[1]} + \frac{H_{\text{gw}}^{[2]}}{T} + H_{\text{gw}}^{[3]} \ln\left(T\right) + H_{\text{gw}}^{[4]} T\right)\right\} \tag{A3-6}$$

Table A3-4 summarizes the ν_{g}^{∞} and the Henry's constant parameters ($H_{\text{gw}}^{[1]}, H_{\text{gw}}^{[2]}, H_{\text{gw}}^{[3]}$ and $H_{\text{gw}}^{[4]}$).

Table A3-4. Molar volume of gas at infinite dilution condition[16] and Henry's constant parameters ($H_{\text{gw}}^{[1]}, H_{\text{gw}}^{[2]}, H_{\text{gw}}^{[3]}$ and $H_{\text{gw}}^{[4]}$).[17]

Molecule	$\nu_{\text{gas}}^{\infty}$ [cm^3/mol]	$H_{\text{gw}}^{[1]}$ [-]	$H_{\text{gw}}^{[2]}$ [K]	$H_{\text{gw}}^{[3]}$ [-]	$H_{\text{gw}}^{[4]}$ [K^{-1}]
H_2	26.7±0.2	-86.855	4178.717	10.4935	0.00632
CO_2	33.9±0.4	-159.868	8742.426	21.6712	-0.0011

Appendix 3-5 Densities of aqueous tetra-*n*-butyl ammonium salt solution

Density, ρ, of aqueous solution for tetra-*n*-butyl ammonium chloride (TBAC) and tetra-*n*-butyl ammonium fluoride (TBAF) were measured with a Stabinger viscometer SVM3000 (Anton Paar GmbH). Tables A3-5 and A3-6 summarize experimental densities of TBAC and TBAF aqueous solutions at 0.1 MPa, respectively.

Table A3-5. Densities of tetra-*n*-ammonium chloride (TBAC) aqueous solutions at 0.1 MPa.

	TBAC concentration								
[mol%]	0.0	0.6	1.3	2.0	2.6	3.0	3.3	3.7	4.1
[wt%]	0.0	8.6	16.9	24.3	29.4	32.3	34.2	37.4	39.8
T [K]	Density, ρ, of TBAC aqueous solution [g/cm^3]								
288.2	0.9994	0.9963	0.9949	0.9945	0.9938	0.9933	0.9927	0.9917	0.9907
293.2	0.9984	0.9949	0.9930	0.9920	0.9909	0.9901	0.9895	0.9883	0.9872
298.2	0.9972	0.9934	0.9910	0.9895	0.9880	0.9870	0.9862	0.9849	0.9838
303.2	0.9957	0.9916	0.9888	0.9868	0.9849	0.9838	0.9830	0.9815	0.9803
308.2	0.9941	0.9897	0.9864	0.9840	0.9819	0.9806	0.9797	0.9781	0.9768
313.2	0.9922	0.9875	0.9839	0.9811	0.9787	0.9773	0.9764	0.9764	0.9733
318.2	0.9901	0.9851	0.9812	0.9780	0.9754	0.9739	0.9729	0.9711	0.9697

Table A3-6. Densities of tetra-*n*-ammonium fluoride (TBAF) aqueous solutions at 0.1 MPa.

	TBAF concentration								
[mol%]	0.0	0.6	1.3	2.0	2.6	3.0	3.3	3.7	4.1
[wt%]	0.0	8.1	16.0	22.9	27.9	31.1	33.1	35.8	38.2
T [K]	Density, ρ, of TBAF aqueous solution [g/cm^3]								
298.2	0.9971	0.9945	0.9930	0.9925	0.9918	-	-	-	-
303.2	0.9957	0.9927	0.9908	0.9897	0.9887	0.9870	0.9864	0.9855	0.9840
308.2	0.9940	0.9908	0.9884	0.9869	0.9856	0.9836	0.9831	0.9820	0.9804
313.2	0.9921	0.9887	0.9859	0.9840	0.9823	0.9803	0.9796	0.9785	0.9769
318.2	0.9901	0.9864	0.9832	0.9810	0.9791	0.9769	0.9762	0.9749	0.9733
323.2	0.9878	0.9839	0.9804	0.9779	0.9757	0.9735	0.9727	0.9714	0.9696
328.2	0.9854	0.9812	0.9775	0.9747	0.9723	0.9700	0.9692	0.9678	0.9659

Densities, ρ, of TBA salts aqueous solutions were described by Eqs. (A3-7) and (A3-8):[18]

$$\rho^{\mathrm{L}}_{\mathrm{TBA\,salt}} = \rho^{\mathrm{L}}_{\mathrm{W}} + \sum_{i=1}^{3} o_i \left(100 w_{\mathrm{TBA\,salt}}\right)^i \tag{A3-7}$$

$$o_i = a_i T^2 + b_i T + c_i \tag{A3-8}$$

where $w_{\mathrm{TBA\,salt}}$ is the mass fraction of TBA salt and $\rho^{\mathrm{L}}_{\mathrm{W}}$ is the density of pure water as described by Eq. (A3-9):

$$\rho^{\mathrm{L}}_{\mathrm{W}} = -4.04318 \times 10^{-6} T^2 + 2.13909 \times 10^{-3} T + 0.718781 \tag{A3-9}$$

The a_i, b_i and c_i are fitting parameters. Figure A3-2 shows correlation results of the density of TBA salt aqueous solutions at 303 K and 0.1 MPa, and Table A3-7 summarizes the fitting parameters and ARD as described by Eq. (A3-10). Densities of TBAB aqueous solutions were obtained from literature data.[18]

$$\mathrm{ARD}\ \% = \frac{1}{N} \sum_{i}^{N} \left| \frac{\rho_{\mathrm{exp}} - \rho_{\mathrm{calc}}}{\rho_{\mathrm{exp}}} \right| \times 100 \tag{A3-10}$$

Table A3-7. Fitting parameters for densities of tetra-*n*-butyl ammonium (TBA) salts.

TBA salt	TBAB	TBAC	TBAF
a_1 [$\times 10^{-8}$ g/(K^2·cm^3)]	-2.5534	-5.1741	3.4887
b_1 [$\times 10^{-5}$ g/(K·cm^3)]	1.2324	2.8282	-2.5404
c_1 [$\times 10^{-4}$ g/(cm^3)]	-6.6735	-44.020	40.120
a_2 [$\times 10^{-10}$ g/(K^2·cm^3)]	52.594	77.630	-3.5598
b_2 [$\times 10^{-7}$ g/(K·cm^3)]	-35.638	-51.536	-1.0291
c_2 [$\times 10^{-5}$ g/(cm^3)]	60.659	86.360	7.9944
a_3 [$\times 10^{-11}$ g/(K^2·cm^3)]	-6.7218	-10.538	14.036
b_3 [$\times 10^{-8}$ g/(K·cm^3)]	4.6078	7.0959	-8.3610
c_3 [$\times 10^{-6}$ g/(cm^3)]	-7.9381	-12.074	12.163
$w_{\text{TBA salt}}$ [-]	0.0 – 0.5	0.0 – 0.4	0.0 – 0.4
T [K]	293 – 328	288 – 318	298 – 328
ARD %	0.0008	0.0060	0.0182

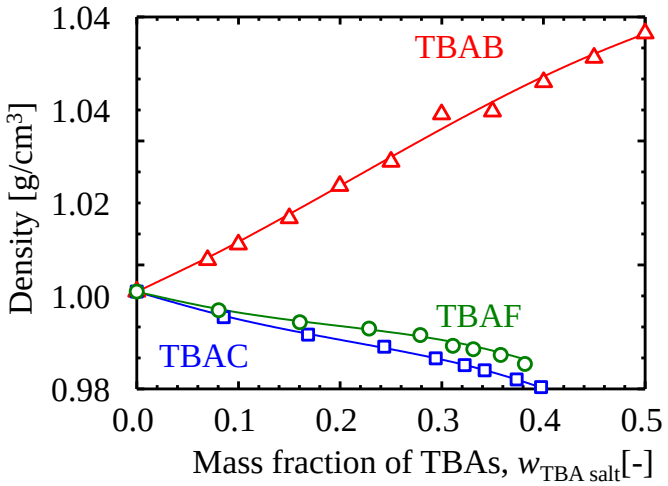

Figure A3-2. Correlation results for the osmotic coefficient for tetra-*n*-butyl ammonium (TBA) salts. The lines show correlation results and symbols show experimental data (TBAB: literature data,[18] TBAC, TBAF: this thesis). Colors show anion: red, bromide;[18] blue, chloride; green, fluoride).

Appendix 3-6 Electrolyte Non-Random Two-Liquid (eNRTL) model

The activity coefficients of the tetra-*n*-butyl ammonium (TBA) salt $\gamma_{\text{TBA salt}}$ were calculated from the eNRTL model[19] as described by Eqs. (A3-11) – (A3-13):

$$\gamma_{\text{TBA salt}} = \gamma^*_{\pm\text{mean}} \tag{A3-11}$$

$$\ln\left(\gamma^*_{\pm\text{mean}}\right) = \frac{1}{\upsilon}\left[\upsilon_{\text{c}} \ln\left(\gamma^*_{i=\text{c}}\right) + \upsilon_{\text{a}} \ln\left(\gamma^*_{i=\text{a}}\right)\right] - \ln\left(1 + 0.001 M_{\text{s}} m \upsilon\right) \tag{A3-12}$$

$$\ln\left(\gamma_i^*\right) = \ln\left(\gamma_i^{*\text{PDH}}\right) + \ln\left(\gamma_i^{*\text{NRTL}}\right) \tag{A3-13}$$

where $\gamma^*_{\pm\text{mean}}$ is the average activity coefficient, m is the molality and the υ_{c} and υ_{a} are the numbers of cations and anions in the solution, respectively, with the constraint that $\upsilon = \upsilon_{\text{c}} + \upsilon_{\text{a}}$. In Eq. (A3-12), M_{s} is the molecular weight of the solvent. The $\gamma_i^{*\text{PDH}}$ and $\gamma_i^{*\text{NRTL}}$ in Eq. (A3-13) are the activity coefficient of *i* species of the Pitzer-Debye-Huckel (PDH) and the NRTL model, respectively. The $\gamma_i^{*\text{PDH}}$ is described by Eq. (A3-14):

$$\ln\left(\gamma_i^{*\text{PDH}}\right) = -\sqrt{\frac{1000}{M_{\text{s}}}} A_\phi \left[\frac{2Z_i^2}{\rho} \ln\left(1 + \rho^* I^{0.5}\right) + \frac{Z_i^2 I^{0.5} - 2I^{1.5}}{1 + \rho^* I^{0.5}}\right] \tag{A3-14}$$

where A_ϕ is Debye-Huckel parameter as described by Eq. (A3-15):

$$\begin{aligned} A_\phi = {} & -61.44534 \exp\left(\left(T - T_0\right) / T_0\right) + 2.864468 \left(\exp\left(\left(T - T_0\right) / T_0\right)\right)^2 \\ & + 183.5379 \ln\left(T / T_0\right) - 0.6820223 \left(T - T_0\right) \\ & + 0.0007875695 \left(T^2 - T_0^2\right) + 58.95788 \left(T_0 / T\right) \end{aligned} \tag{A3-15}$$

and T_0 is 273.15 K. In Eq. (A3-15), the Z_i is electric charge of *i* species, the ρ^* is closest approach parameter (= 14.9) and the *I* is ionic strength as described by Eq. (A3-16):

$$I = \frac{1}{2}\sum_i Z_i^{\,2} x_i \tag{A3-16}$$

where *x* is mole fraction of species *i*. The $\gamma_i^{*\mathrm{NRTL}}$ is described by:

$$\ln\left(\gamma_{\mathrm{c}}^{*\mathrm{NRTL}}\right) = \frac{\tau_{\mathrm{ca,s}} x_{\mathrm{s}}^{\,2} G_{\mathrm{ca,s}}}{\left(x_{\mathrm{a}} G_{\mathrm{ca,s}} + x_{\mathrm{c}} G_{\mathrm{ca,s}} + x_{\mathrm{s}}\right)^2} + \frac{\tau_{\mathrm{s,ca}} Z_{\mathrm{c}} x_{\mathrm{s}} G_{\mathrm{s,ca}}}{x_{\mathrm{a}} + x_{\mathrm{s}} G_{\mathrm{s,ca}}} - \frac{\tau_{\mathrm{s,ca}} Z_{\mathrm{a}} x_{\mathrm{a}} x_{\mathrm{s}} G_{\mathrm{s,ca}}}{\left(x_{\mathrm{s}} G_{\mathrm{s,ca}} + x_{\mathrm{c}}\right)^2} - \tau_{\mathrm{ca,s}} G_{\mathrm{ca,s}} - \tau_{\mathrm{s,ca}} Z_{\mathrm{c}} \tag{A3-17}$$

$$\ln\left(\gamma_{\mathrm{a}}^{*\mathrm{NRTL}}\right) = \frac{\tau_{\mathrm{ca,s}} x_{\mathrm{s}}^{\,2} G_{\mathrm{ca,s}}}{\left(x_{\mathrm{a}} G_{\mathrm{ca,s}} + x_{\mathrm{c}} G_{\mathrm{ca,s}} + x_{\mathrm{s}}\right)^2} + \frac{\tau_{\mathrm{s,ca}} Z_{\mathrm{a}} x_{\mathrm{s}} G_{\mathrm{s,ca}}}{x_{\mathrm{c}} + x_{\mathrm{s}} G_{\mathrm{s,ca}}} - \frac{\tau_{\mathrm{s,ca}} Z_{\mathrm{c}} x_{\mathrm{c}} x_{\mathrm{s}} G_{\mathrm{s,ca}}}{\left(x_{\mathrm{s}} G_{\mathrm{s,ca}} + x_{\mathrm{a}}\right)^2} - \tau_{\mathrm{ca,s}} G_{\mathrm{ca,s}} - \tau_{\mathrm{s,ca}} Z_{\mathrm{a}} \tag{A3-18}$$

$$G_{\mathrm{ca,s}} = \exp\left(-\alpha \tau_{\mathrm{ca,s}}\right) \tag{A3-19}$$

$$G_{\mathrm{s,ca}} = \exp\left(-\alpha \tau_{\mathrm{s,ca}}\right) \tag{A3-20}$$

where α is the nonrandomness factor (=0.2) and the $\tau_{\mathrm{ca,s}}$ and $\tau_{\mathrm{s,ca}}$ are fitting parameters. The x_{s}, x_{c} and x_{a} were calculated with consideration for the gas solubility (Appendix 3-7). Figure A3-3 shows correlation results of the activity coefficient of TBA salt in aqueous solutions at 298 K and 0.1 MPa, and Table A3-8 summarizes the eNRTL parameters and ARD as described by Eq. (A3-21).

$$\mathrm{ARD}\ \% = \frac{1}{N}\sum_i^N \left| \frac{\gamma_{\mathrm{TBA\,salt,exp}} - \gamma_{\mathrm{TBA\,salt,calc}}}{\gamma_{\mathrm{TBA\,salt,exp}}} \right| \times 100 \tag{A3-21}$$

Table A3-8. Parameters determined for the eNRTL model for aqueous tetra-*n*-butyl ammonium (TBA) salt solutions.

TBA salt	*m* [mol/kg-H_2O]	$\tau_{ca,s}$ [-]	$\tau_{s,ca}$ [-]	ARD %
TBAB	0.1 – 3.0	-3.6179	8.0993	2.61
TBAC	0.1 – 2.0	-2.1991	2.7004	4.49
TBAF	0.1 – 1.6	-4.3541	3.5464	1.85

m: molality.

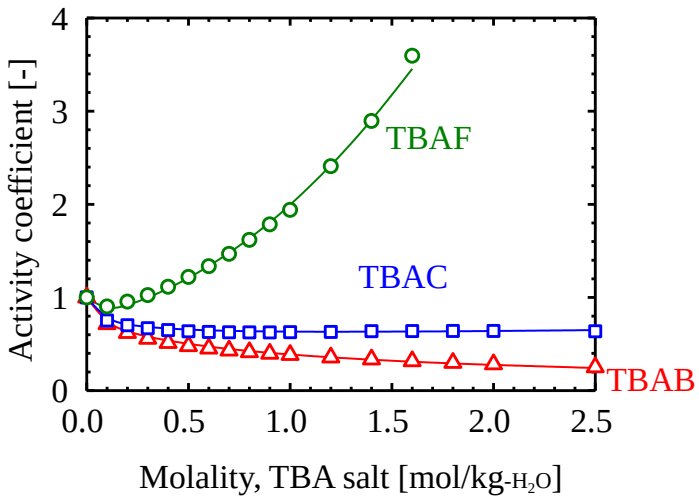

Figure A3-3. Correlation results for the osmotic coefficient for tetra-*n*-butyl ammonium (TBA) salts. Lines show correlation results and symbols show experimental data.[13,14] Colors show anion: red, bromide;[13] blue, chloride;[13] green, fluoride.[14]

Appendix 3-7 Mole fraction with consideration for gas solubility

Assumption: tetra-*n*-butyl ammonium (TBA) salt is treated as a molecular species.

Mole fraction of water in aqueous TBA salt solution is described by Eq. (A3-22) as:

$$x_{\mathrm{w}} = \frac{n_{\mathrm{w}}}{n_{\mathrm{w}} + n_{\mathrm{salt}}} = \frac{1}{1 + \frac{n_{\mathrm{salt}}}{n_{\mathrm{w}}}} = \frac{1}{1 + 0.001 m M_{\mathrm{w}}} \tag{A3-22}$$

where m is molality and M_{w} is molecular weight of water. The mole fraction of TBA salt in aqueous solution with consideration for gas solubility, $x^{\mathrm{L}}_{\mathrm{TBA\,salt}}$, was described by Eqs. (A3-23) – (A3-27) as:

For a gas-water mixture:

$$x_{\mathrm{gas}} = \frac{n_{\mathrm{gas}}}{n_{\mathrm{w}} + n_{\mathrm{gas}}} \tag{A3-23}$$

rearranging,

$$\frac{n_{\mathrm{gas}}}{n_{\mathrm{w}}} = \frac{x_{\mathrm{gas}}}{1 - x_{\mathrm{gas}}} \tag{A3-24}$$

For a salt-water mixture:

$$x_{\mathrm{salt}} = \frac{n_{\mathrm{salt}}}{n_{\mathrm{w}} + n_{\mathrm{salt}}} \tag{A3-25}$$

rearranging:

$$\frac{n_{\mathrm{salt}}}{n_{\mathrm{w}}} = \frac{x_{\mathrm{salt}}}{1 - x_{\mathrm{salt}}} \tag{A3-26}$$

For gas-salt-water mixture:

$$x^{\mathrm{L}}_{\mathrm{TBA\,salt\,w}} = \frac{n_{\mathrm{salt}}}{n_{\mathrm{w}} + n_{\mathrm{salt}} + n_{\mathrm{gas}}} = \frac{\frac{n_{\mathrm{salt}}}{n_{\mathrm{w}}}}{1 + \frac{n_{\mathrm{salt}}}{n_{\mathrm{w}}} + \frac{n_{\mathrm{gas}}}{n_{\mathrm{w}}}} = \frac{\frac{x_{\mathrm{salt}}}{1 - x_{\mathrm{salt}}}}{1 + \frac{x_{\mathrm{salt}}}{1 - x_{\mathrm{salt}}} + \frac{x_{\mathrm{gas}}}{1 - x_{\mathrm{gas}}}} \tag{A3-27}$$

Assumption: tetra-*n*-butyl ammonium (TBA) salt is treated in terms of its cation and anion.
Mole fraction of solvent in aqueous TBA salt solution is described by Eq. (A3-28) as:

$$x_{H_2O} = \frac{n_{H_2O}}{n_{H_2O} + n_c + n_a} = \frac{1}{1 + \frac{n_c + n_a}{n_{H_2O}}} = \frac{1}{1 + 0.001\left(\upsilon_c + \upsilon_a\right) m M_w} \tag{A3-28}$$

where υ_c, υ_a are the valences of the cation and the anion. The x_s, x_c and x_a with consideration for gas solubility (Appendix 3-6) were described by Eqs. (A3-29) – (A3-35) as:
For a H_2O-ions mixture:

$$x_c = \frac{n_c}{n_{H_2O} + n_c + n_a} = \frac{1}{\frac{n_{H_2O}}{n_c} + 1 + \frac{\upsilon_a}{\upsilon_c}} \tag{A3-29}$$

rearranging,

$$\frac{n_c}{n_{H_2O}} = \frac{x_c}{1 - \left(1 + \frac{\upsilon_a}{\upsilon_c}\right) x_c} \tag{A3-30}$$

$$x_a = \frac{n_a}{n_{H_2O} + n_c + n_a} = \frac{1}{\frac{n_{H_2O}}{n_a} + \frac{\upsilon_c}{\upsilon_a} + 1} \tag{A3-31}$$

rearranging,

$$\frac{n_a}{n_{H_2O}} = \frac{x_a}{1 - \left(1 + \frac{\upsilon_c}{\upsilon_a}\right) x_a} \tag{A3-32}$$

For a gas-H_2O-ions mixture:

$$x_{H_2O,mix} = \frac{n_{H_2O}}{n_{H_2O} + n_c + n_a + n_{gas}} = \frac{1}{\frac{n_{H_2O} + n_c + n_a}{n_{H_2O}} + \frac{n_{gas}}{n_{H_2O}}} = \frac{1}{\frac{1}{x_{H_2O}} + \frac{x_{gas}}{1 - x_{gas}}} \tag{A3-33}$$

$$x_{c,mix} = \frac{n_c}{n_{H_2O} + n_c + n_a + n_{gas}} = \frac{\frac{n_c}{n_{H_2O}}}{\frac{n_{H_2O} + n_c + n_a}{n_{H_2O}} + \frac{n_{gas}}{n_{H_2O}}} = \frac{x_c}{1 - \left(1 + \frac{\upsilon_a}{\upsilon_c}\right) x_c} x_{H_2O,mix} \tag{A3-34}$$

$$x_{a,mix} = \frac{n_a}{n_{H_2O} + n_c + n_a + n_{gas}} = \frac{\frac{n_a}{n_{H_2O}}}{\frac{n_{H_2O} + n_c + n_a}{n_{H_2O}} + \frac{n_{gas}}{n_{H_2O}}} = \frac{x_a}{1 - \left(1 + \frac{\upsilon_c}{\upsilon_a}\right) x_a} x_{H_2O,mix} \tag{A3-35}$$

Appendix 4-1 Raman spectra of guest additives

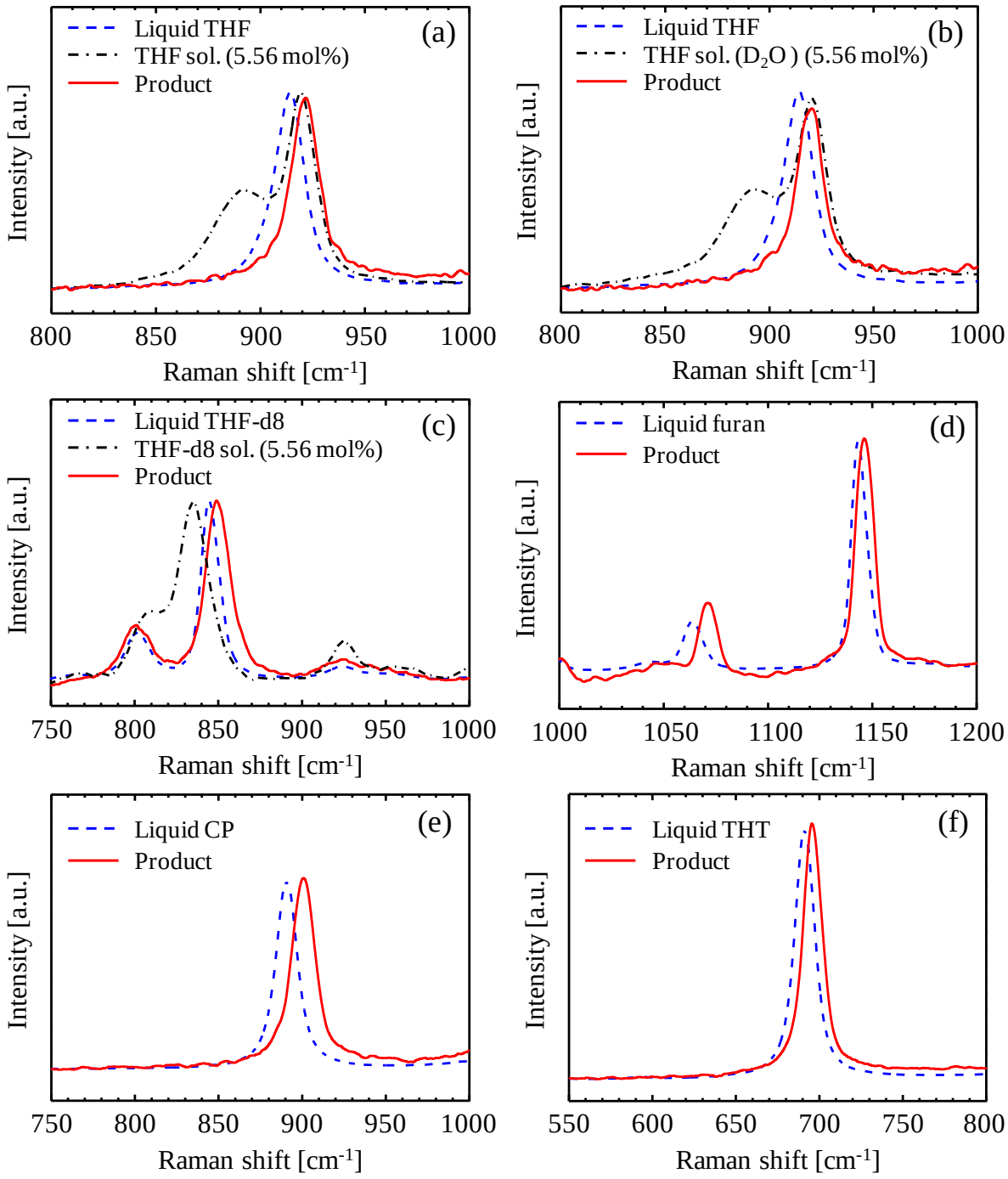

Figure A4-1. Raman spectra of (a) tetrahydrofuran (THF) + water systems, (b) THF + D_2O systems, (c) THF-d8 + water systems, (d) furan + water systems, (e) cyclopentane (CP) + water systems and (f) tetrahydrothiophene (THT) + water systems at room temperature and atmospheric pressure. The continuous (red), dashed-dotted (black) and dashed (blue) lines show clathrate hydrate product, organic aqueous solution and organic liquid, respectively.

Appendix 4-2 X-ray diffraction patterns of clathrate hydrates

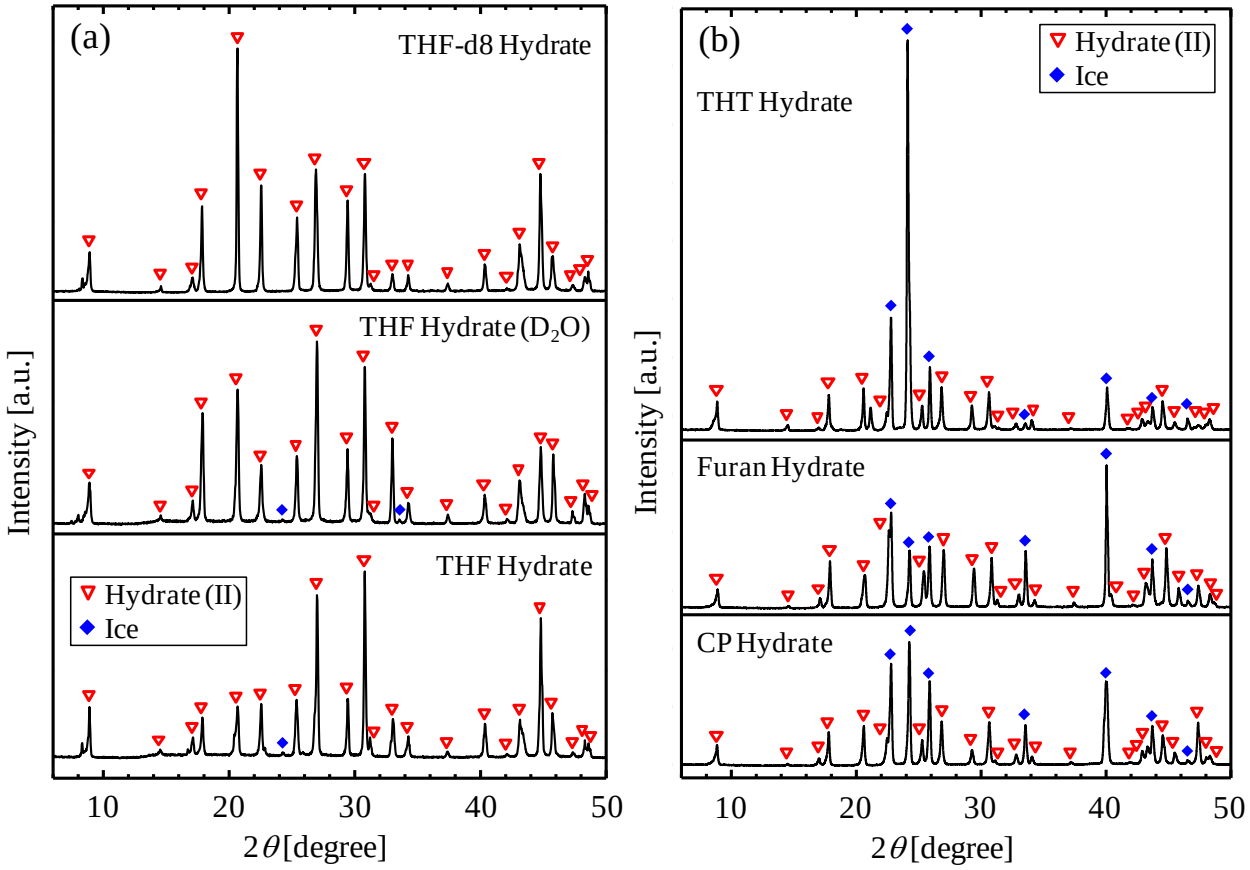

Figure A4-2. XRD patterns of (a) hydrophilic solvent systems (tetrahydrofuran (THF) hydrate, THF hydrate (D_2O) and THF-d8 hydrate) and (b) hydrophobic solvent systems (cyclopentane (CP) hydrate, furan hydrate and tetrahydrothiophene (THT) hydrate) at 123 K. Down-pointing triangles (red) and diamond (blue) show hydrate (sII) and ice peaks, respectively.

Appendix 4-3 Raman spectra of hydrogen included in hydrates

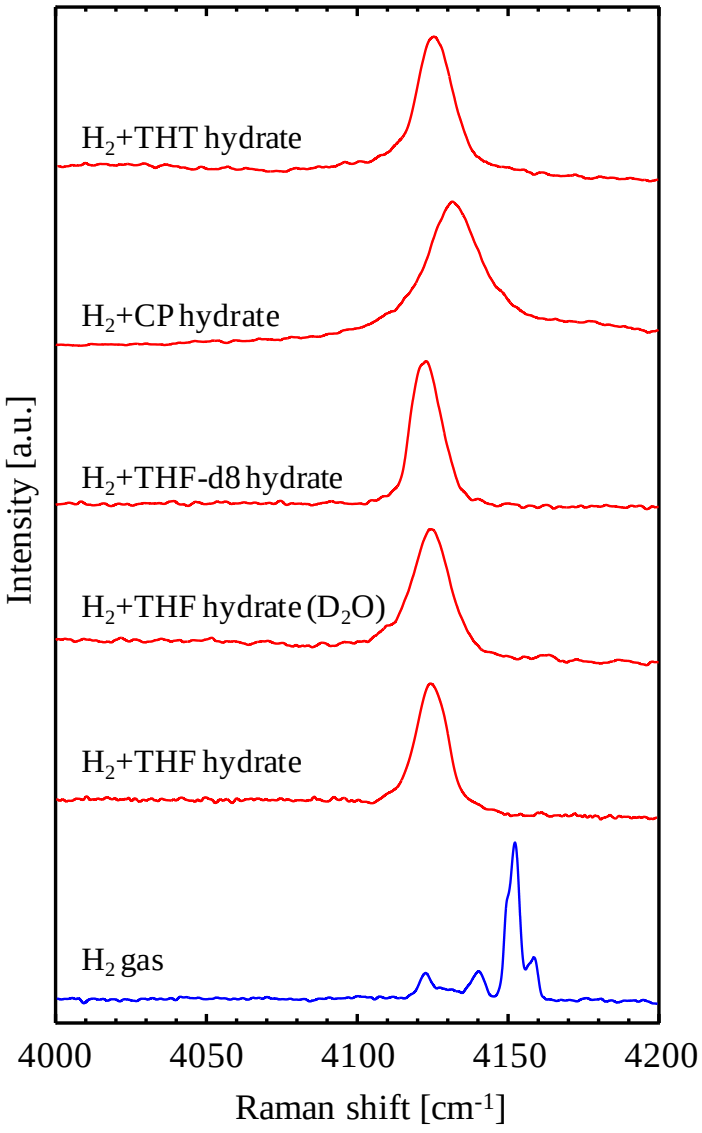

Figure A4-3. Raman spectra of H_2 in gas phase (blue) and clathrate hydrates (H_2+tetrahydrofuran (THF), H_2+THF (D_2O), H_2+THF-d8, H_2+cyclopentane (CP) and H_2+tetrahydrothiophene (THT)) phase (red) at room temperature.

Appendix 4-4 Pressure dependence of hydrogen adsorption

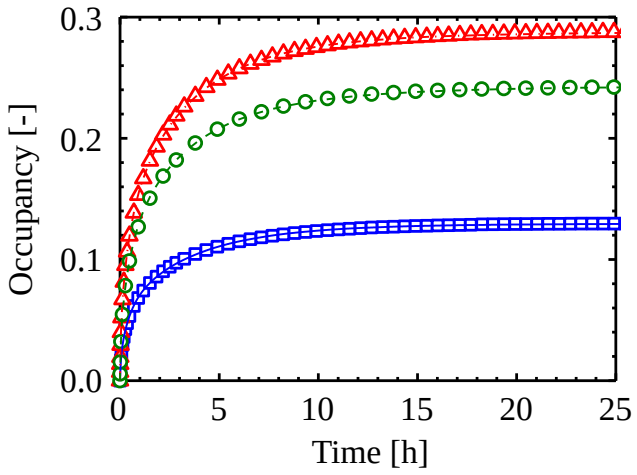

Figure A4-4. Correlated of H_2 adsorption rates in tetrahydrofuran (THF) clathrate hydrate particles at 269 K with multiple adsorption resistant (MAR) model. Red triangles (dashed-dotted line), green circles (dashed line) and blue squares (continuous line) show at 10 (Run 5), 8 (Run 2) and 4 (Run 4) MPa, respectively.

Appendix 4-5 Temperature dependence of hydrogen adsorption

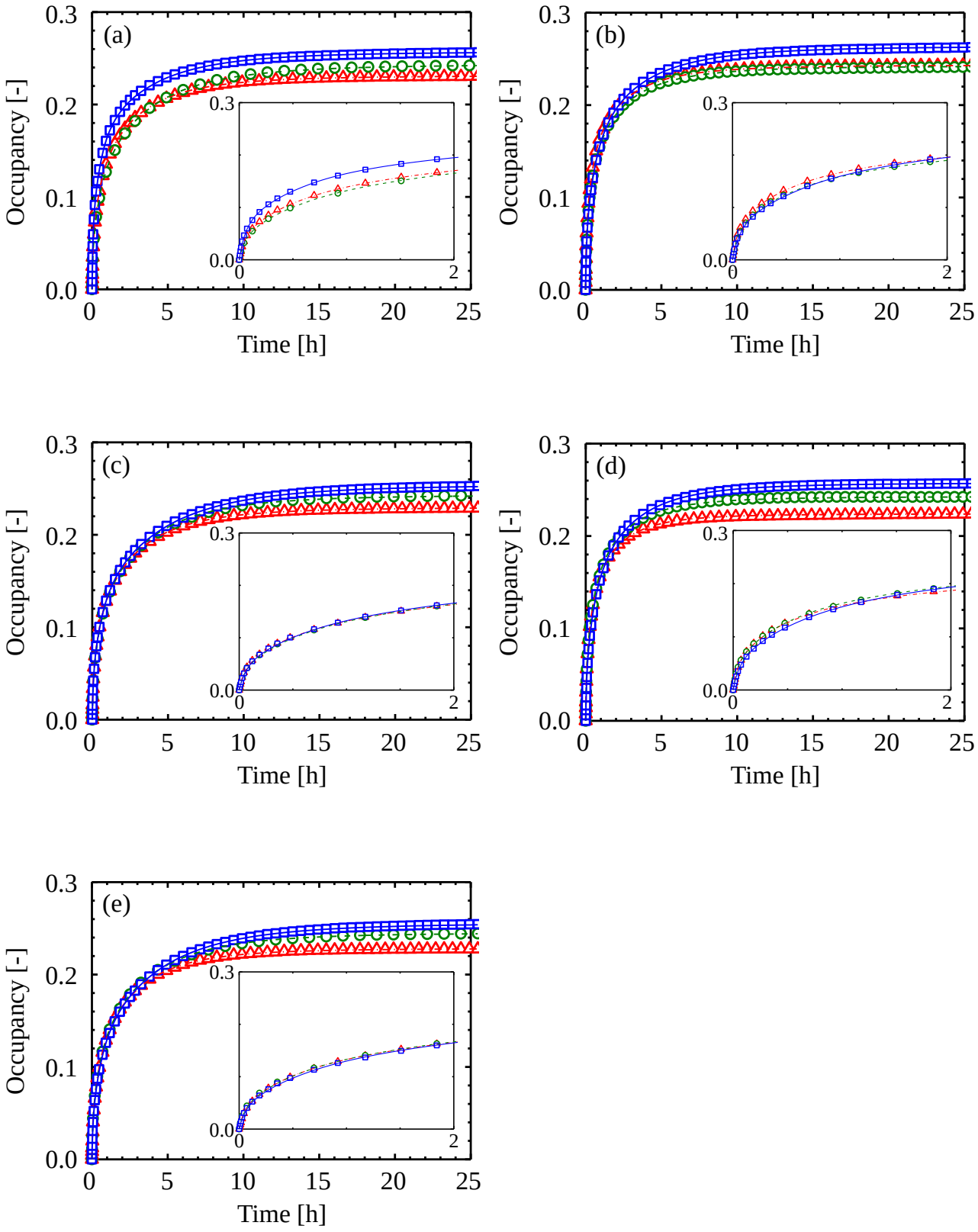

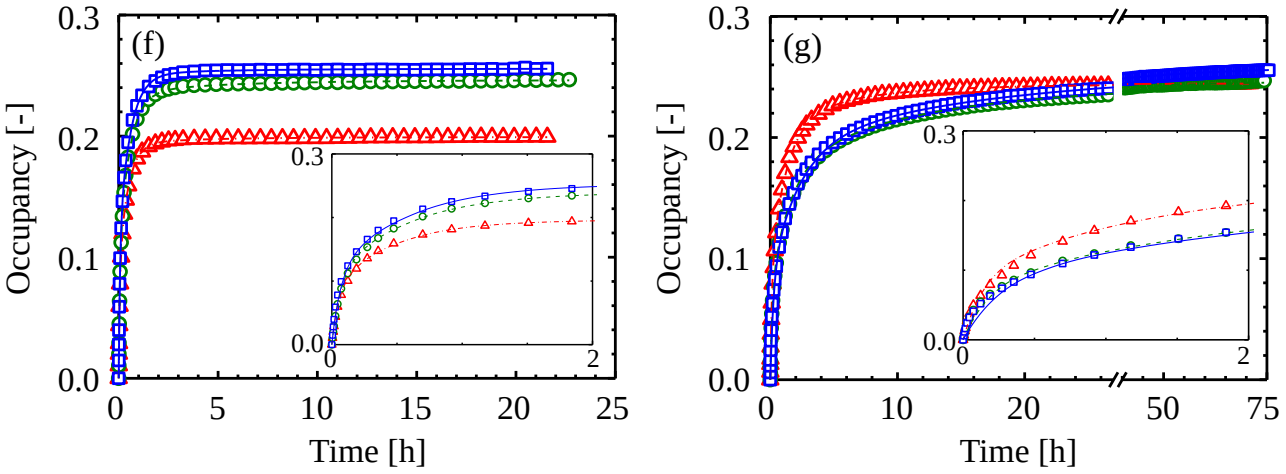

Figure A4-5. Correlated H_2 adsorption rates for (a) 5.6 mol% tetrahydrofuran (THF) (Run 1 – 3), (b) 6.2 mol% THF (Run 6 – 8), (c) 5.6 mol% THF (D_2O) (Run 12 – 14), (d) 6.2 mol% THF (D_2O) (Run 15 – 17), (e) 5.6 mol% THF-d8 (Run 18 – 20), (f) furan (Run 21 – 23) and (g) cyclopentane (CP) (Run 24 – 26) clathrate hydrate particles at 8 MPa with multiple adsorption resistant (MAR) model. Blue squares (continuous line), green circles (dashed line) and red triangles (dashed-dotted line) show at 273, 269 and 265 K, respectively. Inset: expanded view at 0 – 2 h.

Appendix 5-1 Uncertainty of selectivities

The uncertainty of the selectivities was estimated from the H_2 composition difference between initial and final conditions of the experiment. The H_2 composition used was the average value ± standard deviation. The standard deviations of the H_2 composition were 0.0004 – 0.0007. Table A5-1 summarizes the relationship between the selectivity and the combination of the H_2 composition at initial and final conditions of the experiment.

Table A5-1. Relationship between the selectivity, S_{H_2/CO_2} and the combination of the H_2 composition $y_{H_2} \pm \sigma$ at initial and final conditions of the experiment. The σ is the standard deviation.

S_{H_2/CO_2} [-]	$y_{H_2,initial}$ [-]	$y_{H_2,final}$ [-]
Minimum	$y_{H_2,mean} + \sigma$	$y_{H_2,mean} - \sigma$
Median	$y_{H_2,mean}$	$y_{H_2,mean}$
Maximum	$y_{H_2,mean} - \sigma$	$y_{H_2,mean} + \sigma$

The uncertainty of the selectivity, $u\left(S_{H_2/CO_2}\right)$ was defined as Eq. (A5-1):

$$u\left(S_{H_2/CO_2}\right)\% = \frac{\sigma_{S_{H_2/CO_2}}}{S_{H_2/CO_2,mean}} \times 100 \qquad \text{(A5-1)}$$

where $S_{H_2/CO_2,mean}$ and $\sigma_{S_{H_2/CO_2}}$ are the average and the standard deviation of S_{H_2/CO_2}, respectively. The selectivities were calculated from $S_{H_2/CO_2,minimum}$, $S_{H_2/CO_2,median}$ and $S_{H_2/CO_2,maximum}$. Table A5-2 summarizes the uncertainties of the selectivity for runs 16 – 20 (Chapter 5).

Table A5-2. Uncertainty of the selectivities, $u\left(S_{H_2/CO_2}\right)$ and selectivity, S_{H_2/CO_2} and standard deviation, $\sigma_{S_{H_2/CO_2}}$ for runs 16 – 20 (Chapter 5).

	Minimum	Median	Maximum	Mean	Std. Dev.	Uncertainty
Run	S_{H_2/CO_2} [-]				$\sigma_{S_{H_2/CO_2}}$ [-]	$u\left(S_{H_2/CO_2}\right)$%
16	25.31	28.02	31.25	28.19	2.97	10.5
17	9.13	12.22	17.09	12.81	4.01	31.3
18	14.83	18.82	24.84	19.49	5.04	25.9
19	25.81	32.06	41.46	33.11	7.88	23.8
20	11.24	15.05	21.25	15.85	5.05	31.8

Appendix 5-2 Differential scanning calorimetry of semi-clathrate hydrates

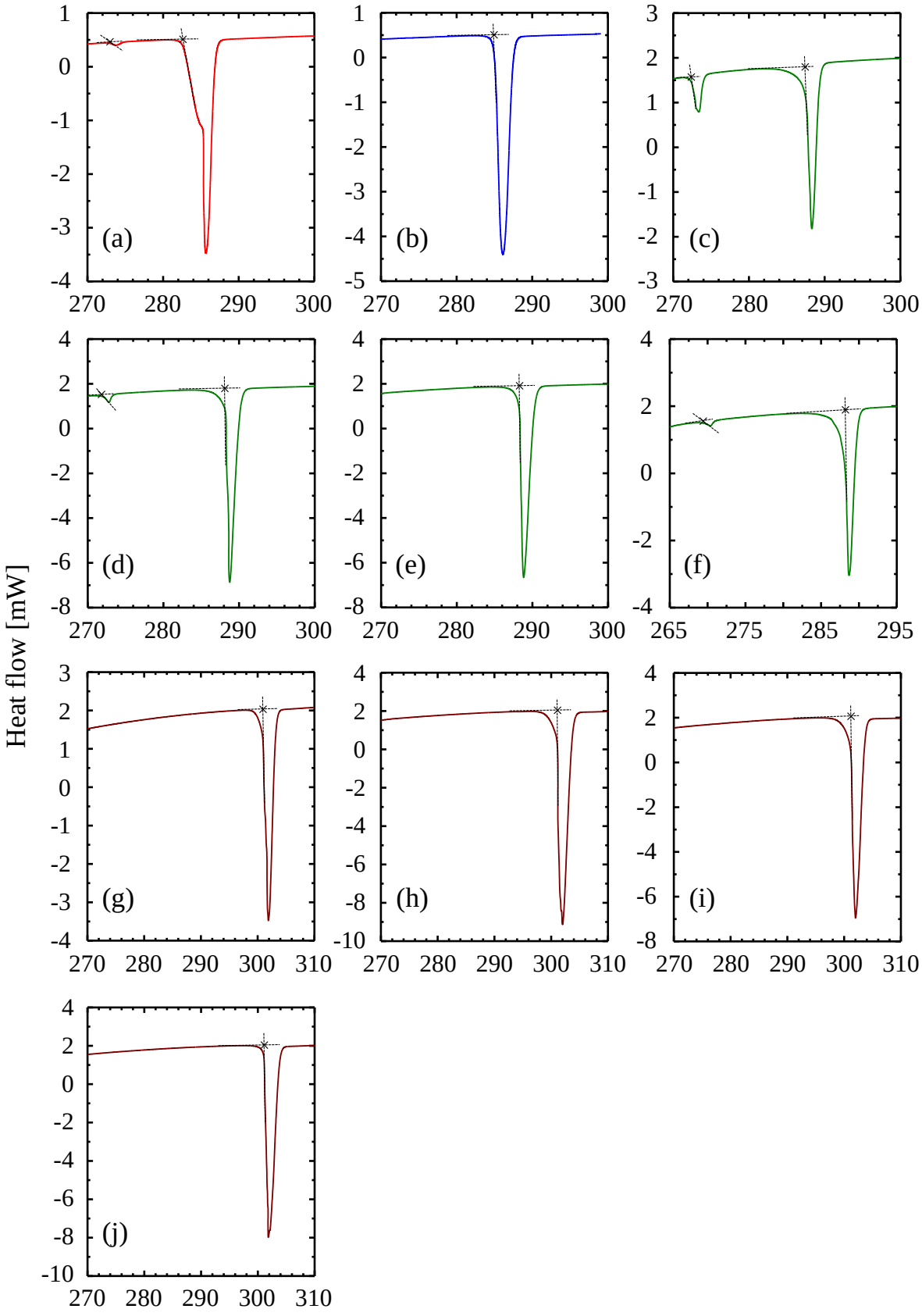

Figure. A5-1. Differential scanning calorimeter (DSC) curves of TBA salts semi-clathrate hydrates decomposition process at atmospheric pressure for a heating rate of 1 K/min. Symbol:×: estimated decomposition temperature for each structure. Red line (a) HS-I TBAB semi-clathrate hydrate, blue line (b) TS-I TBAB semi-clathrate hydrate, green lines (c – f) TBAC semi-clathrate hydrates and brown lines (g – j) TBAF semi-clathrate hydrates. TBAB semi-clathrate hydrates were formed at (a) 2.6 mol% TBAB and 274 K (HS-I rich and ice), (b) 3.7 mol% TBAB and 283 K (TS-I rich). TBAC semi-clathrate hydrates were formed at (c) 2.6 mol% TBAC and 276 K (TS-I and ice), (d) 3.0 mol% TBAC and 276 K (TS-I and ice), (e) 3.2 mol% TBAC and 276 K (TS-I) and (f) 3.7 mol% TBAC and 276 K (TS-I and ice). TBAF semi-clathrate hydrates were formed at (g) 3.0 mol% TBAF and 276 K (TS-I or SCS-I), (h) 3.0 mol% TBAF and 296 K (TS-I or SCS-I), (i) 3.3 mol% TBAF and 276 K (TS-I or SCS-I) and (j) 3.3 mol% TBAF and 296 K (TS-I or SCS-I).

Appendix 5-3 Raman spectra of semi-clathrate hydrates

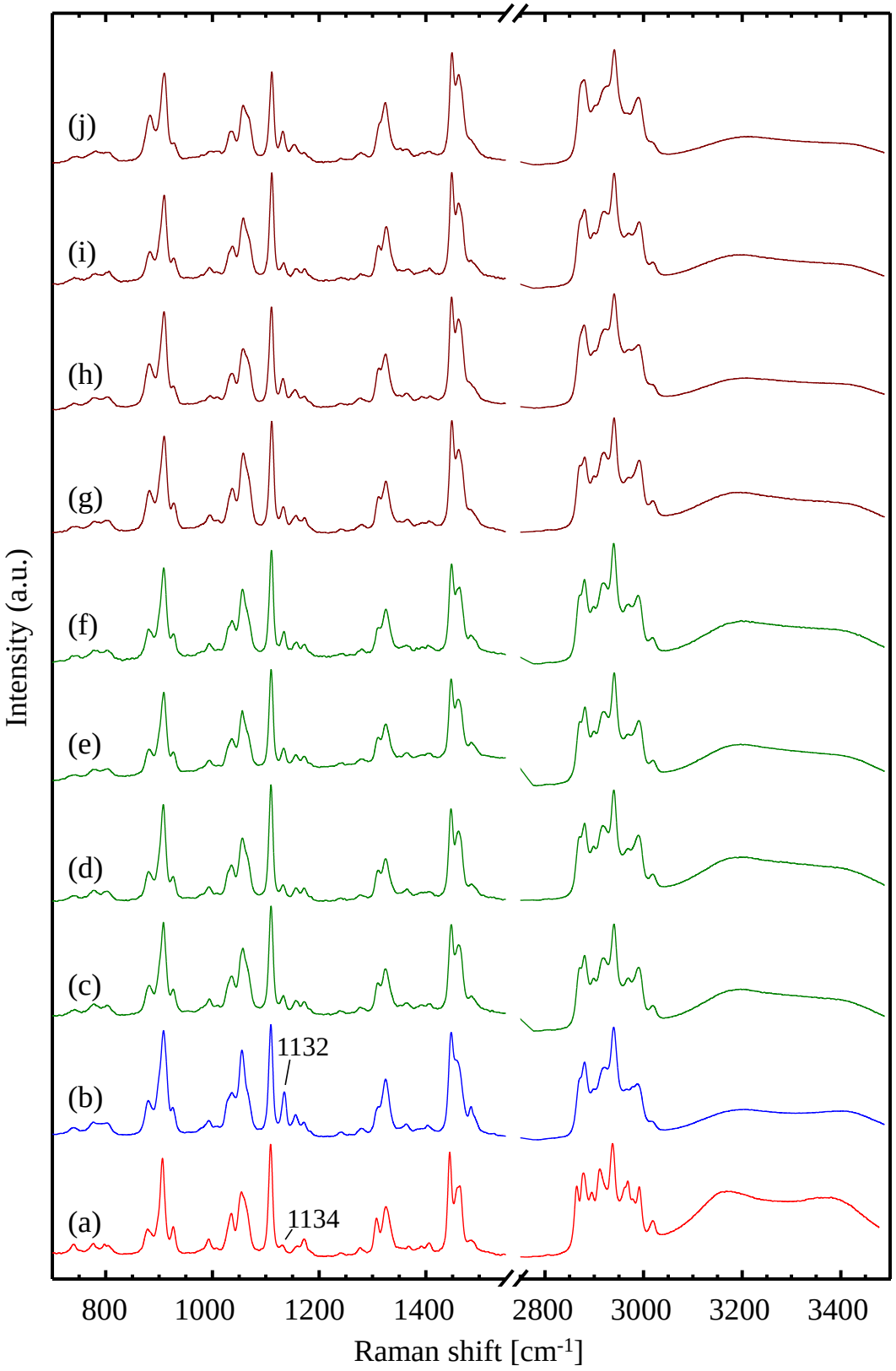

Figure. A5-2. Raman spectra for TBA salts systems at room temperature, atmospheric pressure. Red line (a) HS-I TBAB semi-clathrate hydrate,[20] blue line (b) TS-I TBAB semi-clathrate hydrate,[20] green lines (c – f) TBAC semi-clathrate hydrates and brown lines (g – j) TBAF semi-clathrate hydrates. TBAB semi-clathrate hydrates were formed at (a) 2.6 mol% TBAB and 274 K (HS-I rich and ice), (b) 3.7 mol% TBAB and 283 K (TS-I rich). TBAC semi-clathrate hydrates were formed at (c) 2.6 mol% TBAC and 276 K (TS-I), (d) 3.0 mol% TBAC and 276 K (TS-I), (e) 3.2 mol% TBAC and 276 K (TS-I) and (f) 3.7 mol% TBAC and 276 K (TS-I). TBAF semi-clathrate hydrates were formed at (g) 3.0 mol% TBAF and 276 K (TS-I or SCS-I), (h) 3.0 mol% TBAF and 296 K (TS-I or SCS-I), (i) 3.3 mol% TBAF and 276 K (TS-I or SCS-I) and (j) 3.3 mol% TBAF and 296 K (TS-I or SCS-I). The Raman peak around 1134 cm^{-1} depends on TBAB semi-clathrate hydrate structure.

Appendix 5-4 Effect of formation temperature on structure of 2.6 mol% tetra-*n*-butyl ammonium bromide (TBAB) semi-clathrate hydrates

The TBAB semi-clathrate hydrate forms tetragonal structure-I (TS-I) and hexagonal structure-I (HS-I).[9,10] The formed semi-clathrate hydrate structures were confirmed with Raman spectroscopy (NRS-5100, JASCO, Tokyo) at room temperature and atmospheric pressure, and with differential scanning calorimeter (DSC). The green laser used in the Raman measurements had a wavelength of 532 nm and the grating used was 1800 gr/mm. The objective lens was twenty fold. Spectral resolution was 1 cm^{-1} and exposure times used for the TBAB semi-clathrate hydrates were 25 s, with the cumulative number being three. Raman peaks can be observed at around 700-1500 and 2800-3000 cm^{-1} corresponding to the TBAB molecule, and the broad peak at 3200-3400 cm^{-1} corresponds to O-H vibration of the water molecule. Then, two wavenumbers in the center of these regions were set at 1100 cm^{-1} and 3150 cm^{-1} and used to compare the samples.

For DSC analyses, sample pans used were alodine aluminum with a simple crimp seal. The decomposition temperature for each heating rate was calibrated by using ice and gallium at a heating rate of 1 K/min in the DSC with a flow rate of 40 $cm^3 \cdot min^{-1}$ of nitrogen. About 2 - 5 mg of sample was placed in the sample pan that was kept in a refrigerator before being loaded into the DSC cell. The sample was cooled to 233 K with dry ice and methanol solution. Then, the sample was heated to 318 K at a heating rate of 1 K/min. The decomposition temperature for each sample was determined from the intersection of the tangent of the endothermic curve and standard baseline on the lower temperature side of the endothermic peak.

Table A5-3 summarizes hydrate formation conditions, adsorbent characteristics and

thermophysical properties of the prepared TBAB samples. Results are discussed in detail in the following sections below. Figure A5-3 shows the Raman spectra for the 2.6 mol% TBAB semi-clathrate hydrates.

Table A5-3. Hydrate formation conditions, adsorbent characteristics and thermophysical properties according to 2.6 mol% tetra-*n*-butyl ammonium bromide (TBAB) semi-clathrate hydrate formation temperature (T_{form}), and degree of supercooling (ΔT). The A_{ratio} is the Raman peak area ratio of the peak at 1134 cm^{-1} to the peak at 1109 cm^{-1}.

T_{form} [K]	ΔT [K]	A_{ratio} [-]	DSC peak [K]		
			TS-I	HS-I	Ice
281.6	1.2	0.37	286.4	-	-
278.1	4.7	0.17	284.0	281.5	272.5
274.1	8.7	0.07	-	282.2	272.5
			284.6[21]	282.8[21]	-

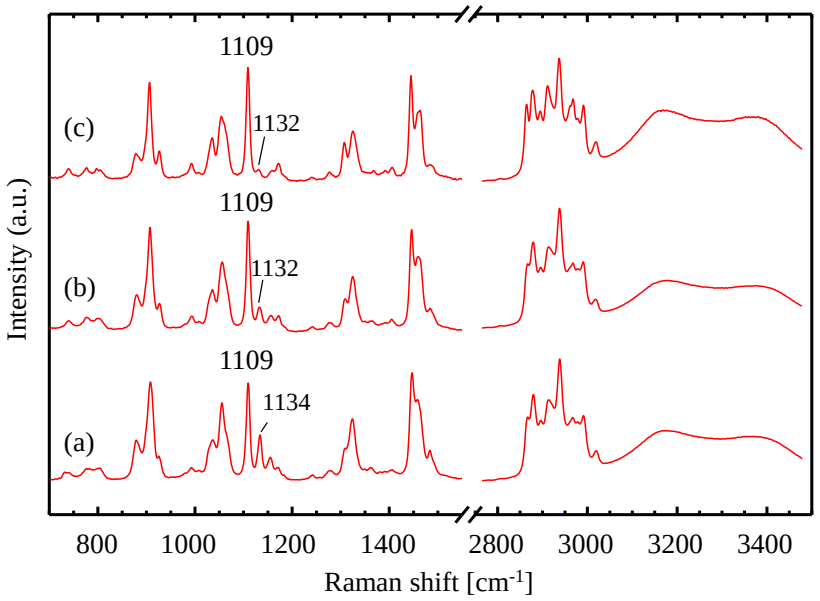

Figure A5-3. Raman spectra for 2.6 mol% tetra-*n*-butyl ammonium bromide (TBAB) semi-clathrate hydrate at room temperature, atmospheric pressure. TBAB semi-clathrate hydrates were formed at (a) 281.6 K (TS-I rich), (b) 278.1 K (mixture of TS-I, HS-I and ice) and (c) 274.1 K (HS-I rich). The Raman peak 1109 cm^{-1} was assumed as the independent of the semi-clathrate hydrate structure. The Raman peak around 1134 cm^{-1} depends on TBAB semi-clathrate hydrate structure.[22]

The Raman peak around 1134 cm^{-1} for the TBAB semi-clathrate hydrate structure is known to change greatly with structure.[22] Thus, the Raman peak at 1109 cm^{-1} was assumed as being independent of the semi-clathrate hydrate structure and the structure of 2.6 mol% TBAB semi-clathrate was assessed by the peak area ratio of the peak at 1134 cm^{-1} to the peak at 1109 cm^{-1}. The peak area ratios (Table A5-3) for the degree of supercooling of 1, 5 and 9 K were 0.37, 0.17 and 0.07, respectively. These results indicate that the hydrate structure was HS-I rich for 2.6 mol% TBAB for a degree of supercooling of 9 K.

Figure A5-4 shows DSC curves for the 2.6 mol% TBAB semi-clathrate hydrates. The decomposition temperature point for the 2.6 mol% TBAB semi-clathrate hydrate at a degree of supercooling of 1 K were 286.4 K (Figure A5-4 a). This value (Table A5-3) was close to that the literature value of 285.2 K for 3.7 mol% TBAB semi-clathrate hydrate of TS-I,[21] and so it can be concluded that the sample (Figure A5-4 a) was rich in TS-I. The decomposition temperature point for 2.6 mol% TBAB semi-clathrate hydrate at a degree of supercooling of 5 K was 272.5, 281.5 and 284.0 K (Figure A5-4 b, Table A5-3). Since the literature values (Table A5-3) for 2.6 mol% TBAB semi-clathrate hydrate of TS-I and HS-I were 284.6 and 282.8 K, respectively, it can be concluded that the sample (Figure A5-4 b) prepared with 5 K supercooling was a mixture of ice, TS-I and HS-I. The decomposition temperature point for 2.6 mol% TBAB semi-clathrate hydrate at a degree of supercooling of 9 K was 272.5 and 282.2 K (Figure A5-4 b, Table A5-3). Since the peak of TS-I was not observed, analysis shows that the sample consisted of mainly HS-I. However, some TS-I cannot be excluded as the peak might be hidden by the small peak observed for ice (Figure A5-4 c). The 2.6 mol% TBAB semi-clathrate hydrate prepared with a degree of supercooling of 9 K was

used in the adsorption experiments since it consisted mainly of HS-I.

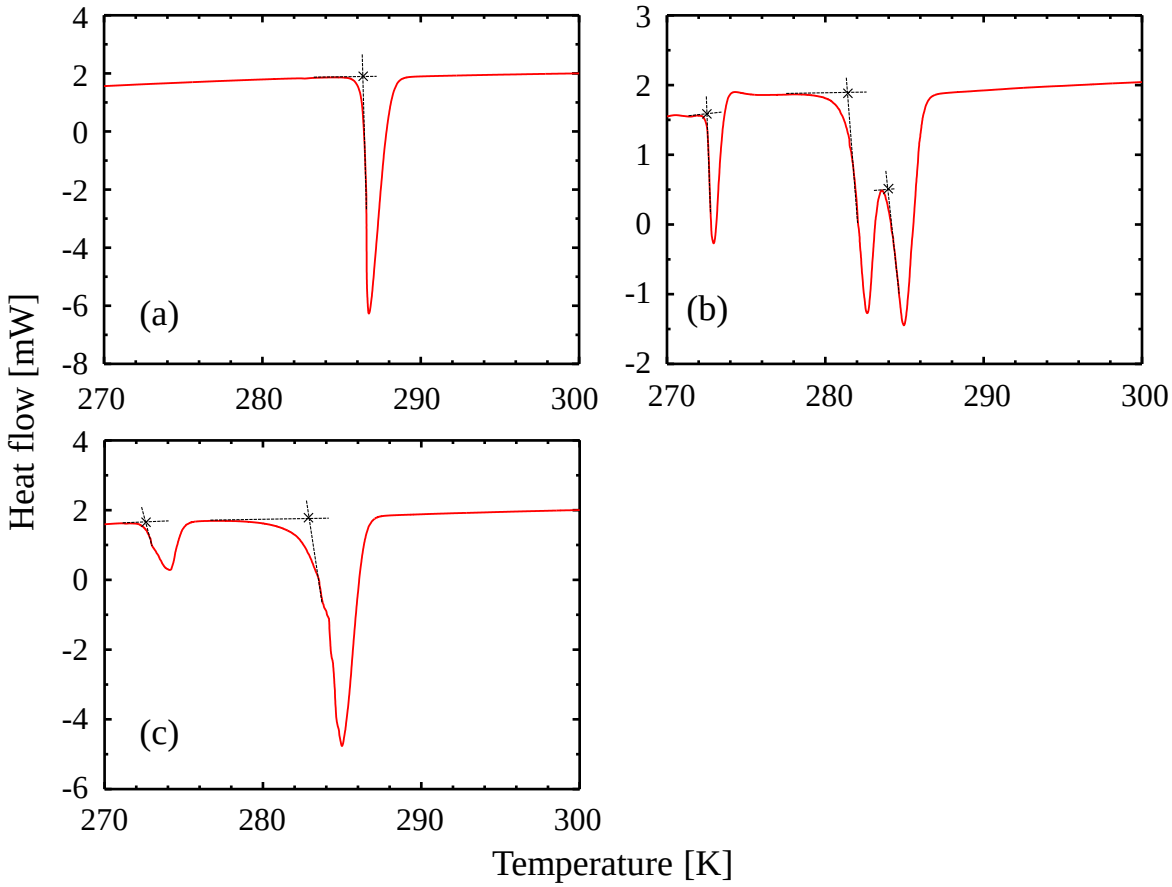

Figure A5-4　Differential scanning calorimeter (DSC) curves of 2.6 mol% tetra-*n*-butyl ammonium bromide (TBAB) semi-clathrate hydrate decomposition process at atmospheric pressure for a heating rate of 1 K/min. Symbol:×: decomposition temperature for each structure. TBAB semi-clathrate hydrates were formed at (a) 281.6 K (TS-I rich), (b) 278.1 K (mixture of TS-I, HS-I and ice) and (c) 274.1 K (HS-I rich)

References

1. Poling BE, Reid RC, Prausnitz JM, O'Connell JP. *The properties of gases and liquids*. 5th edition ed.McGraw-Hill; New York. 2001.
2. Spano JO, Heck CK, Barrick PL. Liquid-vapor equilibria of hydrogen-carbon dioxide system. J Chem Eng Data. 1968;13:168-171.
3. Yorizane M, Yoshimura S, Masuoka H. Vapor liquid equilibrium at high pressure (N_2-CO_2, H_2-CO_2 system). Kagaku Kogaku. 1970;34:953 - 957.
4. Tsang CY, Streett WB. Phase equilibria in the H_2/CO_2 system at temperatures from 220 K to 290 K and pressures to 172 MPa. Chem Eng Sci. 1981;36:993-1000.
5. Bezanehtak K, Combes GB, Dehghani F, Foster NR, Tomasko DL. Vapor-liquid equilibrium for binary systems of carbon dioxide plus methanol, hydrogen plus methanol, and hydrogen plus carbon dioxide at high pressures. J Chem Eng Data. 2002;47:161-168.
6. NIST Chemistry WebBook. http://webbook.nist.gov/chemistry/. Accessed March, 2013.
7. Deiters UK. Calculation of densities from cubic equations of state. AIChE J. 2002;48:882-886.
8. Joung IS, Cheatham TE. Determination of alkali and halide monovalent ion parameters for use in explicitly solvated biomolecular simulations. J Phys Chem B. 2008;112:9020-9041.
9. Shimada W, Shiro M, Kondo H, Takeya S, Oyama H, Ebinuma T, Narita H. Tetra-*n*-butylammonium bromide-water (1/38). Acta Crystallogr C. 2005;61:O65-O66.
10. Davidson DW. *Water - A Comprehensive Treatise*. Vol 2.Plenum Press; New York. 1973.
11. Dyadin YA, Terekhova IS, Polyanskaya TM, Aladko LS. Clathrate hydrates of tetrabutylammonium fluoride and oxalate. J Struct Chem. 1976;17:566-571.
12. Komarov VY, Rodionova TV, Terekhova IS, Kuratieva NV. The cubic superstructure-I of tetrabutylammonium fluoride $(C_4H_9)_4NF\cdot 29.7H_2O$ clathrate hydrate. J Inclusion Phenom Macro. 2007;59:11-15.
13. Lindenbaum S, Boyd GE. Osmotic + activity coefficients for symmetrical tetraalkyl ammonium halides in aqueous solution at 25 ºC. J Phys Chem-Us. 1964;68:911-917.
14. Wen WY, Saito S, Lee CM. Activity and osmotic coefficients for four symmetrical tetraalkylammonium fluroides in aqueous solutions at 25 ºC. J Phys Chem-Us. 1966;70:1244-1248.
15. Krichevsky JD, Kasarnovsky JS. Thermodynamical calculations of solubilities of nitrogen and hydrogen in water at high pressures. J. Am. Chem. Soc. 1935;57:2168-2172.

16. Moore JC, Battino R, Rettich TR, Handa YP, Wilhelm E. Partial molar volumes of gases at infinite dilution in water at 298.15 K. J Chem Eng Data. 1982;27:22-24.

17. Klauda JB, Sandler SI. Phase behavior of clathrate hydrates: a model for single and multiple gas component hydrates. Chem Eng Sci. 2003;58:27-41.

18. Belandria V, Mohammadi AH, Richon D. Volumetric properties of the (tetrahydrofuran + water) and (tetra-*n*-butyl ammonium bromide + water) systems: Experimental measurements and correlations. J Chem Thermodyn. 2009;41:1382-1386.

19. Chen CC, Britt HI, Boston JF, Evans LB. Local composition model for excess gibbs energy of electrolyte systems .1. single solvent, single completely dissociated electrolyte systems. AIChE J. 1982;28:588-596.

20. Komatsu H, Hayasaka A, Ota M, Sato Y, Watanabe M, Smith RL. Measurement of pure hydrogen and pure carbon dioxide adsorption equilibria for THF clathrate hydrate and tetra-*n*-butyl ammonium bromide semi-clathrate hydrate. Fluid Phase Equilib. 2013;357:80-85.

21. Oyama H, Shimada W, Ebinuma T, Kamata Y, Takeya S, Uchida T, Nagao J, Narita H. Phase diagram, latent heat, and specific heat of TBAB semiclathrate hydrate crystals. Fluid Phase Equilib. 2005;234:131-135.

22. Hashimoto S, Sugahara T, Moritoki M, Sato H, Ohgaki K. Thermodynamic stability of hydrogen + tetra-*n*-butyl ammonium bromide mixed gas hydrate in nonstoichiometric aqueous solutions. Chem Eng Sci. 2008;63:1092-1097.

Publications

[1] Hiroyuki Komatsu, Hiroki Yoshioka, Masaki Ota, Yoshiyuki Sato, Masaru Watanabe, Richard L. Smith Jr., and Cor J. Peters,

Phase Equilibrium Measurements of Hydrogen-Tetrahydrofuran and Hydrogen-Cyclopentane Binary Clathrate Hydrate systems,

Journal of Chemical Engineering Data, **55**, 2214-2218 (2010)

(Chapters 2 &3)

[2] Hiroyuki Komatsu, Masaki Ota, Richard L. Smith, Jr. and Hiroshi Inomata,

Review of CO_2-CH_4 clathrate hydrate replacement reaction laboratory studies – Properties and kinetics,

Journal of the Taiwan Institute of Chemical Engineers, **44**, 517-537 (2013)

(Chapters 1&2)

[3] Hiroyuki Komatsu, Atsushi Hayasaka, Masaki Ota, Yoshiyuki Sato, Masaru Watanabe and Richard L. Smith Jr.,

Measurement of pure hydrogen and pure carbon dioxide adsorption equilibria for THF clathrate hydrate and tetra-n-butyl ammonium bromide semi-clathrate hydrate,

*Fluid Phase Equilib*ria, **357**, 80-85 (2013)

(Chapter 5)

[4] Hiroyuki Komatsu, Masaki Ota, Yoshiyuki Sato, Masaru Watanabe and Richard L. Smith Jr., Multiple adsorption resistance model for constituent molecular effects in hydrogen clathration kinetics in clathrate hydrate particles,

Chemical Engineering Science, **108**, 270-282 (2014)

(Chapter 4)

[5] Hiroyuki Komatsu, Masaki Ota, Yoshiyuki Sato, Masaru Watanabe and Richard L. Smith Jr., Hydrogen and carbon dioxide adsorption with tetra-*n*-butyl ammonium semi-clathrate hydrates for gas separations,

AIChE Journal, Submitted (2014)

(Chapter 5)